

Loughborough University Institutional Repository

Pigments for the 21st century

This item was submitted to Loughborough University's Institutional Repository by the/an author.

Additional Information:

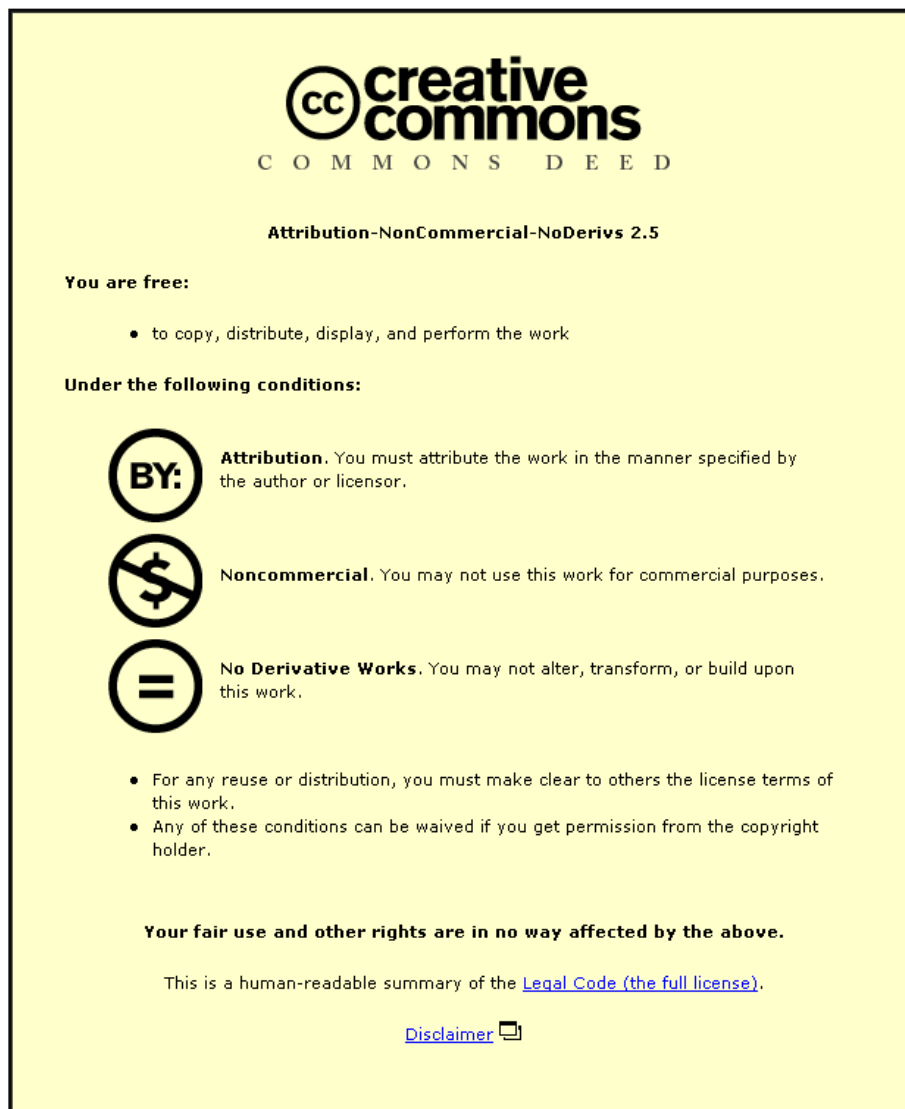
- A Doctoral Thesis. Submitted in partial fulfilment of the requirements for the award of Doctor of Philosophy of Loughborough University.

Metadata Record: <https://dspace.lboro.ac.uk/2134/12528>

Publisher: © Christopher J. Kirk

Please cite the published version.

This item was submitted to Loughborough University as a PhD thesis by the author and is made available in the Institutional Repository (<https://dspace.lboro.ac.uk/>) under the following Creative Commons Licence conditions.



For the full text of this licence, please go to:
<http://creativecommons.org/licenses/by-nc-nd/2.5/>



University Library

Author/Filing Title KIRK, C.J.

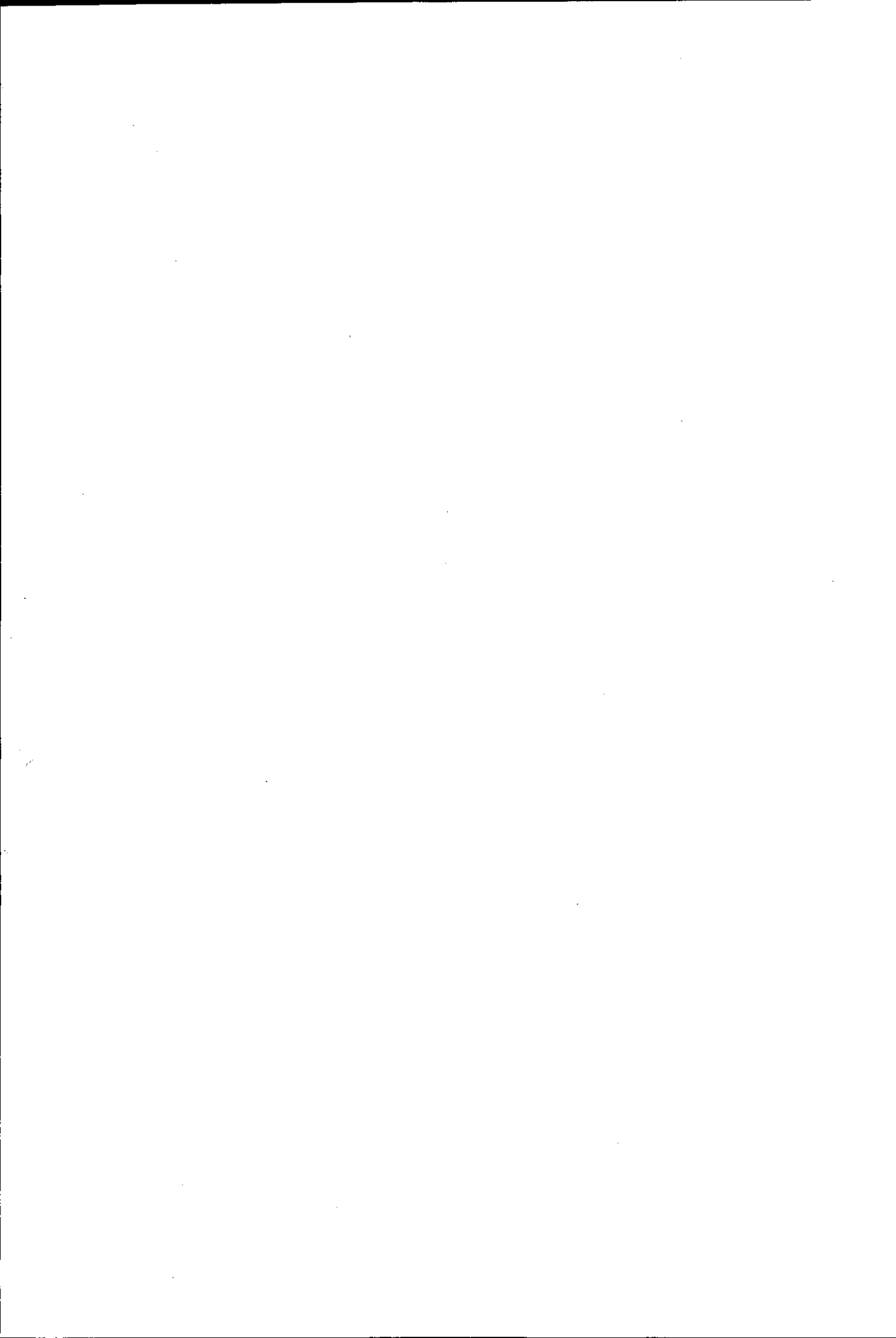
.....
Class Mark T

**Please note that fines are charged on ALL
overdue items.**

--	--	--

0403694299





Pigments for the 21st Century


Christopher J. Kirk

A Doctoral Thesis

Submitted in partial fulfilment of the requirements
for the award of

Ph.D of Loughborough University 2008



 Lehigh University Pittington Library
Date 10/3/09
Class T
Acc No. 0403694299

Abstract

Materials with potential for high temperature inorganic pigment applications (e.g. ceramics) have been synthesised using solid state methods and characterised using powder X-ray and neutron diffraction, magic angle spinning NMR, Mössbauer spectroscopy, UV/Vis spectroscopy and colour measurement techniques.

A number of compounds containing tin (II) and niobium (V) have been modified and doped with various constituents to tailor and widen the colour properties of the bright yellow parent phases. The dark yellow ($L^*(91.28)$, $a^*(13.74)$, $b^*(54.76)$) tin niobium oxide pyrochlores have been re-characterised using neutron diffraction techniques. These materials exhibit both cation and anion disorder caused by a stereoactive lone pair on the tin (II) metal centres. Solid state NMR and Mössbauer studies have shown the presence of tin (IV) on a symmetric site within the primary phase of the pure oxide pyrochlore and methods have been investigated to minimise the tin (II) disproportionation method from where the tin (IV) is derived. A solid solution series between foordite (SnNb_2O_6 , $L^*(92.76)$, $a^*(11.33)$, $b^*(61.22)$) and theurite (SnTa_2O_6) has been prepared with the general formula $\text{SnNb}_{2-x}\text{Ta}_x\text{O}_6$, that is isostructural with both end members. These compounds have been characterised using X-ray diffraction and UV/Vis colour measurement techniques to investigate the loss in colour and changes in structure as a function of niobium content.

A group of new oxychalcogenide compounds, which are based on the tin niobate pyrochlores have been synthesised and studied for use as red/orange pigments ($L^*(69.32)$, $a^*(27.65)$, $b^*(26.14)$). This group of materials contains a rare example of an oxysulfide pyrochlore and the only example of an oxyselenide version of this structure. These compounds have been characterised using neutron diffraction techniques and Rietveld refinement of the data performed to determine the structure. Solid state NMR and Mössbauer spectroscopy have been used to confirm the existence of Sn (IV) in these materials. Colour measurements show a shift towards the red in the colour coordinates as the softer chalcogenides are added and the tin (IV) content falls. Uncoloured cadmium niobium oxide and oxysulfide pyrochlores have been re-evaluated as a direct comparison to the tin series, to investigate any commonality between the only two reported oxysulfide pyrochlore systems. Neutron diffraction techniques have been used for structural characterisation of isotopically pure $^{114}\text{Cd}_2\text{Nb}_2\text{O}_7$ and $^{114}\text{Cd}_2\text{Nb}_2\text{O}_6\text{S}$, and the structural distortions observed in the tin niobates confirmed in these analogous compounds.

A comprehensive study of the lanthanide-doped bismuth oxide phases, $(\text{Bi}_{1-x}\text{Ln}_x)_2\text{O}_3$ ($\text{Ln} = \text{Y}, \text{Er}, \text{Ho}, \text{Dy}, \text{Gd}, \text{Sm}, \text{Nd}, \text{Pr}, \text{La}$), has been carried out. The use of such compounds as potential pigments, as previously reported $(\text{Bi}_{0.6}\text{Sm}_{0.4})_2\text{O}_3$; $L^*(71.21)$, $a^*(16.30)$, $b^*(43.98)$, have been studied. X-ray diffraction techniques have been used to study the metastable defect fluorite structure seen in many of these materials that produces the most well defined colour. The pigment properties of the resulting compounds have been assessed using UV/Vis colour measurement techniques as a function of time to investigate the effect of phase change in colour properties. Structural results have been compared to the high temperature $\delta\text{-Bi}_2\text{O}_3$ structure in order to understand the low stability of this structure.

Solid solutions of $\text{Ca}_{1-x}\text{Sr}_x\text{CuSi}_4\text{O}_{10}$ and $\text{Sr}_{1-x}\text{Ba}_x\text{CuSi}_4\text{O}_{10}$ ($x = 0 - 1$) have been prepared. The effects of the alkali-earths on the structure and colour properties have been studied using X-ray diffraction and colour measurement techniques in order to investigate the instability of some ancient samples to bright light sources.

Keywords: Pigment, red, pyrochlore, oxysulfide, lone-pair, tin, niobium

Acknowledgements

I would like to thank a number of people who made contributions both, academically and emotionally throughout the course of my Ph.D. First and foremost I would like to thank my supervisor Dr. Sandie Dann for giving me this opportunity and for her guidance with work and life in general.

I would like to thank my industrial sponsors Johnson Matthey, and the EPSRC for allowing me to carry out this research. Thanks to everyone at the JM technology centre who helped me exhaustively and tried to point me in the right direction.

Much of the research in this thesis was carried out in collaboration with a number of contributors. Thank you to Duncan O'Brien for carrying out a lot of the groundwork on the tin niobates, thank you also to Emma Kendrick who collaborated on the copper silicates, both through the synthesis of the samples and X-ray diffraction analysis. My gratitude goes to those who helped with the analysis of many of the samples: Professor Mark Smith at University of Warwick for the solid state tin NMR data of both the tin niobates and the tin niobium oxychalcogenides and Dr Mike Thomas from the University of Liverpool for his Mössbauer work on the same samples. Also thank you to my various project students especially George and Michelle who did most of the leg work synthesising the numerous bismuth oxide phases.

Many thanks to the entire Inorganic Chemistry Section who kept me going through the difficult times. Thank you to my mum and dad who believed in me even when I gave them no reason too. Finally thank you to the most important person in the world, my wife. She supported me through my write-up even though she had one to do herself and in the end she was the only reason I managed to finish. Without her everything would have been meaningless.

Abstract.....	I
Acknowledgements.....	II
Contents.....	III
Chapter 1: Introduction.....	1
1.1 The Origins of Colour.....	2
1.1.1. Interaction of Light and Matter.....	2
1.1.2. Excitation-Relaxation Pathways.....	4
1.1.3. Charge Transfer.....	5
1.1.3.1. Metal-Ligand Charge Transfer (MLCT).....	5
1.1.3.2. Inter Valence Charge Transfer (IVCT).....	7
1.1.4. Metal-Centred Electronic Transitions.....	8
1.1.5. Selection Rules.....	9
1.2. Pigments.....	12
1.2.1. The History of Pigments.....	12
1.2.2. Desirable Pigments Properties.....	13
1.2.3. Red Pigments.....	14
1.2.3.1. Cadmium Sulfoselenides.....	15
1.2.3.2. Lead Chromate Pigments.....	16
1.2.3.3. Pigment Toxicity.....	17
1.2.3.4. Possible Replacements.....	18
1.3. The Pyrochlore Structure.....	19
1.3.1. Stereoactive Lone Pairs.....	23
1.4. Rare-Earth Bismuth Oxide.....	24
1.4.1. Structure of δ -Bi ₂ O ₃	25
1.5. Bond Valence Theory.....	26
1.6. The Scope of the Work.....	28
1.7. References.....	30
Chapter 2: Instrumentation and Methodology.....	34
2.1. Sample Preparation.....	35
2.2. Diffraction Experiments.....	36
2.2.1. Diffraction Theory.....	36
2.2.2. X-ray Diffraction.....	38
2.2.2.1. Instrumentation.....	39
2.2.3. Neutron Diffraction.....	41
2.2.3.1. Instrumentation – POLARIS (ISIS).....	41
2.2.3.2. Instrumentation – D20 (ILL, Grenoble).....	43
2.3. Powder Diffraction Data Refinement – The Rietveld Method.....	44
2.3.1. Least Squares Procedure.....	46
2.3.2. Powder Diffraction Profiles Intensities (I_o and I_c).....	47
2.3.2.1. Structure Factor (F_{ph}).....	48
2.3.2.2. Intensity Correction Factors.....	50
2.3.2.3. Peak Profile Functions.....	51
2.4. Nuclear Magnetic Resonance (NMR) Spectroscopy.....	52
2.4.1. Principles of NMR.....	52
2.4.2. The NMR Spectrum.....	54
2.4.3. Solid State NMR.....	56
2.4.3.1. Magic Angle Spinning NMR (MASNMR).....	56
2.5. Mössbauer Spectroscopy.....	57

2.5.1. The Mössbauer Effect.....	58
2.5.2. The Mössbauer Spectroscopy.....	59
2.6. Colour Measurements.....	61
2.6.1. CIE RGB System.....	62
2.6.2. CIE XYZ System.....	64
2.6.3. CIE L*a*b* System.....	66
2.7. References.....	68
Chapter 3: Synthesis and Characterisation of Tin Niobates	69
3.1. Introduction.....	70
3.2. Experimental.....	73
3.2.1. Sn ₂ Nb ₂ O ₇ Pyrochlores.....	73
3.2.2. Sn ₂ Nb ₂ O ₆ -SnTa ₂ O ₆ Solid Solutions.....	74
3.2.3. X-ray Diffraction.....	74
3.2.4. Mössbauer Analysis.....	75
3.2.5. Solid State NMR.....	75
3.2.6. UV/VIS Colour Measurements.....	75
3.3. Results.....	76
3.3.1. Characterisation of Sn ₂ Nb ₂ O ₇	76
3.3.1.1. X-ray Diffraction.....	76
3.3.1.2. ¹¹⁹ Sn MASNMR.....	80
3.3.1.3. ¹¹⁹ Sn Mössbauer Spectroscopy.....	81
3.3.1.4. Neutron Diffraction Analysis.....	83
3.3.1.5. Bond Valence Calculations.....	93
3.3.2. Characterisation of Sn ₂ Nb ₂ O ₆ -SnTa ₂ O ₆ Solid Solution.....	99
3.3.2.1. X-ray Diffraction.....	100
3.3.2.2. UV/VIS Colour Measurements.....	108
3.4 Conclusions.....	110
3.5. References.....	111
Chapter 4: Doped Tin Niobates	112
4.1. Introduction.....	113
4.1.1. Tin Niobium Oxychalcogenides (Sn ₂ Nb ₂ O _{7-x} X _x ; X = S, Se)	114
4.1.2. Chromium (III) Doped Tin Niobates (Sn ₂ Nb _{2-x} Cr ^{III} _x O _{7-x})..	115
4.2. Experimental.....	116
4.2.1. Tin Niobium Oxychalcogenides.....	116
4.2.2. Chromium Doped Niobates.....	116
4.3. X-ray Diffraction.....	117
4.4. Neutron Diffraction.....	117
4.5. Solid State NMR.....	117
4.6. Mössbauer.....	117
4.7. UV/VIS Colour Measurement.....	118
4.8. Results – Tin Niobium Oxychalcogenides.....	118
4.8.1. X-ray Diffraction.....	118
4.8.2. ¹¹⁹ Sn MASNMR.....	119
4.8.3. Mössbauer Spectroscopy.....	120
4.8.4. Neutron Diffraction.....	124
4.8.5. Valence Calculations.....	130
4.8.6. UV/VIS Colour Measurement.....	136

4.9. Results – Chromium Doped Tin Niobates.....	138
4.9.1. X-ray Diffraction.....	138
4.9.2. Neutron Diffraction.....	139
4.9.3. UV/VIS Colour Measurement.....	143
4.10 Conclusions.....	146
4.11. References.....	147
Chapter 5: Synthesis and Characterisation of Cadmium Niobate Pyrochlores	148
5.1. Introduction.....	149
5.2. Experimental.....	150
5.3 X-ray Diffraction.....	151
5.4 Neutron Diffraction.....	152
5.5. Results.....	153
5.5.1. X-ray Diffraction.....	153
5.5.2. Structural Characterisation.....	156
5.5.2.1 Cd ₂ Nb ₂ O ₇	158
5.5.2.2 Cd ₂ Nb ₂ O ₆ S.....	162
5.6. Conclusions.....	165
5.7. References.....	166
Chapter 6: Rare Earth Bismuth Oxides (Bi_{1-x}Ln_x)₂O₃.....	167
6.1. Introduction.....	168
6.2. Experimental.....	169
6.3. X-ray Diffraction.....	170
6.4. UV/Visible Colour Measurements.....	170
6.5. Results - X-ray Diffraction.....	170
6.5.1. Ln ₂ O ₃ -Bi ₂ O ₃ (Ln = Y, Er, Ho, Dy, Gd) Solid Solutions.....	171
6.5.2. Sm ₂ O ₃ -Bi ₂ O ₃ Solid Solutions.....	172
6.5.3. Ln ₂ O ₃ -Bi ₂ O ₃ (Ln = Nd, Pr and La).....	174
6.6. Results – L*a*b* Colour Measurements.....	176
6.6.1. Ln ₂ O ₃ -Bi ₂ O ₃ (Ln = Y, Dy, Gd, Sm).....	176
6.6.2. Ln ₂ O ₃ -Bi ₂ O ₃ (Ln = Ho, Er).....	179
6.6.3. Ln ₂ O ₃ -Bi ₂ O ₃ (Ln = Pr, Nd, La).....	181
6.7. Results – Structural Refinement.....	183
6.7.1. Refinement of Dy Samples.....	184
6.7.2. Valence Calculations.....	191
6.8. High Temperature Study of Bismuth Oxide.....	194
6.8.1. Refinement of δ-Bi ₂ O ₃	197
6.9. Conclusions.....	199
6.10. References.....	201
Chapter 7: Egyptian Blue Series (Ba,Ca,Sr)CuSi₄O₁₀.....	201
7.1. Introduction.....	202
7.2. Experimental.....	204
7.3. X-ray Diffraction Analysis.....	204
7.4. UV/VIS Colour Measurements.....	204
7.5. Results.....	205
7.5.1.X-ray Diffraction.....	205

7.5.1.1. Calcium-Strontium Solid Solution.....	205
7.5.2. Strontium-Barium Series.....	209
7.5.3. UV/VIS.....	212
7.6. Conclusions.....	215
7.7. References.....	217
Chapter 8: Summary and Further Work.....	218

Chapter 1
Introduction

1.1. The Origins of Colour

The primary aim behind the synthesis of inorganic pigments is the formation of intense and durable coloured materials for various applications (plastics, ceramics, glass and coatings). When studying the synthesis and characterisation of such pigments it is helpful to understand the origin of the colours they produce. The colours that are seen every day are dependent on the wavelengths of light that are reflected from surrounding objects and materials. If these wavelengths are in the visual part of the electromagnetic spectrum, between 360-780 nm, the human eye can detect them. The colour that is eventually observed, changes from violet at short wavelengths through blue, green and yellow at medium wavelengths, and finally to orange and red at longer wavelengths (Figure 1.1). As well as the individual wavelengths, combinations of wavelengths can combine to give an even greater variety of shades and colours. Understanding the source of colours seen can be essential to enhancing the colour of existing pigments and the production of new synthetic pigments to replace them.

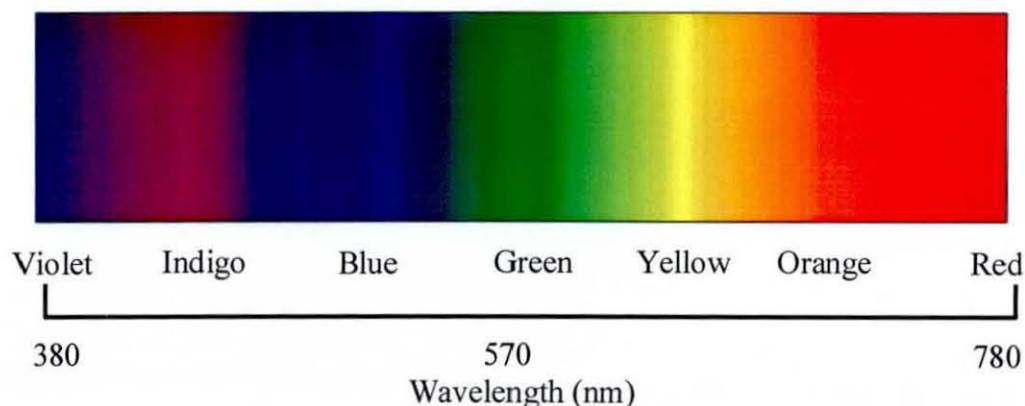


Figure 1.1: The visual spectrum of light

1.1.1. Interaction of Light and Matter

There are many ways in which light can interact with objects and materials in the world around us. When studying the pigment properties of materials the most important by far, due to their influence on the resulting colour, are *absorption* and *scattering*. The *absorption* of light by a material is a process of

photon-induced excitation, where an electron absorbs the energy carried by the photon, which transfers from a ground state to an excited state. The energy difference between the ground and excited states is the same as the energy absorbed from the incident photon. This can be related to the wavelength through Planck's relationship:

$$\Delta E = h\nu \quad \text{[Equation 1.1]}$$

where ΔE is the energy difference between the ground and excited states, h is Planck's constant and ν is the frequency of the incident photon. Since $\nu = c/\lambda$ this equation can also be expressed as:

$$\Delta E = hc/\lambda \quad \text{[Equation 1.2]}$$

where c = the velocity of light and λ = the wavelength of the incident photon. This relationship means that the energy of the electronic transition is inversely proportional to the photon wavelength.

If *absorption* is the only interaction involved, then generally the object in question will be transparent as any light not absorbed will be *transmitted* through. For opaque objects or translucent materials all or part of the light not absorbed is *scattered*, though single or multiple reflections, back to the observer. If the wavelength of the scattered light from an object lies within the visible spectrum, then the object can usually be observed to have the same colour as those reflected wavelengths. The wavelengths that are absorbed are dependent both on the type of atom the electrons belong to, as well as its surrounding environment. For example pure silicon absorbs strongly in the visible region but silicon oxide does not. The range of wavelengths absorbed can also be quite selective, as only certain photon energies will induce a transition. This can be seen in window glass, which is transparent to visible light but absorbs strongly in the ultra-violet (UV), which is relatively close in energy.

1.1.2. Excitation-Relaxation Pathways

The absorption of a photon of a given wavelength is dependent on the presence of available electrons with the correct excitation energies to absorb it. In the case of colour mechanisms, the process of relaxation from the excited to the ground state must be different from that of the original excitation. If the energy of the excitation and relaxation pathway is the same, then the energy of the absorbed photon will be released as a photon of identical wavelength resulting in no net change in colour. In order for a colour to be seen, the energy of the absorbed photon must be totally or partially removed through an alternative relaxation pathway.

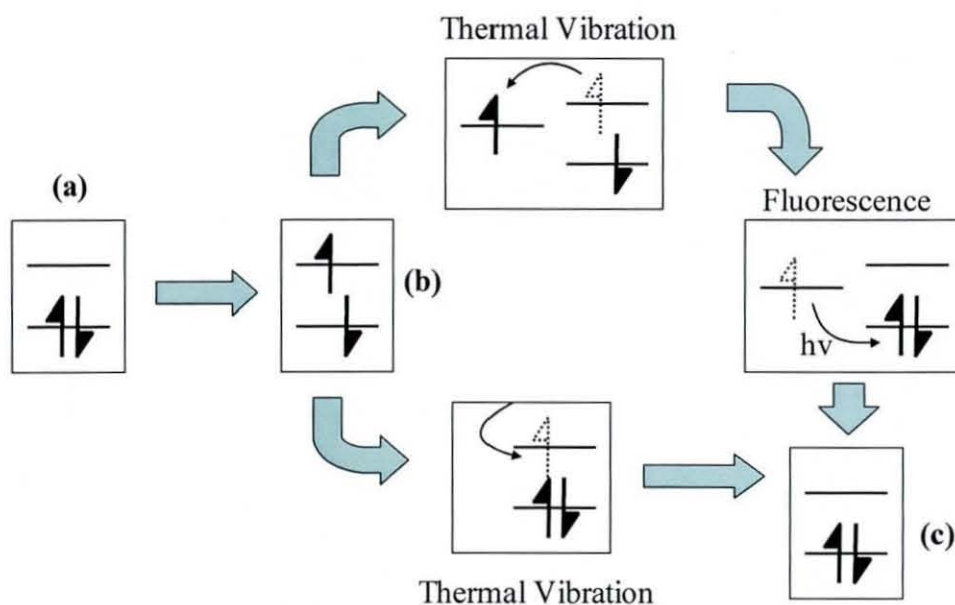


Figure 1.2: Excitation/Relaxation Pathways; (a) Initial Ground State; (b) Excited State, (d) Final Ground State

The most common method of relaxation is by dissipating the absorbed energy as small lattice vibrations. The result has very little discernable effect on the materials structure as it is spread over the whole crystal by causing small vibrations of the atoms on their respective lattice points. This method allows photon of a given wavelength to be absorbed and completely removed from the scattered incident radiation. A second relaxation method is fluorescence where a

photon is absorbed and then released at a later time with a different energy. The energy difference is usually lost in the intervening time through thermal motion. This time, however, a photon is released back into the scattered radiation but it is usually much lower in energy and no longer in the visible region of the spectrum (Figure 1.2).

There are several processes by which the incident photons can be absorbed and the electrons can become excited. Both the amount and wavelength of the light absorbed can be dependent on the type of excitation transition involved. In the case of transitions initiated by the visible spectrum there, are two main types of pathways available. The first are charge transfer mechanisms where the charge of an electron is transferred from an orbital on one atom to an orbital on another. The second type of mechanism is metal centred electronic transitions, where electrons transfer from one orbital to another non-degenerate orbital of the same type in the same atom e.g. *d-d* transitions. These mechanisms are examined in more detail below.

1.1.3. Charge Transfer

The process of charge transfer, as the name suggests, is the transition of electrons from the electronic orbital ground state of one species to the excited state orbital of another. There are two types of charge transfer that exist: metal-ligand charge transfer (MLCT) and metal-metal charge transfer (MMCT). MLCT may be further broken down into two subtypes, transfer from the metal to the ligand and transfer from the ligand to the metal centre.

1.1.3.1. Metal-Ligand Charge Transfer (MLCT)

Metal-ligand charge transfer cannot be described as easily as the scenario described in 1.1.3 implies. There is a large amount of overlap between the electronic orbitals of a metal and a ligand so the electron cannot be said to move from one orbital to another. It is perhaps more accurate to describe the process as the electron moving within the hybrid orbitals from a lower orbital which is predominantly metallic to a second excited orbital which is predominantly ligand-like (Figure 1.3). Metal to ligand charge transfer is commonly seen in

complexes where the ligand has a low-lying π^* orbital in which to accept a transferred electron from a metal d -orbital. This type of transition is commonly seen in metal centres surrounded by aromatic species with large π -orbitals such as aromatic rings and carbonyl species. Since these aromatic ligands are unstable at high temperatures these types of transitions are not usually seen in inorganic pigments.

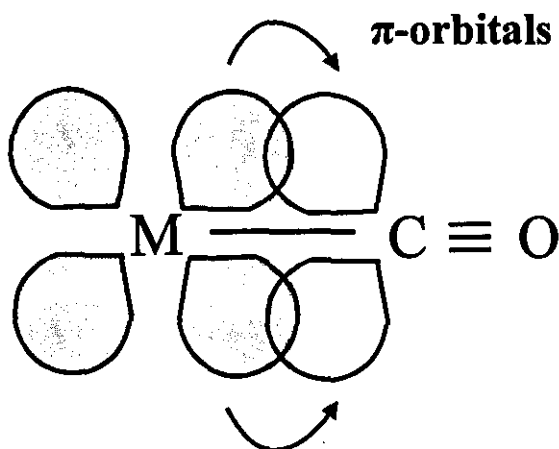


Figure 1.3: Metal-carbonyl charge transfer

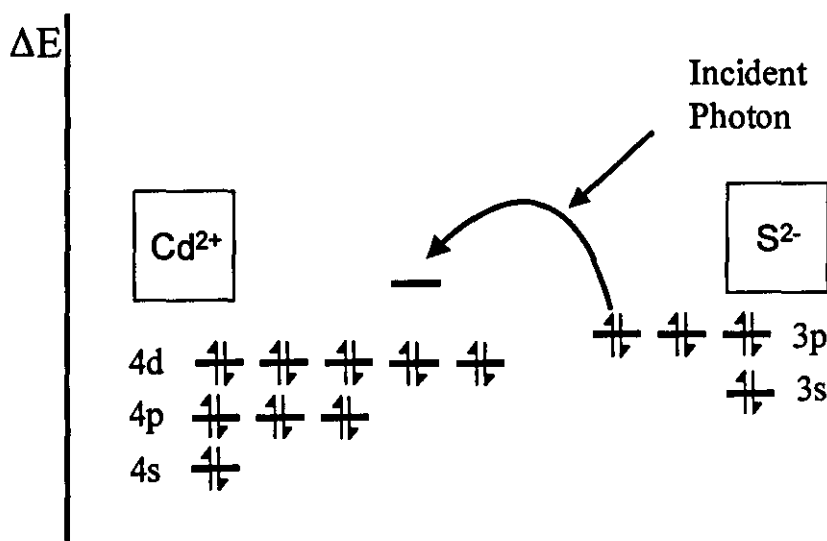


Figure 1.4: Ligand-metal charge transfer in cadmium sulfide compounds

Ligand to metal charge transfer is the exact opposite of the process described above. Here the electron is transferred from the ligand to the metal centre in the

same way. Large anions such as sulfur and selenium have lone pairs of electrons in high-energy orbitals, which may be transferred to a metal centre if it possesses a low-lying empty atomic orbital to accept them. This is the process that creates the bright yellows and reds of the cadmium sulfoselenides as electrons are transferred from the full p -orbital of S and Se to the empty s -orbital of Cd^{2+} . This transfer is able to occur due to the small difference in energy between the $3p$ -orbital of the sulfide anion and the $5s$ -orbital of the cadmium cation. An incident photon supplies the required energy to bridge the difference between the two orbitals and cause the charge transfer (Figure 1.3).

1.1.3.2. *Inter Valence Charge Transfer (IVCT)*

As the name implies IVCT is the transfer of an electron between one valence centre and another, usually between two metals. Due to the lack of hybridisation between metal centres, this kind of transfer is much more clear-cut and more like a classic redox reaction than metal-ligand charge transfer.

The classic example of this kind of behaviour is that of the precious gems based on aluminium oxide materials. Many gemstones, including sapphire, are based on corundum (Al_2O_3). Corundum by itself is colourless, but the addition of transition metal dopants on to the aluminium site can cause the material to take on different colours. Ruby for instance is corundum with a small amount of Cr^{3+} impurity substituted on to the aluminium site which gives the material a red colouration. Sapphires however, are produced from impurities of iron and titanium, neither of which produces an intense colour on their own, but together through charge transfer can create an intense blue.

In sapphire a redox reaction is created between the Fe^{2+} and Ti^{4+} impurities, which can be induced by light (Figure 1.5). An electron is transferred from the ground state of the divalent iron to the excited state of the tetravalent titanium. This process is induced by light wavelengths in the visible spectrum apart from those in the blue region. These are the only wavelengths allowed to be transmitted through the crystal and are seen as the blue sapphire colouration.

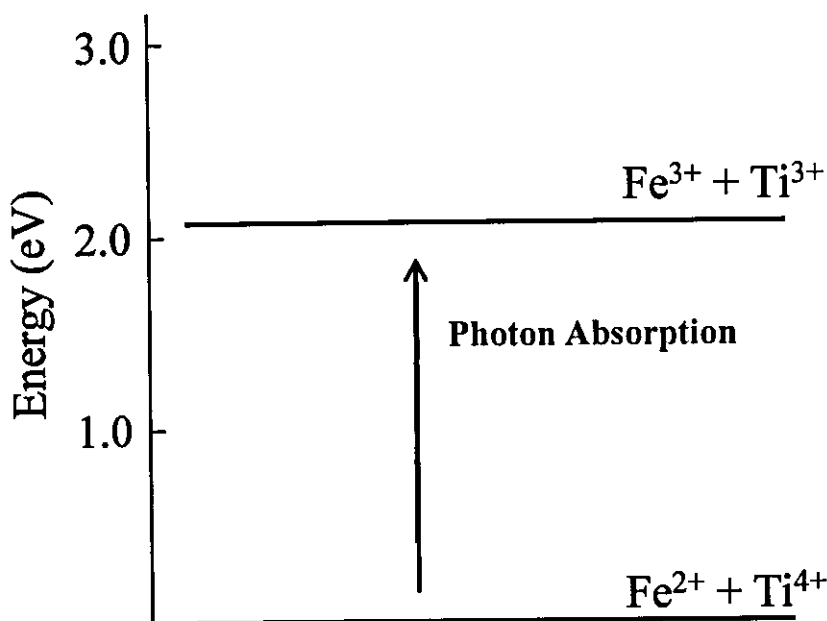


Figure 1.5: Charge Transfer Mechanism

1.1.4. Metal-Centred Electronic Transitions

The most common cause of colour in transition metal chemistry is that of *d-d* electronic transitions. This involves the excitation of *d*-electrons from the ground state to other orbitals in a higher energy state. When metal centres take up polyhedral geometry, the most common being tetrahedral and octahedral, the degenerate *d*-orbitals split into different energy states. Electrons in the lower energy orbitals can then be promoted to the empty higher energy orbitals by photon absorption (Figure 1.6).

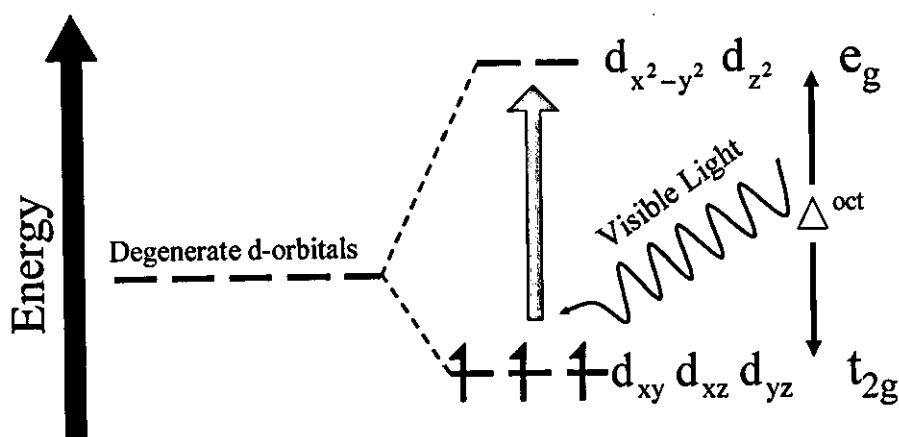


Figure 1.6: *d-d* Electronic Transitions

In heavier metals, such as lanthanides and actinides, a similar transition occurs but involving f -orbitals, the so called f - f transitions. This process is the cause of colour in most metal oxide compounds, as the energy gap between the full oxide p -orbitals and the empty metal based orbitals is too large to undergo ligand to metal charge transfer.

1.1.5. Selection Rules

The wavelengths of light absorbed and scattered, and therefore the colour, are dependent on the energy of the transitions associated with the material. The intensity or brightness of a particular colour, however, is dependent on how often those transitions occur. The intensity of the colour generated is therefore generally controlled by the wavelengths absorbed rather than those that are observed. In order for an intense colouration to be seen, there needs to be a high absorbance of the other wavelengths, otherwise the colour can appear washed out and very pale. Also the changeover between regions of absorption and areas of scattering needs to be sharp otherwise a colour can appear dull and lack lustre. The probability that a particular transition takes place, and therefore the degree of absorption that occurs, is determined by the selection rules.

For a transition to be favourable, and therefore high absorbance to occur, it must comply with Laporte's Selection rule. This states that in order for a transition to be allowed it must be accompanied by a change in parity from orbital to orbital. This means that p to d transitions are allowed as are s to p , however d to d transitions are unfavourable. This explains why pigments where the colour originates from metal d - d transitions are generally much weaker than their charge transfer counterparts and require higher loading levels. The classic example again is that of ruby and sapphire where the d - d transitions of the chromium centres in ruby require a 3% impurity level compared with a 0.01% impurity to get a similar intensity from the charge transfer mechanisms between titanium and iron in blue sapphire.

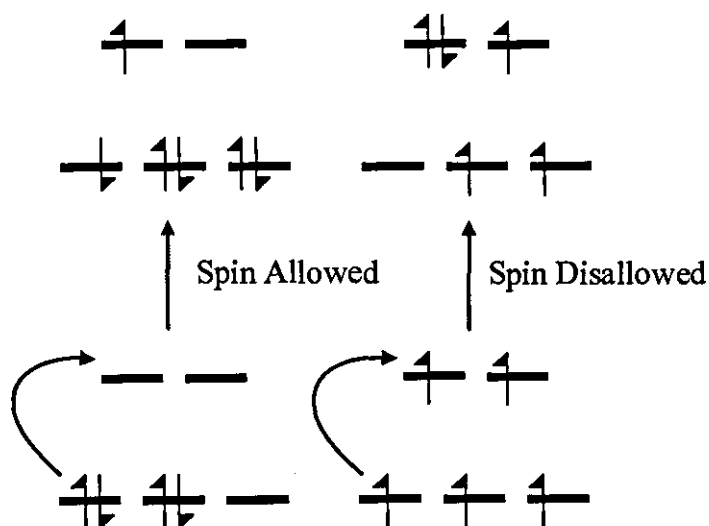


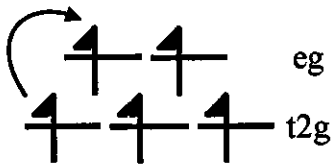
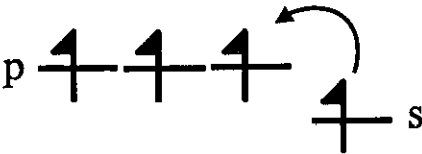
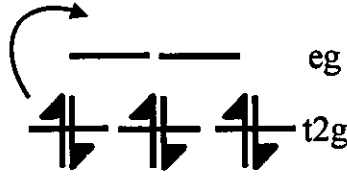

Figure 1.7: Spin allowed and spin disallowed transitions

A final important selection rule that applies to many of these mechanisms is the spin selection rule. Any transition which requires a change in the electron spin orientation is extremely unfavoured due to the large amount of energy required to bring about a change in spin state (Figure 1.5). The intensity of a given transition can be assessed based on whether neither, one or both of these selection rules is obeyed. A transition that obeys both of these rules would be expected to be relatively intense, while one that does not obey either would be very weak. Table 1.1 shows the expected order of transition intensity based on these selection rules.

These selection rules are relaxed, however, as the geometry deviates from a truly centrosymmetric environment. Even in a fully symmetric octahedral environment, Laporte's rules relax through vibration of the ligands and hence temporary loss in symmetry, meaning weak transitions are observed. This also means that compounds with uneven crystal field states where the nuclear vibrations can become asymmetric, and the centrosymmetry is temporarily removed cause Laporte's rule to relax. These exceptions can be used to create colours from d-d transitions that would normally be disallowed. This is seen in some Cr^{3+} doped pyrochlores where asymmetric vibrations on the octahedral site cause a red colouration.¹ In a tetrahedral environment where there is no centre of symmetry, the selection rules are further relaxed and the colour

intensity is typically two orders of magnitude stronger than for an octahedral complex. There are no such circumstances that can be applied to the spin selection rule since transitions that involve a change in electron spin state are always forbidden.

Table 1.1: Comparison of selection rule combinations and relative intensities.

Transition Type	Example	Relative Intensity
Spin forbidden Laporte forbidden	 <p>High spin $d^5 \rightarrow d^5$ transition</p>	0.1
Spin forbidden Laporte allowed	 <p>$s^1 \rightarrow p^3$ charge transfer</p>	1
Spin allowed Laporte forbidden	 <p>Low spin $d^5 \rightarrow d^5$ transition</p>	50
Spin allowed Laporte allowed	 <p>$p^6 \rightarrow s^0$ charge transfer (e.g. CdS/Se)</p>	1000

1.2. Pigments

1.2.1. The History of Pigments

The word pigment originates from the Latin word “pigmentum” which was used to describe a material used in colouring. This terminology was later extended to indicate coloured cosmetic decoration and by the Middle Ages the word pigment was used for all kinds of plant and vegetable extracts used in colouring fabrics. The more modern meaning of the word pigment is a substance of small particles which is practically insoluble in the applied medium and its presence is due to its colour properties alone. The characteristic which distinguishes pigments from dyes and similar materials is their relative insolubility in solvents and binders.

Naturally occurring pigments have been known to exist since prehistoric times and have been used as colorants for over 60,000 years. Cave painters used naturally occurring pigments from the environment. Red and yellow earths came from haematite (iron oxide) or goethite (iron oxyhydroxide) with varying degrees of hydration giving colour variations. Green earths were derived from the aluminosilicate clays celadonite and gluconite; black from charcoal; brown from manganese oxide and white from chalk. Around 2000 B.C natural ochre was burnt with manganese ores to produce red, violet and black pigments for use in pottery. The first synthesised yellow pigments were arsenic sulfide and Naples yellow (lead antimonite).² Ultramarine^{3,4,5} (lapis lazuli), Egyptian blue^{6,7,8} and cobalt aluminium spinel⁹ were the first blue pigments.

The large-scale industrial production of pigments started in earnest in the 18th century with products such as Berlin Blue (1704),¹⁰ cobalt blue (1777), Scheele’s green¹¹, and chrome yellow (1778). In the 19th century ultramarine, Guignet’s green, cobalt pigments, iron oxide pigments and cadmium pigments were developed in quick succession. Development occurred rapidly without consideration of the toxicity or long term effects of the materials produced. In the 20th and now in the 21st century, pigments have become an area of great scientific interest. The past century has seen synthetic colour pigments such as cadmium red, manganese blue, molybdenum red and mixed bismuth oxides come onto the market. Titanium dioxide, with both the anatase and rutile

structure, has been introduced as a new synthetic white pigment to replace lead oxide materials. Lustre pigments (metal effects, nacreous, and interface pigments) have also assumed increasing importance.¹² One of the major challenges over the last ten years has been to find replacements for some of these popular materials with wide-scale usage that contain heavy metals (Cd, Pb, Hg) due to environmental concerns

1.2.2. Desirable Pigment Properties

The main uses of inorganic pigments are in high temperature applications such as glass enamels, ceramics and plastics due to their high thermal stability. It is important in these applications that the resulting pigment materials can be milled to a small uniform particle size with little loss in colour properties. When deciding which pigments are suitable for certain applications there are four basic areas that are considered essential.

- 1) **Colour Properties:** colour, tinting strength or lightening power, hiding power. These determine the efficiency and therefore the economics of a pigment.
- 2) **Chemical and Physical Properties:** chemical composition, moisture and salt content, content of water-soluble and acid-soluble matter, particle size, density and hardness. Such properties determine cost and applicability to different media and types of product.
- 3) **Stability:** resistance towards light, weather, heat and chemicals, anticorrosive properties and retention of the gloss. Clearly such properties govern usage in areas such as car paint or exterior plastics.
- 4) **Behaviour in Binders:** interaction with the binder, dispersibility, special properties, compatibility and solidifying effect. As glazes and binders are themselves chemicals, it is important to investigate the effect of such materials on colour properties before use.

When considering the production of pigments for modern applications, the other major concern, apart from the colour properties, facing the pigment industry today is the use of toxic heavy metals. The majority of inorganic pigments currently in use are based on colour centres that contain heavy metal ions. This is because the use of these elements produces materials with the high thermal and light stability that is highly sought after in inorganic pigment applications. The toxicity of such metal centres has become a major issue for the chemical industry as a whole.

1.2.3. Red Pigments

The major part of this work is concerned with the formation of red or orange coloured materials for use as inorganic pigments. Red coloured materials require many absorption pathways with a range of high-energy electronic transitions to remove the blue and green areas of the visible spectrum. They also need a relatively sharp absorption edge as any potential mixing of the resulting colour can cause the formation of dull brown rather than vibrant red. Also because red is situated at the edge of the visible spectrum, there is a strong likelihood that the scattered light may be pushed out of this region and into infra-red instead. These factors make the formation of red inorganic materials particularly difficult and there are few examples of stable cost effective red pigments.

Table 1.2 shows a list of red pigments along with their chemical name and formula. Apart from the iron (III) oxide based materials, all of the examples contain one of the toxic heavy metals. Unfortunately many of these examples are either commercially unviable due to their high cost and relatively poor colour properties or lack the necessary thermal and chemical stability required for many inorganic pigment applications. Of these examples, probably the best known are the cadmium sulfoselenides and the lead chromates.

Table 1.2: List of commercially available red pigments

Name	Chemical Name	Chemical Formula
Cadmium red	Cadmium sulfoselenide	$\text{Cd}(\text{S},\text{Se})^{13,14}$
Litharge	Tetragonal lead (II) oxide	PbO^{15}
Mars red	Synthetic iron (III) oxide	$\text{Fe}_2\text{O}_3^{16}$
Realgar	Red arsenic sulfide	$\text{As}_2\text{S}_3^{17}$
Red lead	Lead (II,IV) oxide	$\text{Pb}_3\text{O}_4^{18}$
Red ochre	Natural iron (III) oxide	$\text{Fe}_2\text{O}_3^{19}$
Vermillion	Mercuric sulfide	HgS^{20}
Red molybdate chromes	Lead molybdenum chromate	$\text{Pb}(\text{Cr},\text{Mo})\text{O}_4^{21}$

1.2.3.1. Cadmium Sulfoselenides

For many years, one of the most frequently used and yet most controversial pigments in use are the cadmium sulfide based materials. The cadmium sulfides are based on two naturally occurring yet rare cadmium minerals (Figure 1.8). The two cadmium sulfide minerals are closely related to zinc blende and wurtzite and share the same structure. The first mineral greenockite forms hexagonal crystals with the wurtzite structure (space group $P6_3mc$), while the second, hawleyite, is based on the zinc blende mineral sphalerite (space group $F-43m$). Both of these materials have an intense yellow colour, which when produced synthetically give pigments with outstanding performance characteristics and light stability. They are particularly useful in high temperature applications such as thermoplastics, glasses and ceramics due to their relatively high thermal stability.

The bright yellow colour of cadmium sulfide can be further enhanced by the substitution of selenium for sulfur producing the cadmium sulfoselenides. This produces a range of moderately intensely coloured materials that give rise

progressively to orange, red and finally maroon coloured pigments (C.I. Pigment Orange 20) and (C.I. Pigment 108), depending on the degree of replacement.²¹ The shades available can be extended by partially replacing the cadmium ions in the lattice with zinc to give a greenish yellow material. This procedure forms the zinc cadmium sulfide phosphors, which take on a green colouration through phosphorescence after exposure to light. The intensity of the green colour tends to depend on the proportion of zinc and cadmium in the composition. The addition of increasing amounts of zinc sulfide causes the light emitted to shift to shorter wavelengths as the colour becomes increasingly green.²²

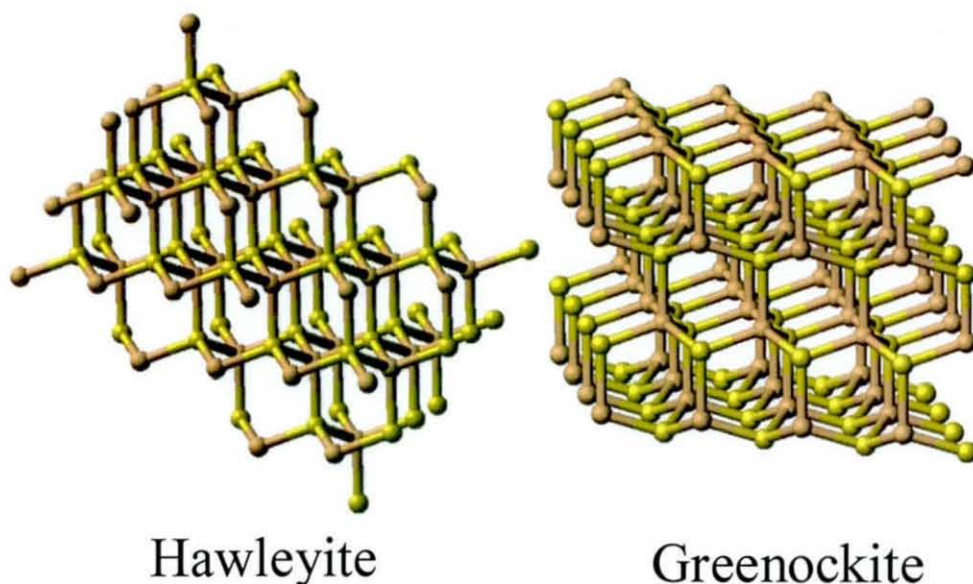


Figure 1.8: The two forms of naturally occurring CdS

1.2.3.2. Lead Chromate Pigments

Lead chromate pigments provide a range of colours including yellow-green, orange and yellow-red. These materials give an extremely bright colouration for inorganic pigments, a good colourfastness and a high opacity for a reasonably low cost. The historic problems associated with the stability of lead chromates, including chromite formation in high light levels and sulfide formation, have been overcome with the use of oxide surface treatment. The variability in the resulting shade of lead chromates is achieved by the formation of solid solutions much like in the case of cadmium sulfides described previously. In the lead

chromates, the situation is complicated by the existence of polymorphism, which can lead to the formation of a range of different coloured materials. The yellow shade pigments are made up of pure PbCrO_4 which crystallises with a monoclinic structure (C. I. Pigment Yellow 34).²¹ The inclusion of sulfate anions into these materials whilst maintaining the monoclinic structure gives rise to lemon-green shades, however PbCrO_4 and PbSO_4 solid solutions can also crystallise with an orthorhombic structure and this produces a range of materials that are dark green in colour. The orange and red pigments are formed by the incorporation of molybdate into the composition forming the so called orange and light red molybdate chromes (C. I. Pigment Red 104).

1.2.3.3. Pigment Toxicity

As previously discussed in section 1.2.2 the toxicity of inorganic materials is becoming increasingly important in many industries and particularly in the pigment industry, where many toxic elements are used. The cadmium sulfoselenides and lead chromates give a large range of cheap brightly coloured red, orange and yellow pigments. Unfortunately cadmium, lead, and chromium (VI) are particularly toxic heavy metals, and as such their use has been largely restricted. Generally their use is restricted by voluntary codes of practice, however legislation does exist in some cases. These forced restrictions have become more frequent in recent years and the use of heavy metals, especially cadmium, have been limited by European Union legislation due to environmental and health risks. In particular these prohibit the use of cadmium pigments or dyes in certain polymers and metallic plating.²³ Also the use of cadmium in many types of packaging, especially food contact packaging has recently been banned.²⁴

The presence of chromium in the case of the lead chromates is a good example of the argument for both the use and elimination of heavy metals from the environment. The chromium (VI) in the above material is highly reactive and easily reduced, which can have harmful implications to humans, animals and plants. Trivalent chromium (III) however, is relatively stable and an essential trace mineral²⁵ highlighting how different oxidation states can result in

completely contrasting toxicological properties. A worldwide consensus against the use of toxic products has led to the expulsion of lead and cadmium containing compounds from the market.^{26,27} There is little direct risk to humans or the environment from heavy metal pigments in their parent form. The stability and insolubility that makes these materials ideal pigments also reduces their bioavailability to the surrounding environment. However there is an increasing concern that the use of these materials at present levels could lead to them converting to soluble forms after incineration²⁸ or disposal. With the exception of ultramarine, titanium dioxide and carbon black pigments almost all inorganic pigments contain potentially harmful heavy metals.

1.2.3.4. Possible Replacements

There have been several materials reported in recent years as possible replacements for heavy metal inorganic pigments. The first and possibly most reported of these are the rare-earth sulfides (Ln_2S_3) and related compounds ALn_2S_4 ($A = \text{Ca}, \text{Ba}, \text{Sr}$).²⁹ These also include the rare-earth sulfide fluorides ($\text{Ln}_3\text{OF}_3\text{S}_2$, $\text{ALn}_2\text{F}_4\text{S}_2$),^{30,31,32} oxysulfides ($\text{Ln}_2\text{O}_2\text{S}$) and oxyfluorosulfides ($\text{Ln}_3\text{OF}_3\text{S}_2$, $\text{Ln}_2\text{O}_{1.5}\text{FS}$).³³ These materials can be prepared to give a range of hues from pale yellow to deep red depending on the rare-earth element. Perhaps the most successful of these rare-earth sulfides is cerium sulfide, which can take a range of shades between yellow and red depending on the amount of alkali doping.³⁴ These materials have been reported as a commercially viable replacement for the cadmium sulfoselenides.³⁵

The most promising development in the production of viable pigment compounds has been the synthesis of a large range of nitrides and oxynitride materials. The introduction of nitrogen into an anionic framework results in a more covalent bond character causing a modification of the properties especially colour properties.³⁶ The primary phase reported are materials with the composition $\text{Ca}_{1-x}\text{La}_x\text{TaO}_{2-x}\text{N}_{1+x}$ ³⁷ ($x = 0 - 1$). The substitution of the "softer" nitrogen atoms for the "harder" oxygen results in an increase in the band gap shifting the colour from red to yellow. Related to the tantalum oxynitrides are the titanium oxynitrides (LaTiO_2N),³⁸ which are more economically viable but

with the loss of some colour properties. These types of oxynitride phase are known to have a perovskite type layered structure and they can contain a range of alkali-earth metals.³⁹ A second series of oxynitride compounds have also be discovered, which crystallise in a defect fluorite type structures⁴⁰ such as the rare-earth tungsten oxynitrides.⁴¹

Although there are alternatives to the heavy metal pigments, many of them discussed here, none of them are perfect solutions. The cerium sulfides and related compounds produce a range of red and orange shade pigments but are tinctorally very weak in comparison to the cadmium sulfoselenides. The oxynitride compounds, on the other hand, produce reds and oranges with very impressive brightness and opacity, however, they require the use of ammonia gas during the synthesis, which does not lend itself to industrial scale up, though the Ta_3N_5 starting material is beginning to be offered commercially⁴². Unfortunately neither cerium sulfide nor the oxynitride materials are entirely air stable and are also known to react with water. The use of such materials as pigments requires the use of polymer or silicate films to avoid contact with both air and water. However the film can act as a diluent which reduces the intensity of the compounds colour, it also adds extra cost and process to the synthesis of the pigment

Despite a large amount of research into this area a real viable alternative to the use of heavy metals has not been found. The cadmium sulfoselenides and molybdate chromes still remain the most cost effective, durable, and colourful of the red/orange pigments available. A large proportion of the work in this thesis is dedicated to finding possible alternatives for use as red/orange inorganic pigments with high thermal and chemical stability.

1.3. The Pyrochlore Structure

One structure with compositional flexibility that has been used to generate materials with many useful properties, including pigments, is the pyrochlore. The name pyrochlore, meaning “green fire”, comes from the naturally occurring mineral $CaNaNb_2O_6(OH,F)$ which decomposes with a green flame upon

heating.⁴³ The pyrochlore group, however, denotes a series of 22 different minerals, which are similar structurally, but diverse in both composition and chemical behaviour. Compounds that are said to have the pyrochlore structure have a face centred cubic arrangement and crystallise in the space group $Fd-3m$. This arrangement has a strong relationship with the fluorite structure (A_2O_4), and often shares many similar properties such as anion conduction and magnetic ordering. In fact the pyrochlore structure can be considered a 2×2 arrangement (A_4O_8) of defect fluorite cells with half of the cation sites doped, and ordered vacancies in one eighth of the anion sites. This final composition is generally described by the formula $A_{2-x}B_2O_6O'$ ($x = 0 - 1$), where one of the anion sites is given the symbol O' as it is separate from the other six both in structure and behaviour.

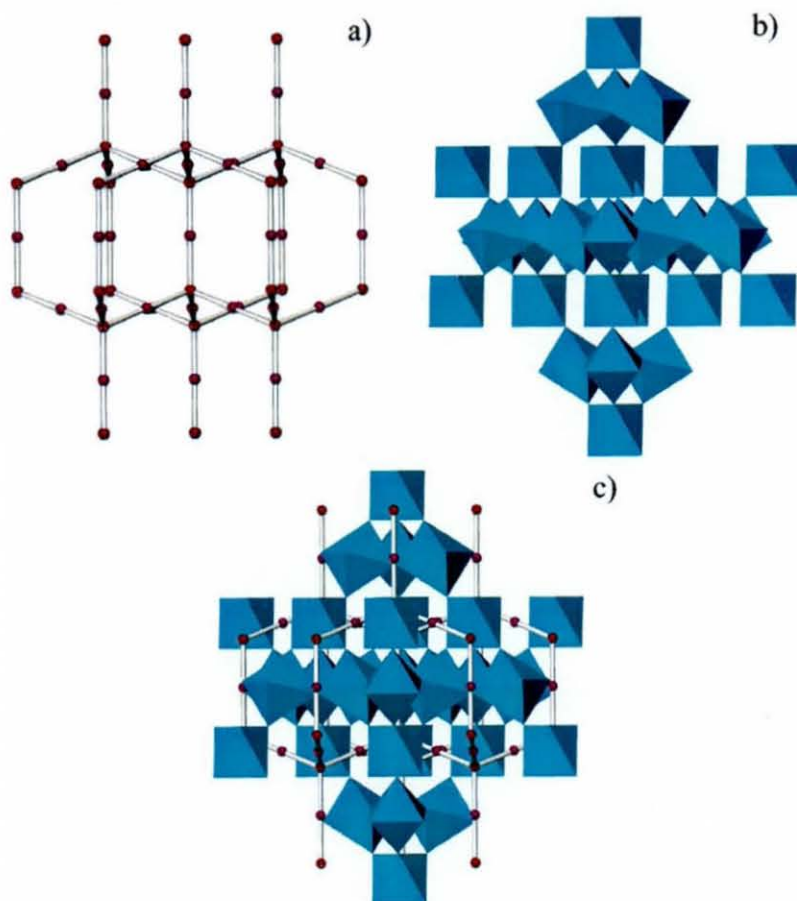


Figure 1.9: Pyrochlore structure a) A_2O' tetrahedral framework, purple spheres are A cations and red spheres are O' anions b) B_2O_6 tungsten bronze type framework with blue corner sharing BO_6 octahedra c) $A_2B_2O_6O'$ pyrochlore structure

The pyrochlore structure consists of two distinguishable frameworks, one of A_2O' tetrahedra similar to the Cu_2O cuprates, and the second of B_2O_6 corner sharing octahedral sheets (Figure 1.9). The octahedral sheets are the backbone of the pyrochlore structure and form large channels through which the A_2O' arrangements are inserted. Although the composition of the B_2O_6 can be altered extensively, the structure remains largely unchanged and fully stoichiometric. It is the A_2O' network that is seen as the root of the versatility of the pyrochlore structure, as it has only a weak interaction with the ridged B_2O_6 network. This allows it to be partially occupied or even totally absent in some cases (e.g. W_2O_6 ⁴⁴), forming non-stoichiometric structures. In many cases the O' anion site has been known to contain certain non-oxide constituents such as OH^- , F^- ,⁴⁵ and S^{2-} ,⁴⁶ which allows the formation of hydroxy, oxyfluoride and oxysulfide structures. There have also been reported cases of completely non-oxide pyrochlores containing fluoride⁴⁷ and chloride⁴⁸ as the only anion. This high compositional flexibility allows the electronic structure of these compounds to be "tailored" by the deliberate charge balancing of almost any B_2O_6 framework with a carefully chosen A_2O' arrangement.

The ideal pyrochlore structure has a high degree of symmetry and usually contains four distinct crystallographic sites. The cations A and B are placed onto two special sites 16c and 16d which are located at $0,0,0$ and $\frac{1}{2},\frac{1}{2},\frac{1}{2}$. The A cation is usually larger (radii larger than ca. 1.0 \AA e.g. Ca, K, Ba, Y, Ce, Pb, U, Sr, Cs, Na, Sb^{3+} , Bi, Th) with a low oxidation state (+2, +3) and the B cation is smaller (Nb, Ta, Ti, Sn, Fe, W)⁴⁹ in a high oxidation state (5+, 4+). The anion sites consist of the 48f which contains the six B_2O_6 oxides and the 8a which contains the O' anion; these are found at $x, \frac{1}{8}, \frac{1}{8}$ and $\frac{1}{8}, \frac{1}{8}, \frac{1}{8}$. The vacant 8b site located at $\frac{3}{8}, \frac{3}{8}, \frac{3}{8}$ is the remains of the one eighth ordered vacancy from the parent fluorite. Commonly the pyrochlore consists of a combination of divalent and pentavalent cations or trivalent and tetravalent species though combinations of all four are known to exist.

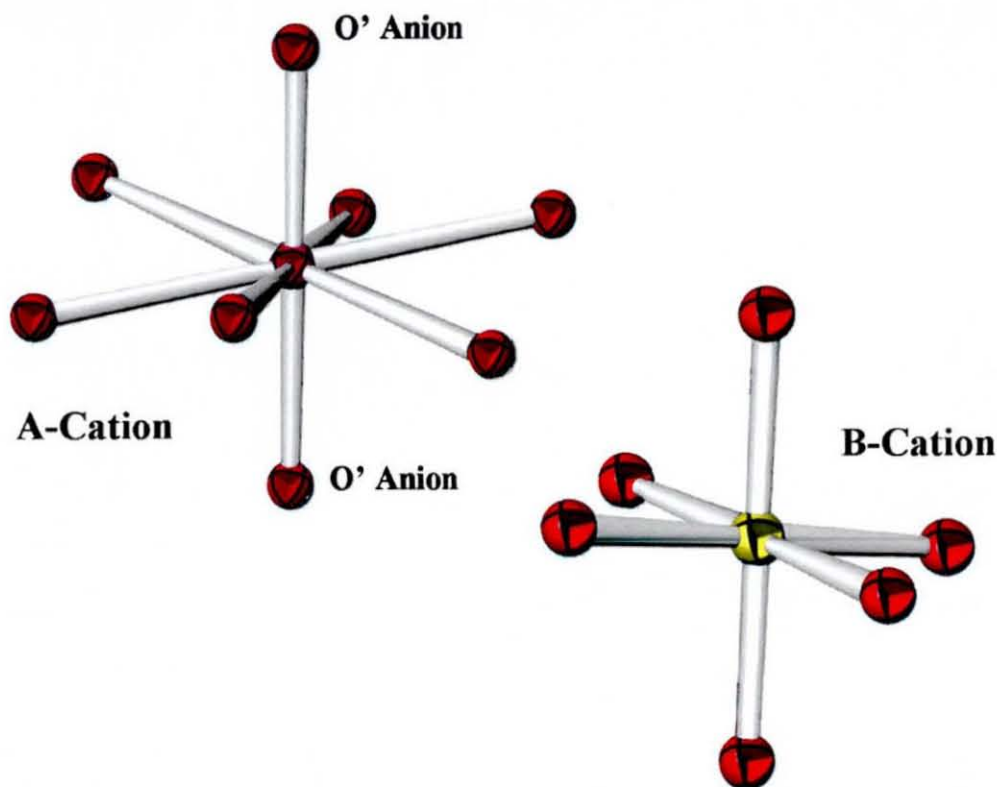


Figure 1.10: *A* and *B* cation geometries in the pyrochlore structure. The O' (8a) anions of the *A* site are indicated.

The combination of these two distinct oxide frameworks produces two very different geometries of the pyrochlore cations (Figure 1.2). The *B* cations, which are the smaller of the two, are bonded to six O²⁻ from the 48f sites forming a trigonal antiprism. This is generally a very symmetrical site and is usually very close to being a perfect octahedral geometry with equal bond lengths and angles approaching 90°. The larger *A* cations however have a much lower symmetry with an 8-coordinate geometry. They have two very short bonds to the 8a O' anions and six longer bonds to the 48f O anions in the walls of the BO₆ channels. These hexagonal channels are a 3-dimensional structure formed by the BO₆ units forming holes along the $\langle 111 \rangle$ direction.

The ability of the pyrochlore structure to accept a large number of different elements and stoichiometries has led to a variety of structural, physical and electrical properties. This includes a whole range of material with important properties such as ferroelectricity,^{50,51,52} conductivity, semiconductivity, and superconductivity.^{53,54} There is also a three fold symmetry of the metal centres

in the structure that lead to interesting magnetic effects like ferromagnetism, antiferromagnetism, and distressed magnetism.^{55,56} The versatility of this structure has led to a number of important industrial applications as electrocatalysts,⁵⁷ fast ion conductors,^{58,59} resistors, sensors⁶⁰ and giant magnetoresistance.⁶¹

The elemental versatility combined with the structural stability of pyrochlore compounds makes them ideal candidates for pigment materials. Many of the reported examples involve the use common pyrochlore compounds with little or no absorbance in the visible spectrum, and then insert colour-producing ions, or chromophores, in order to produce stable pigments. This kind of practice is often seen with rare-earth titanate or stannate pyrochlores ($\text{Ln}_2\text{Ti}_2\text{O}_7$ and $\text{Ln}_2\text{Sn}_2\text{O}_7$ $\text{Ln} = \text{Y, Sm, Gd}$), which have been doped with a number of cations such as Cr^{3+} and V^{5+} producing red and yellow shades.^{62,63} Most of the chromophores that can be substituted into the pyrochlore structure are transition metal cations that rely on *d-d* electronic transitions to produce their colour. This means that the final colours produced tend to be very weak in comparison to existing pigments. There are, however, examples of pyrochlores that do not require additional substituents and produce bright vivid colours, such as the tin niobates, which are discussed in detail in this thesis.

1.3.1. Stereoactive Lone Pairs

A dominant feature of many compounds containing *p*-block elements in low oxidation states is the role played by their lone pairs in creating irregular coordinations.⁶⁴ The majority of examples of this kind of behaviour are seen in compounds containing Pb and Sn in a 2+ oxidation state or Sb and Bi with a 3+ oxidation. In all these cases, the resulting cations have an s^2 electronic configuration, which results in the formation of a lone pair. The properties resulting from the existence of a lone pair are particularly important in coordination chemistry where the lone pair is often stereoactive and affects the geometry of many related structures. However, there are numerous examples of stereoactive lone pairs in the case of ionic solid state compounds, especially in the case of materials containing Sn^{2+} and Bi^{3+} . Here these cations are only found

in very asymmetric environments, where the inclusion of the lone pair can have a number of effects. This can take the form of two short bonds on one side as in α - SnWO_4 ,⁶⁵ three short bonds as in SnSO_4 ⁶⁶ or even four short bonds as in the case of SnO .⁶⁷

In all of the above cases, the Sn^{2+} cation is not on the centre of symmetry for the cell, so the lone pair has only a local effect on the rest of the structure. In some cases the lone pair cation can take up the centre of symmetry and have a much wider influence on the whole cell. Perhaps the most studied examples are those where the lone pair is located on the *A* cation site of the pyrochlore structure, with Bi^{3+} in $\text{Bi}_2\text{Ti}_2\text{O}_7$ ⁶⁸ and Sn^{2+} in $\text{Sn}_2\text{Nb}_2\text{O}_7$ and $\text{Sn}_2\text{Ta}_2\text{O}_7$ ⁶⁹ as the prime examples. The effect of the lone pair on the surrounding structure is complex and is discussed in greater detail later in this thesis.

1.4. Rare-Earth Bismuth Oxide

Bismuth oxide based phases have been extensively studied with the primary focus on their anion conduction properties. The high temperature phase of bismuth sesquioxide (δ - Bi_2O_3) is stable between 730 and 875 °C and its structure is based on a face-centred cubic lattice. Previous studies have found the cell to be a defective fluorite (A_2O_4) with one vacant anion site, though the exact nature of the anion ordering has also had much discussion. The high concentration of vacancies in this particular phase is thought to be the cause of the remarkable oxygen ion mobility seen in these compounds. Efforts to stabilise the defect fluorite structure of this material at room temperature have mainly focused on the substitution of the bismuth cation with a lanthanide metal. Compounds have been synthesised using the whole range of available lanthanides, including related elements such as yttrium. To date the focus of these experiments has been concentrated almost entirely on the anion conduction properties of these materials, however, there has also been a limited amount of research directed towards the pigments properties of these compounds as many of them have a light yellow or orange colouration.

1.4.1. Structure of $\delta\text{-Bi}_2\text{O}_3$

The cubic δ -phase of bismuth sesquioxide occurs at a temperature of 729 °C which is then stable up until the melting point at 824 °C. Upon cooling this phase has been found to be meta-stable down to 650 °C where a tetragonal β -phase forms at 639 °C giving a bcc γ -phase. The structure of the high temperature cubic phase has come under much discussion especially because of a large heat effect of 7.06 kcal/mole that has been detected during the $\alpha \rightarrow \delta$ phase change. The entropy gain between these two phases has been found to be up to 75% of the entropy when moving to the liquid state. This suggests a great deal of disorder in the resulting $\delta\text{-Bi}_2\text{O}_3$ structure which is comparable to that of the liquid state. The disorder of this cubic structure seems to be an example of distortions caused by the Bi^{3+} lone pair.

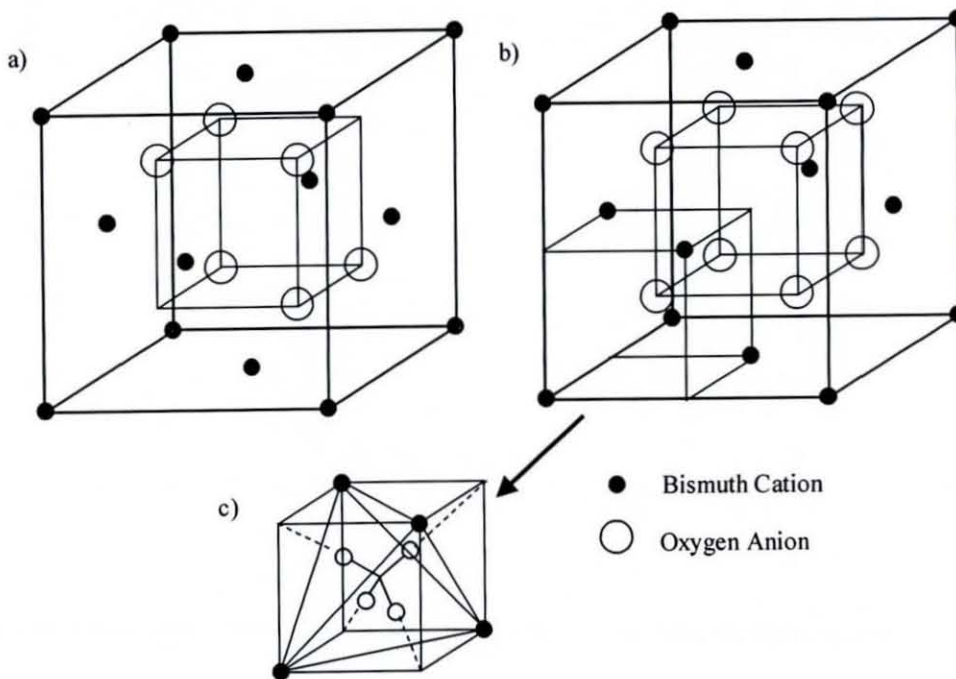


Figure 1.11: Three cubic models for the high temperature phase of $\delta\text{-Bi}_2\text{O}_3$ a) $\text{Pn}3\text{m}$ primitive cell with ordered oxide defects in the 111 direction, b) $\text{Fm}3\text{m}$ standard defect fluorite structure with oxide anions on 8c site c) $\text{Fm}3\text{m}$ displacement of oxide anions to the 38f

Three possible models were suggested for the high temperature δ -phase all based on the cubic fluorite structure with one quarter of the oxide ions removed. The first model proposed by Sillen found the oxygen vacancies to appear in an ordered manner in the 111 direction. This forms a primitive cell in the space group $Pn3m$. The two models suggested by Gattow and Schröder and also Willis were most closely related to the fluorite model being in the same space group ($Fm2m$). In both of these cases the oxygen anions were randomly distributed over all 8 anion sites with a 75% occupancy forming disordered vacancies. These models differ in the fact that the first suggested that the structure was a simple defect fluorite while the second suggested that the oxide anions were further displaced onto four 32f sites surrounding the ideal anion locations. This displacement can occur in four directions in a tetrahedral geometry towards the unoccupied octahedral holes as seen in Figure 1.11.

1.5. Bond Valence Theory

Due to the complex interactions that exist in ionic structures there has always been a difficulty in assigning empirical values to the strength of certain bonds within a structure. The assignment of single, double or triple bonds that is often used in molecular structures, cannot be transferred to the description of ionic structures and so classical bond valence models also become unsuitable. Materials therefore tend to be described in terms of geometric properties such as the close packing of spheres or the linking of polyhedra. These methods however, give no information regarding the strengths of particular bonds or the valence of any given site.

To overcome the limitation of geometrical models, an empirical approach has been developed to describe the properties of bonds in ionic structures. This becomes particularly important when describing mixed valence elements on distinct crystallographic sites and assessing the stability of structural models. A number of workers were responsible for the development of these techniques however the main contributors to the theory were Zachariasen and Brown. A detailed description of the theory was published by Brown⁷⁰ in 1975 and has since been updated by the same author to its present form.⁷¹ This method

attempts to assign valences or strengths to individual bonds, which can then be summed to give a total site valence. The main difference with the classical model is that in this case non-integral numbers can be used to describe a bond valence. In molecular structures where bonds are described in terms of single, double or triple in the new Bond Valence Theory virtually any value is seen as acceptable.

The valence of a particular bond is related to the elements that make up the bond and the distance between them. In most cases the longer the distance between two ions the weaker the interaction between them and the lesser the influence of that bond to the total site valence. The theory is then constructed by the development of a mathematical expression which relates the bond lengths to the associated bond valences. The valence of an individual bond s_{ij} , which is related to the bond length R_{ij} , is summed with other bond lengths associated with the same atom to give the total atom valence.

$$v_j = \sum_i s_{ij} \quad \text{[Equation 1.3]}$$

The bond valence for an observed bond length between two atoms can be mathematically calculated using the mathematical expression shown in Equation 1.4. This expression uses the constants B and R_0 , which are purely empirical and element specific. These constants have been determined experimentally by the examination of the bond lengths in a number of characterised compounds with a specific element in a known oxidation state. Tables containing the constants for many types of bonds have been collated by Brown and can be used in these calculations.⁷⁰

$$s_{ij} = \exp\left[\frac{R_0 - R_{ij}}{B}\right] \quad \text{[Equation 1.4]}$$

R_0 describes the bond length derived for a unit bond valence such as that for a single bond in the classical method. The constant B is related to the slope of the curve that describes the relationship between the bond length and the strength of

interaction for that specific element. The calculated effective valence is usually estimated to be within 0.1 of the actual valence showing that these results cannot always be used definitively. One known limitation to the Bond Valence Theory is that the calculations assume that the crystal structure in question is in a relaxed state.⁷² Systems under compression or expansion will show higher or lower site valences than expected. This gives the effect of the atoms appearing “over bonded” and “under bonded”.

Many of the structures reported in this work have distorted atomic geometries and non-stoichiometric structures, which can then have effects on the local environments of the elements under study. Bond Valence Theory can be used in these circumstances to study the effect of these changes on the bond lengths and overall site valence. They are also useful in determining the validity of a particular structural model during the refinement of diffraction data.

1.6. The Scope Of This Work

The main aim of this work is the search for environmentally friendly replacements for existing heavy metal pigments. This work concentrates primarily on the formation of yellow and orange/red coloured materials in an attempt to replace the cadmium sulfoselenides and lead chromate pigments. Also of interest are compounds with high thermal stability for use in the glass enamel and ceramics industry. Particular attention is paid to the structural chemistry of synthesised compounds and the local geometry around elements in order to understand the effects on the resulting colour.

The majority of this work deals with the synthesis and characterisation of tin niobate pyrochlores and derivatives, due to their bright colouration and high chemical and thermal stability. Related non-pyrochlore tin niobate compounds are also synthesised to probe the cause of the intense colour properties in compounds containing both tin and niobium. Cadmium niobium oxide and oxysulfide compounds are also studied, not as pigments themselves, but as a comparison to synthesised tin niobates. This work was undertaken to try and

understand the mechanism behind the doping of pyrochlores with chalcogenide anions.

Two other series of compounds are also discussed as potential new pigments that have been studied by other authors previously. The first is a complete characterisation of a range of rare-earth bismuth compounds, which have been shown to give a yellow/orange colouration in the right combinations. The second is a collaborative study into ancient Egyptian Blue compounds and related materials, with a full structural characterisation of synthesised solid solutions containing the same structure and an attempt to determine why Egyptian Blue pigments often discolour in natural light.

1.7. References

- ¹ F. Matteucci, G. Cruciani, M. Dondi, G. Baldi, A. Barzanti, *Acta Materialia*, **55** (2007) 2229
- ² A.J. Shortland, P.T. Nicholson, C.M. Jackson, *Archaeometry*, **42** (2000) 153
- ³ J. Klinowski, S.W. Carr, S.E. Tarling, *Nature*, **330(6143)** (1987) 56
- ⁴ I. Hassan, R.C. Peterson, H.D. Grundy, *Acta Cryst. C.* **41** (1985) 1827
- ⁵ B. Gilbet, S. Denoel, G. Weber, and D. Allart, *Analyst*, **128(10)** (2003) 1213
- ⁶ G.A. Mazzocchin, D. Rudello, C. Bragato and F. Agnoli, *J. Cult. Heritage*, **5(1)** (2004) 129
- ⁷ E.M. Hughes, M.J. Pack, S.E. Dann and M.T. Weller, *Anal de Quim*, **93(4)** (1997) 233
- ⁸ H. Jaksch, W. Sieoek, K.L. Weiner and A. Elgoresy, *Naturwissen*, **70(11)** 525 (1983)
- ⁹ G.J. Yan, J.J. Cheng, J. Zhang, and S.L. Chun, *J. Inorg. Mater.* **15(4)** (2000) 660
- ¹⁰ A. Ludi, *J. Chem. Educ.* **58** (1981) 1013
- ¹¹ *Industrial inorganic pigments*, edited by Gunter Buxbaum (Wiley, 1998)
- ¹² J.R. Tan, Y.F. Han, W.X. Hou, X.Z. Chen and X.S. Fu, *Dyes and Pigments*, **52(3)** (2002) 215
- ¹³ A. Domenech-Carbo, M.T. Domenech-Carbo, M. Moya-Moreno, J.V. Geimno-Adelantado, F. Bosch-Reig *Anal. Chim. Acta*, **407(1)** (2000) 275
- ¹⁴ Y.A. Bois, *Critique*, **42(468)** (1986) 487
- ¹⁵ G.D. Smith and R.J.H. Clark, *App. Spec.* **56(6)** (2002) 804
- ¹⁶ O.H. Ionschu, D. Mohanu, A.I. Stoica and G.E. Baiulescu, *Talanta*, **63(4)** (2004) 815
- ¹⁷ V.D. Timofeev and V.F. Pluzhnik. *Doklady. Adademii, Nauk. SSSR.* **150(5)** (1963) 1137
- ¹⁸ *Artists' Pigments: A Handbook of Their History and Characteristics*, Vol. 1, L. Feller, Ed., Cambridge University Press, London 1986, p.109
- ¹⁹ D.C. Smith, M. Bouchard and M. Lorblanchet, *J. Raman Spec.* **30(4)** 347 (1999)
- ²⁰ L. Burgio, D.A. Ciomartin and R.H. Clark, *J. Molecular Struct.* **405(1)** (1997)

-
- ²¹ R.M. Christie, *Colour Chemistry*, RSC Paperbacks, 2001
- ²² W.H. Byler, *J. Opt. Soc. Am.* **37**, 920- (1947)
- ²³ EU Directive 91/338/EEC
- ²⁴ EU Directive 94/62/EEC
- ²⁵ Vincent, J.B. *Proc. Nut. Soc.* **63(01)** (2007) 41
- ²⁶ T. Vigander and S. Langard, *British J. Insust. Med.* **40** (1983) 71
- ²⁷ R.U. Ayres, *Proc. Nat. Acd. Sci. USA*, **89(2)** (1992) 815
- ²⁸ Agency for Toxic Substances and Disease Registry (ATSDR). *Toxicological Profile for Cadmium*. Draft for Public Comment. Public Health Service, U.S. Department of Health and Human Services, Atlanta, GA. 1997.
- ²⁹ L. Brixner. *Mat. Res. Bull.* **19** (1984) 745
- ³⁰ A. Demorgues, A. Tressaud, H. Laronze, P. Gravereau and P. Macaudière, *J. Fluorine Chem.* **107** (2001) 215
- ³¹ T. Schlied, *Z. Anorg. Allg. Chem.* **625** (1999) 1700
- ³² D. Pauwels, A. Demorgues, H. Laronze, P. Gravereau, F. Guillen, O. Isnard and A. Tressaud. *Solid State Sciences*, **4** (2002) 1471
- ³³ A. Demorgues, A. Tressaud, H. Laronze and P. Macaudière, *J. Alloys and Comp.* **323** (2001) 223
- ³⁴ P. Sulcova and M. Trojan, *Dyes and Pigments*, **58** (2003) 59
- ³⁵ H. Laronze, A. Demorgues, A. Tressaud, L. Lozano, J. Granec, F. Guillen, P. Macaudière and P. Maestro, *J. Alloys and Comp.* **275-277** (1998) 113
- ³⁶ R. Marchand, *CR Acad. Sci. Paris IIc* **2** (1999) 669
- ³⁷ M. Jansen and H.P. Letschert. *Nature* **404** (2000) 980
- ³⁸ F. Chevire, F. Tessier, R. Marchand, *EUR. J. Inorg. Chem*, **6** (2006) 1223
- ³⁹ J. Rooke, M. Weller, *Sol. St. Phen.* **90** (2003) 417
- ⁴⁰ M. Perez-Estebanez, R. Pastrana-Fabregas, J. Isasi-Marin, et al. *J. Mater. Res.* **21(6)** (2006) 1427
- ⁴¹ N. Diot, O. Larcher, R. Marchand, J.Y. Kempf, P. Macaudière, *J. All. Comp.* **323** (2001) 45
- ⁴² E. Guenther, M. Jansen, *Mat. Res. Bull.* **36** (2001) 1399
- ⁴³ R.V. Gaines, H.C.W. Skinner, E.E. Foord, B. Mason, A. Rosenzweig, *Dana's New Mineralogy*, Wiley: New York, 1997

- ⁴⁴ R. Nedjar, M. M. Borel, M. Hervieu, B. Raveau, *Mater. Res. Bull.* **23** (1988) 91.
- ⁴⁵ J. Miranday, G. Gauthier, R. DePape, *C. R. Acad. Sci., Ser. B* **273** (1971) 970.
- ⁴⁶ D. Bernard, J. Pannetier, J. Y. Moisan, J. Lucas, *J. Solid State Chem.* **8** (1973) 31.
- ⁴⁷ N. Ruchard, J. Grannec, A. Tressaud, P. Gravereau, *C. R. Acad. Sci. II, Ser. B* **321** (1995) 507.
- ⁴⁸ M. Ledesert, B. Raveau, *J. Solid State Chem.* **67** (1987) 340.
- ⁴⁹ T.G. Leven, J.C. Nino, T.A. Vanderah, C.A. Randall and M.T. Lanagan, *J. Solid State Chem.* **67** (1987) 340
- ⁵⁰ M.A. Subramanian, G. Aravamudan, G.V. Subba Rao, *Prog. Solid State Chem.* **15** (1983) 55
- ⁵¹ G. Jeanne, G. Desgardin, G. Alais, B. Raveau, *J. Solid State Chem.* **15** (1975) 193
- ⁵² D. Bernard, J. Pannetier, J. Lucas *Ferroelectrics*, **21** (1978) 429
- ⁵³ B. J. Kennedy, *Physica B*, **303** (1998) 241
- ⁵⁴ M. Avdeev, M.K. Haas, J.D. Jorgenson, R.J. Cava, *J. Solid State Chem.* **169** 24
- ⁵⁵ A. Ramirez, A.P. Hayashi, A.R.J. Cava, R. Siddharthan, B.S. Shastry, *Nature*, **399** (1999) 333
- ⁵⁶ M.A. Subramanian, CC. Torardi, D.C. Johnson, J. Pannetier, A.W. Sleight, *J. Solid State, Chem.* **72** (1989) 34
- ⁵⁷ L. Minervini, R.W. Grimes, *J. Am. Ceram. Soc.* **83** (2000) 1873
- ⁵⁸ C. Heremans, B.J. Wuensch, J.K. Stalick and E. Prince, *J. Solid.State. Chem.* **117** (1995) 108
- ⁵⁹ B.J. Wuensch, K. W.Eberman, C. Heremans, E.M. Ku, P. Onnerud, E.M.E. Yeo, S.M. Haile, J.K. Stalick, J.D.Jorgensen, *Solid State Ionics* **129** (2000) 111
- ⁶⁰ T.M. Bruton, *J. Solid. State. Chem.* **9**, 173, (1974)
- ⁶¹ Y. Shimakawa, Y. Kubo and T. Manako, *Nature* **379** (1996) 53
- ⁶² E. Lopez-Navarrete, V.M. Orera, F.J. Lazaro, J.B. Carda, M. Ocana *J. Am. Ceram. Soc.* **87**(11) (2004) 2108
- ⁶³ S. Ishida, F. Ren, and N. Takeuchi, *J. Am. Ceram. Soc.* **76**(10) (1993) 2644
- ⁶⁴ E. Hough, D.G. Nicholson, *J. Chem. Soc.: Dal. Trans.* (1981) 2083

-
- ⁶⁵ W. Jeitschko and A.W. Sleight, *Acta Cryst. B*, **30** (1974) 2088
- ⁶⁶ P.J. Rentzeperis, *Z. Krist.* **117** (1962) 431
- ⁶⁷ W.J. Moore and L. Pauling, *J. Amer. Chem. Soc.* **63** (1941) 1392
- ⁶⁸ A.L. Hector, S. B. Wiggin, *J. Solid State Chem.* **177** (2004) 139
- ⁶⁹ T. Birchall and A. W. Sleight, *J. Solid State Chem.* **13** (1975) 118
- ⁷⁰ I.D. Brown *Chem. Soc. Revs.* **7** (1975) 359
- ⁷¹ D. Altermatt, I.D. Brown, *Acta Crystallogr. B* **41** (1985) 240
- ⁷² I.D. Brown, *J. Solid State Chem.* **82** (1989) 122

Chapter 2
Instrumentation and Methodology

2.1. Sample Preparation

The samples synthesised throughout the course of this work were all synthesised using classic solid state methods. This often required the use of very high sintering temperatures, due to the lack of mobility and reactant contact associated with powdered compounds, as well as various reaction environments. A solid state reaction involves the combination of powdered samples, usually metal oxides, to form a homogeneous mixture. This is usually achieved by dry grinding in an agate pestle and mortar; however the use of a suitable volatile solvent can aid the mixing process. Both particle size and homogeneity can affect the success and speed of the resulting reaction. Smaller particle sizes increase the surface area of the reactants and therefore tend to reduce the reaction times and compressing the powders into a pellet can increase the surface contact and again reduce the reaction time. The final factor is to maximise the sintering temperature and therefore increase the mobility of the ions throughout the sample.

The heating of samples in air is the most basic sintering environment, but several others may be utilised depending on the samples in question. At high temperatures the oxidation of metal cations is a major problem which can be avoided by using inert gas environments. Samples are placed in a quartz tube inside a tube furnace while gas is passed into one end and then flows over the sample and out through a bubbler at the other end. This same process can be used for oxidation and oxygen annealing by passing pure oxygen through the tube.

One of the most common methods used for air sensitive compounds, especially those containing reactants with low sublimation temperatures, is that of sealed quartz tubes. Mixed reactants are placed inside a quartz tube which is then evacuated and sealed before heating. This is the primary method used in the synthesis of unstable compounds containing sulphides. The major problem with using sealed tubes is when using elements that react with the quartz and degrade the tube. This can often be avoided by carbonising the inside of the tubes with decomposed acetone, or in the most extreme cases placing the sample in a gold tube before sealing.

2.2. Diffraction Experiments

The analysis of the diffraction of any wavelike particle (electromagnetic radiation, neutrons, electrons) relies on the same basic principle. When matter is placed in the path of a radiation beam it will scatter in various directions that are dependent on the type of matter and the nature of the radiation beam. The analysis of this predictable interaction can be used to gain information about the type and structure of material used to cause the initial diffraction. If the wavelength of the incident radiation beam has a wavelength comparable to the inter-atomic distances in a solid then the type and arrangement of atoms in the material can also be found. For the structural analysis of crystalline solids, a radiation with a wavelength between 0.6 and 1.9 Å is therefore used.

2.2.1. Diffraction Theory

The structure of any crystalline material can be depicted as a three dimensional lattice, repeating in all directions and defined by lattice points. The translational symmetry of the lattice points and therefore the structure of the material can be described by a series of equally spaced planes and lines connecting all the lattice points together. These so called "Miller" planes are labelled according to their h, k and l values (the Miller indices) which also denote the planes position within the cell. A Miller plane can be located by the reciprocals of the fractional intercepts along each of the unit cell directions. For example the plane with the Miller indices 1,2,4 would cut all of the way along the a axis, one half of the way along b and one quarter of the way along c. The distance between two adjacent Miller planes of the same number is called the d-spacing and is given by the symbol d_{hkl} .

In the study of crystalline solids, useful information can only be gained if the diffraction incident occurs in a very specific way. Useful, coherent scattering can only happen when two incident waves diffract off parallel Miller planes with the same Miller indices (Figure 2.1). At this point one of two things can occur: either the waves cancel each other out (destructive interference), or they add together (constructive interference) to give a meaningful interaction. Constructive interference only occurs when the path difference between the two waves is an integral number of wavelengths. Which of the two outcomes occurs is dependent

on a number of factors: the distance between the planes (d_{hkl}), the wavelength of the radiation λ , and the angle of incidence θ . All these factors are related to each other and the path difference between the wave by an equation known as Bragg's Law:¹

$$\text{Path Difference} = WX + XY = 2d_{hkl}\sin\theta = n\lambda \quad [\text{Equation 2.1}]$$

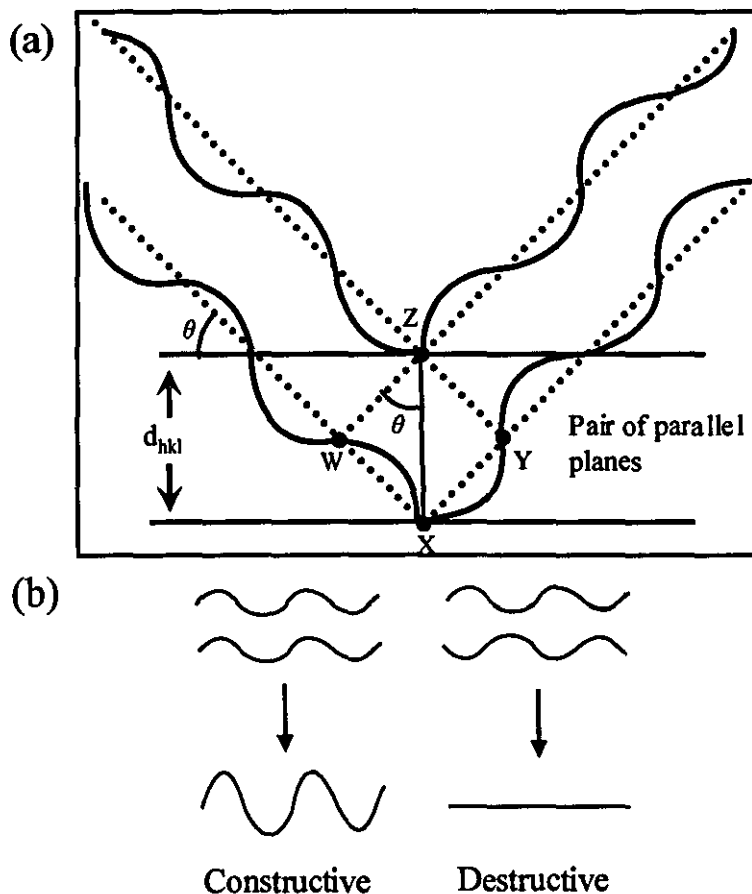


Figure 2.1: a) Diffraction from parallel planes b) Constructive and destructive interference

From Bragg's law it can be deduced that the d -spacing of any Miller plane can be found by knowing both the angle of incidence and the wavelength of the diffracted radiation. Thus from these two types of diffraction experiment are derived:

- 1) Constant wavelength, variable detection angle.
- 2) Constant detection angle, variable wavelength.

The first is by far the most common diffraction experiment and is used by most laboratory X-ray diffraction equipment. A single wavelength is selected and the diffractometer scans through a range of angles producing a diffraction pattern with peaks located on the x-axis by diffraction angle (2θ). The second type is usually only used in large neutron spallation sources where a range of wavelengths are produced. In this case, the angle is held constant and the diffraction patterns are usually plotted in wavelength or time of flight. Which ever type of experiment is performed the result should be a diffraction signal from every lattice plane, resulting in an observed intensity on the diffraction pattern. The symmetry of the lattice then gives rise to certain systematic absences, where intensity is not seen for some planes. These absences arise in the case of non-primitive space groups and from symmetry elements such as glide planes and screw axes. All of these can then be used to determine the space group and structure of the lattice.

2.2.2. X-ray Diffraction

X-rays are the most energetic form of magnetic radiation and generally have a wavelength between 0.05 and 100 Å (5×10^{-12} and 10^{-8} m). X-rays interact with electrons in matter causing them to diffract from the electron clouds surrounding the atoms of crystalline solids. This causes the relative scattering power of an atom to increase with increasing number of electrons, making X-rays better suited to studying heavier elements. The density of the electron cloud surrounding the lattice of most crystals causes the X-rays to have a very low penetration. At very high angles (longer path lengths), the probability of more than one diffraction incident occurring increases exponentially causing a rapid tail off in the coherent scattering intensity; a phenomenon known as form factor.

Commonly X-rays are generated by striking a metal target with highly energetic electrons. If the electrons are of sufficient energy they will cause a core electron to be ejected from a metal atom, resulting in a highly energised state. The gap in the inner electron shell will be filled as an electron from one of the higher shells drops down into the core shell. The energy difference between these two energy levels is emitted as an X-ray photon of a specific energy ($E = h\lambda$ where E is the energy difference, λ is the wavelength and h is Planck's constant).

2.2.2.1. Instrumentation

In the course of this work, powder X-ray diffraction (PXRD) data were collected on a Bruker D8 diffractometer, operating with $K_{\alpha 1}$ radiation (1.5046 Å) and a position sensitive detector. PXRD was used primarily as an initial analysis tool to confirm the success of reactions and to assess phase purity. Samples were typically scanned for a period of 20 min over a 2θ range of 10-60°, with a step size of 0.0147°. The diffraction data were evaluated using the EVA program of the Bruker DIFFRAC software package, which allows the comparison of scanned diffraction patterns to the JCPDS 2005 database (Joint Committee on Powder Diffraction Standards).

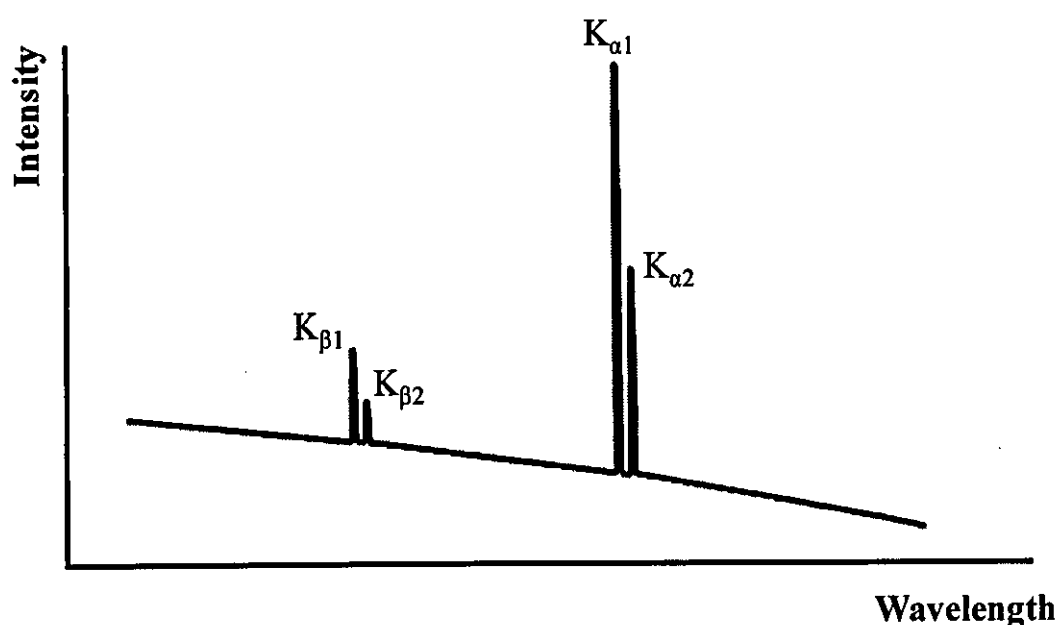


Figure 2.2: Output from a copper X-ray tube.

The single wavelength used is produced by thermionic emission from a water cooled, copper X-ray tube. The range and intensity of wavelengths produced is dependent on the nature of the metal target used. Figure 2.2 shows the typical X-ray output from a copper based X-ray tube, which consists of a series of four peaks at specific wavelengths. The four peaks are labelled $K_{\alpha 1}$, $K_{\alpha 2}$, $K_{\beta 1}$, and $K_{\beta 2}$ which are derived from the electron orbital from which the decay occurs. α and β relate to the orbital that the decaying electron originates from ($\alpha = 2s$ and $\beta = 3s$),

and 1 and 2 relate to the spin state of the electron (1 = spin opposed and 2 = spin aligned).

In order to carry out an X-ray diffraction experiment it is preferable to use a single X-ray wavelength. This can be done by either using a filter made from a metal one atomic number lower than the target (Ni filter for a Cu target) which will filter out the white background radiation and both the K_{β} lines leaving only $K_{\alpha 1}$ and $K_{\alpha 2}$. The D8 diffractometer uses a Ge single crystal monochromator, which when aligned selects a single wavelength; this is preferably the $K_{\alpha 1}$ wavelength as it has the highest intensity. The application of Bragg's law shows that only a single wavelength will exit the crystal at a given angle of diffraction. This is then directed towards the sample and used in the diffraction experiment.

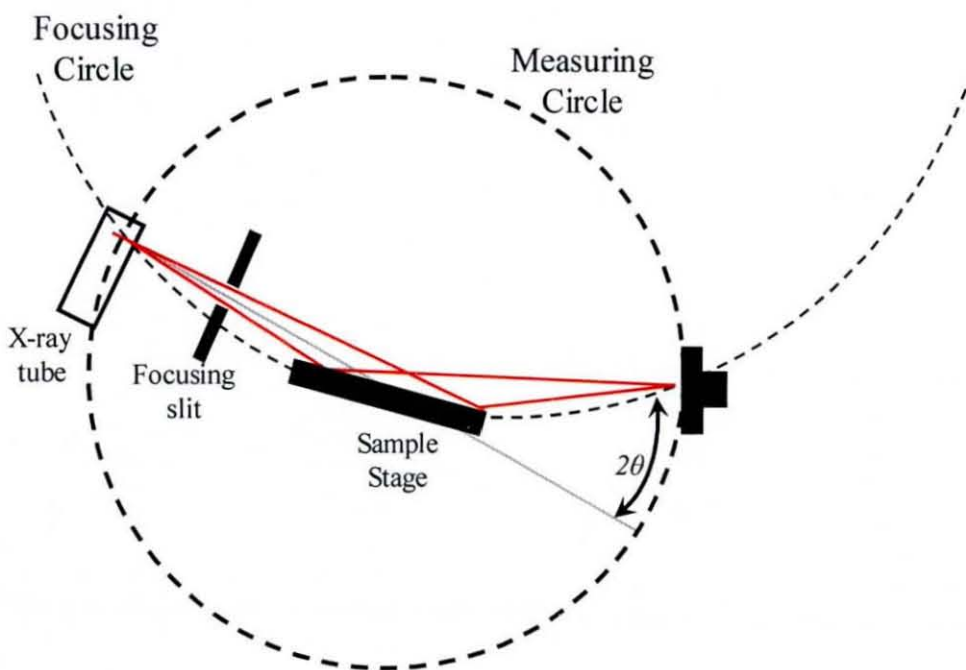


Figure 2.3: Flat plate geometry of the D8 X-ray Diffractometer

Like most laboratory X-ray diffraction equipment, the D8 uses flat plate geometry (Figure 2.3) though the use of transmission X-ray diffraction is becoming more common. The monochromated X-rays are directed towards the surface of a flat sample where they are diffracted and then received by the detector. The detector is

scanned through a range of diffraction angles (2θ) to analyse the various d-spacings in the crystalline structure. The glancing angle (θ) from the surface of the sample is moved at half the speed of the detector thus keeping the X-ray beam in focus.

2.2.3. Neutron Diffraction

A neutron is an uncharged (electrically neutral) subatomic particle which allows them to scatter from the nucleus of an atom rather than the electron cloud. Although the scattering cross section, or probability of scattering, is much lower than that of X-rays there is no strong correlation to the atomic weight. This allows the accurate determination of light atoms in the presence of heavier atoms as well as the ability to distinguish neighbouring elements and even isotopes of the same element. The intrinsic spin $\frac{1}{2}$ nature of the neutron allows magnetic scattering and the probing of local magnetic structures as well as nuclear structures.

2.2.3.1. Instrumentation – POLARIS (ISIS)

During the course of this work two neutron diffraction instruments were used to collect powder neutron diffraction (PND) data. The first was the POLARIS beam line at the ISIS facility in the Rutherford Appleton Laboratory.

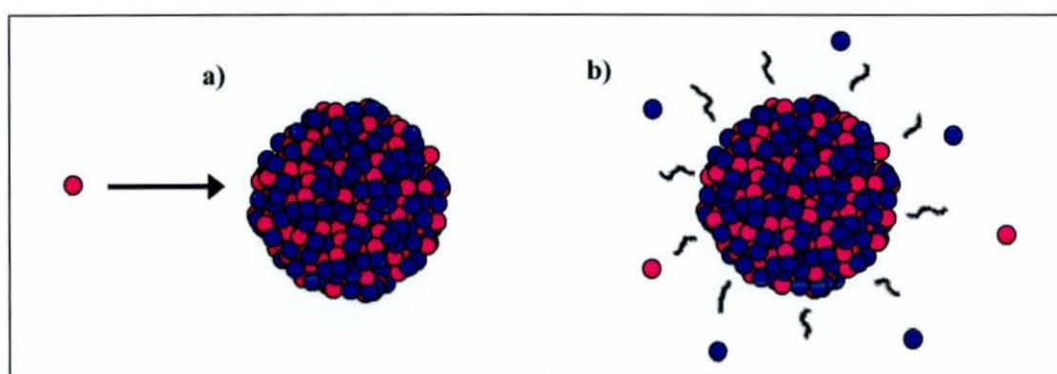


Figure 2.4: a) Energised proton (purple) striking a heavy metal nucleus b) an excited nucleus emitting neutrons (blue) and protons

Here neutrons are produced using a spallation source whereby energetic protons are accelerated towards a heavy metal target (U or Ta). The resulting interaction

produces excited nuclei which lose energy through the emission of neutrons protons and other elementary particles (Figure 2.4). Around 20 neutrons are produced per proton interaction which can then be used for experimentation. The process produces white neutrons which are slowed down by a hydrogenous moderator (water, liquid H₂ or liquid methane), before being diffracted by the sample and detected by the instrument.

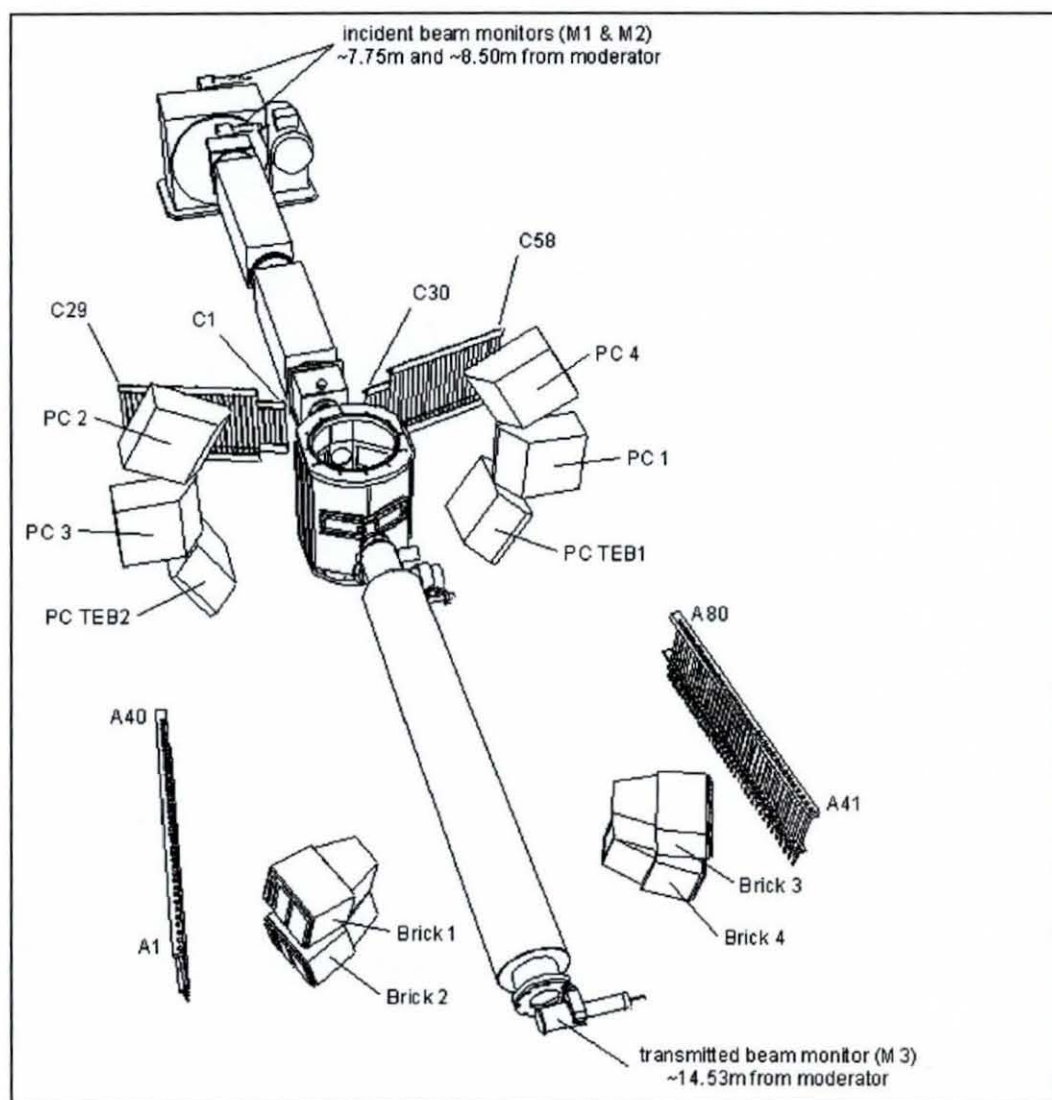


Figure 2.5: Schematic diagram of the POLARIS diffractometer

The POLARIS instrument (Figure 2.5) is a high intensity medium resolution ($\lambda/d/d \sim 5 \times 10^{-3}$) diffractometer with a d-spacing study range of 0.2 – 3.2 Å on the backscattering ³He gas detector bank. As the spallation source produces a range of neutron wavelengths the diffraction patterns are recorded in time of flight from

the source to the detector. The wavelength is then calculated using the De Broglie relation ($\lambda=h/mv$) and from that the d-spacing. Samples are mounted in cylindrical vanadium cans which show very little coherent scattering, and any residual peaks are removed as a background from the experimental diffraction pattern before analysis.

2.2.3.2. Instrumentation - D20 (ILL, Grenoble)

The second neutron diffraction instrument used in the course of this work was the D20 instrument at the Institut Laue-Langevin (ILL) in Grenoble, France.

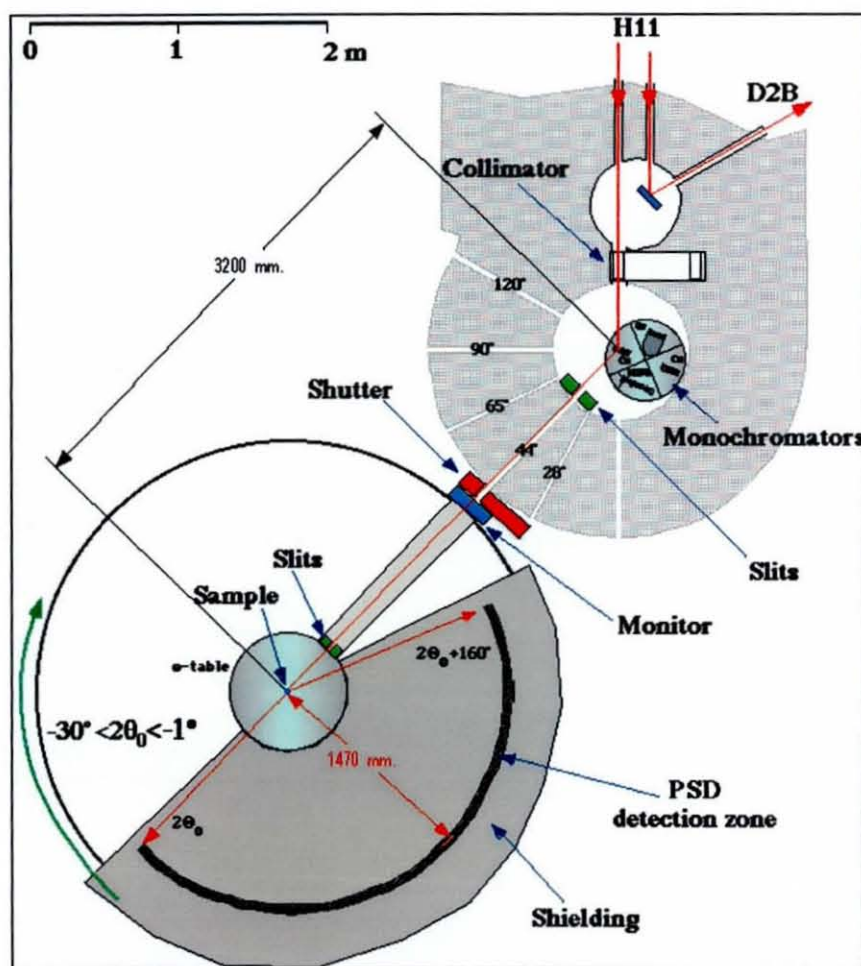


Figure 2.6: Schematic diagram of the D20 diffractometer

The ILL houses a high flux nuclear reactor which produces 1.5×10^{15} neutrons $s^{-1} cm^{-2}$ with a thermal power of 58.3 MW. The D20 instrument shown in Figure 2.6 is a high flux medium resolution powder diffractometer equipped with a large-area position sensitive detector. It is a single wavelength diffractometer which can

operate over a range of wavelengths depending the experiment in question. The complete diffraction pattern has 1536 positions, covering a scattering range of 153.6° . At the highest resolution the neutron flux reaches 10^7 neutrons $s^{-1} cm^{-2}$. In the course of the D20 experiments, a wavelength of 1.36 \AA was selected, and the instrument was set at the highest resolution with slit sizes of 5 mm.

2.3. Powder Diffraction Data Refinement – The Rietveld Method

In order to carry out diffraction analysis on a crystalline solid in the form of a single crystal, it is important to gain the correct alignment to observe and assign reflections. This single crystal method of diffraction experiment is not always practical when it comes to solid state chemistry. The insolubility of many oxide compounds does not lend itself to growing single crystals, and the combination of high reaction temperatures and constant regrinding rarely gives crystals of the size needed for these experiments. In a powder diffraction experiment however the powder contains a large amount of tiny crystals arranged in all possible orientations. When an radiation beam hits a polycrystalline sample it is diffracted in all possible directions at once as determined by the Bragg equation. Each different d-spacing of the crystal gives rise to a diffraction cone with an angle also determined by the Bragg equation. Each cone is a series of closely spaced dots which are the diffractions from individual crystals (Figure 2.7).

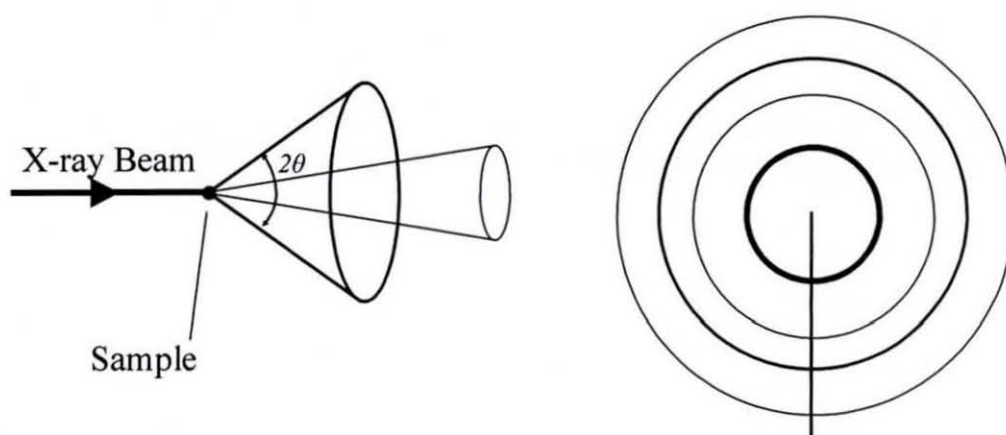


Figure 2.7: Diffraction Cones from a polycrystalline sample and the resulting pattern

When detected the diffraction cones would form a pattern of concentric circles of various intensities. A diffraction pattern is effectively a slice of the cone pattern with the intensities of the lines represented by peaks. The peaks represent reflections from different lattice planes and are at specific locations, 2θ or time of flight, which relate to the d-spacing of the particular Miller plane that the reflection relates to. The location of the peaks can be converted to the d-spacing of each plane and using this information the structures space group and unit cell dimension can be found ($a, b, c, \alpha, \beta, \gamma$).

The final powder diffraction pattern is affected by a number of factors. The number and location of the Bragg peaks is dependent on the size and space group of the unit cell. The relative intensities of the peaks are dependent on structural factors, such as the type and location of atoms within the cell and their corresponding temperature factors. The extraction of this kind of information can often be a complicated and time consuming exercise, involving the measurement of the height and area of all Bragg reflections. In more complicated structures this is not always successful as such experiments contain many Bragg reflection, some of which overlap to such an extent that it makes the extraction of individual peaks impossible. In order to fully characterise the structure from a powder diffraction pattern a mathematical method known as the Rietveld method is often used.

The Rietveld method, developed by Dr Hugo Rietveld in 1969,³ allowed crystallographers to interpret powder diffraction patterns without the complications of measuring overlapping peaks. The method involves the comparison of a calculated model to the observed profile from the diffraction experiment. A starting model, containing all the relevant structural and instrumental parameters, is used to form a calculated profile and then an iterative least squares procedure is used to minimise the difference between them. By making small modifications to the calculated profile parameters the structure is refined to a minimum difference and the final structure can be extracted.

Throughout the course of this work powder X-ray diffraction data and neutron diffraction data (both constant wavelength and time of flight) were refined using the GSAS suite of programs.²

2.3.1. Least Squares Procedure

GSAS uses a non-linear iterative least squares method to minimise the difference between the observed data intensity and the calculated values derived from a series of crystallographic expressions. The minimisation function is given as:

$$M = f_h \sum M_h \quad \text{[Equation 2.2]}$$

The M_h term can be made up of multiple data sets, either powder (M_p) or single crystal (M_s), each of which occupies a separate histogram with GSAS. Each histogram also has a weighting factor (f_h) used to balance the contributions from each data set. The contribution to the minimisation function by powder diffraction data is given by:³

$$M_p = \sum w(I_o - I_c)^2 \quad \text{[Equation 2.3]}$$

The M_p function is dependent on the sum of the squared difference of the observed (I_o) and the calculated (I_c) intensities for each observation point. The weighting factor w is the reciprocal of the observed intensity ($1/I_o$) and allows differences at high intensities to have less contribution than the same differences at low intensities. The quality of the least squares refinement at this point is indicated by a series of residual functions. These cover the entire pattern and are defined in [Equation 2.4].

$$R_p = \frac{\sum |I_o - I_c|}{\sum I_o} \quad \text{[Equation 2.4]}$$

and

$$R_{wp} = \sqrt{\frac{M_p}{\sum w I_o^2}} \quad \text{[Equation 2.5]}$$

A third residual function known as the “expected R_{wp} ” can be calculated from the statistics of the refinement and is given by:

$$\text{expected } R_{wp} = \frac{R_{wp}}{\sqrt{\chi^2}} \quad [\text{Equation 2.6}]$$

The χ^2 is often used as a “goodness of fit” term and is a good indication of the progress of the refinement - in most cases a χ^2 value of less than 10 would indicate an acceptable refinement result. This statistical value is calculated from:

$$\chi^2 = \frac{M}{(N_{obs} - N_{var})} \quad [\text{Equation 2.7}]$$

where N_{obs} is the total number of observations in all histograms and N_{var} is the number of variables in the least squares refinement.

2.3.2. Powder Diffraction Profile Intensities (I_o and I_c)

The calculation of both the observed and calculated intensities can be largely dependent on the diffraction method used; however the basic theory is the same for both. The total normalised profile intensity, I_o , at a given point in the powder diffraction pattern is contributed to by the nearby reflections and the background scattering. When using constant wavelength (CW) diffraction methods the intensity contribution is the same across the whole pattern. In time of flight (TOF) experiments however the intensity changes with wavelength intensity variation of the radiation source. The normalised intensities for TOF data is given by:

$$I_o = \frac{I'_o}{WI_i} \quad [\text{Equation 2.8}]$$

where I'_o is the number of counts observed in a channel of width W , and I_i is the incident intensity derived from the instrument specifications. For CW data the equation is simplified to:

$$I_o = \frac{I'_o}{I_i} \quad [\text{Equation 2.9}]$$

The calculated intensity is derived from a number of contributions both from instrument variations and crystallographic information in the following function:

$$I_c = I_b + S_h \sum S_{ph} (F_{ph}^2 H [T - T_{ph}] K_{ph}) \quad [\text{Equation 2.10}]$$

The calculated intensity equation is a sum of the background intensity I_b and the sum of the Bragg intensities ($Y_{ph} = (F_{ph}^2 H [T - T_{ph}] K_{ph})$). S_h and S_{ph} are scaling factors for the given histogram and phase of that histogram.

The Bragg intensity function for a reflection can be separated into two types of contribution: structural factors and profile correctional factors. The first type is given by the structure factor for the given reflection (F_{ph}) and includes the temperature factors, positions, occupancies and scattering of each atom in the asymmetric unit.

2.3.2.1. Structure Factor (F_{ph})

The structure factor for both single crystal and powder diffraction refinements is calculated in the standard way from the atomic coordinates form factors and temperature factors, and are the same for both X-ray and neutron diffraction. The form factor expression is the usual complex quantity:

$$F_{ph} = A_{ph} + B_{ph} \quad [\text{Equation 2.11}]$$

Where A and B are the real and imaginary parts of the structure factor. The space group routines for inversion centres are simplified by always placing them on the origin. Since the observed intensity is related to the square of this quantity the following equation is calculated for all diffraction data.

$$F_C^2 = A^2 + B^2 \quad [\text{Equation 2.12}]$$

In the case of real crystalline structures the scattered intensity is modified from its allowed location to include anomalous dispersion contributions from

imperfections in the lattice structure. For X-ray diffraction, the form factor contributions included the dispersion contributions and are effected by the atomic site fraction (x) and the thermal motion contributions (T'').

$$f = xT''(f_0 + f' + if'') \quad [\text{Equation 2.13}]$$

From this the real (A) and imaginary (B) expressions can be further broken down into three components each:

$$A = A_0 + A' - B'' \quad [\text{Equation 2.14}]$$

$$B = B_0 + B' + A'' \quad [\text{Equation 2.15}]$$

where

$$\begin{aligned} A_0 &= \sum_i x_i T_i'' f_{oi} \cos 2\pi h \cdot r & B_0 &= \sum_i x_i T_i'' f_{oi} \sin 2\pi h \cdot r \\ A' &= \sum_i x_i T_i'' f_i' \cos 2\pi h \cdot r & B' &= \sum_i x_i T_i'' f_i' \sin 2\pi h \cdot r \\ A'' &= \sum_i x_i T_i'' f_i'' \cos 2\pi h \cdot r & B'' &= \sum_i x_i T_i'' f_i'' \sin 2\pi h \cdot r \end{aligned} \quad [\text{Equation 2.16}]$$

In the case of neutron diffraction the form factor contributions become effectively zero so the contributions become equal to the real scattering lengths (b_0). A few elements and isotopes do show some anomalous scattering so:

$$f = xT''(b_0 + b' + ib'') \quad [\text{Equation 2.17}]$$

When using powder diffraction methods the averaging process means that the intensity of a reflection also contains elements of Friedel reflection pairs. The above component is then modified for powder diffraction to represent this new intensity.

$$F^2 = (A_0 + A')^2 + B''^2 + (B_0 + B')^2 + A''^2 \quad [\text{Equation 2.18}]$$

The temperature factor (T'') or thermal motion is a correction for the time dependent vibrations of the atoms from their mean locations. This causes a

reduction in the scattered intensity which is modelled isotropically by the following expression.

$$T'' = e - (8\pi^2 U_{iso} \sin^2 \theta / \lambda^2) \quad [\text{Equation 2.19}]$$

The above temperature factor (equation 2.19) uses the isotropic temperature factor for each atom (U_{iso}). The assumption that the temperature factors are isotropic is only true for the highly symmetrical, special sites of certain cubic space groups. A more accurate analysis of most instances models the thermal parameters as an anisotropic ellipsoid.⁴

$$T'' = e - \left[2\pi^2 \left(u_{11}h^2a^{*2} + u_{22}k^2b^{*2} + u_{33}l^2c^{*2} + 2u_{12}hka^*b^* + 2u_{23}klb^*c^* + 2u_{13}hla^*c^* \right) \right] \quad [\text{Equation 2.20}]$$

2.3.2.2. Intensity Correction Factors

The second set of contributions to the Bragg intensity ($F_{ph}^2 H(T-T_{ph}) K_{ph}$) are derived from the profile corrections to the structural factors. $H(T-T_{ph})$ is the profile peak shape function for the reflection at position, T , displaced from its expected position, T_{ph} . K_{ph} is an intensity correction from the product of various geometric and other correctional factors for that reflection given by the equation:

$$K_{ph} = \frac{E_{ph} A_h O_{ph} M_p L}{V_p} \quad [\text{Equation 2.21}]$$

E_{ph} is an extinction correction, M_p is the reflection multiplicity, L is the angle dependent correction (Lorentz-polarisation), O_{ph} is a preferred orientation correction and V_p is the unit cell volume for the phase.

A_h is the absorption coefficient which is dependent on the geometry of the diffraction method used. The first is for sample cans commonly used in the neutron diffraction experiments, where the absorption ($A_B = \mu R/\lambda$) for a cylindrical sample is calculated according to an empirical formula.⁵ The second is for flat plate (Bragg-Brentano) X-ray diffraction geometry, correcting for surface

roughness, and is a normalised form of the Pitschke, Herman and Mattern function.⁶

Generally all of the above terms are similar for both neutron and X-ray diffraction with the exception of the absorption correction and preferred orientation correction. Absorption corrections at the ISIS facility bear a complicated relationship to the wavelength profile of the neutron source. They are therefore usually removed prior to refinement along with the vanadium can background. The preferred orientation for cylindrical samples is also assumed to be negligible.

2.3.2.3. Peak Profile Functions

The comparison of intensities is performed at every point and requires the construction of the calculated profile to accurately describe the shape of the Bragg peaks. Generally the peak shape in constant wavelength neutron and X-ray diffraction techniques is pseudo-Voigt and is described by a multi-term Simpson's rule integration⁷ of the pseudo-Voigt function.

$$H(\Delta T) = \sum_{i=1}^n g_i F(\Delta T') \quad [\text{Equation 2.22}]$$

where the pseudo-Voigt is

$$F(\Delta T') = \eta L(\Delta T', \Gamma) + (1 - \eta) G(\Delta T', \Gamma) \quad [\text{Equation 2.23}]$$

The L and G terms are the Gaussian and Lorentzian contributions to the peak shape and η is a mixing factor which is defined by the equation:

$$\eta = N_A + N_B(2\theta) \quad [\text{Equation 2.24}]$$

where N_A and N_B refinable parameters allowing the background to be refined as a function of 2θ . Γ is a function of the Gaussian full width half maximum (FWHM) of the peak.

2.4. Nuclear Magnetic Resonance (NMR) Spectroscopy

The discovery of Nuclear Magnetic Resonance (NMR) in the mid forties heralded the development of a highly sensitive analytical technique. Since its creation, NMR spectroscopy has been heavily focused on hydrocarbon chemistry due to their high solubility in suitable solvents. The study of other nuclei in a variety of solutions has steadily increased over the years but is still used by a relative few. Unfortunately the use of solution NMR is of very little use for the insoluble compounds studied in solid state chemistry. The development of Magic Angle Spinning NMR (MASNMR) has seen a huge increase in both variety of elements and samples studied in the solid state.

2.4.1. Principles of NMR

Every atomic nucleus has a value known as a quantum spin number (I), which is related to the number of protons and neutrons of each elemental isotope. The quantum spin number, which is predicable to a certain extent, can take the value of any integer (1, 2, 3...), half-integer (1/2, 3/2, 5/2..) or zero. Any nucleus with a spin quantum greater or less than zero has a magnetic moment, derived from its spin, and is therefore affected by magnetic fields. The nuclear magnetic moment (μ) measures the extent of the effect that the magnetic field will have and it is directly proportional to the spin.

$$\mu = \frac{\gamma h}{2\pi} \quad \text{[Equation 2.25]}$$

where γ is a proportionality constant, specifically related to the nucleus in question, known as the gyromagnetic ratio.

Under normal circumstances the nuclear magnetic spin states of the nucleus are effectively degenerate, however when the nucleus is placed in an external magnetic field these spin states will split. This results in the spin of the nucleus adopting $2I + 1$ spin state configurations which are aligned with the magnetic field or opposed to it. For example for nuclei with a quantum number of $\frac{1}{2}$ eg. ^1H , ^{13}C

will adopt two spin states in an applied magnetic field, one aligned (+½) and one opposed (-½).

In the presence of an applied magnetic field (B), the energy of interaction for a given spin state (m_I) is related to the field and the nuclear magnetic moment by the following equation.

$$E = \frac{\gamma \hbar}{2\pi} m_I B \quad [\text{Equation 2.26}]$$

Under the influence like of an applied magnetic field the spin state will split from the degenerate energy state into the different energy levels of the component spin states. The occurrence of NMR transitions between the different energy levels are only allowed between neighbouring energy levels ($\Delta m_I = \pm 1$). This means that the energy of an NMR transition is dependent only on the applied field and the nuclear magnetic moment according to the following relationship.

$$\Delta E = \frac{\gamma \hbar B}{2\pi} \quad [\text{Equation 2.27}]$$

The NMR transitions are induced by an applied electromagnetic radiation source but only if the transitions energy and the applied radiation energy are the same. If the energy of the applied radiation ($E = h\nu$) and the transition energy are combined an NMR transition can only occur when:

$$\nu = \frac{\gamma B}{2\pi} \quad [\text{Equation 2.28}]$$

This allows the energy of any NMR transition to be found by varying the wavelength of the radiation and/or the magnetic field. The point where the field and the wavelength are at the right values for a transition to occur is known as the resonance position.

A spin $\frac{1}{2}$ nucleus in a magnetic field will have spin states with two orientations which will split into two energy field. The spin aligned state ($+\frac{1}{2}$) will be lowest in energy and is given the symbol α , and the spin opposed state ($-\frac{1}{2}$) will be highest in energy and given the symbol β . This allows for two possible NMR transitions, either an increase in energy from nuclear absorption ($\alpha \rightarrow \beta$) or a decrease in energy from induced emission ($\beta \rightarrow \alpha$). If the populations of these two levels are equal then no net transfer in energy can occur and no measurable effect would exist. However if the sample is in equilibrium then the Boltzmann distribution is still applicable. If N_α and N_β are the occupation of the corresponding spins state then:

$$\frac{N_\beta}{N_\alpha} = \exp(-h\nu/kT) \quad [\text{Equation 2.29}]$$

As $h\nu \ll kT$ then

$$\frac{N_\beta}{N_\alpha} = 1 - h\nu/kT \quad [\text{Equation 2.30}]$$

The Boltzmann distribution shows us that the lower energy spin state must have a higher occupation, although this difference in most cases is very small (1 in 100000). This means at the resonance point there is an increase in absorption and an NMR signal can be obtained. Since the absorption coefficient is the same from any nucleus the signal strength is proportional to the number of nuclei in the sample.

2.4.2. The NMR Spectrum

When an external magnetic field is applied to a nucleus it is shielded from the full effects by the motion of the surrounding electrons creating their own opposing magnetic field. The actual effect felt by the nucleus is therefore reduced depending on amount of shielding taking place. The effective magnetic field felt by the nucleus is therefore given by:

$$B_{eff} = B_0(1 - \sigma) \quad \text{[Equation 2.31]}$$

where σ is the shielding constant. The shielding constant changes with the chemistry of the local environment resulting in a change in the resonance frequency needed to cause a transition. This means that several resonance frequencies can exist for one type of nuclei depending on the amount of different local environments. The NMR spectrum therefore, consists of a number of resonances each corresponding to a different chemical environment. The location of each resonance is given a chemical shift value (ppm) and the size of the resonance is dependent on the number of nuclei in that environment.

The chemical shift is defined as the nuclear shielding divided by the applied field and as this is only dependent on the nucleus and its environment a suitable reference compound is always needed. The chemical shift can then be found by the following equation:

$$\delta = \left[(B_{ref} - B_{sample}) / B_{ref} \right] \times 10^6 \text{ ppm} \quad \text{[Equation 2.32]}$$

where δ is the chemical shift B_{ref} is the reference field, and B_{sample} is the sample magnetic field. The difference in resonance frequency between the sample and the reference is also proportional to the spectrometer frequency; therefore all three values are needed to interpret chemical shift.

A number of factors effect the amount of shielding at the nucleus and therefore the size of the chemical shift. The existence of electronegative neighbouring atoms or the influence of hydrogen bonds can both decrease shielding, while delocalised electron clouds and π -bonding can increase it.

2.4.3. Solid State NMR

The chemical shift anisotropy is caused by a number of factors, such as chemical shielding, dipole-dipole coupling and quadrapole couple, and manifests itself as a broadening of the recorded signal. In solution NMR, the effect is dependent on the molecular orientation of the species being analysed. The rapid isotropic tumbling

of the molecules changes the orientation of the species fast compared to the magnitude of the chemical shift anisotropy. This averages out the orientation effects to zero meaning the broadening is rarely observed.

In solid state NMR experiments, the sample in question is usually powdered and contains many crystallites in random orientations. Since the crystalline lattice holds the atoms rigid the chemical shift anisotropy is now dependent on the orientation of the crystals contained within the sample. This results in the NMR spectrum of powders to contain broad lines, as all the different orientations of the sample contained give rise to different spectral lines. This broadening is especially harmful when there are several inequivalent sites many of which may have overlapping spectral lines. It is therefore necessary in solid state NMR to apply techniques which decrease these effects and therefore increase the resolution of the resulting spectra.

2.4.3.1. Magic Angle Spinning NMR (MASNMR)

Magic angle spinning NMR is the basis for almost all solid state NMR experiments, where it's used in the reduction of chemical shift anisotropy and the removal of heteronuclear and homonuclear coupling. It is also used to narrow the lines seen from quadrupolar nuclei allowing a much larger range of elements to be studied.

Magic angle spinning has the effect of averaging out the orientation of the various species in a similar fashion to a liquid solution. The dependence of the orientation of the nuclear spin interactions to the chemical shift is known as the Zeeman interaction which is of the form $(3\cos\beta-1)/2$. This relationship is used to scale anisotropic interactions where β is the angle which describes the orientation of the sample in the applied magnetic field. In order to lose any contribution from these interactions and the associated line broadening this equation must equal zero. This happens when β is equal to 54.7° , or the 'magic angle' (Figure 2.8).

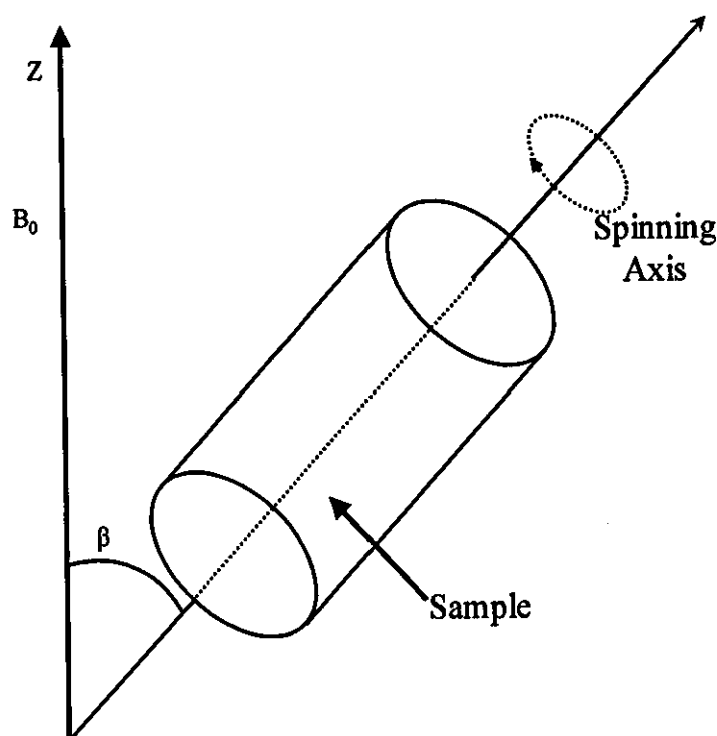


Figure 2.8: Magic Angle Spinning NMR sample alignment

2.5. Mössbauer Spectroscopy

Discovered by Rudolph Mössbauer in 1957-8,⁸ the Mössbauer effect is the recoilless nuclear emission or absorption of a γ -ray, without thermal broadening. The application of this effect in the study of compounds in the solid state has grown rapidly since its discovery and is now known as Mössbauer spectroscopy (also nuclear gamma resonance spectroscopy). The primary feature which has made the technique so widespread is the production of electromagnetic radiation with a very narrow energy range. This allows the probing of very small energy variations in the interaction of the nucleus with its surrounding electrons.

The effect was originally identified in the nucleus of ^{191}Ir however the effect has since been seen in a total of 88 γ -ray transitions in the isotopes of over 42 different elements.⁹ The criteria required for a practical application of this effect, however, has restricted Mössbauer spectroscopy to a handful of elements notably iron, tin, antimony, tellurium, iodine, xenon, europium, gold and neptunium. Due to the advantageous combination of properties shown by the tin nucleus and the

high natural abundance of ^{118}Sn , Mössbauer spectroscopy was used extensively for the study of tin based compounds in this work.

2.5.1. The Mössbauer Effect

The most effective way to visualise γ -ray photon emission, and therefore the evolution of Mössbauer spectroscopy, is to start with an isolated atom in the gaseous phase. The atom can be said to be in one of two energy states: the ground state (E_g) or the excited state (E_{ex}) with the energy difference between these two states being E . The kinetic energy possessed by the atom through thermal motion (E_k) can be derived from the mass of the nucleus (M) and its velocity (V_x) in direction at the given point. Therefore total energy of an excited atom above its *resting* ground state would be calculated from a combination of the two terms.

$$E + E_k = E + \frac{1}{2}MV_x^2 \quad \text{[Equation 2.33]}$$

The emission of a γ -ray photon, as the atom undergoes a nuclear transition from the excited state to the ground state, produces a recoil velocity (v) in accordance with the laws of motion. If we assume that the emission and the recoil both occur in the dimension of the initial velocity (V_x) and that there is no movement in the other two directions then a γ -ray photon of energy E_γ is produced leaving the ground state atom with a new velocity $V_x + v$. Thus according to the conservation of momentum:

$$E + MV_x^2 = E_\gamma + M(V_x + v)^2 \quad \text{[Equation 2.34]}$$

The energy of the emitted photon (E_γ) is therefore less than that of the nuclear transition (E) as some is lost during the recoil of the gaseous atom. The energy difference (δE) between E_γ and E can therefore be described as the change in kinetic energy from the excited state to the ground state.

$$\delta E = E - E_\gamma = M(V_x + v)^2 - MV_x^2 \quad \text{[Equation 2.35]}$$

$$\delta E = E - E_\gamma = Mv^2 + MvV_x \quad \text{[Equation 2.36]}$$

In order for this type of emission to be useful spectroscopically the emitted radiation must be absorbed by a target absorber of the same type. Ideally for this excitation to occur the energy of the γ -ray photon must equal the energy of excitation, E . It has been shown however that the energy of the γ -radiation is always less than the energy of the nuclear transition due to the loss of energy due to recoil.

Mössbauer realised that he could effectively make the mass (M) very large by using the solid matrix of a crystal lattice as apposed to an isolated atom. The recoil energy therefore is taken up by the lattice as a whole, since there is not enough energy to eject an atom from its site. Neither can the energy be taken up by the lattice vibrations as a time average of zero is already established within the decay time. Since M is very large and the lattice vibrations are quantised it can then be said that for a fraction of events the energy E must be completely transferred to the γ -ray photon ($E = E_\gamma$). This form of recoilless emission is known as the Mössbauer effect.

2.5.2. Mössbauer Spectroscopy

The principle aim of a Mössbauer experiment is to tune the energy of the emitted γ -radiation, using the Doppler effect, to the energy gap between the ground and excited states in a target absorber. By oscillating the source with respect to the absorber and detector a range of energies can be produced. Movements towards the absorber cause a shorter wavelength and higher energy, movements away from the source causing the opposite effect.

A Mössbauer experiment consists of a radioactive source, which is a solid matrix containing the excited nuclei of a suitable isotope. This source is placed next to a second matrix, the absorber, which is a similar material containing the same isotope in the ground state. The source is oscillated at different speeds to produce a range of wavelengths, which is either absorbed by the target or passes through to the detector.

If the energy difference between the ground and excited state of the target absorber is the same as the produced γ -ray radiation then a proportion of the radiation will be absorbed and be seen as a decrease in count rate. As the velocity of oscillation is changed the Doppler shift becomes lesser or greater and the absorbance will decrease gradually to zero (maximum count rate) leaving a well defined resonance. The location of the resonance maximum will be shown as an oscillation velocity. This figure is called the chemical shift and is quoted with reference to the source used, for example a ^{57}Fe source is quoted as α -iron.

The chemical shift is effectively a measurement of how different the chemistry of the absorber system is to that of the source. The major influence of this shift is a measurement of the electrostatic interaction between the nucleus and surrounding s -electrons. The chemical shift is therefore dependent on a number of factors including the number of s -electrons and the effect of the higher p , d and f shells due to shielding effects, as well as the electronegativity of the surrounding ions. The chemical shift is described by the following equation:

$$\delta E = K[\psi(0)]^2 R^2 \quad \text{[Equation 2.37]}$$

E is the energy of interaction $\psi(0)$ is the s -electron density around the nucleus and R is the radius of the nucleus. Since the radius of the atom is largely dependent on the electronic state of the nucleus then any differences between the wavefunction of the source and absorber must be taken into account. [Equation 2.38] therefore includes this to become:

$$\text{Chemical Shift} = K(R_s^2 - R_g^2)(\psi^s(0)^2 - \psi^g(0)^2) \quad \text{[Equation 2.38]}$$

R_s and R_g are now considered to be independent of the chemical environment and are unaffected by the wavefunctions of the source and absorber. Approximation of equation 2.35 gives:

$$\text{Chemical Shift} = 2KR^2 \left(\frac{\delta R}{R} \right) [\psi^s(0)^2 - c] \quad \text{[Equation 2.39]}$$

where c is the source characteristic and δR the difference in radius between ground and excited states.

While the s -electron density at the nucleus determines the shift there two other factors which effect the type of resonance that occurs. The first factor is the symmetry of the electron field which can cause a phenomenon called quadrapole splitting. If the quantum spin number is greater than or equal to one then the nucleus becomes unsymmetrical and takes on an ellipsoid configuration. This leads to an asymmetric field and therefore an electric field gradient (EFG) which is related to the symmetry of the nucleus. If the orbitals are completely filled the EFG would be zero as this leads to a symmetrical orbital. The d and f electrons can also contribute to the EFG but not to the same degree giving a lower quadrapole split. Spherically symmetrical distributions such as high spin d^5 however also give a zero EFG.

The second factor is influenced by magnetic ordering effects, both external and internal, which cause the nuclear spin quantum levels to split into their components. This gives six transitions which are equally spaced with intensity ratios of 3:2:1:1:2:3.

2.6. Colour Measurements

During the course of this work, the pigmentary properties of the synthesised materials were evaluated using a Perkin Elmer UV/Vis Lamda 30 spectrometer fitted with a reflectance attachment. The reflectance properties of each sample were analysed over the visible spectrum, between 380 and 700 nm, in comparison to a "pure white" barium sulphate standard. The reflectance apparatus allows the measurement of the wavelengths of light which make up a sample's perceivable colour. In order to produce quantifiable values for which colour can be characterised and compared the visible spectrum must be converted into colour measurement values. Throughout the course of this work colour measurement data was recorded using the *Commission Internationale de l'Eclairage* $L^*a^*b^{*10}$ system which is the standard used in the case of pigments and paints. This colour system is an adaptation of the CIE XYZ colour space which in turn is

derived from the original RGB colour description method – all three are explained here.

2.6.1. CIE RGB System¹¹

The foundations for the original CIE XYZ colour space and the later L*a*b* system was performed in the 1920's by W. David Wright¹² and John Guild.¹³ They both independently conducted a series of experiments to study the tricolour detection method of the human eye. In both cases three colours of constant wavelength but variable brightness were combined in order to reproduce a monochromatic test colour. The three colours, which became known as the primary colours, consisted of light with wavelengths of 700nm (red), 546.1 nm (green) and 435.8 nm (blue).

Not all colours could be reproduced in this manner however, since some required the use of negative values for one of the primary wavelengths. This was achieved by adding an amount of one of the primary wavelengths to the test colour before comparison. Using a combination of these methods it was possible to reproduce all perceived colours in the visible spectrum. The results from both experiments were combined into three colour matching functions $r(\lambda)$, $g(\lambda)$ and $b(\lambda)$, which would become known as the CIE RGB. These functions described the necessary proportions of the primary colours needed to reproduce a monochromatic test colour at a given wavelength (Figure 2.9).

Rather than specifying the brightness of each primary colour as proposed by Wright and Guild the curves are normalised so that the area beneath each curve is the same. This area is fixed to a particular value by specifying that:

$$g(\lambda) = V(\lambda) \quad \text{[Equation 2.40]}$$

where $V(\lambda)$ is the photopic luminous efficiency function. By proposing that the primaries be standardized in this way, the CIE established an international system of objective colour notation.

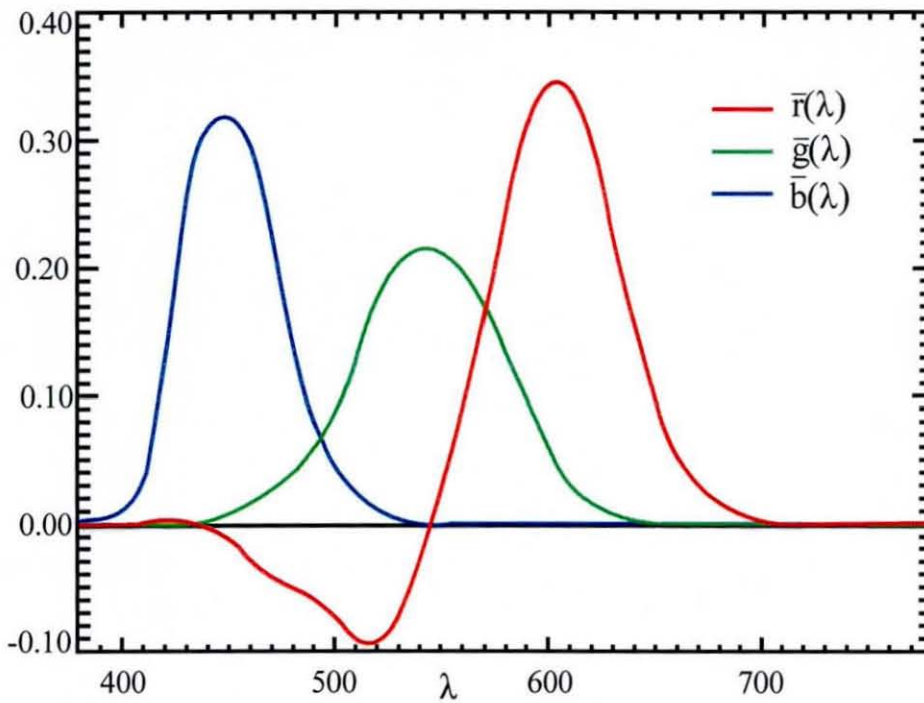


Figure 2.9: CIE RGB colour matching functions.¹⁴

Although these colour functions are dependent on the test colour being monochromatic, it can also apply to mixed wavelengths as well. If a test colour is made up of a combination of wavelengths then the primary colours needed to reproduce it will be a combination of the colour functions for each monochromatic wavelength when viewed separately. For example a test colour containing two wavelengths will have primary strengths that are a combination of $R_1G_1B_1$ which are the primaries for beam 1 and $R_2G_2B_2$ for beam 2. The resulting matching values R,G,B are derived from the following equations, known as Grassmann's Law.

$$\begin{aligned}
 R_1 + R_2 &= R \\
 G_1 + G_2 &= G \\
 B_1 + B_2 &= B
 \end{aligned}
 \quad \text{[Equation 2.41]}$$

Grassmann's Law is then described in general terms by saying that for a colour of given *spectral power distribution* $I(\lambda)$ RGB equals:

$$\begin{aligned}
 R &= \int I(\lambda)r(\lambda)d\lambda \\
 G &= \int I(\lambda)g(\lambda)d\lambda \\
 B &= \int I(\lambda)b(\lambda)d\lambda
 \end{aligned}
 \tag{Equation 2.42}$$

By using Grassmann's Law a reflectance spectrum can be converted to the RGB value associated with the perceived colour produced by that spectrum. The CIE RGB colour space, however, is only reliable when studying the colour of light rays. In order to properly compare the colour of materials the XYZ or L*a*b* system must be used.

2.6.2. CIE XYZ System¹⁴

The XYZ colour system is derived from the RGB system and was designed to have a linear relationship to the original system. It was assumed that in this case Grassmann's Law would still hold true and the $r(\lambda)$, $g(\lambda)$ and $b(\lambda)$ colour matching functions could be directly replaced by $x(\lambda)$, $y(\lambda)$, $z(\lambda)$. The primary reason for the production of this second colour space was a desire to have all perceived colours described by three values that were greater than or equal to zero. There were several other requirements that were introduced for computational simplicity. Firstly it was found that the $z(\lambda)$ function could effectively be zero for any wavelength above 650 nm. The second requirement was that $y(\lambda)$ would be equal to the *photopic luminous efficiency function* $V(\lambda)$ in the same way as the $g(\lambda)$ function above. The final and most influential requirement was that the so called "white point" or point of equal energy would appear at $x = y = z = 1/3$.

The design of the XYZ system was such that the Y value became a measure of the brightness of colour. This allowed the whole system to be visualised in a two dimensional representation of x and y (Figure 2.10) the x and y values are functions of the three values and are calculated from:

$$\begin{aligned}
 x &= \frac{X}{X+Y+Z} \\
 y &= \frac{Y}{X+Y+Z}
 \end{aligned}
 \tag{Equation 2.43}$$

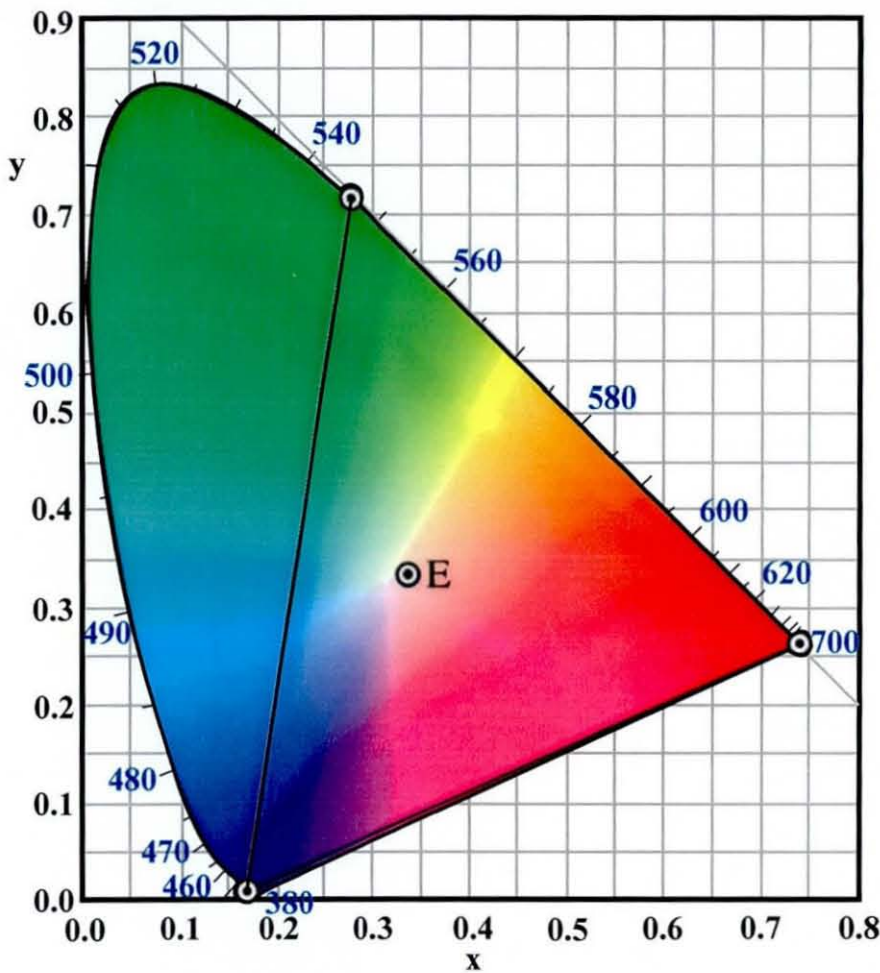


Figure 2.10: CIE 1931 xy chromaticity diagram¹⁴

The above chromaticity curve (Figure 2.10), has an outer monochromatic locus where the colour of each light wavelength is represented and labelled in nm, with the three RGB primaries are also shown at 700, 546.1 and 435.8 nm. The E represents the “white point” or equal energy point representing the bright white value of the described system. This is the point where the spectral energy per wavelength is the same for every wavelength recorded. The original RGB values can be converted to the XYZ colour space using a standardized transformation shown below:

$$\begin{bmatrix} X \\ Y \\ Z \end{bmatrix} = \frac{1}{b_{21}} \begin{bmatrix} b_{11} & b_{12} & b_{13} \\ b_{21} & b_{22} & b_{23} \\ b_{31} & b_{32} & b_{33} \end{bmatrix} = \frac{1}{0.17697} \begin{bmatrix} 0.49 & 0.31 & 0.20 \\ 0.17697 & 0.081240 & 0.01063 \\ 0.00 & 0.01 & 0.99 \end{bmatrix} \begin{bmatrix} R \\ G \\ B \end{bmatrix} \quad [2.44]$$

2.6.3. CIE L*a*b* System

While the XYZ colour space was able to characterise a colour using a series of three positive values, there were problems when trying to compare colours or explain colour differences. Unfortunately colours perceived by the eye follow a non linear relationship which does not allow for the direct comparison between one XYZ value and another. This causes an excessive representation of the green hues and bunching of the red violet and blue hues in the corners of the ellipse.

The L*a*b* or Lab system is an attempt to mimic the logarithmic responses of the eye and therefore linearise the differences between colours. Colours are described by three values: L* which is a measure of the luminescence or brightness of a sample (0 = black, 100 = white), a* is the position between magenta and green (negative green, positive magenta) and b* is the position between yellow and blue (negative blue and positive yellow). This means that the Lab colour space can only be correctly visualised in a three dimensional model, with the chromatic a/b axis on the horizontal and the brightness at right angles to it (Figure 2.11).

The XYZ colour system can be transformed to the Lab system using the following transformation:

$$\begin{aligned} L^* &= 116f(Y/Y_n) - 16 \\ a^* &= 500[f(X/X_n) - f(Y/Y_n)] \\ b^* &= 200[f(Y/Y_n) - f(Z/Z_n)] \end{aligned} \quad \text{[Equation 2.45]}$$

In this equation X_n , Y_n , and Z_n represent the CIE XYZ values for the reference white point and:

$$f(t) = t^{1/3} \text{ for values of } t > 0.008856 \quad \text{[Equation 2.46]}$$

or

$$f(t) = 7.787t + 16/116 \text{ for all other values.} \quad \text{[Equation 2.47]}$$

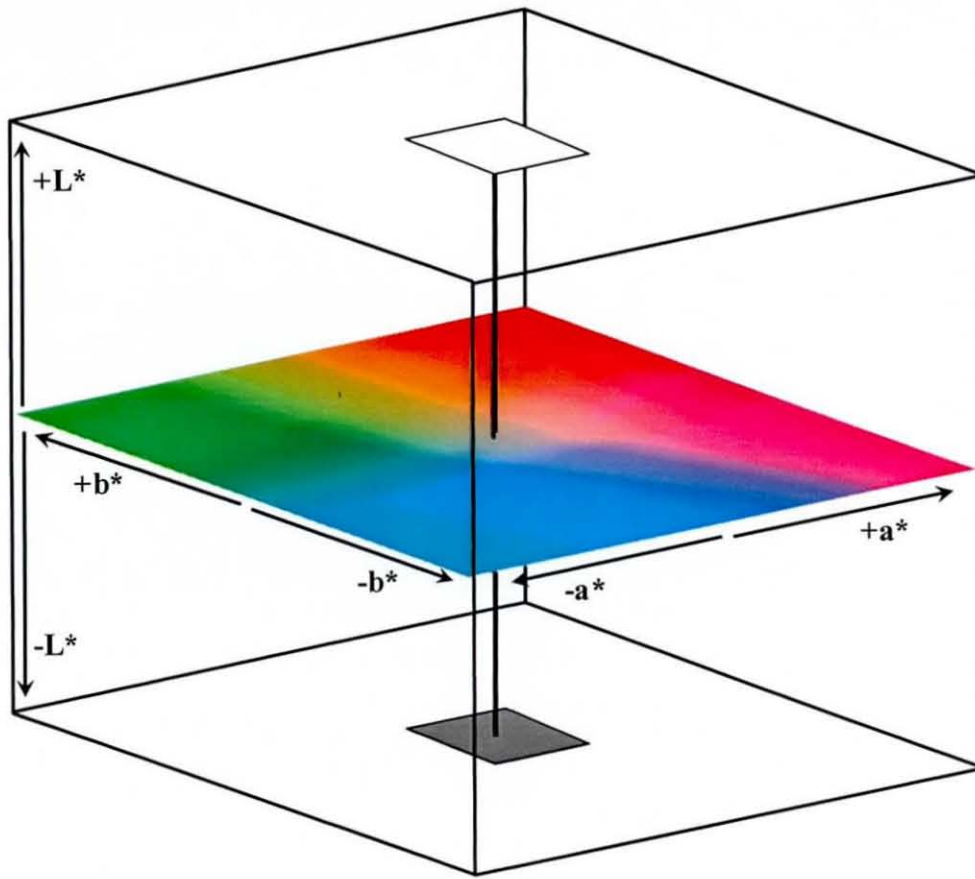


Figure 2.11. The CIE $L^*a^*b^*$ colour space model

2.7. References

-
- ¹ W.H.Bragg, W.L. Bragg, *Rev. Soc.* (1915)
 - ² A.C. Larson, R.b. Von Dreele, 2000. General Structure Analysis System (GSAS)
Los Alamos National Laboratory report LAUR, 86.
 - ³ H.M. Rietveld, *J. Appl. Cryst.* **2** (1969) 65
 - ⁴ H.M. Rietveld. *Acta Cryst.* **22** (1967) 151
 - ⁵ N.N. Lobanov & L. alte da Veiga, *6th European Powder Diffraction Conference*,
Abstract P12-16, Aug. 22-25 (1998)
 - ⁶ Pitscke, Hermann and Mattern, *Powder Diffraction*, **8** (1993) 74
 - ⁷ C.J.Howard *J. Appl. Cryst.*, **15** (1982) 615
 - ⁸ R.L.Mössbauer. *Z. Physik*, **151** (1957)124
 - ⁹ N. N. Greenwood and T. C. Gibb. *Mössbauer Spectroscopy*. Chapman and Hall
Ltd. 1971. SBN 412 10710 4
 - ¹⁰ K.McLaren, *J. Soc. Dyers. Colour.* **92** (1976) 338
 - ¹¹ CIE (1924). *Commission Internationale de l'Eclairage Proceedings*. Cambridge
University Press, Cambridge
 - ¹² W.D.Wright *Trans. Opt. Soc.* **30** (1928) 141
 - ¹³ J. Guild *Philos. Trans. Roy. Soc. Lond.* **A320** (1931) 149
 - ¹⁴ CIE (1931). *Commission Internationale de l'Eclairage Proceedings*. Cambridge
University Press, Cambridge

Chapter 3
Synthesis and Characterisation
of Tin Niobates

3.1. Introduction

Tin niobium oxide compounds were first discovered in the form of a naturally occurring mineral foordite, which was originally found near the Sebaya river, Rwanda. Both foordite, and its tantalum analogue theurite,¹ can be easily synthesised in the laboratory and have the general formula $\text{Sn}^{\text{II}}\text{M}^{\text{V}}_2\text{O}_6$ ($\text{M} = \text{Nb}, \text{Ta}$). The synthetic compound crystallises in a monoclinic space group, $C2/c$, with $a = 17.093$, $b = 4.877$, and $c = 5.558 \text{ \AA}$ and $\beta = 90.85^\circ$. The structure consists of a double layer of corner sharing NbO_6 octahedra separated by a sheet of edge sharing SnO_8 square anti-prisms between them. The anti-prisms have been shown to be distorted significantly by a stereo-active lone pair located on the tin metal centre (Figure 3.1).² The distortion manifests itself as a lengthening of the bonds on the side associated with the lone pair and an increase in the angles between these bonds to create the space required for the lone pair.

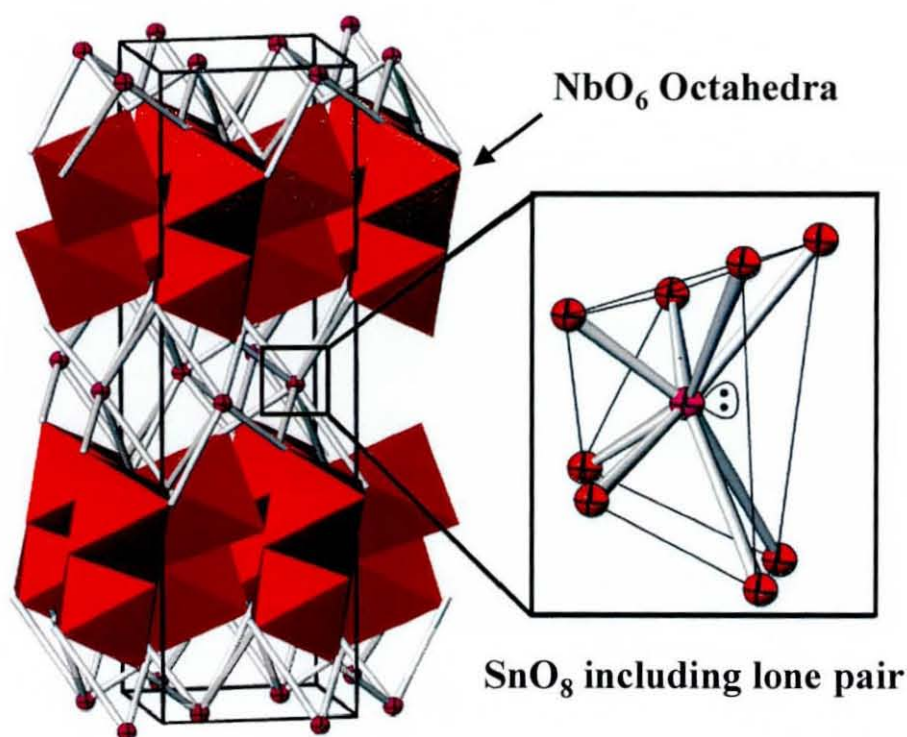


Figure 3.1: (a) Foordite structure (b) SnO_8 anti-prism distorted by tin lone pair.

Compounds of the Sn-Nb-O composition were found to form phases with the pyrochlore structure as early as 1955³ and were given the general formula

$\text{Sn}_2\text{Nb}_2\text{O}_7$. Several attempts were made in the following years to fully characterise the structure of these compounds with various degrees of success.⁴⁻⁶ Rather than having a classic pyrochlore structure, these phases were found to exclusively form non-stoichiometric^{4,5} phases, and tin Mössbauer studies⁶ identified a significant amount of Sn^{4+} in the primary phase. Mössbauer spectroscopy was also able to show that the isomer shift of the Sn^{2+} species was consistent with the existence of a stereoactive lone pair. Not only was this the first example of lone pair distortions in a pyrochlore structure, but it also occurred on the centre of symmetry of the structure; the *A* cation site. It was not understood at the time how the lone pair distortions would affect the symmetry of the whole system.

A full structural characterisation of these compounds was not carried out until some years later by Birchall and Sleight.⁷ By this point there were already many examples of compounds containing divalent tin usually in distorted or asymmetrical geometries.^{8,9,10,11} The lone pair distortions in these examples were usually modelled by the lengthening of a number of bonds on one side of the tin site to accommodate the electron lone pair. In the case of the tin niobates however, there appeared to be no obvious space to place the electron lone pair on the *A* cation site. The authors hypothesised that the tin could be statically displaced onto a surrounding site of lower symmetry in an attempt to model the lone pair distortions (see figure 3.2). It was also found that the detected Sn^{4+} content appeared to be in a relatively symmetrical environment similar to that of SnO_2 . Since this clearly could not be the case if the Sn^{2+} was on a asymmetrical *A* site, and also due to the size similarities with Nb^{5+} , the authors concluded that the Sn^{4+} resided in the symmetrical octahedral environment of the *B* cation site. A final general formula for the pyrochlore phase was therefore reported as $\text{Sn}^{\text{II}}_{2-x}\text{Nb}^{\text{V}}_{2-y}\text{Sn}^{\text{IV}}_y\text{O}_{7-(x-y/2)}$.

Very little research followed Birchall and Sleight's detailed paper until more recently, when a series of papers by Cruz *et al.* on tin niobates and tin lead niobates studied the ferroelectric properties of these compounds.^{12,13} Although the work of Cruz *et al.* used more current techniques, such as MASNMR in order to better characterise the structure, they still relied heavily on X-ray diffraction as

the primary analysis tool. The authors still used Birchall and Sleights's original model to re-characterise the tin niobate structure as well as characterise the lead based phases using these updated techniques and Rietveld analysis of powder X-ray diffraction data.

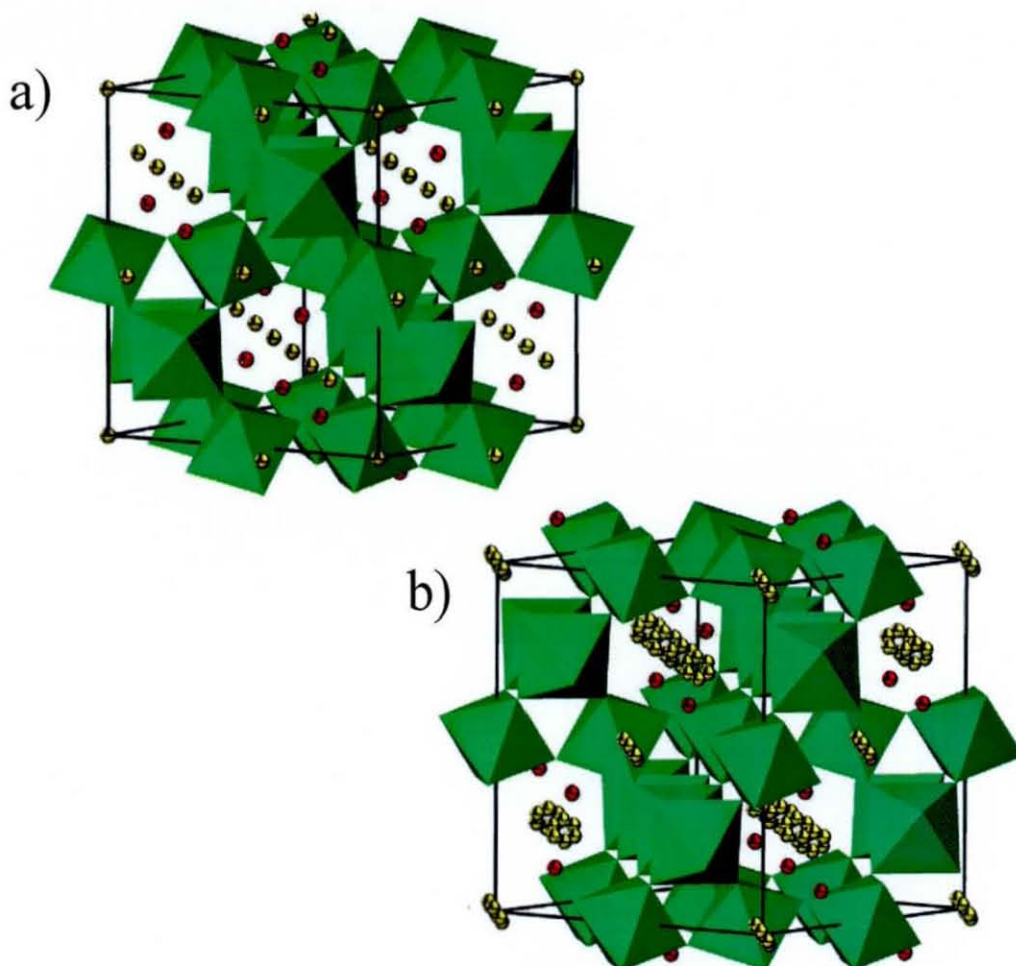


Figure 3.2: a) Ideal pyrochlore structure showing the green NbO₆ octahedra, and the Sn²⁺ (yellow) and O²⁻ (red) running in the channels between them. b) Birchall and Sleights model showing the Sn²⁺ displaced onto the six 96h sites

Both the original mineral, foordite, and the more recently reported pyrochlore structures have been described as bright yellow in colour. Although several structural studies have been carried out and various uses for related compounds have been put forward, there is no known study on the use of these compounds as inorganic pigments. There is also very little material studying the nature and

cause of the intense colouration observed in these materials, despite the fact that the removal of either the tin or niobium seems to disrupt the mechanism. This effect causes both the tantalum-doped analogues and other niobate based pyrochlores to be colourless.¹⁴

This section reports a study of the tin niobium compounds forming foordite and pyrochlore structures and their analysis as possible inorganic pigments. A re-determination of the structure of the tin niobate pyrochlore was carried out using neutron diffraction techniques. These analyses were coupled with new Mössbauer and MASNMR results to give a complete characterisation of these compounds. An attempt was made to understand the colour mechanism of these compounds by studying the structure of SnNb_2O_6 - SnTa_2O_6 solid solution. Colour measurements were taken of the synthesised compounds to quantify the change in colour depending on the ratio of tantalum to niobium.

3.2. Experimental

3.2.1. $\text{Sn}_2\text{Nb}_2\text{O}_7$ Pyrochlores

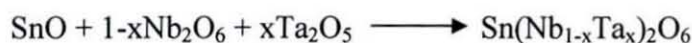
Tin niobium oxide pyrochlore samples were synthesised by mixing SnO and Nb_2O_5 in a 2:1 molar ratio. The powdered reactants were weighed, and then mixed homogeneously by grinding in an agate pestle and mortar. The mixed powder was then sealed in an evacuated quartz tube to protect the Sn^{2+} species from oxidation in the air.



The samples were heated to 1000°C at a rate of 2°C min^{-1} and this temperature was maintained for 10 h, resulting in a complete reaction to a yellow polycrystalline powder. The samples were left to cool to room temperature and then the polycrystalline powers were carefully removed from the quartz tubes. The heat treatment of the powders had caused them to sinter so were reground to form a free flowing powder.

3.2.2. SnNb₂O₆-SnTa₂O₆ Solid Solutions

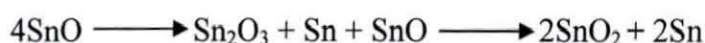
The tin niobate-tantalate solid solutions were synthesised by mixing SnO, Nb₂O₅ and Ta₂O₅. The amount of tantalum was increased in 0.2 increments to form samples with a range of compositions from SnNb₂O₆ to SnTa₂O₆. Powdered samples were wet ground, in acetone, using an agate pestle and mortar to assure homogeneous mixing. The resulting powders were compressed into pellets in a die press, placed in alumina crucibles and then sintered in a nitrogen atmosphere to protect the Sn²⁺ from oxidation. The samples were heated at 900 °C for 10 h to give a series of samples ranging from bright yellow (SnNb₂O₆) to white (SnTa₂O₆).



3.2.3. X-ray Diffraction

Samples were analysed using X-ray diffraction on a Bruker D8 instrument, using monochromated copper K_{α1} radiation, in the range of 10-100° 2θ over a period of 12 hrs and a step size of 0.014°. Collected diffraction data were used for phase purity analysis and the initial characterisation of the unit cell size. Data were also studied by Rietveld structural refinement using the GSAS¹⁵ suite of refinement programs.

Diffraction data from the Sn₂Nb₂O₇ sample showed the presence of a small tin metal impurity alongside the primary phase (Figure 3.3). The impurity is thought to originate from the disproportionation of SnO to SnO₂ and Sn metal, which occurs at elevated temperatures.



The presence of the tin metal affects both the quality of the refinement and the final colouration of the potential pigment material. This impurity was easily removed after synthesis prior to further analysis by washing with warm concentrated HCl. The diffraction patterns from the SnNb_{2-x}Ta_xO₆ solid solutions showed no such impurity so acid treatment was not required.

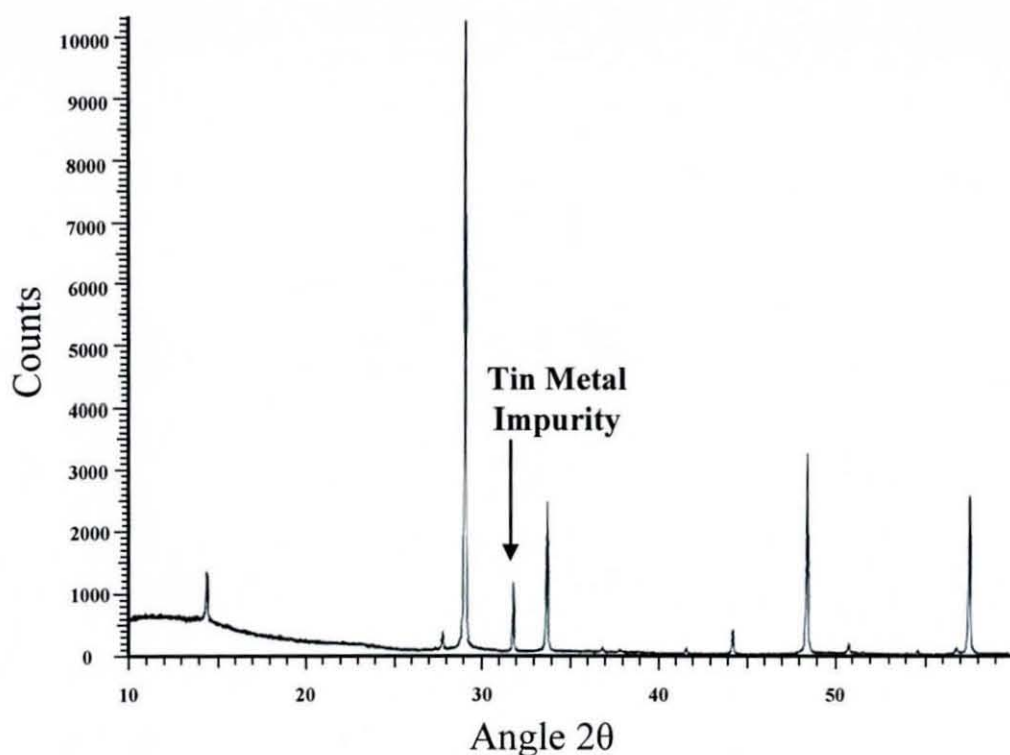


Figure 3.3: Diffraction pattern of $\text{Sn}_2\text{Nb}_2\text{O}_7$ showing tin metal impurity

3.2.4. Mössbauer Analysis

The local environment of the tin species within the sample was analysed using MASNMR and Mössbauer spectroscopy. ^{119}Sn Mössbauer spectra were collected at room temperature using a conventional spectrometer with a double ramp waveform to give a flat background.

3.2.5. Solid State NMR

^{119}Sn MASNMR was used to analyse the samples with a Varian 200 MHz spectrometer over a chemical shift range of 1000 to -2500 ppm.

3.2.6. UV/VIS Colour Measurements

The colour properties of each sample were assessed using UV/VIS spectrometry. Data were collected over the visible spectrum between 380 – 700 nm on a Perkin Elmer Lambda 30. The UV/VIS data were processed using the Perkin Elmer Colour Methods Software program with UV WinLab V3 to give quantifiable colour measurements.

Samples were ground in a pestle and mortar to form a fine powder, while taking care not to alter the colour properties of the material. The sample holders supplied with the UV/Vis spectrometer were found to be unsuitable for the prepared samples. Instead samples were mounted in plastic powder X-ray diffraction holders supplied with the Bruker D8 9-place sample holder, consisting of a squat cylinder with a small cylindrical hole on the top surface in order to receive material (Figure 3.4). Samples were compressed to give a flat reflectance surface and to give the required stability to allow for the powder to be mounted vertically in the reflectance device.

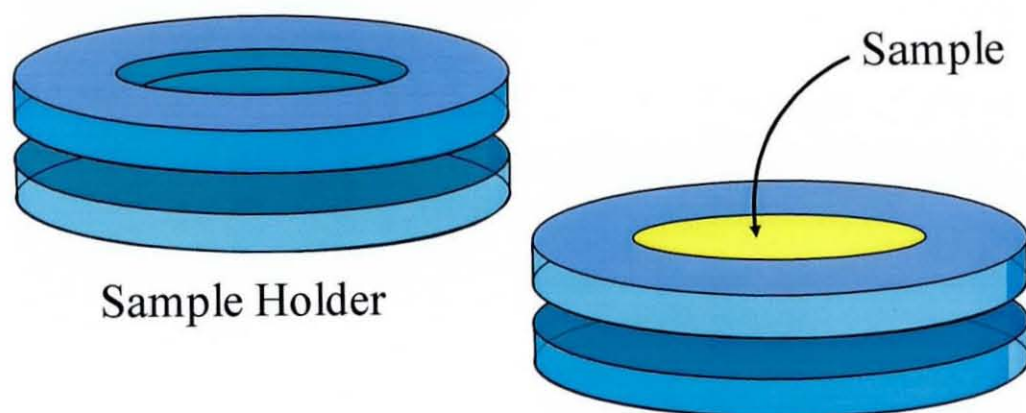


Figure 3.4: Diagram of the plastic sample holders use in the UV/Vis colour measurement experiments

Data were collected in the visible part of the light spectrum between 400 and 700 nm for colour analysis. A sample of barium carbonate (BaCO_3), supplied with apparatus, was used to give a 100% reflectance (brilliant white) reference value.

3.3. Results

3.3.1. Characterisation of $\text{Sn}_2\text{Nb}_2\text{O}_7$

3.3.1.1. X-ray Diffraction

X-ray diffraction analysis of the acid washed tin niobate sample, showed a single crystalline phase where all reflections could be indexed using a cubic pyrochlore structure (Fd-3m) with a cell parameter $a \sim 10.5 \text{ \AA}$. A least squares refinement

was carried out on the data using the GSAS suite of structural characterisation programs. The refinement was initiated using an ideal pyrochlore model ($\text{Sn}_2\text{Nb}_2\text{O}_6\text{O}'$) with Sn^{2+} on the $16c$ site $(0,0,0)$, Nb on the $16d$ site $(\frac{1}{2},\frac{1}{2},\frac{1}{2})$, and O and O' on the $48f(x,\frac{1}{8},\frac{1}{8})$ and $8a$ sites $(\frac{1}{8},\frac{1}{8},\frac{1}{8})$ respectively. As expected it quickly became apparent that the ideal pyrochlore was a poor approximation of the tin niobates structure giving high refinement results ($wRp = 25\%$, $Rp = 16\%$) as seen in Figure 3.5. In this case, it was hypothesised that there were two possible sources for the poor refinement results. The first was the very high temperature factor on the tin metal centre ($U_{\text{iso}} = 0.43252 \text{ \AA}^3$) and the second was the stoichiometry of the synthesised phase.

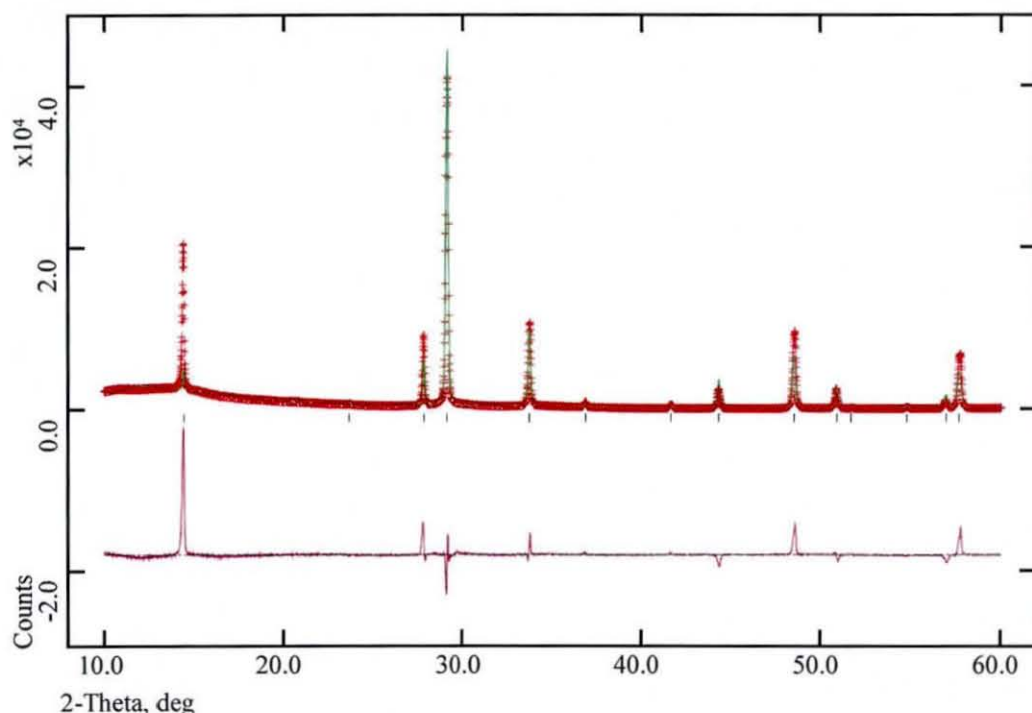


Figure 3.5: X-ray diffraction pattern showing the refinement results of the ideal pyrochlore starting model.

Previous studies by Birchall and Sleight and Cruz *et al.* had determined that these phases were exclusively non-stoichiometric and contained both Sn^{2+} and O' vacancies on their respective sites. Mössbauer studies have also detected a small quantity of Sn^{4+} within the primary phase which appears to reside on the same site as the niobium. The non-stoichiometry of these compounds, including the quantity of Sn^{4+} , appears to be variable and is dependent on the synthesis

conditions such as firing temperature and time. Previously there had been no reported evidence of a connection between the amount of Sn^{2+} and Sn^{4+} within the structure, and the composition had always thought to take the form $\text{Sn}^{2+}_{2-x}(\text{Nb}_{2-y}\text{Sn}^{4+}_y)\text{O}_{7-x-y/2}$. However, considering the fact that all of the Sn^{4+} content is derived from the disproportionation of the Sn^{2+} , and no other impurity has been found, it is a reasonable assumption that there is a connection.

Experiments into alternative synthesis routes have found that the tin niobates can also be formed from a mixture of tin metal and SnO_2 rather than SnO . This shows that the disproportionation can be reversible given the right conditions, allowing for an equilibrium between the amount of Sn^{2+} in the structure and the amount of Sn^{4+} and tin metal impurities. If this is the case then this would mean that the amount of Sn^{4+} would be equal to half of the vacancies on the Sn^{2+} site giving a composition of $\text{Sn}^{2+}_{2-x}(\text{Nb}_{2-x/2}\text{Sn}_{x/2})\text{O}_{7-5x/4}$. Studies have shown that the amount of Sn^{2+} in the structure ranges from 1.5-1.7 depending largely on the synthesis method employed. An average value of 1.6 was chosen as a starting model giving an initial formula of $\text{Sn}_{1.6}(\text{Nb}_{1.8}\text{Sn}_{0.2})\text{O}_{6.5}$.

Figure 3.6 shows an X-ray diffraction pattern of $\text{Sn}_2\text{Nb}_2\text{O}_7$ collected between 10° and $60^\circ 2\theta$. Close analysis of the data showed the presence of a 442 Bragg reflection in the diffraction pattern. This has been reported by previous authors and is known to be a "forbidden" reflection in case of pyrochlore compounds, and usually indicative of a distortion or deviation from the classic pyrochlore structure. Although the reflection is not strictly forbidden for the $Fd-3m$ space group, electron density from the a , c , d , and f sites of an ideal pyrochlore do not contribute to it. Its detection implies the existence of higher multiplicity sites such as the e , g and h sites, or the presences of highly isotropic thermal motion not usually seen in ionic cubic structures. Both of these scenarios are evidence of distortions caused by the existence of a stereoactive lone pair reported in previous studies.

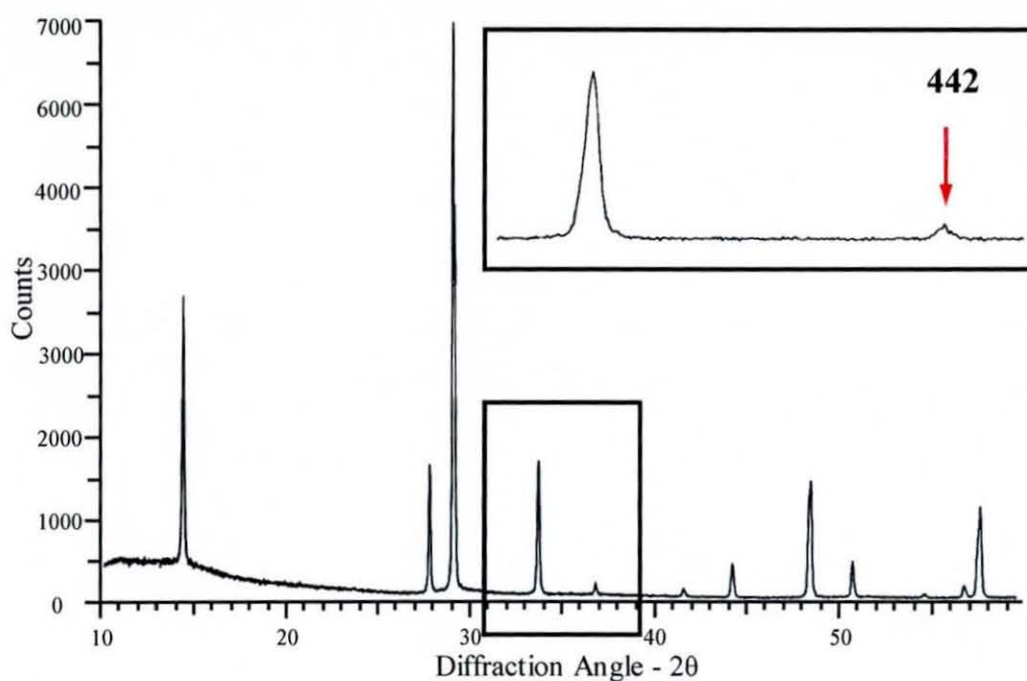


Figure 3.6: X-ray diffraction pattern of the $\text{Sn}_2\text{Nb}_2\text{O}_7$ pyrochlore with the “forbidden” 442 reflection indicated by the red arrow

The initial refinement model was altered to include the additions contained in the model put forward by Birchall and Sleight and later used by Cruz *et al.* The Nb^{5+} cation and oxide anions are kept on their ideal sites with the addition of a small Sn^{4+} content on the niobium site that was detected from Mössbauer data. The Sn^{2+} site was statically displaced onto a surrounding, lower symmetry 96h site in order to model the lone pair distortions. This site allows enough space for the insertion of the lone pair, and at the same time accounts for the appearance of the 442 reflection seen above. A second way of modelling this type of distortion is by placing very large anisotropic thermal parameters on the Sn^{2+} in order to artificially increase the size of the ideal *A* cation site. In this case however, the location of this special site was such that the size and shape of the allowed thermal ellipsoid was not sufficient to effectively model the distortions.

Refinement of this model produced results which, though superior to the ideal pyrochlore model, were still unacceptable, having both high R factors ($wR_p = 25\%$ and $R_p = 21\%$) and a χ^2 value of 23.83. These compounds are known to produce a high amount of diffuse scattering from the distorted Sn^{2+} environment,

which appeared as a broadening of the base of reflections across the whole spectrum. This affected the ability of the refinement program to model the peak profiles of the detected reflections and caused higher than expected thermal parameters.

3.3.1.2. ^{119}Sn MASNMR

Solid state NMR spectra were collected for the tin niobium oxide pyrochlores in order to probe the local environments of the cation centres. Previous studies of ^{91}Nb NMR¹² spectra had shown a single resonance indicative of a highly symmetrical environment as expected from the pyrochlores octahedral site. Analysis was therefore concentrated on the eight-fold Sn (II) site to further understand the effects of the lone pair disorder. ^{119}Sn NMR spectra recorded on the tin niobates by Cruz *et al.* reported the detection of a single resonance at around 600-700 ppm. This was at conflict with Mössbauer studies carried out previously which indicated that, not only were there two Sn^{2+} environments detected, but also that there was a small Sn^{4+} presence which should be detected as a second resonance. Several studies that utilised ^{119}Sn NMR indicated that there was a great deal of overlap in the locations of Sn^{2+} and Sn^{4+} environments in the NMR spectra. It was therefore hypothesised that both resonances could appear at the same frequency effectively appearing as one resonance.

The original NMR spectra from the Cruz *et al.* publication was extended between 1000 to -2500 ppm in order to detect any other resonances that may fall outside of the range originally studied. The resulting NMR spectrum is shown in Figure 3.7 and as expected displays the same resonance at -650ppm, which has been detected previously. There was however a second environment located at -1150 ppm, which has not been previously reported. The original resonance at -650 ppm displays a high degree of anisotropy in the peak shape while the new environment is relatively symmetrical. An anisotropic peak shape is usually caused by the presence of several overlapping resonances in the same location. This could be evidence supporting the theory put forward by Cruz *et al.* that both the Sn^{2+} and Sn^{4+} environments resonate at the same frequency. This theory, however, does not explain the detection of the second resonance at -1150 ppm

which, due to the relative symmetry of the peak, is unlikely to result from a distorted site such as that of Sn^{2+} in this structure.

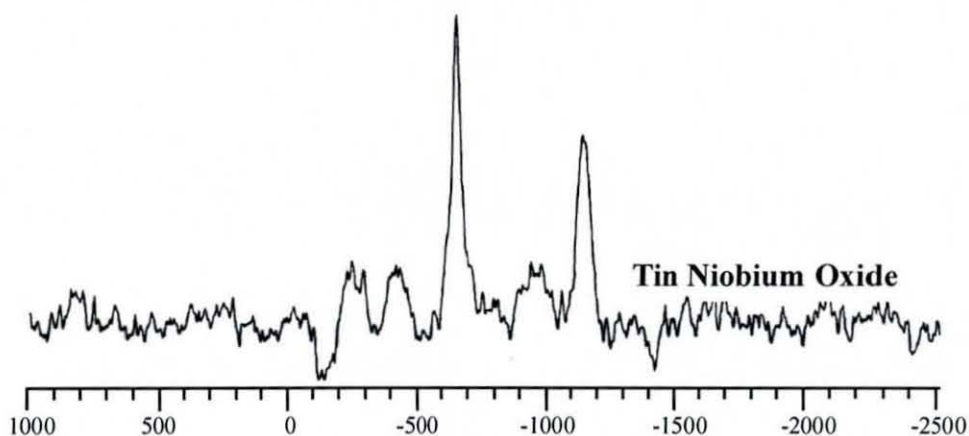


Figure 3.7: ^{119}Sn solid state NMR of tin niobate pyrochlore.

The second resonance at 1150 ppm has a relatively symmetrical shape which indicates a single environment of high symmetry; it has therefore been assigned to the octahedral Sn^{4+} environment. Apart from the two main resonances there appeared to be several small signals that create a wave-like background around the two main peaks. As this only appears in the tin active region, it is thought to be from trace amounts of amorphous tin silicate (SnSiO_3) caused by the reaction of SnO with the quartz sealed tubes.

3.3.1.3. ^{119}Sn Mössbauer Spectroscopy

The ^{119}Sn Mössbauer spectrum of the tin niobium oxide and samples, shown in Figure 3.8, consists of a series of three peaks. The peaks can be resolved in terms of three components being two doublets, forming the peaks at 2.1 and 4.1 mm s^{-1} , and a singlet which appears to have a similar chemical environment to the SnO_2 source material. The isomer shift values of the two doublets is characteristic of a Sn^{2+} species, and the singlet may be ascribed to the Sn^{4+} component detected by previous authors and in the NMR.

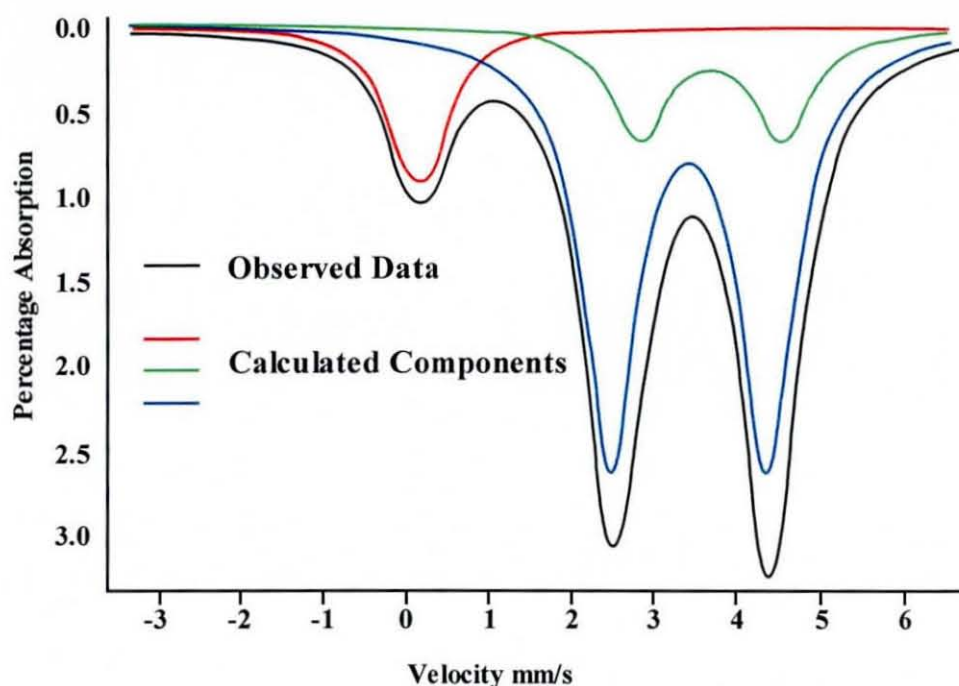


Figure 3.8: Mössbauer spectrum of tin niobate pyrochlore.

The observed quadrupole splitting contains information on the distribution of the $5p$ over both the bonds and the tin lone pair. The size of this splitting indicates a very low symmetry environment which is expected from an eight fold site with electron pair distortions. The fact that there appears to be two doublets in the observed signal indicates that the tin (II) has two distinct chemical environments of equally low symmetry. It has been concluded in the past that the local environment of the tin (II) site consists of $6+2$ surrounding anion sites producing an eight fold coordination. It was thus hypothesised that the non-stoichiometry of the pyrochlore in question would produce a proportion of sites with $6+2$ anions and a proportion with less oxygens in the local environment. Although the hypothesis may be valid in theory, no other examples can be found of this kind of behaviour in other non-stoichiometric pyrochlores.

The isomer shift value of the singlet has been found to be nearly identical to that of SnO_2 . This indicates a highly symmetric octahedral environment closely resembling the pyrochlores B cation site rather than the lower symmetry A cation site. This evidence coupled with that of the MASNMR and the size similarities between the Sn (IV) cation and Nb (V), all points towards the Sn (IV) being placed on the same site as the niobium.

3.3.1.4. Neutron Diffraction Analysis

The X-ray diffraction experiments seen previously were not as successful in refining the structure as required, producing relatively high R_p and wR_p and higher than expected temperature factors on some atoms. These problems indicated that the initial refinement model needed some adjustment to accurately describe the structure. Another concern was the diffuse scattering effects associated with the tin lone pair distortions, which had been originally reported by Cruz *et al.* These broadening effects at the base of every reflection proved difficult to model using GSAS's existing peak profile parameters for constant wavelength X-ray diffraction data.

In order to better understand the tin lone pair distortions and their effect on the surrounding anion framework, neutron diffraction data were collected for the tin niobium oxides. Neutron diffraction was chosen because of its high sensitivity to small atomic distortions, such as those that may arise from the presence of a tin lone pair. This is due to the fact that neutrons diffract from the atoms nucleus rather than its electrons, allowing the ability to study small atomic variations that may not affect the surrounding electron cloud. Neutron diffraction is also more suited to studying lighter anions especially when in the presence of heavier metal cations, such as tin and niobium, which may obscure scattering from the surrounding oxides.

The recorded neutron diffraction data were refined using the modified pyrochlore model used in the X-ray diffraction experiments seen previously. The Sn^{2+} was statically displaced from the ideal $16c$ (0,0,0) site to a surrounding $96h$ site (0.01,0.01,-0.02), and a small quantity of Sn^{4+} (5%) was placed on the $16d$ site with the niobium. Refinement results although relatively low ($wR_p = 2.67\%$, $R_p = 3.79\%$), the data was not fitted as well as expected which is evident in high χ^2 (67.2) and the difference between the observed and calculated profiles (Figure 3.9). The observed difference was most likely caused by large temperature factors detected on the $8a$, O' site implying that there was a problem with the location of the atom not detected by X-ray diffraction.

Table 3.1: Refined Atomic Parameters for $\text{Sn}_2\text{Nb}_2\text{O}_7$ using the modified pyrochlore model of Birchall and Sleight.

Atom	Site	x	y	z	Occu	U_{iso} (x100)
Sn^{2+}	96h	0.0168(3)	0.0168(3)	-0.0318(3)	0.148(2)	1.55(7)
Nb^{5+}	16d	$\frac{1}{2}$	$\frac{1}{2}$	$\frac{1}{2}$	0.908(1)	1.06(2)
Sn^{4+}	16d	$\frac{1}{2}$	$\frac{1}{2}$	$\frac{1}{2}$	0.092(1)	1.06(2)
O	48f	0.4359(1)	$\frac{1}{8}$	$\frac{1}{8}$	1.000	1.02(1)
O'	8a	$\frac{1}{8}$	$\frac{1}{8}$	$\frac{1}{8}$	0.749(2)	3.64(16)

Formula = $\text{Sn}_{1.77}(\text{Nb}_{1.89}\text{Sn}_{0.11})\text{O}_{6.84}$ $a = 10.57881(4)$ $wRp = 0.0325$, $Rp = 0.0398$

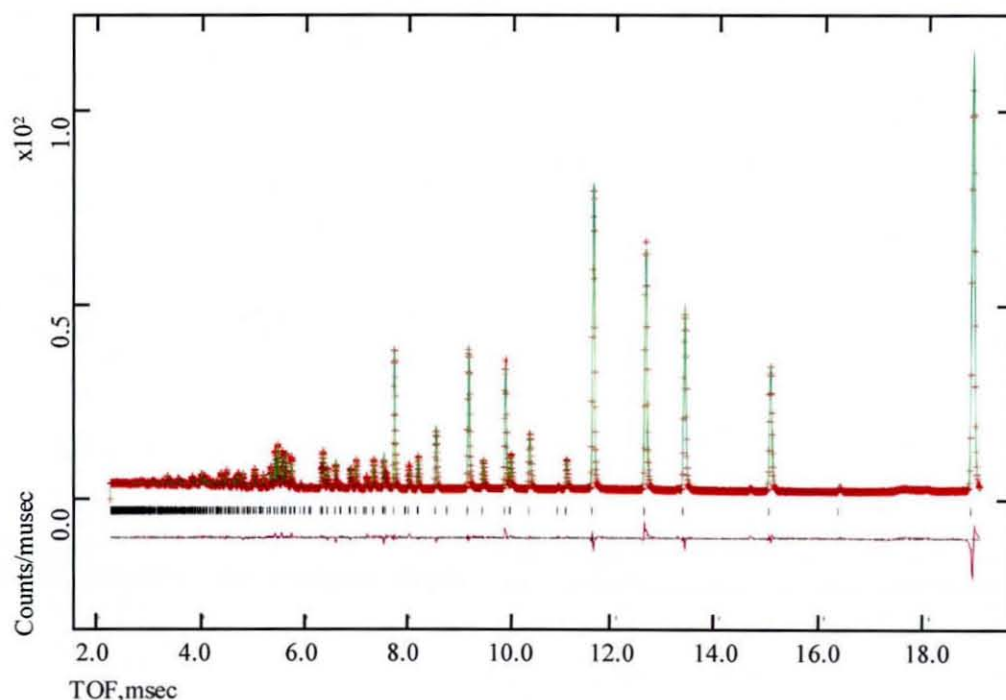


Figure 3.9: Neutron diffraction refinement results for $\text{Sn}_2\text{Nb}_2\text{O}_7$ using the modified pyrochlore model of Birchall and Sleight. (Red line = observed data; green line = calculated data; purple line = difference)

Since the discovery of the tin niobates there have been other reported examples of lone pair interactions in pyrochlore structures, most notably that of $\text{Bi}_2\text{Ti}_2\text{O}_7$.¹⁶

In this example the distortions caused by the bismuth lone pair caused a second set of distortions to occur in the O' frame work. This again was modelled by displacing the anion onto a surrounding site of lower symmetry as observed in the lone pair cation. This type of distortion has also been used in niobate pyrochlores, though the static displacements were caused by an atypical composition ($\text{ZnBiNb}_2\text{O}_7$)¹⁷ rather than lone pair influences. It seemed probable that a similar situation could be occurring in the tin niobates that would be undetectable by X-ray diffraction due to the high electron density from the adjacent tin cations. This would explain both the large χ^2 and high thermal parameters on the O' anion site seen in the refinement of the initial model.

The refinement model was altered to allow for the anion distortions thought to occur on the O' site by static displacement. The 8a site was moved from its ideal location (0.125, 0.125, 0.125) to a surrounding 32e (Table 3.2). As before the static displacement of the 8a site to the lower symmetry 32e site causes a decrease in the occupancy of the site. This follows the idea that the sites are an average representation and that only one of them will be occupied at any one time. In this case the occupancy is decreased to 1/4 of its original value as the same amount of atoms moves from 8 sites to 32 sites.

The non-stoichiometry of the Sn^{2+} and O' sites, and the Sn^{4+} content is modelled as seen before by assuming that all the Sn^{4+} content is from the disproportionation of Sn^{2+} . This results in the Sn^{2+} , Sn^{4+} and O' stoichiometries being constrained by the general formula $\text{Sn}^{2+}_{(2-x)}[\text{Nb}^{5+}_{(2-x/2)}\text{Sn}^{4+}_{x/2}]\text{O}_6\text{O}'_{1-x-x/4}$. With the addition of the detected anion distortions, the calculated R factors below 3% ($wRp = 0.168$, $Rp = 0.271$) and the temperature factors for the anion site dropped to within acceptable values ($B_{\text{iso}} = 1.24\text{\AA}^3$).

Table 3.2: Initial refinement input for the three models used in the characterisation of $\text{Sn}_2\text{Nb}_2\text{O}_7$

Ideal Pyrochlore Structure			
Atom	Site	Location	Occupancy
Sn^{2+}	16c	0,0,0	1.00
Nb^{5+}	16d	$\frac{1}{2}, \frac{1}{2}, \frac{1}{2}$	1.00
O^{-2}	48f	$0.4, \frac{1}{8}, \frac{1}{8}$	1.00
O^{-2}	8a	$\frac{1}{8}, \frac{1}{8}, \frac{1}{8}$	1.00
Birchall and Sleight Model ⁷			
Atom	Site	Location	Occupancy
Sn^{2+}	96h	0.01,0.01,-0.02	0.15
Nb^{5+}	16d	$\frac{1}{2}, \frac{1}{2}, \frac{1}{2}$	0.95
Sn^{4+}	16d	$\frac{1}{2}, \frac{1}{2}, \frac{1}{2}$	0.05
O^{-2}	48f	$0.4, \frac{1}{8}, \frac{1}{8}$	1.00
O^{-2}	8a	$\frac{1}{8}, \frac{1}{8}, \frac{1}{8}$	0.78
Final Refinement Model (based on $\text{Bi}_2\text{Ti}_2\text{O}_7$) ¹⁶			
Atom	Site	Location	Occupancy
Sn^{2+}	96h	0.01,0.01,-0.02	0.15
Nb^{5+}	16d	$\frac{1}{2}, \frac{1}{2}, \frac{1}{2}$	0.95
Sn^{4+}	16d	$\frac{1}{2}, \frac{1}{2}, \frac{1}{2}$	0.05
O^{-2}	48f	$0.4, \frac{1}{8}, \frac{1}{8}$	1.00
O^{-2}	32e	0.1,0.1,0.15	0.19

The refined atomic parameters and cell dimensions are shown in Table 3.2 along with the resulting R factors, cell parameter and calculated composition. The calculated amount of Sn^{2+} in the structure was calculated to be 1.54 formula units or a 77% occupation of the available sites. As discussed previously the loss of 0.46 formula units of Sn^{2+} through the disproportionation reaction produces 0.23 of Sn^{4+} that is substituted in for Nb^{5+} on the 16d site. The occupation of the O' site is calculated from the amount of Sn^{2+} and Sn^{4+} in the structure in order to charge balance the final composition. This results in just over half of the available anion sites being unoccupied, effectively making the majority of the Sn^{2+} sites 7-coordinate rather than the usual 8-coordinate.

Table 3.3: Refined atomic parameters for the distorted pyrochlore model.

Atom	Site	X	y	z	Occupancy	U_{iso} x100
Sn^{2+}	96h	0.0145(5)	0.0145(5)	-0.0292(5)	0.132(0)	2.33(9)
Nb^{5+}	16d	$\frac{1}{2}$	$\frac{1}{2}$	$\frac{1}{2}$	0.896(1)	1.12(2)
Sn^{4+}	16d	$\frac{1}{2}$	$\frac{1}{2}$	$\frac{1}{2}$	0.104(1)	1.12(2)
O	48f	0.4362(3)	$\frac{1}{8}$	$\frac{1}{8}$	1.000	1.08(5)
O'	32e	0.0876(2)	0.0876(2)	0.1624(2)	0.120(2)	1.24(3)

Formula = $\text{Sn}_{1.54}(\text{Nb}_{1.77}\text{Sn}_{0.23})\text{O}_{6.45}$ $a = 10.5355(2)$ $R_p = 0.0167$, $wR_p = 0.027$

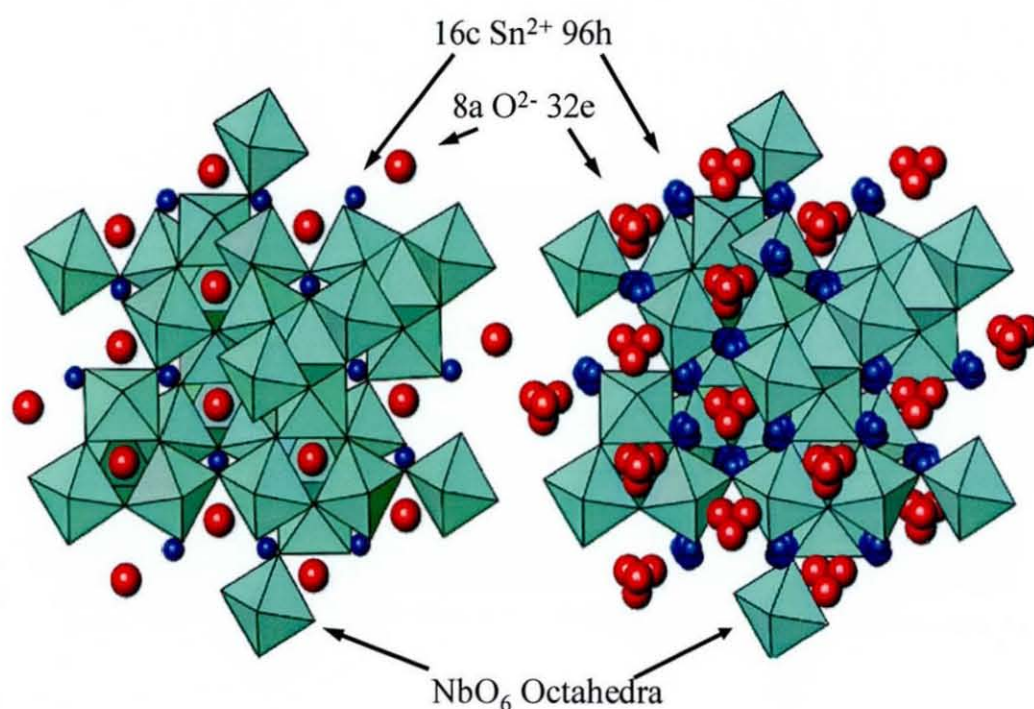


Figure 3.10: Pictorial representation of the ideal pyrochlore and modified structures (Red = Sn^{2+} , Blue = O^{2-} , Green = NbO_6 octahedra).

Figure 3.10 shows a comparison between the ideal pyrochlore structure and that of the modified lone pair model used in the refinement. In a cubic pyrochlore the niobium cations form an interconnecting framework of oxide octahedra which

form channels or tunnels through out the structure. In this case, the framework remains structurally unaltered, apart from the substitution of a proportion of the Nb^{5+} ions with Sn^{4+} , and is represented in the diagram by the green polyhedra. Normally the Sn^{2+} cations (blue spheres) are located in the centre of the niobium channels and are separated by the O' anions (red spheres). In the case of the modified model the cations are displaced from this ideal site towards the walls of the channels onto one of six surrounding sites, this forms a hexagonal arrangement of Sn^{2+} atoms as shown Figure 3.10. The displacement of the cation site results in the distortion of the neighbouring O' anions which again are statically displaced forming a tetrahedron of possible sites resulting in a four fold decrease in occupancy.

Tables 3.4 and 3.5 show the bond lengths and angles extracted from the refinement of the neutron diffraction data. The results for the $\text{Nb}^{5+}/\text{Sn}^{4+}$ show a fairly symmetrical octahedral environment, with bond angles approaching 90° and an equal centrosymmetric distance from the surrounding anions. This shows that the niobate framework is relatively unaffected by the tin lone pair distortions, and is much like that of an ideal pyrochlore. The substitution of the Sn^{4+} into the site is charged balance by removing anions from the O', which is only associated with the Sn^{2+} . This allows for all of the $\text{Nb}^{5+}/\text{Sn}^{4+}$ sites to retain a relatively octahedral geometry, which is in agreement with results from the tin NMR and Mossbauer.

The bond lengths and angles shown in Table 3.4 for the tin (II) cation show a range of values indicating the distorted nature of this site. In an ideal pyrochlore the *A* cation site, where the tin is located, has an eight coordinate geometry with six longer bonds and two short ones. The longer bonds are made up of six $48f$ oxide anions which make up the walls of the channels running throughout the structure. In an ideal case the *A* cation would take up a centrosymmetric position in the centre of the channel making all six bonds the same length. The two shorter bonds are to the remaining $8a$ anion site which links the *A* cations into a chain running throughout the structure. Again in an ideal case both of these bonds would be the same length and directly oppose each other, with a bond angle of 180° between them.

Table 3.4: Selected bond lengths for niobium and divalent tin centres.

Bond	Bond Length (Å)
Nb ⁵⁺ /Sn ⁴⁺ -O	1.98001(10)
Sn ²⁺ -O	2.343(4)
Sn ²⁺ -O	3.09(8)
Sn ²⁺ -O x 2	2.5497(25)
Sn ²⁺ -O x 2	2.922(4)
Sn ²⁺ -O' x 2	2.075(6)
Sn ²⁺ -O' x 2	2.142(6)
Sn ²⁺ -O'	2.307(5)
Sn ²⁺ -O'	2.244(7)
Sn ²⁺ -O'	2.996(7)
Sn ²⁺ -O'	3.005(6)

Table 3.5: Selected bond angles for niobium and divalent tin

Atoms	Angle (°)
O-Nb ⁵⁺ /Sn ⁴⁺ -O	90.522(10)
	89.478(10)
O-Sn ²⁺ -O	61.073(35), 69.63(16)
O'-Sn ²⁺ -O	106(32), 82.11(27), 92.23(22), 117.54(21)
O'-Sn ²⁺ -O'	161.1(4), 133.00(35), 163.73(16), 160.3(4), 144.18(22), 162.53 (19)

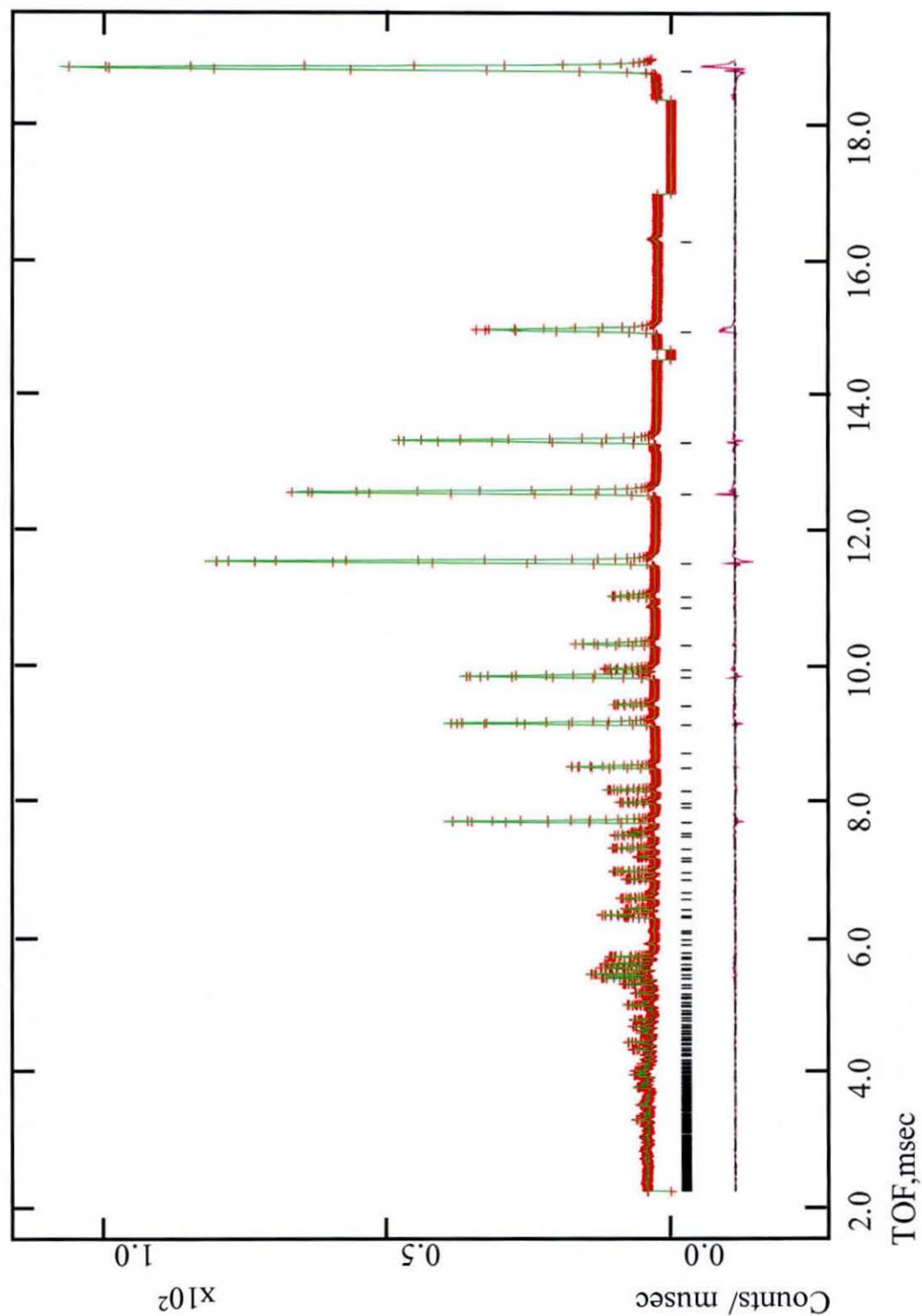


Figure 3.11: Refinement X-ray diffraction pattern for $\text{Sn}_2\text{Nb}_2\text{O}_7$; red crosses are the observed data, green line is the calculated profile and the purple line is the difference

The distorted Sn^{2+} environment, shown in Figure 3.12, has a much more complicated arrangement than that seen in a normal pyrochlore structure. The two $8a$ oxide sites have been replaced by $32e$ sites above and below the tin cation, which consists of a tetrahedron of possible anion locations with the ideal site in the centre. As shown previously only one of these sites is occupied at any given time so the overall geometry of the tin site does not change. The six $48f$ anion sites have not changed from the original model; however the inclusion of the lone pair forces the tin cation from its centralised position toward the walls of the niobate channels. This causes a lengthening of the bonds on one side and a shortening of the opposite side as the tin moves away from one wall and towards another.

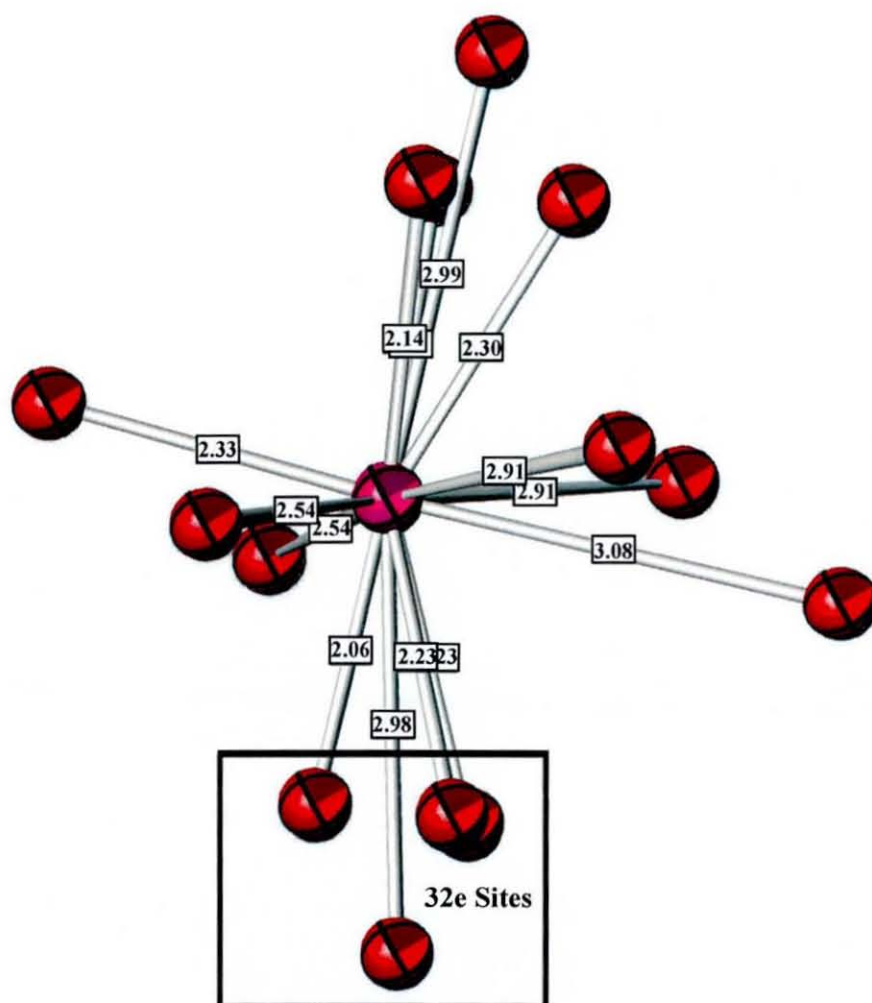


Figure 3.12: The distorted Sn^{2+} environment with the metal cation in the centre (purple) and surrounding oxide anions (red)

If a cross section is taken of one of the niobate channels it can be seen that they are hexagonal with one of the 48f oxide sites on each vertex as seen in Figure 3.13. In an ideal pyrochlore the cation will be centralized in the channel with equal distance between each vertex as shown on the left hand side of this figure. In the lone pair model the cation is moved closer to one of the atoms, forming the short 2.33 Å bond, and away from the opposite wall forming the long 3.08 Å. The other four bonds then change in length to form two bonds of 2.54 Å and two bonds of 2.91 Å depending on whether they are situated adjacent to the short or the longer of the two bonds.

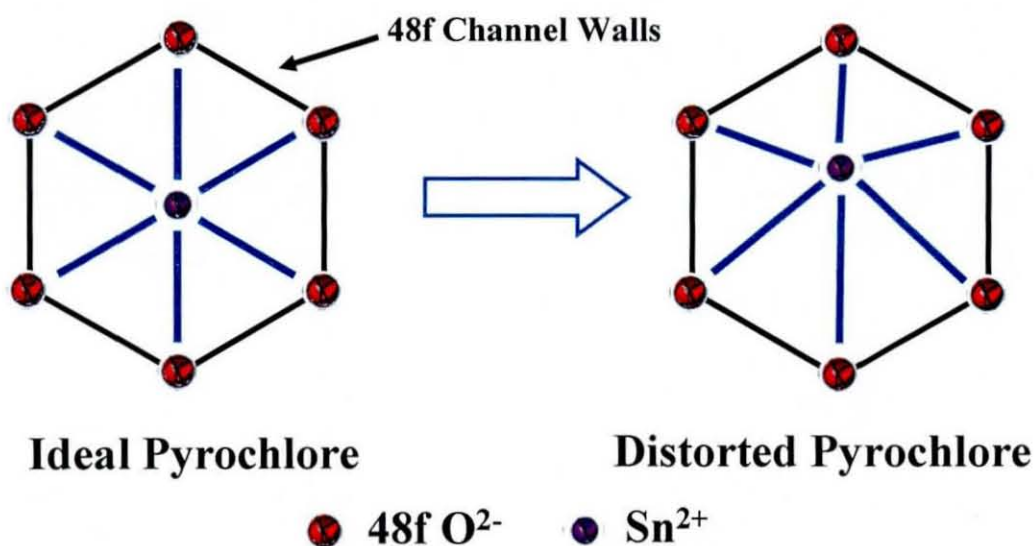


Figure 3.13: Cross Section of Pyrochlore Niobate Channels.

As previously mentioned the O' anion site is also distorted by the lone pair of the adjacent tin cation. This results in a static displacement of the oxide onto one of four 32e sites that form a tetrahedron around the ideal site in the centre. In an ideal 8a site the central anion is surrounded by four cation sites, which form a larger tetrahedron around the oxide site. In the distorted model these cation sites are located at the faces of the 32e tetrahedron, as seen in Figure 3.14, with three sites a very short distance away (2.06-2.30 Å) and one at the opposite vertex of a very long bond length (2.99 Å). Conversely this means that whichever of the four 32e sites is occupied will have three short Sn-O bond lengths and one long bond

length. This means that a large number of the tin sites must also contain one of the longer of these bonds. This has implications towards the stability of the Sn^{2+} as this longer bond length would be effectively non-bonding and would not contribute to the valence of the site. Since at least half of the O' oxides are also vacant due to the non-stoichiometry of these compounds the theoretical valence is further reduced.

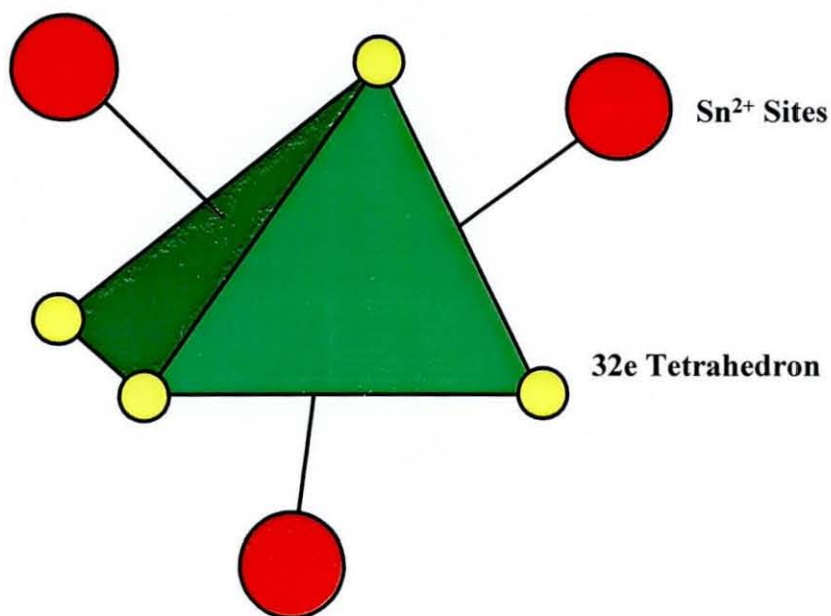


Figure 3.14: 32e Tetrahedron.

3.3.1.5. Bond Valence Calculations

The descriptions of the three main sites above are based on the assumption that the structure is fully stoichiometric where all possible sites are fully occupied. Another major factor in the structure of these compounds is the cation vacancies on the Sn^{2+} site and anion vacancies on the O' site. The Sn^{2+} has been previously described as an 8 coordinate site, however the refined composition ($\text{Sn}_{1.54}(\text{Nb}_{1.77}\text{Sn}_{0.23})\text{O}_{6.45}$) shows that less than half of the O' sites are in fact occupied. This would mean that the vast majority if not all of the sites would be seven coordinate or six coordinate sites rather than eight coordinate. The conclusion that the Sn^{2+} site in these compounds could be seven coordinate has been hypothesised previously in a study of tin lead niobate pyrochlores by Cruz *et al.* The idea was put forward that all of the tin sites had to be 7-coordinate to

allow the inclusion of the tin lone pair on the vacated $8a$ site. Bond valence calculations carried out on this site showed it to have a value of 1.62, which is much too low when compared to the ideal value of 2.00. In this case however the high valence of the lead site balanced the low valence of the tin site out. In a pure tin compound however this is not the case and the low valence cannot be negated in this way. It is also likely that the formation of an entirely 7-coordinate tin structure would cause the formation of ordered vacancies and a change in the symmetry of the cell. This kind of behaviour would be indicated by the presence of supercell reflections caused by these added symmetry elements that the ordered anion holes would create. Close analysis of the longer wavelength reflection showed no evidence of such supercell reflections indicating that the anion vacancies were random and averaged over the entire structure.

The addition of the $32e$ site in place of the ideal $8a$ site used in the model Cruz *et al* allowed for an increase in the valence of the tin site. The static displacement of this site produced a range of valence values depending on which of the four available sites is occupied. As seen in Figure 3.14 the $32e$ tetrahedron produces a range of bond lengths forming three shorter and one longer bond, which produced a site valence of 1.76 - 1.69 for the short bonds and 1.58 for the longer bond. It could be hypothesised that a complementary bonding arrangement is reached whereby the sites that are occupied only show the shorter bond lengths and not the longer one. Any place where a longer bond is mandated by the surrounding arrangement a vacancy is inserted (see Figure 3.15) in order to raise the valence of the occupied sites. The removal of the long bond between the Sn^{2+} and the $32e$ oxides is paramount to gaining the correct bond valence. Even in an eight coordinate geometry the use of one of these bonds would cause the valence to drop to 1.219, too low for a stable site. It can be calculated that in order for the above bonding arrangement to occur that $\frac{1}{4}$ of all Sn^{2+} sites must be unoccupied to allow for the number of vacancies required. This ties very well with the composition and implies that the non-stoichiometry of these compounds is caused by the above bonding arrangement in order to raise the low Sn^{2+} bond valence caused by the lone pair distortions.

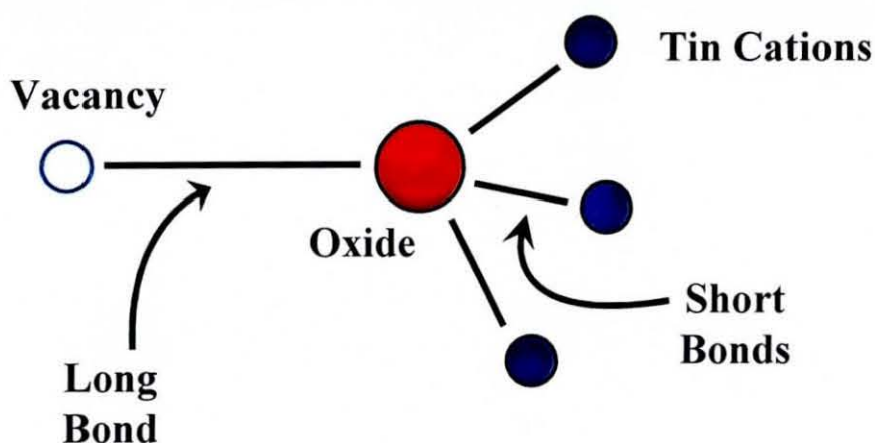


Figure 3.15: Oxide Site

The possible Sn^{2+} site valence can be enhanced further by looking closely at the relationship between the tin sites and the $32e$ O' sites. Figure 3.15 shows a representation of the six $96h$ sites (yellow) surrounding an ideal $16c$ site in the centre. Above them is the base of the $32e$ tetrahedral (red) showing three of the four sites that give the shorter bond lengths to the tin sites. It can be seen that each oxide anion site is closely related to two tin sites in the layer below, this allows for the shortest possible bond length to be selected preferably in each case leading to a much higher site valence. Theoretically this effect could be the route cause of the O' site distortions seen both here and in other lone pair pyrochlores. The lone pair would force the cation onto one of these six surrounding sites and then the oxide must also become distorted in order to retain the shortest bond length possible.

Although the above bonding arrangements go a long way to explaining the non-stoichiometry and the distortions in these compounds, they are still insufficient in the creation of a stable tin environment. The non-stoichiometry of the O' site forces the existence of 7-coordinate Sn^{2+} and even with the above restrictions a valence for this kind of site of 1.707 is still very low. This means that the structure cannot contain entirely 7-coordinate tin sites as it needs the 8-coordinate sites to bring the site valence up to an acceptable figure. This also means that the Cruz *et al.* conclusion that the tin lone pair is located on one of the vacated O' sites cannot be correct for pure tin niobates as these sites will not always be vacant.

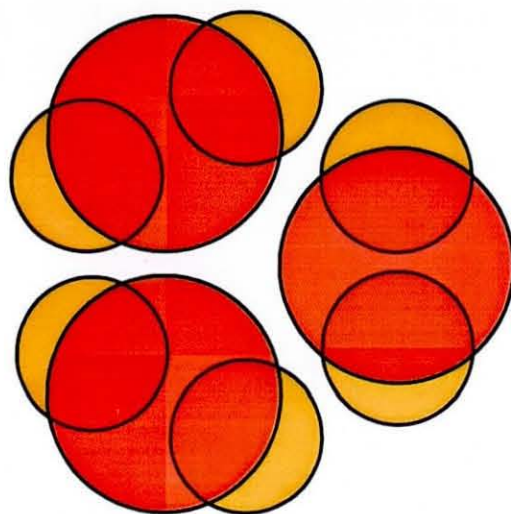


Figure 3.16: Relationship between 96h Sn^{2+} sites (yellow) and 32e O' oxygen sites (red)

Although the enhanced bonding arrangements only brings the valence of the 7-coordinate tin site up to 1.707 it has the effect of increasing the 8-fold site valence up to 2.435. It can be calculated that for the valence of the Sn^{2+} to be within acceptable boundaries of 2.0 ± 0.1 , the proportion of 8-fold sites needs to be around 30-50% of the total. In order for this to occur the vacancies within the structure need to cluster together so that if an Sn^{2+} site is 7- or 6-coordinate then it will tend to be vacant. By studying the pyrochlore structure in detail this can be shown to be feasible for a single cell, and therefore feasible across the entire structure.

Figure 3.17 shows an extended pyrochlore unit cell with the cation layers separated so that the interplane O' site can be visualised. In this example the 48f oxides anions have been removed, as they play no role in the non-stoichiometry of the phase. The cation layers consist of 6-coordinate niobium (yellow) and 8-coordinate tin (blue) with the O' oxides in between (red). The pyrochlore unit cell consists of five cation layers with four lattice points for each cation in each of the middle three layers and two in each of the top and bottom layers. This equates to 16 lattice points for the niobium (16d) and 16 for the tin (96h with 1/6 occupancy) in the total unit cell.

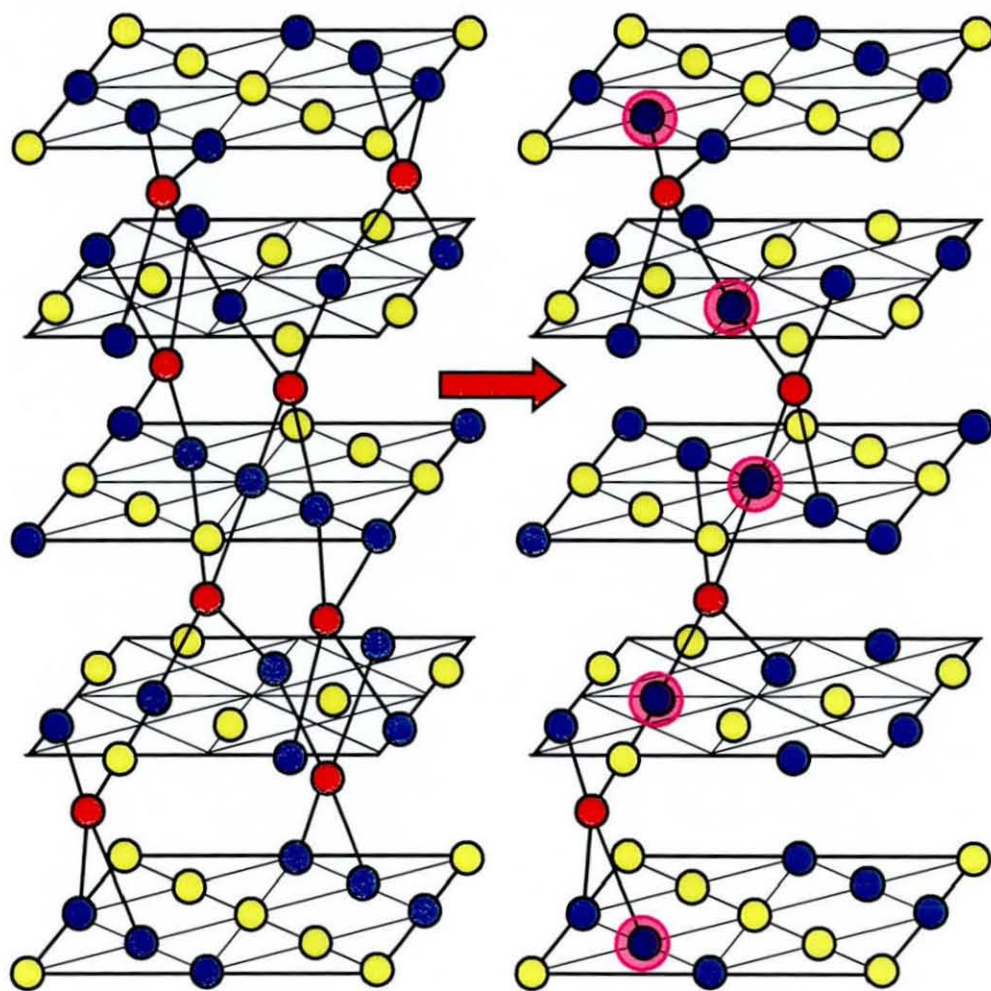


Figure 3.17: Extended Pyrochlore Unit Cell; Yellow atoms = Nb^{5+} ; Blue atoms = Sn^{2+} ; Red atoms = O^{2-} . Purple circle = 8-coordinate tin site.

The left hand example shows a fully stoichiometric unit cell which has two O' oxide anions between each cation layer which are linked through the tin centres. Each tin is bonded to two of these anions giving them an eight coordinate geometry. The right hand example shows the non-stoichiometric model with the anion vacancies inserted by removing oxides from between the layers. The refine composition shows that just over half of the O' sites are left vacant, this equates to the loss of approximately one O' anion from each interlayer space. As expected the removal of anions in this way makes the majority of Sn^{2+} either 6-

or 7-coordinate, however at least one atom per layer is left 8-coordinate (purple circle).

Close examination of the middle three layers show that one lattice point out of four is left 8-coordinate which means that $\frac{1}{4}$ of the cations in the structure will be 8-coordinate and $\frac{3}{4}$ will be either 6 or 7 coordinate. This is not enough to ensure a stable site as it has been previously calculated that 30-50% need to be 8-coordinate to bring the valence up to near 2.0. However the calculated composition shows that almost $\frac{1}{4}$ of the Sn^{2+} sites are also left vacant. If we assume that Sn^{2+} vacancies are only inserted in areas of lower valence (6- and 7-coordinate sites) as seen in Figure 3.17, then the 8-coordinate sites will still remain within the structure.

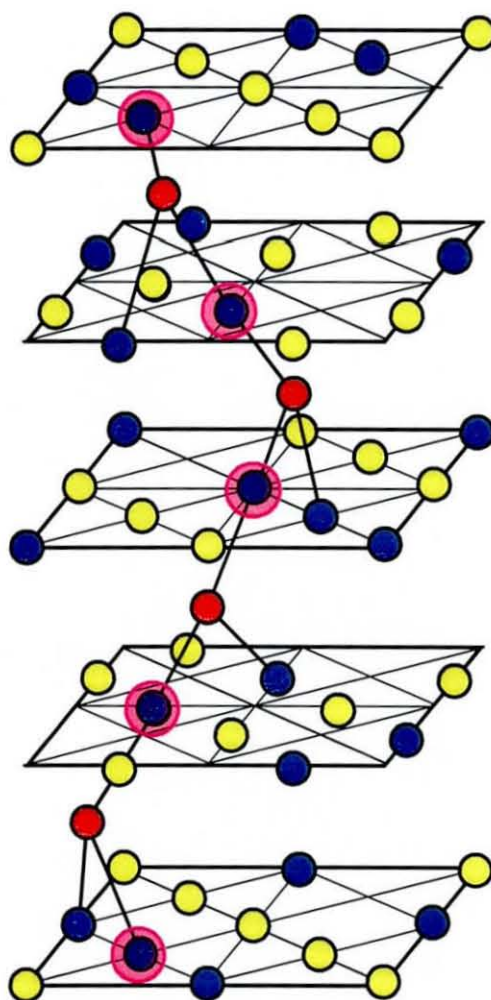


Figure 3.18: Final extended structure Yellow atoms = Nb^{5+} ; Blue atoms = Sn^{2+} ;
Red atoms = O^{2-} . Purple circle = 8-coordinate tin site.

The insertion of the cation vacancies would leave 1/3 of the sites as eight coordinate and the remaining sites seven coordinate, which is within the calculated region of stability. Figure 3.18 shows the final extended structure with the Sn^{2+} vacancies inserted into the structure. These vacancies are inserted are thought to appear in such a way that the O' ions become 3 coordinate to remove the fourth longer bond as seen before. The site valence for Sn^{2+} in such a model is calculated as 1.92 within the acceptable boundaries for the bond valence parameters.

The conclusion that the pure tin niobate structure can only be stable when there are both 7 and 8-coordinate sites in the unit cell negates the theory that the tin lone pair can be located on one of the vacated O' sites. The most likely place for the lone pair to be placed is on the now vacated 16c site located in the centre of the 96h ring (Figure 3.19). Not only is this site vacant across the structure, regardless of geometry, it is also located in closer proximity to the Sn^{2+} centre.

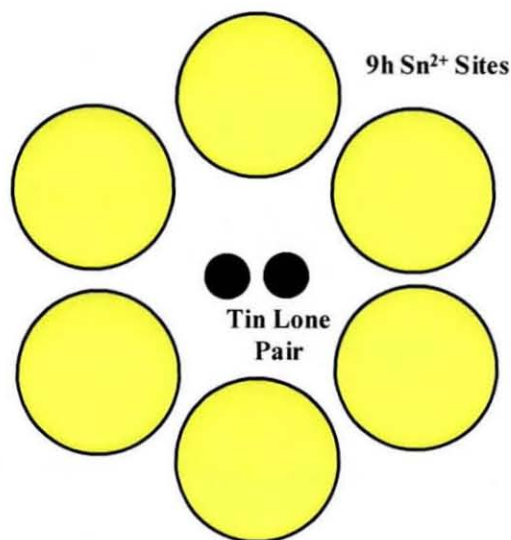


Figure 3.19: Tin lone pair

3.3.2. Characterisation of SnNb_2O_6 – SnTa_2O_6 Solid Solution

The research carried out on the tin niobates has been focused on their structural irregularities rather than chemical and physical properties. This has led to very little existing information regarding the most apparent characteristic of these compounds, their bright yellow colour. As niobium (V) has no remaining

d-electrons, which are most often associated with colouration in inorganic compounds, the only explanation is an alternative mechanism, such as charge transfer, is occurring. Previous authors have also used this same hypothesis by arguing that electrons transferred from the oxide anions may cause the niobium to be reduced from Nb^{5+} to Nb^{4+} . This idea is backed up by the existence of several Nb^{4+} compounds with a bright yellow colouration. Certainly the mechanism by which any transfer occurs appears to be independent of the structure, as it occurs in both the pyrochlore based tin niobates and the monoclinic foordite compounds. Also of particular interest is explaining why this phenomenon only occurs in the tin niobates and not in other niobate compounds.

A study has been carried out to discover the effects gradually substituting the niobium cation with the tantalum ion, which is very similar in both size and chemical behaviour, to the colour properties of the resulting compounds. For the subject of this study solid solutions of the foordite structure were chosen rather than the pyrochlore structure seen before. This was to ensure that the exact composition would be known and that the colour properties would not be affected by the non-stoichiometry of the synthesised phases. Solid solutions of the foordite structure and the tantalum analogue have the general formula $\text{SnNb}_{2-x}\text{Ta}_x\text{O}_6$ and display a very different structure to what is seen in the pyrochlore compounds discussed above. These compounds crystallise in a monoclinic space group *C2/c* rather than the cubic *Fd-3m* and have a much more stable Sn^{2+} environment resulting in a completely stoichiometric composition. Both the foordite based tin niobates and the pyrochlore compounds seen previously have a bright yellow colouration, which appears to be influenced by the composition rather than in the structure. Studying the loss of colour across the tin niobium/tantalum solid solutions were carried out using solid state UV/Vis. Rietveld refinement was carried out on the X-ray diffraction data of each compound to detect any structural changes that may have an effect.

3.3.2.1. X-ray Diffraction

X-ray diffraction analysis of the tin niobium/tantalum solid solutions showed that there is very little difference across the whole range of the series. All the

compounds analysed gave virtually identical diffraction patterns with only very little difference between the peak positions or phase composition. Looking at the crystal radii of Ta^{5+} and Nb^{5+} it can be seen that in a six coordinate environment both ions have a radii of 0.78, which would account for the lack of variation in the reflection locations. Unlike the pyrochlore based materials no other tin impurities were detected in the diffraction patterns confirming that disproportionation was either not occurring or was fully reversed in the formation of the primary phase. All of the patterns could be indexed in the monoclinic space group C2/c with $a \sim 17$, $b \sim 5$, $c \sim 5.5$ and $\beta = 90.5$.

Table 3.6: Initial atomic parameters for the refinement of $SnNb_{1-x}Ta_xO_6$

Atom	Site	x	y	z	Occupancy
Sn^{2+}	4a	0.00	0.272	$\frac{1}{4}$	1.000
Nb^{5+}	8b	0.330	0.247	0.325	1.000
O3	8b	0.431	0.404	0.398	1.000
O4	8	0.362	0.039	0.361	1.000
O5	8	0.223	0.432	0.348	1.000

The X-ray diffraction data for each of the compositions was structurally refined using the mineral foordite ($SnNb_2O_6$) as the starting model shown in Table 3.6. With the addition of tantalum to the compounds it was assumed that there was a direct substitution between the niobium and the tantalum. As no other niobium or tantalum were detected in the X-ray diffraction patterns it was also assumed that the proportion of tantalum oxide added was equal to the amount of tantalum in the final composition, giving a general formula of $SnNb_{2-x}Ta_xO_6$. Initial refinement results showed that although niobium and tantalum are very similar in size there was still a marked effect on the calculated cell parameters.

Table 3.7: Cell parameters for the $\text{Sn}_{1-x}\text{Ta}_x\text{Nb}_2\text{O}_6$ solid solutions

	a (Å)	b (Å)	c (Å)	β (°)
SnNb_2O_6	17.0432(3)	4.8722(1)	5.5652(1)	90.902(1)
$\text{SnNb}_{1.8}\text{Ta}_{0.2}\text{O}_6$	17.0561(4)	4.8713(1)	5.5651(1)	90.901(2)
$\text{SnNb}_{1.6}\text{Ta}_{0.4}\text{O}_6$	17.0725(5)	4.8716(1)	5.5643(2)	90.890(2)
$\text{SnNb}_{1.4}\text{Ta}_{0.6}\text{O}_6$	17.0745(5)	4.8667(2)	5.5585(2)	90.896(2)
$\text{SnNb}_{1.2}\text{Ta}_{0.8}\text{O}_6$	17.0834(5)	4.8643(2)	5.5555(2)	90.890(2)
$\text{SnNb}_{1.0}\text{Ta}_{1.0}\text{O}_6$	17.0913(5)	4.8639(2)	5.5549(2)	90.899(2)
$\text{SnNb}_{0.8}\text{Ta}_{1.2}\text{O}_6$	17.1126(4)	4.8619(1)	5.5515(1)	90.912(2)
$\text{SnNb}_{0.6}\text{Ta}_{1.4}\text{O}_6$	17.1203(5)	4.8598(2)	5.5492(2)	90.915(2)

Table 3.7 shows the cell parameters resulting from the refinement of the $\text{SnNb}_{2-x}\text{Ta}_x\text{O}_6$ solid solutions. The refinements were only completed up to a tantalum content of 1.4 due to the very poor refinement factors resulting from the remaining compositions. The synthesis method used whereby all of the materials were formed together caused the tantalum rich materials to have very poor crystallinity indicating that they may require much higher calcinations temperatures. The structural patterns emerging from the refined compositions were clear enough so that the results could be extrapolated to include the uncharacterised materials.

Table 3.7 shows the refined cell parameters for the whole series for comparison. The change in cell lengths and angles is only slight, as the ionic radii of niobium and tantalum are very similar, however there is a definite pattern seen as more tantalum is added. Fig 3.21 and 3.22 below shows the change in cell parameter versus the dopant level of the tin niobates. Although the two cations are almost identical there is a slight size increase on the move down the group from niobium to tantalum, which should translate as a small increase in the overall cell size. There is an increase in the a cell parameter however there is also a subsequent decrease in both the b and c parameters.

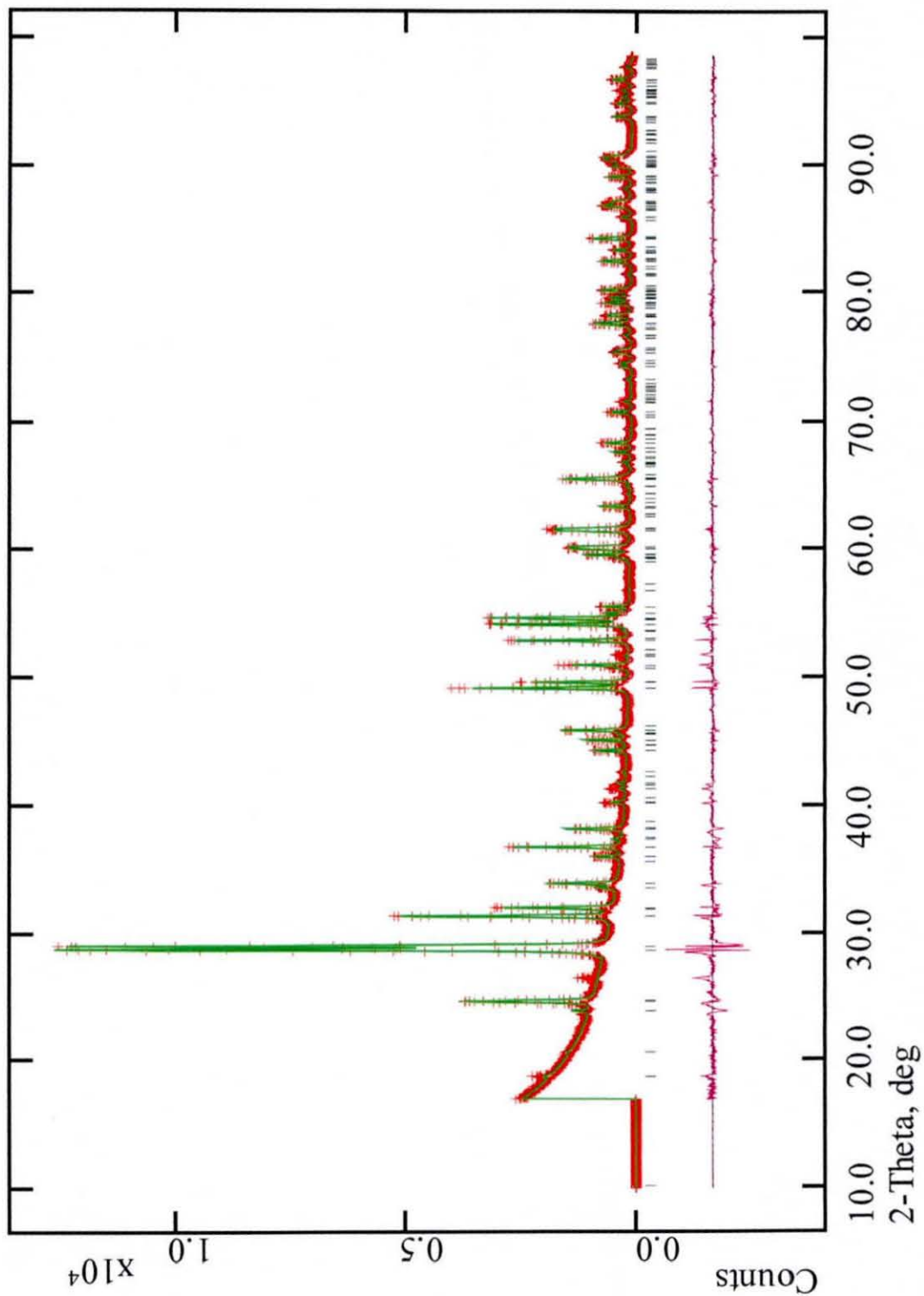


Figure 3.20: Refinement X-ray diffraction pattern for SnNb_2O_6 ; red crosses are the observed data, green line is the calculated profile and the purple line is the difference

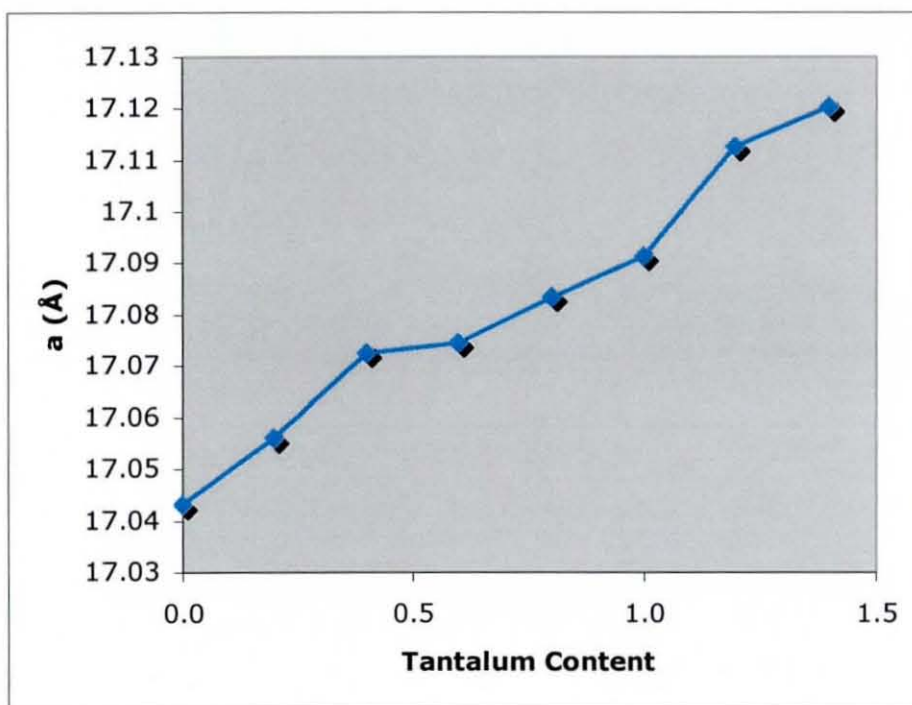


Figure 3.21: Chart of cell parameter a versus tantalum dopant level

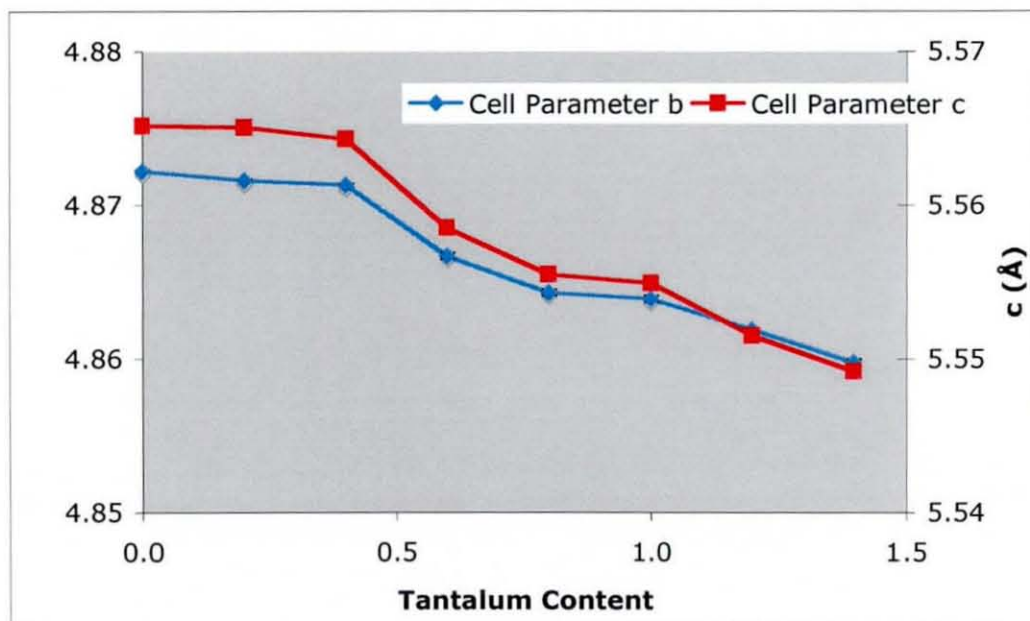


Figure 3.22: Cell Parameters b and c versus tantalum dopant level

In the case of the direct substitution of one metal cation for another any change in cell parameters can usually be entirely attributed to the ionic radii and the electronic behaviour of the two ions. In the case of niobium and tantalum the ionic radii of the two cations are almost identical, which would normally lead to

only very small changes in the cell parameters. Looking at the refinement results shows that in fact there is a significant difference between all of the cell parameters, with the largest change being in the a parameter. Figure 3.21 is a graph showing the change in cell parameter a with increasing tantalum content, while Figure 3.22 shows the same but for the b and c parameters. There is an obvious pattern in the three cell parameters as the a parameter increases with the amount of tantalum, while the b and c parameters both decrease. The close correlation between the change in cell parameters b and c and cell parameter a indicates that there is a relationship between the increase and decrease of these unit cell lengths.

Table 3.8: Selected bond lengths and angles for SnNb_2O_6

	Sn-O3 (Å)	Sn-O4 (Å)	O4-Sn-O(°)	O4-Sn-O3 (°)
SnNb_2O_6	2.124(13)	2.794(17)	137.3(6)	58.9(5)
	2.467(14)	3.048(16)	56.71(29)	91.6(5)
$\text{SnNb}_{1.8}\text{Ta}_{0.2}\text{O}_6$	2.365(14)	2.953(16)	144.6(6)	55.6(5)
	2.325(15)	2.985(16)	56.56(29)	97.1(5)
$\text{SnNb}_{1.6}\text{Ta}_{0.4}\text{O}_6$	2.362(16)	2.966(17)	145.1(6)	54.53(5)
	2.386(17)	3.004(17)	56.27(31)	98.2(5)
$\text{SnNb}_{1.4}\text{Ta}_{0.6}\text{O}_6$	2.352(19)	2.995(20)	145.8(7)	54.4(5)
	2.383(18)	3.003(20)	56.1(4)	96.6(6)
$\text{SnNb}_{1.2}\text{Ta}_{0.8}\text{O}_6$	2.297(17)	2.976(21)	146.2(8)	53.3(5)
	2.413(19)	3.013(21)	57.0(4)	99.1(5)
$\text{SnNb}_{1.0}\text{Ta}_{1.0}\text{O}_6$	2.308(17)	2.982(20)	145.8(8)	56.7(5)
	2.421(19)	2.982(20)	56.6(4)	97.7(5)
$\text{SnNb}_{0.8}\text{Ta}_{1.2}\text{O}_6$	2.261(17)	2.989(20)	146.9(7)	52.9(5)
	2.428(19)	3.000(21)	56.4(4)	98.7(5)
$\text{SnNb}_{0.6}\text{Ta}_{1.4}\text{O}_6$	2.242(17)	2.986(20)	147.1(7)	59.5(5)
	2.405(20)	3.009(20)	56.5(4)	98.3(6)

Table 3.8 above shows selected bond lengths and angles for the tin centre of the foordite structure. Like the pyrochlore seen previously the tin atom has a stereoactive lone pair, however in the case of this structure the site used has the

room for both the ion and the lone pair. The location of the lone pair electrons can be seen in the diagram in Figure 3.23 below as is identified by its influence on the surrounding bonds. The lone pair causes a lengthening of bonds on one side of the tin environment with a shortening on the opposite side (2.915 Å and 2.989 Å for the long bonds and 2.293 Å and 2.433 Å for the shorter bonds). The presence of the lone pair in between the four longer bonds also causes the bonds on that side to splay out as far away from the electrons as possible.

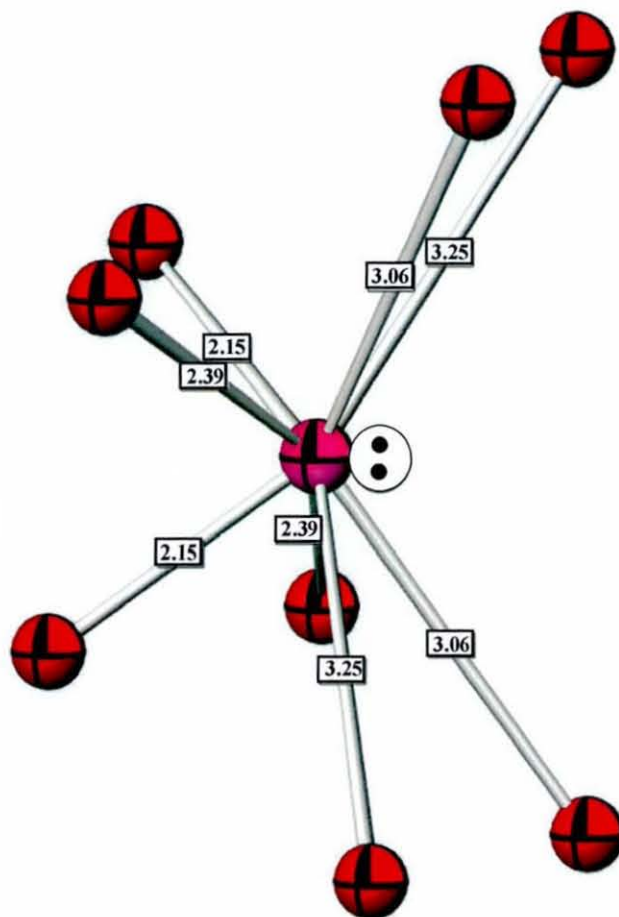


Figure 3.23: Tin local environment in SnNb_2O_6

As the amount of tantalum is increased not only does the cell parameters change but the geometry of the Sn^{2+} environment alters significantly. The addition of Ta^{5+} is accompanied by a lengthening of the bonds around the lone pair and an increase in the angles between them. This could indicate that the s -electrons of the Sn^{2+} are becoming increasingly lone pair active, which then has a greater effect on the structure. The change in the geometry of the Sn^{2+} centre also has a

wider influence on the unit cell structure. As the bonds around the lone pair increase in length and move away from each other this has the effect of increasing the distance between the niobate layers resulting in a larger a parameter. Conversely the increase in the bond angles also decreases the distance between the tin centres within each layer. This has the effect of decreasing the cell lengths parallel to the tin layers namely the b and c parameters. The change in the structure of the cell can therefore be attributed solely to the electronic effects between the tin and niobium and not to a change in ionic radius.

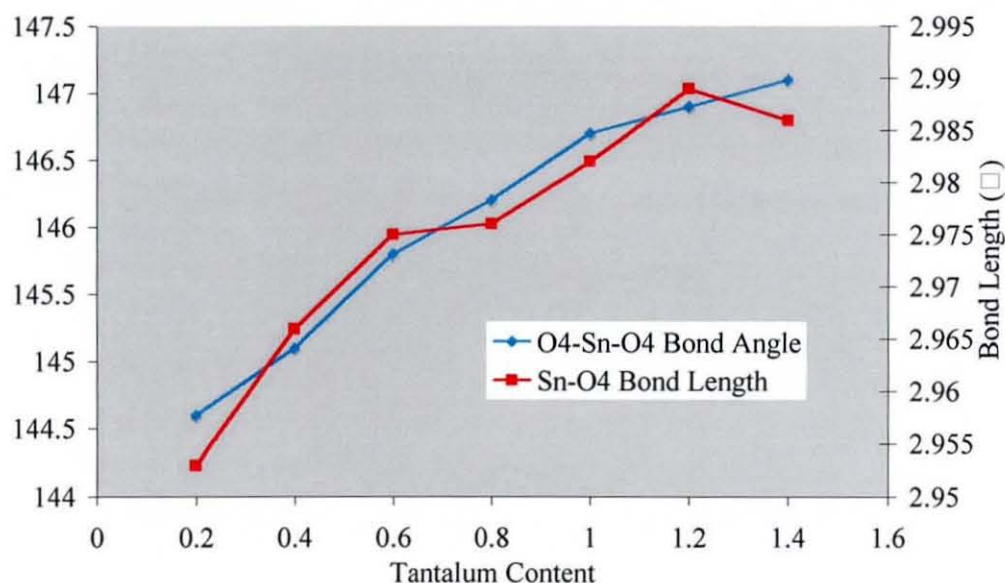


Figure 3.24: Sn²⁺-O4 bond length and angle versus tantalum content

The increasing length of the bond and the widening of the angle between them could be attributed to the stereochemistry of the tin lone pair. As the amount of tantalum is increased the activity of the lone pair appears to increase effectively forcing the bonds away from its electron density. The decrease in activity in the case of niobium rich compounds may be due to an electron transfer mechanism removing some of the electron density from the lone pair to the niobium. It has been reported. This kind of behaviour has been reported in the case of bismuth pyrochlore compounds where there is extensive mixing of the Bi $6p$ and the B cation d orbitals.^{18,19} This mixing of the $6p$ orbital has the effect of reducing the stereochemical influence of the $6s$ lone pair.²⁰ Due to the similarities between the chemistry of bismuth and tin it is likely that a similar mechanism is occurring in

with the tin lone pair also. This orbital mixing effect is obviously much stronger in niobium rather than tantalum due to the difference in energy levels between the $\text{Nb}^{5+} 4d$ and the $\text{Ta}^{5+} 5d$ orbitals.

3.3.2.2. UV/VIS Colour Measurements

One of the primary aims in investigating this group of compounds was to investigate the role which niobium has on the colour properties of tin niobate compounds in general. UV/VIS spectra were taken of each compound in the $\text{SnNb}_{2-x}\text{Ta}_x\text{O}_6$ solid solution in order to map the effect that reducing the amount of niobium (V) in these compounds had on the reflectance and colour.

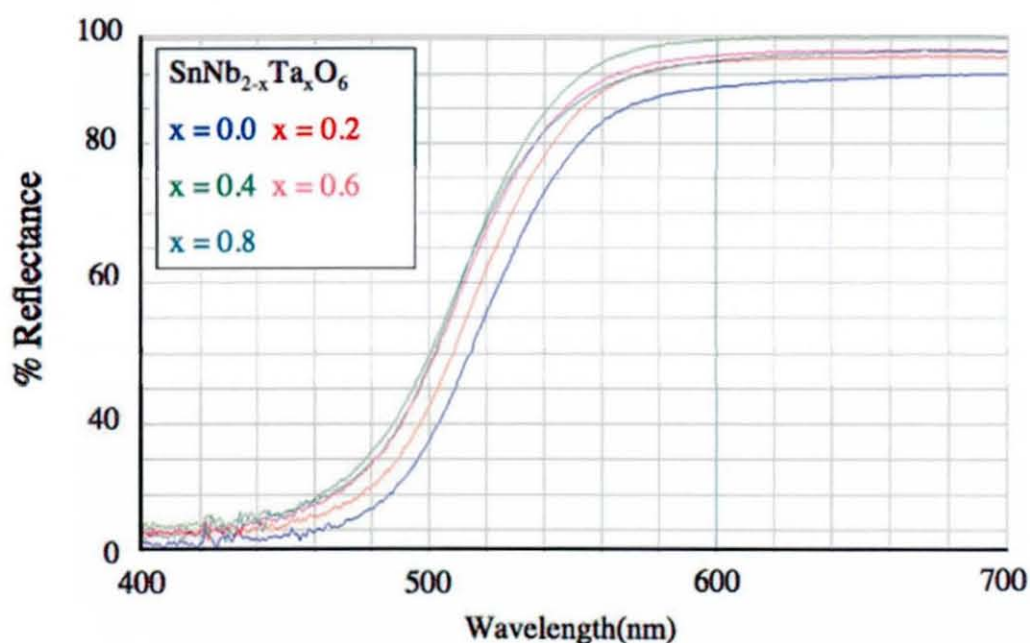


Figure 3.25: Colour measurement data for $\text{SnNb}_{2-x}\text{Ta}_x\text{O}_6$ ($x = 0 - 0.8$)

The UV/VIS spectra of the of the niobium rich end of the series (Ta content $0 \rightarrow 0.8$) (Figure 3.25) changed very little from compound to compound. In general the addition of tantalum increased the overall reflectance of the samples as they become slightly brighter. However this effect was only really seen on the first step between SnNb_2O_6 to $\text{SnNb}_{1.8}\text{Ta}_{0.2}\text{O}_6$ and after this the overall reflectance remained similar for all the compounds.

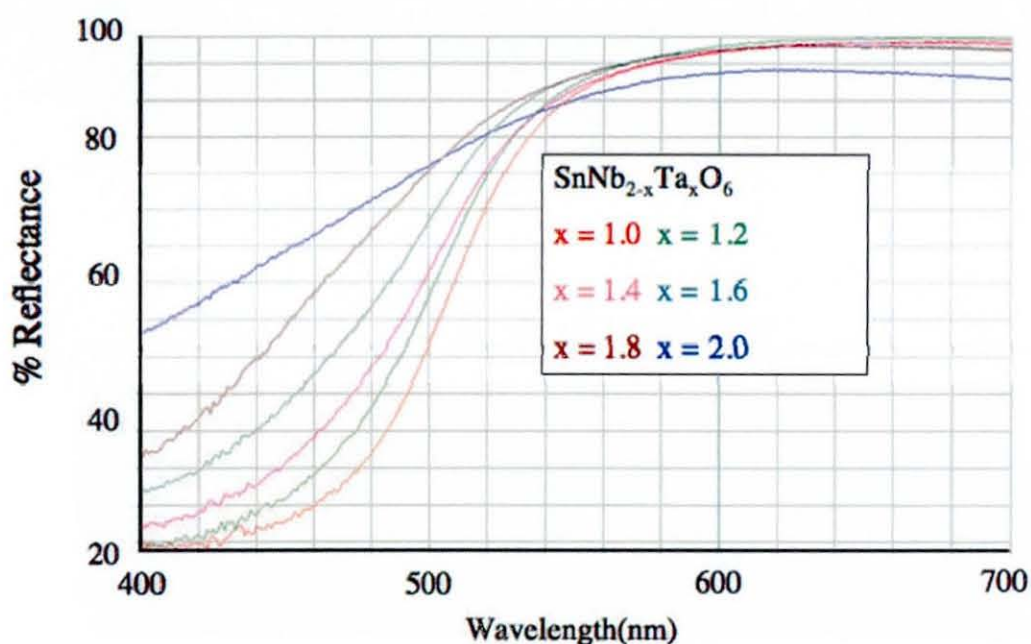


Figure 3.26: Colour measurement data for $\text{SnNb}_{2-x}\text{Ta}_x\text{O}_6$ ($x = 1.2 - 2.0$)

The trend seen above continues into the tantalum rich part of the series (Ta content $1.0 \rightarrow 2.0$) till the tantalum content reaches 1.4 at which point the absorption edge between the absorbing and reflecting regions flattens out as the materials begin to reflect wavelengths across the entire visible spectrum. The change in the absorbance of these materials is seen as a colour change between the bright yellow of the niobium rich compounds to the light cream of the pure tantalum analogue.

The origin of the intense colour of the tin niobates is not fully understood, though it appears that it is dependent on both the tin and the niobium. The replacement of either of these metals results in a almost total loss of colour, such as in the colourless cadmium niobate and tin tantalate pyrochlores. The evidence for this interaction and the intensity of the resulting colour implies that the absorption mechanism is likely to be a charge transfer between the two colour mechanisms. The obvious transfer route has already been discussed as a cause of the reduction in the stereoactivity of the tin lone pair. This mixing of the tin $5p$ and niobium $4d$ orbitals gives a ideal absorption pathway between the $5s$ lone pair and the vacant d -orbitals of Nb^{5+} .

3.4. Conclusions

The study of the tin niobate pyrochlores reported in this chapter has resulted in a complete structural characterisation of these compounds using neutron diffraction techniques. The addition of the distorted 32e oxide sites, which were not utilised by either Birchall and Sleight or Cruz *et al*, has brought the structure into line with most other lone pair pyrochlores.

Solid state NMR and Mössbauer spectroscopy have confirmed the presence of a significant Sn⁴⁺ content in the primary pyrochlore phase. The extended NMR spectra have shown a separate Sn⁴⁺ signal at 1150 ppm that had not previously been detected. The conclusion that the Sn⁴⁺ in the pyrochlore structure is from the tin disproportionation reaction and therefore is intrinsically connected to the Sn²⁺, has given a new general composition of Sn²⁺_{2-x}(Nb_{2-x/2}Sn_{x/2})O_{7-5x/4}.

Bond valence calculations have been used explain both the non-stoichiometry of the pyrochlore phase and the 32e oxide anion distortion used in this and other lone pair pyrochlore structures. The 32e distortion occurs in order to shorten the bond length between the oxide anions and the distorted 96h site of the Sn²⁺ metal centre. The use of the 32e site creates three short and one long bond, requiring that around ¼ of the tin sites be vacant to avoid the destabilising effects of the longer bond. The composition of the tin niobate pyrochlores require that on average all of the Sn²⁺ sites are 7-coordinate. Valence calculations have also shown that some of the sites must be 8-coordinate resulting in localised bonding arrangements. This negates the theory put forward that the lone pair is located on one of these vacated sites. The lone pair has therefore been hypothesised to be located on the 16c site, which is located in the centre of the 96h sites.

Structural characterisation and colour measurement analysis of the SnNb_{2-x}Ta_xO₆ (x = 0 – 1) solid solution has confirmed that the bright yellow of the tin niobates is related to a Sn²⁺/Nb⁵⁺ interaction and not on any structural modifications. The mixing of the tin 5p and niobium 4d orbitals in the pyrochlore structure gives an ideal charge transfer pathway for the 5s lone pair. A similar pathway may also be present in Sn₂Nb₂O₆ though no such interaction has been reported.

3.5. References

- ¹ P. Cernay, A.-M. Fransolet, T.S. Ercit, R. Chapman, *Can. Mineral.* **26** (1988) 889
- ² T.S. Ercit, P. Cerney, *Can. Mineral.* **26** (1988) 899
- ³ M. Gasperin, *Compt. Rend.* **240** (1955) 2340
- ⁴ V.K. Trunov, Y.U.P. Simanov, L.M. Koomba, *Z. Strukt. Khim* **4** (1968) 227
- ⁵ D.Bodiot, *Rev. Chim. Mineral.* **5** (1968) 569
- ⁶ D.J. Stewart, O. Knop, R.E. Meads, W.G. Parker, *Canad. J Chem.* **51** (1973) 1041
- ⁷ T. Birchall, A.W. Sleight, *J. Solid State Chem.*, **13** (1975) 118
- ⁸ W. Jeitschko, A.W. Sleight, *Acta. Cryst.* **B28** (1972) 3174
- ⁹ W. Jeitschko, A.W. Sleight, *Acta. Cryst.* **B30** (1974) 2088
- ¹⁰ R.J. Rentzeperis, *Z. Krist.* **117** (1962) 431
- ¹¹ W.J. Moore, L. Pauling, *J. Amer. Chem. Soc.* **63** (1941) 1392
- ¹² L.P. Cruz, J.-M. Savariault, J.-C. Jumas, J.D. Pedrosa de Jesus, *J. Solid State Chem.* **159** (2001) 349
- ¹³ L.P. Cruz, J.-M. Savariault, C.M. Morais, C. Fernandez, J.D. Pedrosa de Jesus, J. Rocha, *J. Solid State Chem.* **177** (2004) 1549
- ¹⁴ D. Bernard, J. Pannetier, J. Y. Moisan, J. Lucas, *J. Solid State Chem.* **8** (1973) 31
- ¹⁵ A.C. Larson, R.b. Von Dreele, 2000. General Structure Analysis System (GSAS) Los Alamos National Laboratory report LAUR, 86
- ¹⁶ A.L Hector, S. B. Wiggin, *J. Solid State Chem.* **177** (2004) 139
- ¹⁷ I. Levin, T. G. Amos, J. C. Nino, T. A. Vanderah, C. A. Randall and M. T. Lanagan, *J. Solid State Chem.* **168** (2002) 69
- ¹⁸ P.A. Cox, J.B. Goodenough, P.J. Tavener, D. Telles, and R.G. Edgell, *J. Solid State Chem.* **62** (1986) 360
- ¹⁹ K.S. Lee, D.K. Seo, and M.H. Whangbo, *J. Solid State Chem.* **131** (1997) 405
- ²⁰ B.J. Kennedy, *Mater. Res. Bull.* **32** (1997) 479

Chapter 4
Doped Tin Niobates

4.1. Introduction

The research reported in Chapter 3 discussed the structural re-characterisation of the tin niobium oxide pyrochlore using neutron diffraction techniques. The most intriguing properties of this compound were its bright yellow colouration coupled with the high stability of the pyrochlore structure, thus making it an ideal candidate for a high temperature inorganic pigment. Although the compound is yellow at room temperature, it makes a transition to dark red upon heating above 500 °C. The colour of the material then subsequently changes colour upon cooling back to the original bright yellow. The transition from yellow to red on heating and *vice versa* on cooling happens gradually rather than at a certain temperature. This implies that there are existing transfer bands within the electronic configuration which could be utilised to form a compound which could be used as a red inorganic pigment. Unfortunately it appears that this change in colour is not due to any structural changes so it cannot be stabilised by cation doping, such as in rare-earth doped zirconia. It does indicate however, that the enhancement of the colour is possible and that ideally it could happen at room temperature, providing the appropriate dopant could be found.

The use of cationic and anionic dopants was the most obvious route to reproducing the red colour shift, and the results are reported here. The doping methods used in the case of this structure were to follow one of two basic aims:

- 1) To reduce the amount of Sn^{2+} lost to disproportionation, in order to increase the $\text{Sn}^{2+}:\text{Nb}^{5+}$ interaction thought to be responsible for the bright colouration.
- 2) To insert an ion that increases the $\text{Sn}^{2+}:\text{Nb}^{5+}$ interaction, or the insertion of a "chromophore" which alters the colouration of the compound.

The practice of doping host oxide structures with a variety of cations is a well known method of producing effective ceramic or glass pigments. The process attempts to combine the high temperature and chemical stability of an oxide framework with the colour properties of the dopant, which is termed the "chromophore". In the case of mixed valence metal dopants (for example doping

a 4+ ion with a 6+ ion) the reaction is usually facilitated by the addition of a charge balancing cation such as calcium, although it is not always required. A good example of this is the vanadium (V) doping of a yttrium stannate pyrochlore to produce the yellow $Y_{2-x}Ca_xSn_{2-x}V_xO_7$ mixed oxide.¹ The pyrochlore oxides have long been known as effective host compounds for such studies due to their extremely high stability and the versatility of the structure to allow a variety of elements and stoichiometries. While the doping of materials with cation centres is relatively common, there is a lack of examples concerning the doping of oxide anion frameworks. Unfortunately the choices of suitable anions that are both stable and of the right size and oxidation state are limited. Usually this kind of chemistry is seen in layered structures whereby the inter-plane distances can expand or contract to allow the insertion of different anions.

There are three doped tin niobate pyrochlores reported in this section produced through both cation and anion doping, all of which have been studied for use as possible inorganic pigments.

4.1.1. Tin Niobium Oxychalcogenides ($Sn_2Nb_2O_{7-x}X_x$; X = S, Se)

The primary compounds discussed in this chapter are the tin niobium oxychalcogenide pyrochlores, which are an example of anion doped systems. They are synthesised with the general formula $Sn_2Nb_2O_{7-x}X_x$ (X = S or Se) and allow the inclusion of sulfide and selenium anions whilst still maintaining the cubic pyrochlore space group. The ability of pyrochlores to accept chalcogenide anions is extremely rare, the only other known example being that of the cadmium niobate oxysulfides.^{2,3} Also of great interest is the unique inclusion of selenium in these structures as there are no known examples of this kind of behaviour. The ability of niobate pyrochlores to accept these sulfide anions is not fully understood and is discussed here as well as later in regards to the cadmium niobates.

The addition of sulfide and selenide to these structures causes the colour to change from yellow to bright orange and finally to dark red depending on the amount and type of chalcogenide dopant used. Unlike most sulfides and

selenides, these compounds tend to retain the high temperature and chemical stability of their pyrochlore parents. Because of this they have been proposed as new orange-red inorganic pigments for the glass and ceramics industry.

4.1.2. Chromium (III) Doped Tin Niobates ($\text{Sn}_2\text{Nb}_{2-x}\text{Cr}^{\text{III}}_x\text{O}_{7-x}$)

The second group of compounds reported herein are the chromium doped tin niobates, general formula $\text{Sn}_2\text{Nb}_{2-x}\text{Cr}_x\text{O}_{7-x}$. Recently there has been a great deal of interest in the doping of a variety of materials with the trivalent chromium cation^{4,5} especially in relation to their colour properties. Both rare-earth titanate and stannate pyrochlores ($\text{Y}_2\text{Ti}_2\text{O}_7$, $\text{Y}_2\text{Sn}_2\text{O}_7$ and $\text{Nd}_2\text{Sn}_2\text{O}_7$) have been doped with chromium (III) species to produce red hue compounds which have been studied as possible pigments.^{6, 7} The Cr^{3+} cation, usually associated with the dark green of Cr_2O_3 , has a d^3 configuration and hence prefers the octahedral environment of the pyrochlore *B* cation site. There are several electronic transitions associated with this arrangement which are all forbidden by Laporte's selection rule due to the equal parity of the ground and excited states.^{6,8} These rules however can be relaxed in the case of unusual crystal field states or nuclear vibrations. It follows that when Cr^{3+} is substituted for Ti^{4+} or Sn^{4+} in the above structures, the resulting transitions result in a red colouration of the compound.

The chromium (III) doping of *B* cation sites seen in pyrochlores was applied to the tin niobates in order to enhance the colouration in the same way. This was thought to be achieved in two ways. Firstly the relaxation of the electronic transition selection rules would hopefully result in the red shift observed in the rare-earth titanates. The second method was by the retardation of the Sn^{2+} disproportionation reaction seen previously in the pure oxides. The replacement of Nb^{5+} with a lower valence Cr^{3+} cation would increase the non-stoichiometry of the system, and cause oxide vacancies to be inserted into the anion framework. The inclusion of Sn^{4+} , produced in the disproportionation reaction, into the structure and its replacement of Nb^{5+} also introduces anion vacancies in the same way. The addition of Cr^{3+} to this site would make the production of this second set of anion vacancies unfavourable and would therefore force the tin to remain in its divalent state.

4.2. Experimental

4.2.1. Tin Niobium Oxychalcogenides

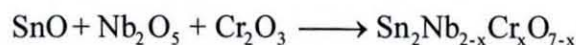
Tin niobium oxychalcogenide samples were synthesized using the same method as the oxide samples discussed previously. SnO and Nb₂O₅ powders were mixed with either SnS or SnSe in weighed stoichiometric amounts. The SnS or SnSe were formed prior to reaction or formed *in situ* by adding Sn and S/Se powder. The powdered reactants were intimately ground in a pestle and mortar and then sealed in an evacuated quartz tube. Samples were heated to 1000 °C at a rate of 2 °C min⁻¹ and this temperature was maintained for 10 h.



The resulting products were a series of powders with colours ranging from light orange to dark red depending on the quantity of chalcogenide added. Elemental analysis showed the maximum chalcogenide dopant level to be 0.3 with any excess giving rise to a SnS or SnSe impurity. Samples were washed in warm conc. hydrochloric acid prior to further analysis to remove any tin metal or tin chalcogenide impurities.

4.2.2. Chromium Doped Niobates

Chromium doped tin niobium oxides were synthesised by homogeneously mixing together stoichiometric amounts of SnO, Nb₂O₅ and Cr₂O₃. Samples were wet ground with acetone to ensure homogeneous mixing of the small amounts of chromium oxide. The samples were dried and then sealed in evacuated quartz tubes to protect the divalent tin from oxidation. Samples were heated to 1000 °C at 2 °C min⁻¹ in a tube furnace, and that temperature was maintained for 10 h.



The reacted products were polycrystalline solids with a range of different colouration dependent on the dopant level. Samples up to and including a dopant level of 0.4 became increasingly orange as more chromium was added. Samples

with chromium compositions of 0.5 and above began to appear dirty and then finally became green in colouration.

4.3. X-ray Diffraction

X-ray diffraction analysis was performed on a Bruker D8 diffractometer with a Cu X-ray tube producing monochromated $K\alpha_1$ radiation. Collected data were used for initial unit cell characterisation and phase purity analysis.

4.4. Neutron Diffraction

Tin niobium oxychalcogenide samples and the chromium doped tin niobates were synthesised for neutron diffraction analysis. Samples of tin niobium oxysulfide and oxyselenide with a dopant level of 0.3 ($\text{Sn}_2\text{Nb}_2\text{O}_{6.7}\text{S}_{0.3}$ and $\text{Sn}_2\text{Nb}_2\text{O}_{6.7}\text{Se}_{0.3}$) were prepared for detailed characterisation. Samples with the maximum dopant level were selected as these would show the maximum deviation from the ideal pyrochlore structure. Chromium doped tin niobates with the composition $\text{Sn}_2\text{Nb}_{2-x}\text{Cr}_x\text{O}_{7-x}$ where $x = 0.1, 0.2, 0.3$ and 0.4 were also analysed using neutron diffraction techniques. Time of flight neutron diffraction data were collected at room temperature on the POLARIS instrument at the ISIS facility, Rutherford Appleton Laboratory (RAL). The samples were structurally characterised using a full profile Rietveld refinement of the collected neutron data. The refinement procedure was applied using the GSAS suite of structural analysis computer programs.

4.5. Solid State NMR

^{119}Sn MASNMR was used to analyse the oxysulfide and oxychalcogenide samples with a Varian 200 MHz spectrometer over a chemical shift range of 1000 to -2500 ppm.

4.6. Mössbauer

The local environment of the tin species within the sample was analysed using MASNMR and Mössbauer spectroscopy. ^{119}Sn Mössbauer spectra were collected

at room temperature using a conventional spectrometer with a double ramp waveform to give a flat background.

4.7. UV/Vis Colour Measurement

The colour properties of each sample were assessed using UV/VIS spectrometry. Data were collected over the visible spectrum between 380 – 700 nm on a Perkin Elmer Lambda 35. The UV/VIS data were processed using the Perkin Elmer Colour Methods Software program with UV WinLab V3 to give quantifiable colour measurements.

4.8. Results – Tin Niobium Oxychalcogenides

4.8.1. X-ray Diffraction

X-ray diffraction techniques were used as an initial analysis tool to confirm the formation of the pyrochlore phase and to assess the purity of that phase. The diffraction patterns of all the oxychalcogenide samples were indexed in the cubic pyrochlore structure (Fd-3m) with cell sizes ranging from 10.57-10.60 Å. Also detected at this point was the existence of the "forbidden" 442 reflection in the diffraction pattern. This indicated that the lone pair disorder seen in the pure oxide materials was still present in the doped samples. There was a slight increase in the cell size with increase in dopant level to allow for the addition of the larger chalcogenide anions. The addition of increased amounts of sulfur resulted in large amounts tin sulfide impurities indicating that a maximum dopant level had been achieved.

Samples of tin niobium oxysulfide and oxyselenide with a dopant level of 0.3 ($\text{Sn}_2\text{Nb}_2\text{O}_{6.7}\text{S}_{0.3}$ and $\text{Sn}_2\text{Nb}_2\text{O}_{6.7}\text{Se}_{0.3}$) were prepared for detailed characterisation. Samples with the maximum dopant level were selected, as these samples are the furthest from the ideal pyrochlore structure. The samples were washed with concentrated hydrochloric acid after preparation due to the detection of tin metal and tin sulfide impurities.

4.8.2. ^{119}Sn MASNMR

As for the tin niobium oxide samples in the previous chapter, oxychalcogenide samples were analysed using NMR to probe the local tin environments within. Samples of the composition $\text{Sn}_2\text{Nb}_2\text{O}_{6.7}\text{S}_{0.3}$ and $\text{Sn}_2\text{Nb}_2\text{O}_{6.7}\text{Se}_{0.3}$ were selected for analysis by ^{119}Sn MASNMR as they represent the highest deviation from the ideal composition. The NMR spectrum shown in Figure 4.1 is that of tin niobium oxysulfide recorded between 1000 and -2500 ppm. The main signal at *ca.* -650 ppm occurs in the same region as that of the tin niobium oxide seen in Chapter 3. The peak still shares the same anisotropy of the oxide material which implies that the Sn^{2+} lone pair that was seen in the previous samples is still present here. There is however no additional signals which may be assigned to tin environments that are closely associated with sulfide anions. This signal may appear in a similar region to the main oxide so the overlap would make distinguishing them difficult. The second possibility is that the signal to noise ratio associated with tin NMR may be too poor to separate the peak from the background.

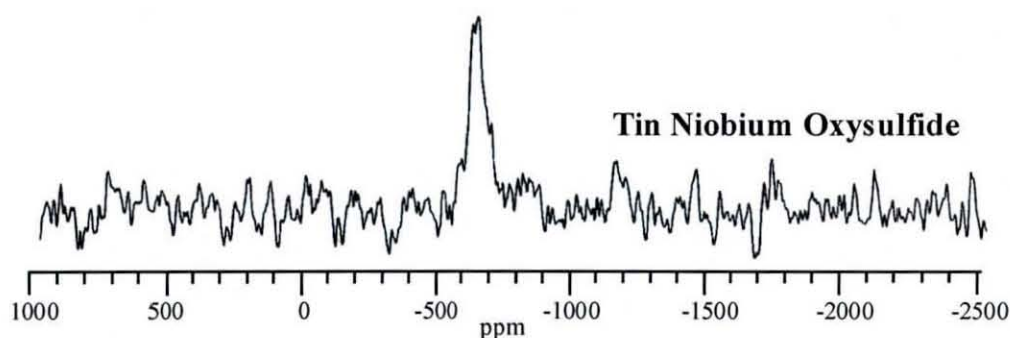


Figure 4.1: ^{119}Sn NMR spectrum of tin niobium oxysulphide

On closer analysis it is still possible to locate the remains of the Sn^{4+} environment at -1200 ppm that was so prominent in the oxide compounds. This shows that although the Sn^{4+} component of the tin niobates was still present it was much lower in the case of the oxysulfide compounds. Though the peak was too small to estimate the symmetry of the Sn^{4+} environment, its position indicates that it plays a similar role to that in the oxide compounds.

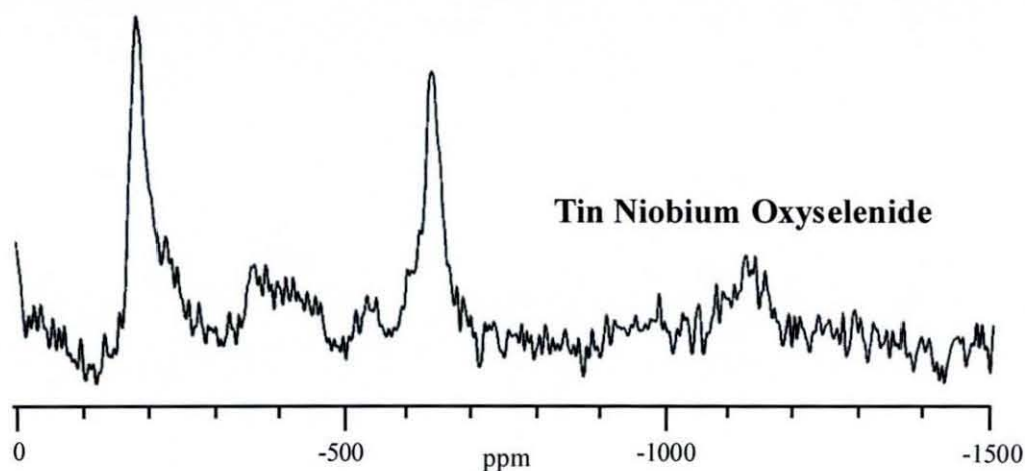


Figure 4.2: ^{119}Sn NMR spectrum of tin niobium oxyselenide

Figure 4.2 above shows the NMR spectrum of the oxyselenide pyrochlore compound. It shares many similarities to the oxide and oxysulfide samples seen before with a Sn^{2+} environment at -650 ppm and Sn^{4+} at -1130 ppm. There appears to be increase in the amount of Sn^{4+} in this system compared to the oxysulfide above, however it is still much less than the oxide. The obvious difference however is the third peak at -200 ppm that is not seen in any of the other samples. A likely possibility is that this signal can be assigned to Sn^{2+} environments within the pyrochlore that are closely associated with selenium anions. No such signal, however, is present for the oxysulfide pyrochlores, which should give a similar environment. The second possibility for this signal is that it represents a SnO or SnSe impurity, both of which resonate in this region,^{9,10} but not detected by X-ray diffraction. This would explain the lack of a sister signal in the oxysulfide compounds and the peaks position far from the main Sn^{2+} signal.

4.8.3. Mössbauer Analysis

The ^{119}Sn Mössbauer analysis was performed on tin niobium oxysulfide samples with dopant levels of 0.1, 0.2 and 0.3. The spectrum for the sample with the composition $\text{Sn}_2\text{Nb}_2\text{O}_{6.7}\text{S}_{0.3}$ is shown in Figure 3.4 below. As with the oxide samples there are three peaks consisting of one Sn^{4+} and a Sn^{2+} doublet. As was the case for the NMR, there appears to be no extra signals that could be associated with Sn^{2+} environments containing sulfide anion. The Sn^{2+} doublet is

very similar to the oxide compounds seen before, and is easily resolvable into two doublets; one which has been assigned to eight coordinate Sn^{2+} environments and one to those that are less than eight-fold. It would be expected that if an increase in the number of anion sites could cause two measurably different chemical environments, as seen above, then a change in anion should as well. However, due to size restrictions of the various sites it may be postulated that sulfur or selenium may only appear in non-stoichiometric environments and not in the full eight-fold geometries.

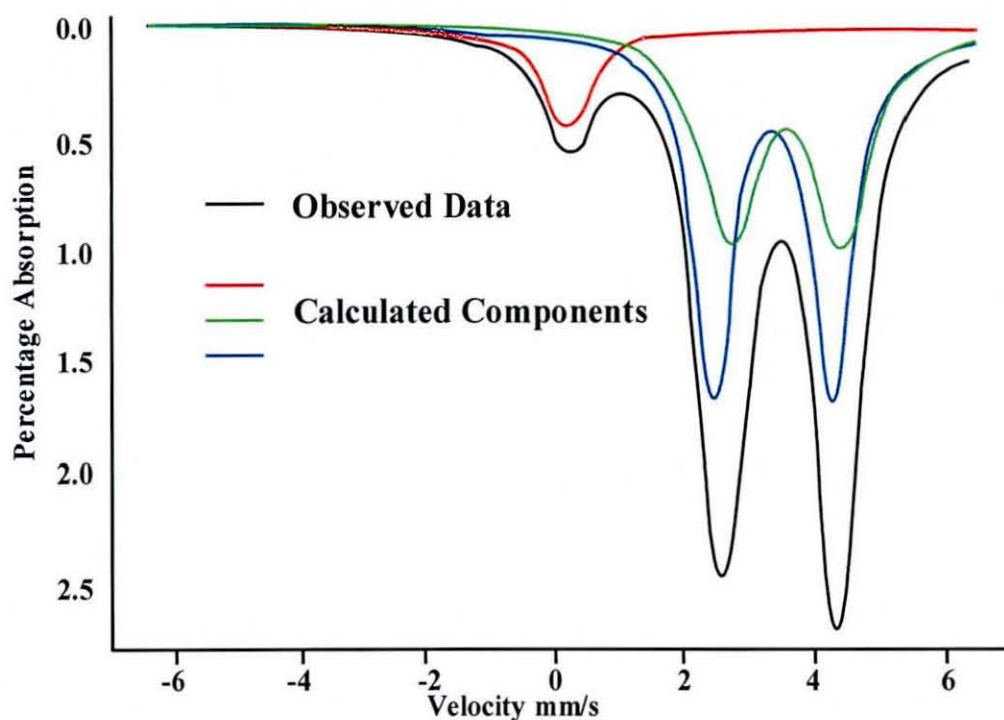


Figure 4.3: ^{119}Sn Mössbauer spectrum of $\text{Sn}_2\text{Nb}_2\text{O}_{6.7}\text{S}_{0.3}$

Table 4.1 shows the results from the peak fitting of the Mössbauer data shown above. Represented, is the percentage of the total tin signal that is assignable for each of the Sn^{2+} doublets and Sn^{4+} signal. The results show the calculated percentages for oxysulfide samples containing 0.1, 0.2 and 0.3 sulfide anions as well as the oxide seen in the last chapter. As there is good separation between the two doublets and the Sn^{4+} singlet, we can safely assume that the ratios between the Sn^{2+} and Sn^{4+} species are accurate. These results are in agreement with the MASNMR as they also suggest that the amount of Sn^{4+} decreases with the addition of sulfur. This is thought to be due to the reducing properties of the

sulfur and also the preference for interactions between the soft donor-accepter pair of Sn^{2+} and S^{2-} .

Table 4.1: Mössbauer Signal fitting results showing shift, splitting and percentage of tin attributed to each signal

Sample	Sn^{4+} Site			Sn^{2+} Site 1			Sn^{2+} Site 2		
	I.S.	Q.S.	%	I.S.	Q.S.	%	I.S.	Q.S.	%
$\text{Sn}_2\text{Nb}_2\text{O}_7$	0.16	0.31	13.0	3.69	1.70	18.3	3.41	1.89	68.7
$\text{Sn}_2\text{Nb}_2\text{O}_{6.9}\text{S}_{0.1}$	0.18	0.35	12.6	3.62	1.69	36.7	3.38	1.82	50.7
$\text{Sn}_2\text{Nb}_2\text{O}_{6.8}\text{S}_{0.2}$	0.19	0.31	8.7	3.64	1.69	39.1	3.37	1.82	52.2
$\text{Sn}_2\text{Nb}_2\text{O}_{6.7}\text{S}_{0.3}$	0.19	0.32	4.9	3.61	1.73	48.9	3.36	1.85	46.2

Table 4.1 shows the percentage contribution of each detected environment to the total calculated signal. Though individual percentages are shown for each of the Sn^{2+} doublets, the high overlap would make the relative amount of tin contributing to each doublet inaccurate. However a general trend is seen as the percentage of tin contributing to the smaller doublet increases on the addition of sulfur up to a ratio of around 50:50 for $\text{Sn}_2\text{Nb}_2\text{O}_{6.7}\text{S}_{0.3}$. If we assume that the hypothesis above is correct and that one doublet is due to a fully coordinated eight-fold tin site and the second is due to partially coordinated one, then this would imply an increase in the number of fully occupied sites. Since it is already known that the amount of Sn^{4+} decreases with the addition of sulfur it can be assumed that the amount of Sn^{2+} will increase in response. This would have a net effect of decreasing the anion vacancies within the structure and increasing the amount of fully occupied Sn^{2+} sites.

Table 4.2: Relative amounts of Sn^{2+} and Sn^{4+} in the tin niobium pyrochlores calculated from the Mössbauer Data.

Sample	Total %	
	Sn^{4+}	Sn^{2+}
$\text{Sn}_2\text{Nb}_2\text{O}_7$	13.0	87.0
$\text{Sn}_2\text{Nb}_2\text{O}_{6.9}\text{S}_{0.1}$	12.6	87.4
$\text{Sn}_2\text{Nb}_2\text{O}_{6.8}\text{S}_{0.2}$	8.7	91.3
$\text{Sn}_2\text{Nb}_2\text{O}_{6.7}\text{S}_{0.3}$	4.9	95.1

From the Mössbauer data in table 4.2 the ratio between Sn^{2+} and Sn^{4+} in the synthesised compounds can be calculated: By using the following assumptions this ratio can be used to generate the composition of the sample in question:

- 1) The *B* cation site must be fully filled *i.e.* the total amount of Sn^{4+} added to the total amount of Nb^{5+} must equal a full site.
- 2) All of the sulfur added is assumed to appear in the final product composition.
- 3) All of the Sn^{4+} is produced through the disproportionation of Sn^{2+} to Sn^{4+} and Sn^0 . This requires that the total amount of Sn^{4+} must equal half of the Sn^{2+} missing from the ideal pyrochlore composition.

The validity of the final assumption is obviously questionable but is necessary for the formation of final compositions as the relative proportions of Sn^{4+} to Nb^{5+} are not known. The assumption is accurate insofar that the amount of Sn^{4+} cannot **exceed** half of the Sn^{2+} lost as there is no other source available. There could however conceivably be **less** than half in the compound if some of the Sn^{4+} is lost as an impurity. As there were no other Sn^{4+} compounds detected in either the X-ray or the neutron diffraction it can be assumed that any amount not contained in the pyrochlore itself would be so small to be negligible.

Table 4.3: Compositions calculated from the Sn Mössbauer results

Synthesised Composition	Tin Ratios		Calculated Formula
	Sn (II)	Sn (IV)	
$\text{Sn}_2\text{Nb}_2\text{O}_7$	13.0	87.0	$\text{Sn}_{1.54}(\text{Nb}_{1.77}\text{Sn}_{0.23})\text{O}_{6.42}$
$\text{Sn}_2\text{Nb}_2\text{O}_{6.9}\text{S}_{0.1}$	12.6	87.4	$\text{Sn}_{1.55}(\text{Nb}_{1.78}\text{Sn}_{0.22})\text{O}_{6.34}\text{S}_{0.1}$
$\text{Sn}_2\text{Nb}_2\text{O}_{6.8}\text{S}_{0.2}$	8.7	91.3	$\text{Sn}_{1.68}(\text{Nb}_{1.84}\text{Sn}_{0.16})\text{O}_{6.40}\text{S}_{0.2}$
$\text{Sn}_2\text{Nb}_2\text{O}_{6.7}\text{S}_{0.3}$	4.9	95.1	$\text{Sn}_{1.81}(\text{Nb}_{1.91}\text{Sn}_{0.09})\text{O}_{6.47}\text{S}_{0.3}$

4.8.4. Neutron Diffraction

Neutron diffraction data were collected from both tin niobium oxychalcogenide samples ($\text{Sn}_2\text{Nb}_2\text{O}_{6.7}\text{S}_{0.3}$ and $\text{Sn}_2\text{Nb}_2\text{O}_{6.7}\text{Se}_{0.3}$) for analysis using Rietveld refinement. The use of neutron diffraction was chosen, as in the pure oxide compounds, because of its increased sensitivity for studying both the tin lone pair distortions and lighter elements. This was particularly important in the case of the oxychalcogenides as the main focus of the refinements were the inclusion of the relatively light sulfur and selenium anions. The study of sulfur using X-ray diffraction techniques is particularly difficult in the case of oxysulfides as it contains exactly twice as many electrons as oxygen. In the refinement of the data this often results in sulfur being confused as two oxide ions as the electron density would be almost identical.

The starting model used for in the refinement of both oxychalcogenide samples was the distorted pyrochlore model that was developed for the tin niobates in the previous chapter, and the final refined parameters are shown in Table 4.4. The major difference between the pure oxides and the two compounds under study here was the inclusion of the oxychalcogenide anions into the structure. The only anion sites available in the pyrochlore structure are the $48f$ and distorted $32e$ either of which could potentially include the sulfide anion. The $48f$ site however makes an unlikely location as it makes up the bulk of the pyrochlores anion framework which would be heavily affected by the addition of a larger anion. The Sn^{4+} and Nb^{5+} cations are located on the same site and share an octahedral

geometry, which in the tin niobium oxide, is made up of six $48f$ oxide anions. The synthesis of a sulfide or selenide would cause a proportion of these sites to be occupied by chalcogenide anions and would cause this geometry to be distorted. This distortion would be detectable in both the NMR and Mössbauer spectra however both show that then Sn^{4+} is in a relatively symmetrical geometry.

The exclusion of the $48f$ anion site as a possible location for the sulfide the only remaining choice is the distorted $32e$ site. In the pure oxide compound seen previously the parent site of the $32e$ is the $8a$ in ideal pyrochlore structure and is often differentiated from the other anion site by the label O' . This site is known to be the more versatile of the anion locations and is often partially filled, and sometimes altogether vacant in many pyrochlore structures. In addition the O' site can also be occupied by non oxide anions such as F^- and OH^- in oxyfluoride and oxyhydroxide pyrochlores.¹¹ This implies that the ability of this site to accept larger anions may have been passed to the $32e$ site in the tin niobate pyrochlore investigated here. In addition the distortion of this site also has the effect of enlarging it further in much the same way that the tin site is enlarged in order to contain the lone pair. Finally this is site also the location of the anion vacancies that affect the stoichiometry of the pyrochlore composition. This again points to the versatility of the A_2O anion framework that would allow the chalcogenide substitution to occur.

Tables 4.4 and 4.5 show the atomic coordinates and refinement results of the tin niobium oxychalcogenide pyrochlores. The final compositions of the synthesised compounds have been calculated as $\text{Sn}_{1.81}(\text{Nb}_{1.91}\text{Sn}_{0.09})\text{O}_{6.47}\text{S}_{0.3}$ ($wRp = 1.81\%$ and $Rp = 3.75\%$) and $\text{Sn}_{1.62}(\text{Nb}_{1.81}\text{Sn}_{0.19})\text{O}_{6.22}\text{Se}_{0.3}$ ($wRp = 3.95\%$ and $Rp = 5.18\%$). When compared to the pure oxide compound from the previous chapter the general trend is the same as predicted in the Mössbauer and MASNMR. The oxide has the highest amount of Sn^{4+} , however this decreases on the substitution of selenium and further when substituting sulfur. The addition of the chalcogenide anions also seems to affect the disorder of the Sn^{2+} and O' sites. The deviation of the $96h$ site from its ideal locations increases by the same

amount in both the sulfide and selenide samples, conversely the O' deviation decreases in exactly the same way.

Table 4.4: Refined results and atomic parameters for $\text{Sn}_2\text{Nb}_2\text{O}_{6.7}\text{S}_{0.3}$. Standard errors are shown in parenthesis.

Atom	Site	x	Y	z	Occup	100xU _{eq}
Sn ²⁺	96h	0.0192(5)	0.0192(5)	-0.0206(3)	0.151(1)	2.57(85)
Nb ⁵⁺	16d	0.5000(0)	0.5000(0)	0.5000(0)	0.953(1)	1.03(1)
Sn ⁴⁺	16d	0.5000(0)	0.5000(0)	0.5000(0)	0.047(1)	1.03(1)
O	48f	0.4370(1)	0.1250(0)	0.1250(0)	1.000(0)	1.27(1)
O'	32e	0.0891(5)	0.0891(5)	0.1609(5)	0.116(1)	2.66(23)
S	32e	0.0891(5)	0.0891(5)	0.1609(5)	0.075(1)	2.66(23)

$$\text{Sn}_{1.81}(\text{Nb}_{1.91}\text{Sn}_{0.09})\text{O}_{6.47}\text{S}_{0.3} \quad a = 10.57430(2) \text{ \AA} \quad R_p = 0.0204 \quad wR_p = 0.0448$$

Table 4.5: Refined results and atomic parameters for $\text{Sn}_2\text{Nb}_2\text{O}_{6.7}\text{Se}_{0.3}$. Standard errors are shown in parenthesis.

Atom	Site	x	y	Z	Occup	Beq
Sn ²⁺	96h	0.0194(13)	0.0194(13)	-0.0248(7)	0.135(1)	3.65(8)
Nb ⁵⁺	16d	0.5000(0)	0.5000(0)	0.5000(0)	0.904(1)	0.80(3)
Sn ⁴⁺	16d	0.5000(0)	0.5000(0)	0.5000(0)	0.096(1)	0.80(3)
O	48f	0.4370(1)	0.1250(0)	0.1250(0)	1.000(0)	0.87(5)
O'	32e	0.0897(5)	0.0897(5)	0.1602(5)	0.055(1)	2.07(21)
Se	32e	0.0897(5)	0.0897(5)	0.1602(5)	0.075(0)	2.07(21)

$$\text{Sn}_{1.62}(\text{Nb}_{1.81}\text{Sn}_{0.19})\text{O}_{6.22}\text{Se}_{0.3} \quad a = 10.5777(11) \text{ \AA} \quad wR_p = 0.0435 \quad R_p = 0.0522$$

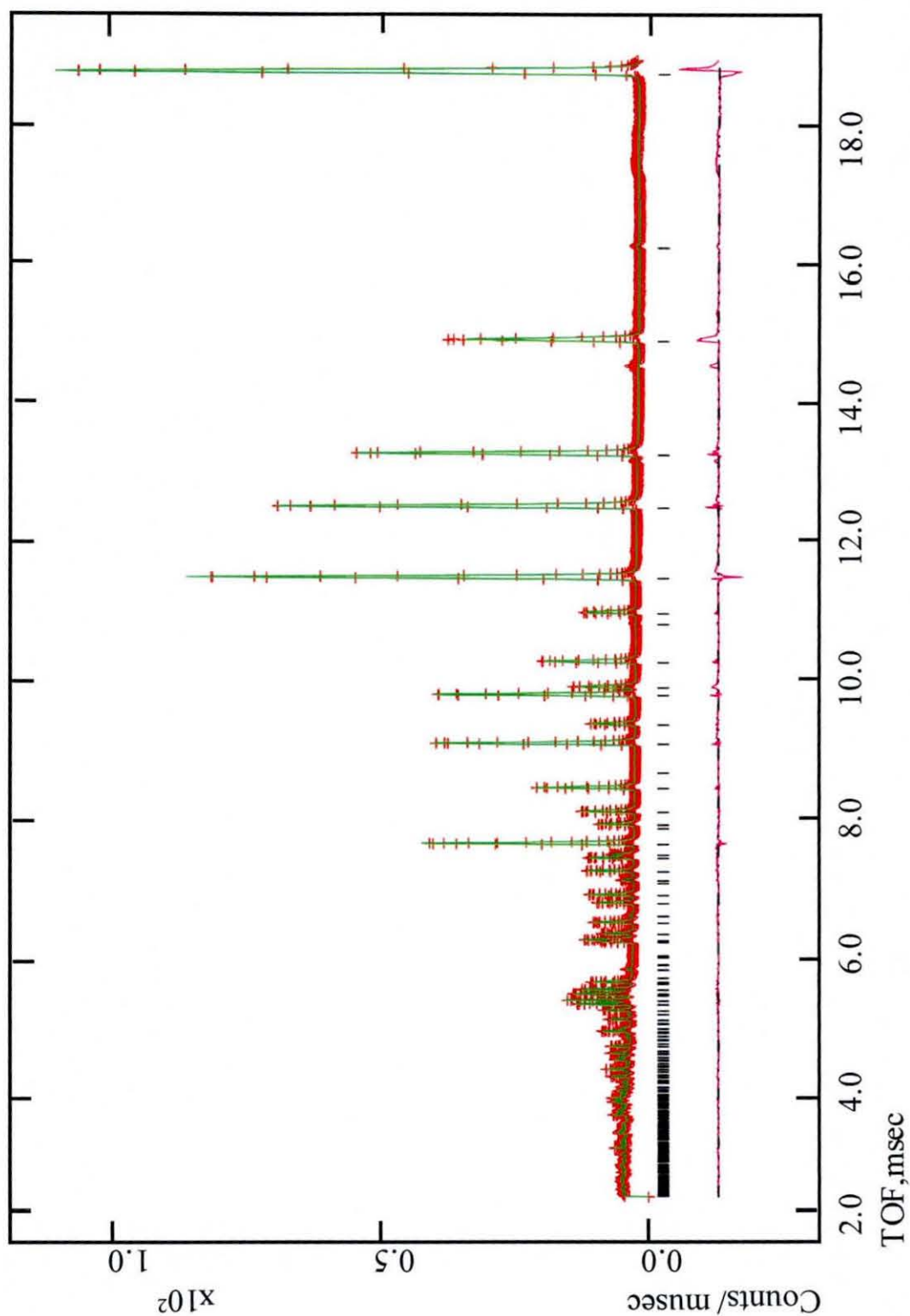


Figure 4.4: Refinement results from the structural characterisation of $\text{Sn}_{1.81}(\text{Nb}_{1.91}\text{Sn}_{0.09})\text{O}_{6.47}\text{S}_{0.3}$; red crosses are observed data, green line is calculated profile and purple line is the difference curve.

Table 4.6: Selected bond lengths of niobium and divalent tin in the oxychalcogenide samples.

	$\text{Sn}_{1.81}(\text{Nb}_{1.91}\text{Sn}_{0.09})\text{O}_{6.47}\text{S}_{0.3}$	$\text{Sn}_{1.62}(\text{Nb}_{1.81}\text{Sn}_{0.19})\text{O}_{6.22}\text{Se}_{0.3}$
$\text{Nb}^{5+}/\text{Sn}^{4+}-\text{O} \times 6$	1.98449(9)	1.985(10)
$\text{Sn}^{2+}-\text{O}$	2.365(4)	2.338(19)
$\text{Sn}^{2+}-\text{O}$	3.078(3)	3.119(13)
$\text{Sn}^{2+}-\text{O} \times 2$	2.862(11)	2.925(6)
$\text{Sn}^{2+}-\text{O} \times 2$	2.893(13)	2.567(5)
$\text{Sn}^{2+}-\text{O}'/\text{S} \times 2$	2.041(4)	2.064(25)
$\text{Sn}^{2+}-\text{O}'/\text{S} \times 2$	2.175(3)	2.170(26)
$\text{Sn}^{2+}-\text{O}'/\text{S}$	2.338(19)	2.228(22)
$\text{Sn}^{2+}-\text{O}'/\text{S}$	2.410(12)	2.326(26)
$\text{Sn}^{2+}-\text{O}'/\text{S}$	3.101(1)	3.038(28)
$\text{Sn}^{2+}-\text{O}'/\text{S}$	2.910(3)	2.875(27)

Table 4.7: Selected bond lengths of niobium and divalent tin in the oxychalcogenide samples.

	$\text{Sn}_{1.81}(\text{Nb}_{1.91}\text{Sn}_{0.09})\text{O}_{6.47}\text{S}_{0.3}$	$\text{Sn}_{1.62}(\text{Nb}_{1.81}\text{Sn}_{0.19})\text{O}_{6.22}\text{Se}_{0.3}$
$\text{O}-\text{Nb}^{5+}/\text{Sn}^{4+}-\text{O}$	90.211(10)	90.154(35)
	89.789(10)	89.846(35)
$\text{O}-\text{Sn}^{2+}-\text{O}$	61.166(12)	60.97(6)
	68.818(12)	69.68(21)
$\text{O}'-\text{Sn}^{2+}-\text{O}$	110.678(13), 83.792(7)	109.0(11), 85.2(8)
	99.248(9), 115.719(5)	91.7(6), 114.5(7)
$\text{O}'/\text{S}-\text{Sn}^{2+}-\text{O}'/\text{S}$	161.07(3), 133.73(12)	159.3(8), 134.3(6)
	144.86(7), 162.54(5)	164.97(32), 145.9(5)

The bond lengths and angles shown in Tables 4.6 and 4.7 shows that the increase in the disorder of the Sn^{2+} site has had little effect on the lengths of the six bonds to the $48f$ anion sites. There is a slight increase in these lengths but they still range from 2.3 up to 2.8 Å. The major change is in the lengthening of one of the O^{\prime} ($32e$) bonds as the tetrahedral distortion lengthens. Sn^{2+} - O^{\prime} appears much longer in the oxysulfide compounds and longer still in the oxyselenides. This reflects the chalcogenide's preference for a longer bond length than oxide anions and prevents the site from becoming over bonded. The second increase is that of the niobium octahedron bond lengths which have increased to *ca.* 1.985 Å in both compounds. This is a direct result of the loss of Sn^{4+} in the doped samples which increases the overall valence of the site. This allows the niobium to adopt a longer bond length without under bonding the whole site.

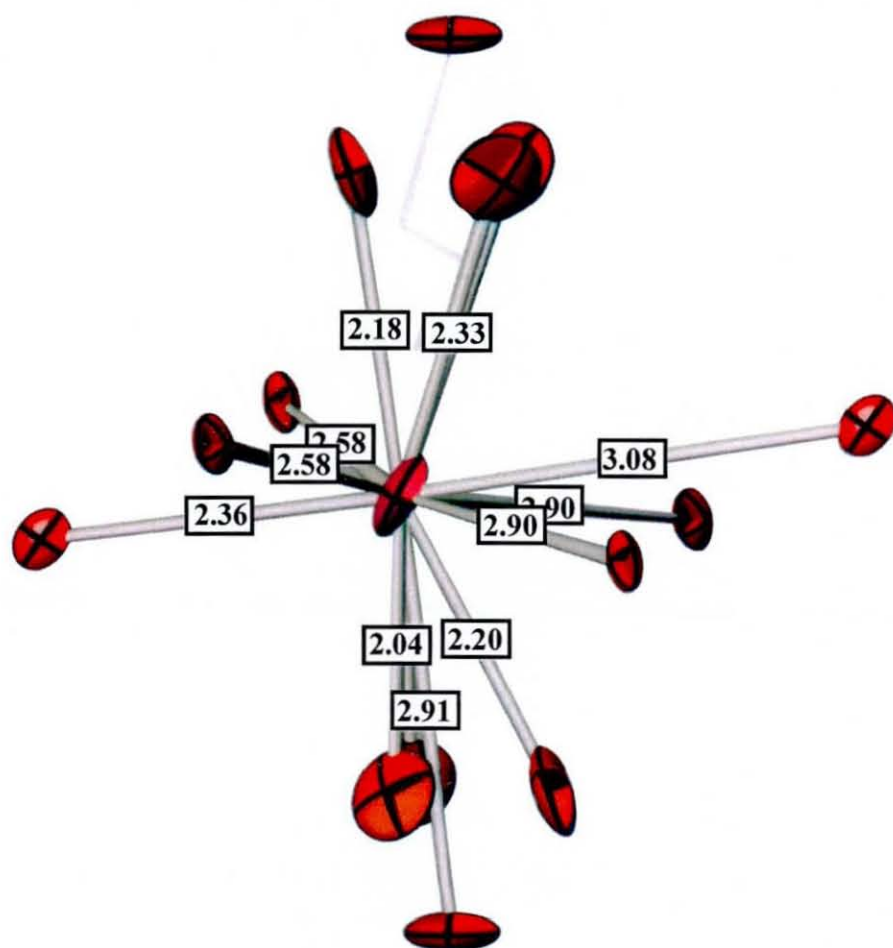


Figure 4.5: Sn^{2+} geometry in $\text{Sn}_{1.81}(\text{Nb}_{1.91}\text{Sn}_{0.09})\text{O}_{6.47}\text{S}_{0.3}$; Purple atom = Sn^{2+}
Red atoms = O^{2-}

4.8.5. Valence Calculations

Valence calculations have been carried out to analyse the stability of the distorted Sn^{2+} site in the tin niobium oxychalcogenides. In the previous chapter the measured distortions on the Sn^{2+} site, caused by the presence of the tin lone pair, also brought about distortions on the neighbouring O' anion site. Valence calculations showed that the distortions allowed the Sn-O' bond length to be as short as possible thereby raising the valence of the whole site. This was required because of the relatively large distance between the Sn^{2+} site and the O' site in this structure. In the case of the oxychalcogenides however, this distortion may not be needed, as the increased size of the sulfur and selenium anions allows the formation of much longer bonds. This allowed for two possible structures for the oxychalcogenide pyrochlores, one where the sulfide and selenide anions are on the same site as the oxide anions and one where they resided on the ideal $8a$ site instead.

Table 4.8: All possible lengths associated with the Sn^{2+} centre. The Sn-O bonds are those to the $48f$ sites and the Sn-O' bonds are those to the $32e$ sites

Bond	Bond Length	Number	Bond Valence
Sn-O	2.562	2	0.195
	2.917	2	0.075
	3.083	1	0.048
	2.360	1	0.337
Sn-O'	2.273	1	0.426
	2.162	2	0.575
	2.140	1	0.61
	2.252	2	0.451
	2.800	1	0.103
	2.784	1	0.107
Sn-S	2.273	1	1.355
	2.162	2	1.83
	2.140	1	1.942
	2.252	2	1.435
	2.800	1	0.326
	2.784	1	0.341

Table 4.8 shows the calculated bond lengths for the tin niobium oxysulfide pyrochlore along with the number of possible bonds and the bond valence for each one. The 32*e* site on which the O' and S sites resides is only partially occupied so not all of these bonds will be present in every Sn²⁺ environment. Refining the structure using the ideal 8*a* site instead gives very similar refinement results and bond lengths/angles. The major difference between the two structures is the change in bond length between the Sn²⁺ centre and the S²⁻ anion. The decrease in the multiplicity of the site causes the number of possible bond lengths to decrease to two: 2.310 and 2.326 Å. These give bond valences of 1.226 and 1.174 respectively for each bond. All six of the Sn-O bonds are present in every Sn²⁺ centre as all of the 48*f* anion sites are fully occupied. These six 48*f* bonds contribute 0.925 to the total valence of each Sn²⁺ site, with the rest coming from the remaining two bonds to the 32*e* or 8*a* sites. Since the 32*e* and the 8*a* sites are all partially occupied not all of the above bond lengths will be used in every site. Which bond lengths are used is dependent on the model used (32*e* or 8*a* sulfide site), the surrounding bonding arrangement, and whether the Sn²⁺ centre is a pure oxide or contains a S²⁻ anion.

In the case of the pure oxide pyrochlore seen in the previous chapter, the relatively long Sn-O bond lengths and the large amount of Sn²⁺ and O²⁻ vacancies meant that the majority of possible Sn²⁺ sites tended to be under-bonded. This was solved by a complex bonding arrangement, the aim of which was to maximize the valence of the available sites and therefore the stability of the structure. This had the effect of reducing the amount of possible Sn²⁺ sites that could be used in the structure and dictated the insertion of vacancies. In the case of the oxychalcogenides however, this was not the case, as the sulfur and selenium anions are able to form stable arrangements with much longer bond lengths than oxygen. This has the effect of causing the opposite problem whereby a number of Sn²⁺ sites would be over-bonded when associated with a sulfide or selenide anion. It also had the effect of increasing the number of choices available when determining the structure of a Sn²⁺ site. Because of the number of combinations of factors that influence the valence of this site it was difficult to assign an absolute valence parameter. Instead it is helpful to discuss

valency in terms of an average site which is a combination of all of the above factors.

As stated previously, six of the eight bonds associated with an Sn^{2+} site are universal to all environments and represent the $48f$ oxide anions. As they contribute a total of 0.925 to the site valence, the remaining two bonds must contribute around 1.075 to give the ideal value of 2.0. There are a number of different possible sites, which must be considered to attain an average site valence. For the purpose of this calculation, a number of assumptions have been made, such as the fact that it is assumed that every Sn^{2+} environment will contain a maximum of one sulfide anion. This is based on the low likelihood that two sulfide anions will be in close enough proximity for an 8-coordinate to be formed, and the instability this would cause on the Sn^{2+} site. The second assumption is that there are no 6-coordinate sites in the calculation for precisely the same reasons. This does not require the non-existence of this type of sites, merely that there would be too few to have any effect. These assumptions still leave several possible sites including pure oxide sites both 7- and 8-coordinate, 8-coordinate oxysulfide sites (one Sn-O and one Sn-S bond), and 7-coordinate oxysulfide sites. Diagrams of these four different sites can be seen in Figure 4.6a. In order to make a average valence for all Sn^{2+} sites the valence has to be calculated for the different sites, shown here based on the various bonds that make them up and the proportion of them throughout the structure.

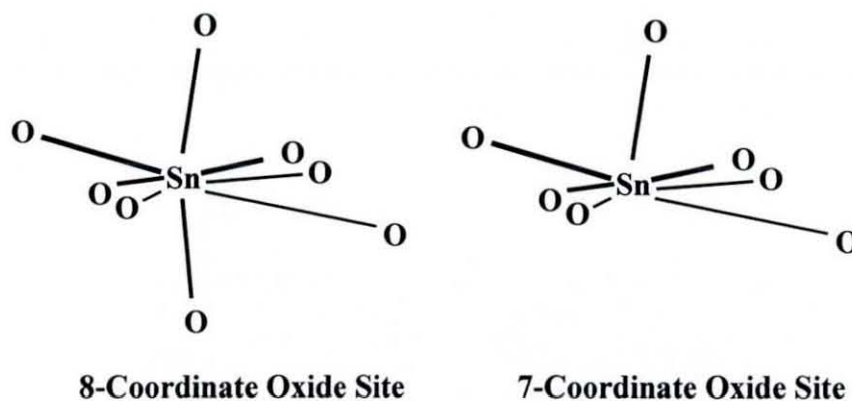


Figure 4.6a: 8-Coordinate and 7-Coordinate oxide sites in



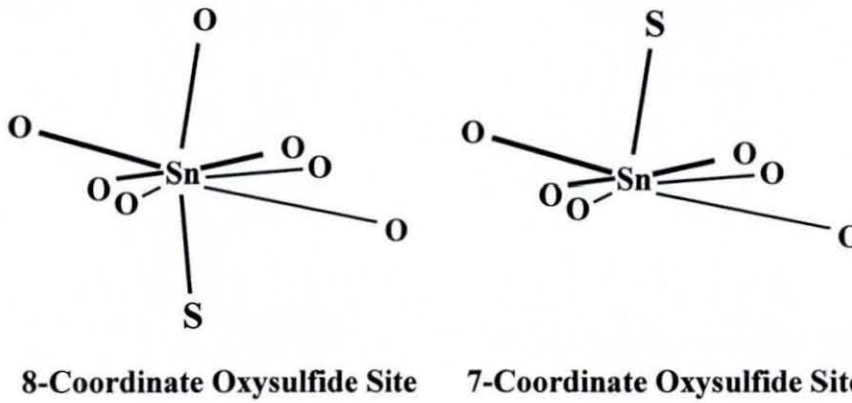


Figure 4.6b: 8-coordinate and 7-coordinate oxysulfide sites in $\text{Sn}_{1.81}(\text{Nb}_{1.91}\text{Sn}_{0.09})\text{O}_{6.47}\text{S}_{0.3}$

- 8-Coordinate Oxide Site Valence.

The 8-coordinate oxide site consists of six bonds to the $48f$ anions which contribute 0.925 to the total valence and two $32e$ oxides which can contribute between 0.103-0.575 each. Each $32e$ site has four possible locations consisting of three short bonds and one long bond to each Sn^{2+} site. The average bond valence contribution calculated from the eight available bond lengths can be shown to be 0.412 for each bond. This gives a total average site valence of $0.925 + 0.412 + 0.412 = 1.749$

- 7-Coordinate Oxide Site Valence.

The valence of the 7-coordinate site can be calculated in much the same way but with a contribution from only one $32e$ oxide instead of two. This gives an average site valence of $0.925 + 0.412 = 1.337$

- 8-Coordinate Oxysulfide Site Valence

In this case the major contribution still comes from the $48e$ oxide anions as seen in the previous two examples. For the oxysulfide the remaining valence contribution comes from one $32e$ oxide site and one sulfide anion. The valence of the oxysulfide site is dependent on the model used in the refinement, whether the $32e$ site or the $8a$ site is used for the sulfide anion. In the case of the $32e$ site the arrangement is similar to the oxide example before whereby three quarters are shorter bonds and a quarter is longer bonds, which gives an average sulfide

bond valence of 1.311. With the 8*a* site there are only two possible bond lengths, which have a 50:50 distribution throughout the structure. This gives an average sulfide bond valence of 1.20 in this case. This means that the average bond valence for the 8-coordinate oxysulfide site is $0.925 + 0.412 + 1.311 = 2.648$ when using the 32*e* site and $0.925 + 0.412 + 1.20 = 2.537$ for the 8*a* site.

- 7-Coordinate Oxysulfide Site Valence

As for the 7-coordinate oxide site the valence for this site is calculated in the same way but with the removal of the oxide bond. This gives an average site valence of $0.925 + 1.311 = 2.236$ when using the 32*e* site and $0.925 + 1.2 = 2.125$ for the 8*a* site.

Once the average site valences were calculated they needed to be combined in the right proportions to give an accurate valence total. The final refined formula for the tin niobium oxysulfide pyrochlore was $\text{Sn}_{1.81}(\text{Nb}_{1.91}\text{Sn}_{0.09})\text{O}_{6.47}\text{S}_{0.3}$ from which the final proportions can be calculated. The number of 7-coordinate and 8-coordinate sites within the structure can be determined by looking at the total number of anion vacancies. In this case around one third (33%) of the anion sites were left vacant due to the non-stoichiometry of the structure. This equates to two thirds of the Sn^{2+} sites being 8-coordinate and one third being 7-coordinate on average. Since 30% of the 32*e*/8*a* anions are sulfides it can be approximated that 30% of all Sn^{2+} sites are closely associated with a sulfide anion. The total valence of the resulting site is dependent on whether the 32*e* or 8*a* site is used in each case. This means that in total 9.9% (30% of 33%) of the available Sn^{2+} sites are 7-coordinate oxysulfides giving a total valence contribution of 0.221 when using a 32*e* site and 0.211 when using the 8*a* site. It can also be shown that the remaining 7-coordinate sites or 23.1% of the available Sn^{2+} sites are oxides giving a valence contribution of 0.308. The elimination of the 7-fold sites requires that the remaining 67% of Sn^{2+} sites are 8-coordinate. As before 30% of these locations will be closely associated with a sulfide anion forming an oxysulfide site, again the valence in this case will be dependent on the sulfide site used. Therefore 20.1% of the total Sn^{2+} will be 8-coordinate oxysulfide with a valence contribution of 0.532 in the case of the 32*e* site and 0.510 for the 8*a*

site. Finally the remaining 46.9%, almost half of the total of Sn^{2+} sites, will form an 8-coordinate oxide site. This contributed a final 0.820 to the final valence figure of the Sn^{2+} site.

By adding together all the valence results for all four sites a final valence figure was achieved for the Sn^{2+} site. The valence figures for both models were calculated to be 1.881 for the $32e$ model and 1.849 for the $8a$ model. Neither of these valences were close enough to the ideal value of 2.0 to be considered a stable site. However, looking at the refined composition it can be seen that not all of the Sn^{2+} sites are occupied, as 9.5% of them were left vacant. In the pure oxide example studied in the previous chapter the preferential bonding arrangement meant that sites of low valence were removed as vacancies to bring the total valence up. In the case of the oxysulfide however no bonding arrangement is needed, however these vacancies have to be removed from the calculations. This boosts the average site valence by around 10% producing a result of 2.07 when placing the sulfide on the $32e$ site and 2.04 for the $8a$ site. Both of these results are well within the margin for error for a stable site when considering bond valence parameters. The $8a$ site model has a valence closer to the ideal value for a Sn^{2+} site, however the difference is not great enough to assign one model over the other. The increased size of the sulfur anion increases the amount of overlap between the $8a$ site and the surrounding $32e$ sites. This made it increasingly difficult to detect which one of these models is more accurate or whether a combination of the two is being used.

Like the oxide samples in Chapter 3 the oxysulfide pyrochlores have been shown to be non-stoichiometric. In the pure oxide example the vacancies in the oxide framework were used to avoid the longer bond created by the formation of the $32e$ site. The inclusion of sulfide into the structure negates this need, due to the increased stability of the longer bond lengths. The decrease in the amount of anion vacancies and the increase in Sn^{2+} occupation is evidence of this increase in the valence of the Sn^{2+} site. The vacancies in the oxysulfide pyrochlores are still present; however in this case they are required to remove areas of high valence rather than low valence. The formation of the 7-coordinate sites is

fundamental in ensuring that the Sn^{2+} sites do not become over bonded. It may be that there is equilibrium between the cation and anion sites that changes depending on whether the Sn^{2+} sites are becoming over or under bonded. Outside influences such as excessive grinding and different firing temperatures may have an effect on the density of the unit cell and therefore the bond lengths and valence. This would then affect the number of cation and anion vacancies producing the range of compositions seen in these compounds.

4.8.6. UV/Vis Colour Measurement

UV/Vis spectra were recorded over the visible region for samples of the composition $\text{Sn}_2\text{Nb}_2\text{O}_{7-x}\text{S}_x$ ($x = 0.1, 0.2, 0.3$) for colour measurement quantification.

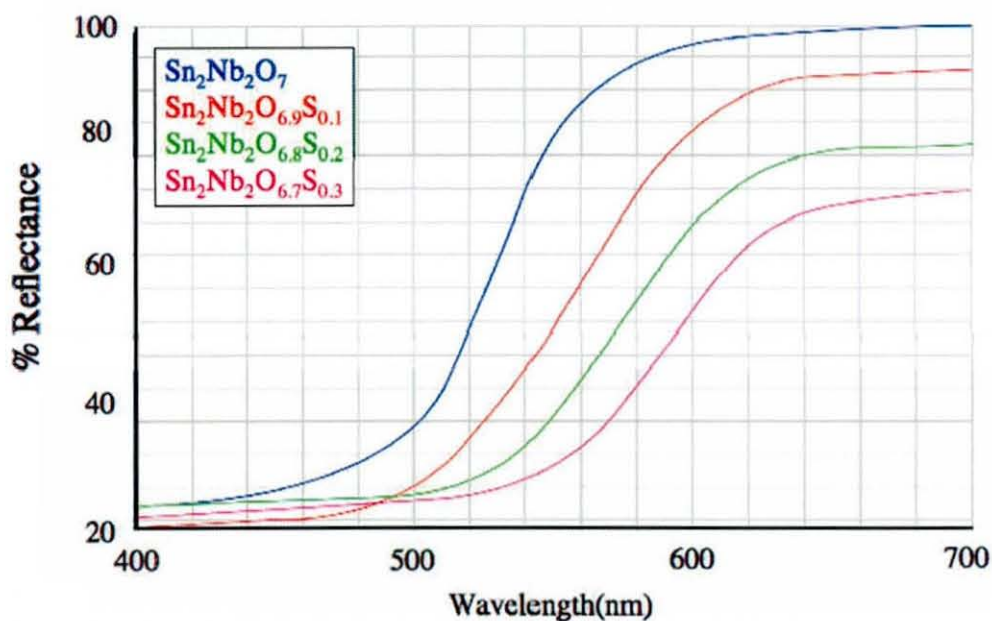


Figure 4.7 Solid state visible spectra for the tin niobium oxides and oxychalcogenides

The recorded spectra are shown in Figure 4.7 along with $\text{Sn}_2\text{Nb}_2\text{O}_7$ for comparison. The $\text{Sn}_2\text{Nb}_2\text{O}_7$ spectrum (blue) shows a high absorption of light at low wavelengths in the blue/green regions and a high reflectance at higher wavelengths in the orange/red regions. The sharp absorption edge appears between 510 and 550 nm in the yellow regions of the visible spectrum. On the addition of sulfur from 0.1 (red) to 0.2 (green) and 0.3 (pink) the absorption edge

moves to the right to higher wavelengths. This is reflected in the colour of the compounds as a transition from yellow to orange. As sulfur is added the absorption edge also flattens and the overall reflectance decreases. This is seen as a dulling of the absorbed colour as more and more light is absorbed. Table 4.9 shows the $L^*a^*b^*$ values calculated from the UV/Vis spectra taken from the oxysulfide samples.

Table 4.9: CIE $L^*a^*b^*$ values for oxychalcogenide doped samples

Sample	L^*	a^*	b^*
$\text{Sn}_2\text{Nb}_2\text{O}_7$	91.28	13.74	54.76
$\text{Sn}_2\text{Nb}_2\text{O}_{6.9}\text{S}_{0.1}$	82.35	25.20	49.79
$\text{Sn}_2\text{Nb}_2\text{O}_{6.8}\text{S}_{0.2}$	75.32	27.90	34.43
$\text{Sn}_2\text{Nb}_2\text{O}_{6.7}\text{S}_{0.3}$	69.32	27.65	26.14

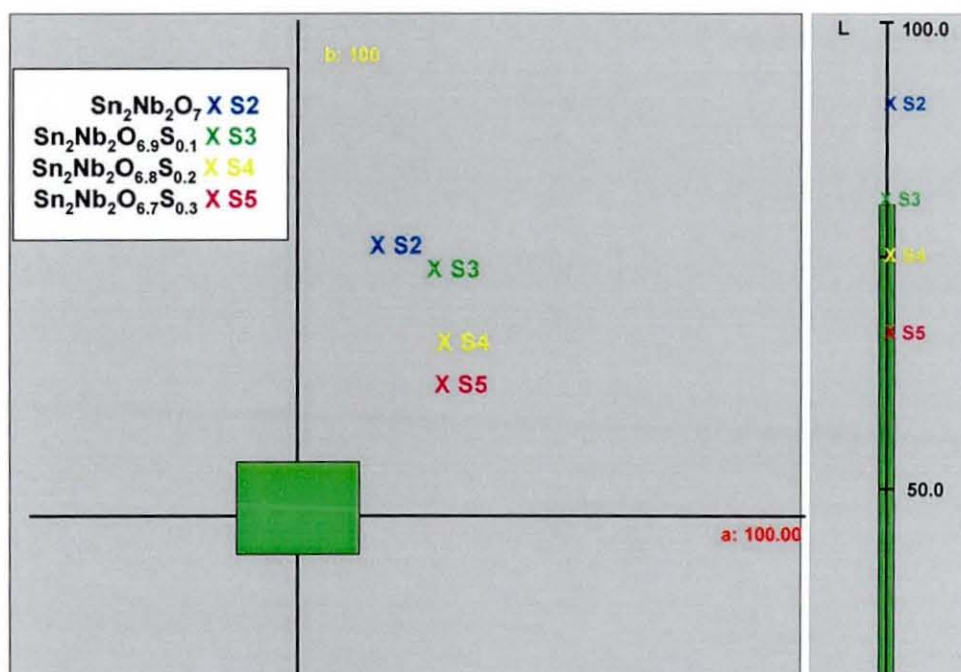


Figure 4.8: Colour matrix of calculated $L^*a^*b^*$ results from the tin niobium oxysulfides. The window on the left shows the colour location on the a^*b^* axis and the right window shows the brightness or L^* value of that colour.

Figure 4.8 shows a 2-D representation of the 3-D $L^*a^*b^*$ colour space. As sulfur is added there is an initial increase in the red component as the colour moves from yellow to orange. As more sulfur was added the red component remained stationary and the yellow component decreased. This reduction in the yellow component has the same effect as increasing the red component as the samples move from orange to red.

4.9. Results – Chromium Doped Tin Niobates

4.9.1. X-ray Diffraction

The addition of chromium to the tin niobate materials resulted in a series of light orange samples up to chromium content of 0.4. Above this value the samples begin to take on a green colouration and then become completely green at higher dopant levels.

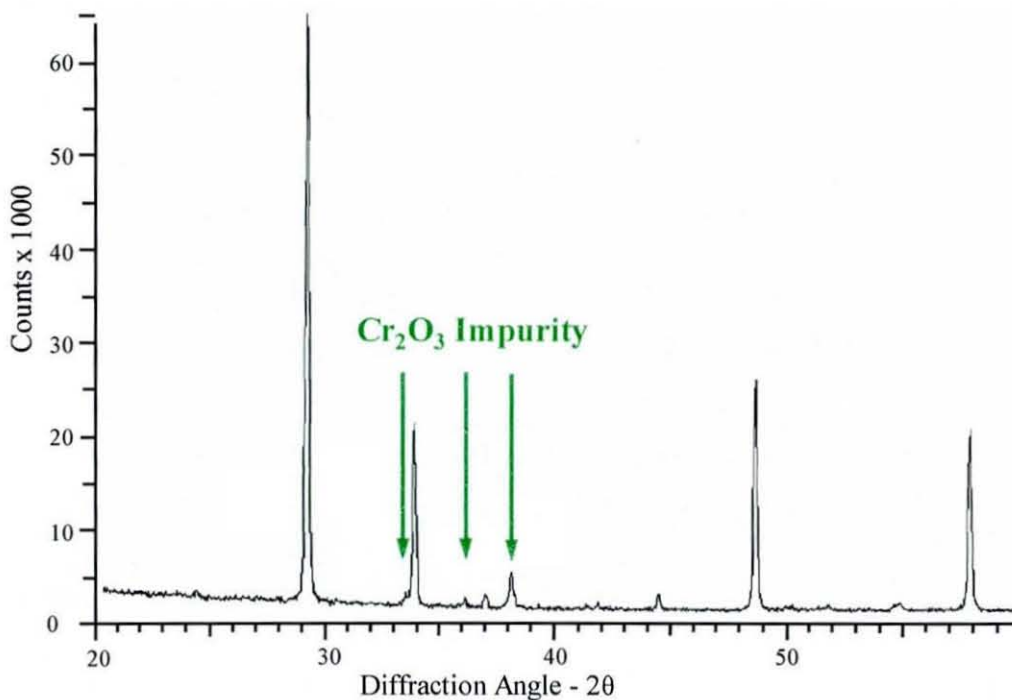


Figure 4.9: An X-ray diffraction pattern of the $\text{Sn}_2\text{Nb}_{1.5}\text{Cr}_{0.5}\text{O}_{6.5}$ pyrochlore with a Cr_2O_3 impurity shown by green arrows

Inspection of the samples using X-ray diffraction analysis revealed that the green colouration was due to an increasing Cr_2O_3 impurity (Figure 4.9). The maximum chromium dopant quantity seems to appear at levels between 0.3 and 0.4 with any excess chromium added remaining unreacted. This is most likely caused by

the increasing levels of oxide vacancies in the structure. As more niobium (V) is replaced by chromium (III) anion vacancies are inserted to charge balance the lower oxidation state. A point is reached where the structure can no longer accept any more anion holes before becoming unstable leaving Cr_2O_3 as an impurity.

4.9.2. Neutron Diffraction

Samples of the composition $\text{Sn}_2\text{Nb}_{2-x}\text{Cr}_x\text{O}_{7-x}$ with $x = 0.1, 0.2,$ and 0.3 were prepared for structural analysis using neutron diffraction methods. Diffraction data were collected on the POLARIS instrument at the RAL. Collected data were analysed using the Rietveld method on the GSAS suite of refinement programs. The results for the Rietveld refinement of the prepared chromium doped tin niobates are shown in Tables 4.11 - 4.13. The samples were refined using the tin niobate pyrochlore model used in the previous chapter for the oxychalcogenide samples. The niobium and 48f oxide anions were placed on their ideal locations as in the previous refinement. As before the divalent tin and final anion site were statically displaced from their ideal locations to the surrounding 96h and 32e sites.

Table 4.11: Neutron refinement results for $\text{Sn}_2\text{Nb}_{1.9}\text{Cr}_{0.1}\text{O}_{6.9}$ composition

Atom	Site	X	y	z	Occupancy	B_{iso}
Sn^{2+}	96h	0.0141(8)	0.0141(8)	-0.0303(7)	0.133(0)	1.544
Nb^{5+}	16d	0.5000(0)	0.5000(0)	0.5000(0)	0.950(1)	1.156
Cr^{3+}	16d	0.5000(0)	0.5000(0)	0.5000(0)	0.050(1)	1.156
O	48f	0.435822(31)	0.12500(0)	0.12500(0)	1.000(0)	1.003
O'	8a	0.08880(19)	0.08880(19)	0.16120(19)	0.125(2)	2.282

$$\text{Sn}_{1.59}\text{Nb}_{1.9}\text{Cr}_{0.1}\text{O}_{6.5} \quad a = 10.57796(5) \quad \text{wRp} = 0.0173 \quad \text{Rp} = 0.0385$$

Table 4.12: Neutron refinement results for $\text{Sn}_2\text{Nb}_{1.9}\text{Cr}_{0.2}\text{O}_{6.8}$ composition

Atom	Site	x	y	z	Occupancy	B_{iso}
Sn^{2+}	96h	0.0142(6)	0.0142(6)	-0.0308(5)	0.148(1)	1.544
Nb^{5+}	16d	0.5000(0)	0.5000(0)	0.5000(0)	0.900(0)	1.156
Cr^{3+}	16d	0.5000(0)	0.5000(0)	0.5000(0)	0.100(0)	1.156
O	48f	0.435206(31)	0.12500(0)	0.12500(0)	1.000(0)	1.003
O'	8a	0.09027(18)	0.09027(18)	0.15973(18)	0.144(2)	2.282

$$\text{Sn}_{1.776}\text{Nb}_{1.8}\text{Cr}_{0.2}\text{O}_{6.576} \quad a = 10.56177(5) \quad wRp = 0.0199 \quad Rp = 0.0462$$

Table 4.13: Neutron refinement results for $\text{Sn}_2\text{Nb}_{1.7}\text{Cr}_{0.3}\text{O}_{6.7}$ composition

Atom	Site	x	y	z	Occupancy	B_{iso}
Sn^{2+}	96h	0.0137(9)	0.0137(9)	-0.0313(6)	0.152(1)	1.544
Nb^{5+}	16d	0.5000(0)	0.5000(0)	0.5000(0)	0.850(0)	1.156
Cr^{3+}	16d	0.5000(0)	0.5000(0)	0.5000(0)	0.150(0)	1.156
O	48f	0.43487(4)	0.12500(0)	0.12500(0)	1.000(0)	1.003
O'	8a	0.09208(25)	0.09208(25)	0.15792(25)	0.129(2)	2.282

$$\text{Sn}_{1.824}\text{Nb}_{1.7}\text{Cr}_{0.3}\text{O}_{6.516} \quad a = 10.54870(13) \quad wRp = 0.0219 \quad Rp = 0.0564$$

Due to the size similarity between chromium (III) and niobium (V), 0.755 Å for Cr^{3+} versus 0.78 Å for Nb^{5+} in an octahedral environment, it was concluded that they must both reside on the 16c site. Originally Sn^{4+} was added to all the chromium doped samples to account for the disproportionation that usually occurs during the synthesis of these compounds. However only in the 0.1

samples could this quantity be refined, all other samples refined to give only niobium and chromium on the $16d$.

The atomic coordinates for the chromium doped tin niobates are closer related to the pure oxide samples seen in Chapter 3 than to the oxychalcogenide samples. The deviation of the Sn^{2+} site from its ideal location is much lower than in the oxysulfide samples and actually decreases with increasing dopant level. This implies a connection between the amount of disorder on the tin site and the composition of the niobium site. A similar effect is seen in the oxysulfide whereby the disorder of this site increases with the reduction of Sn^{4+} .

The results confirm the results from the X-ray diffraction data showing a decrease in the cell size with the addition of chromium (III) oxide to the samples. The decrease in cell size would perhaps expected to be larger, it being only in the order of 0.03 \AA , however it is counterbalanced by the increased amount of Sn^{2+} species on the A cation site. The increase in the amount of Sn^{2+} cations and the loss of Sn^{4+} are both evidence that the amount of disproportionation is decreased by the addition of the lower oxidation state species. The amount of Sn^{2+} has increased to give almost a full A cation site in the case of the 0.4 doped species and even more than the highly reducing sulphur environments seen in the previous chapters.

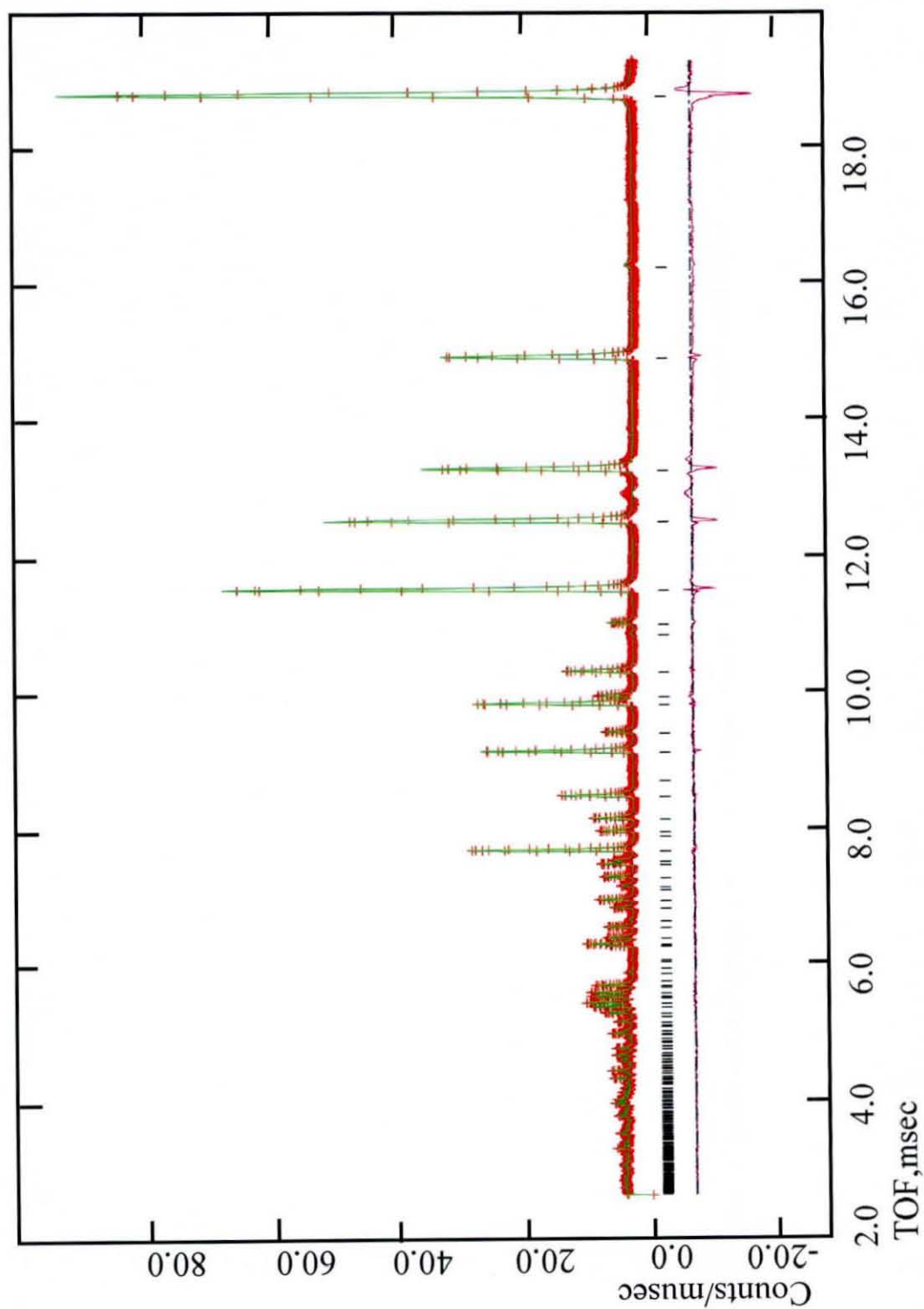


Figure 4.10: Refinement results from the structural characterisation of $\text{Sn}_2\text{Nb}_{2-x}\text{Cr}_x\text{O}_{7-x}$; red crosses are observed data, green line is calculated profile and purple line is the difference curve.

4.9.3. UV/VIS Colour Measurements

Reflectance data were collected for chromium doped samples with chromium contents of 0-0.8 for treatment with a colour measurement computer program. The range analysed was limited only to the visible range of the spectrum between 400 and 700 nm. The chromium doped samples all gave similar visible spectra as the colour does not change dramatically across the series. All the samples reflected strongly in the orange red regions between 600-700 nm and absorbed strongly at lower wavelengths as expected for an orange sample.

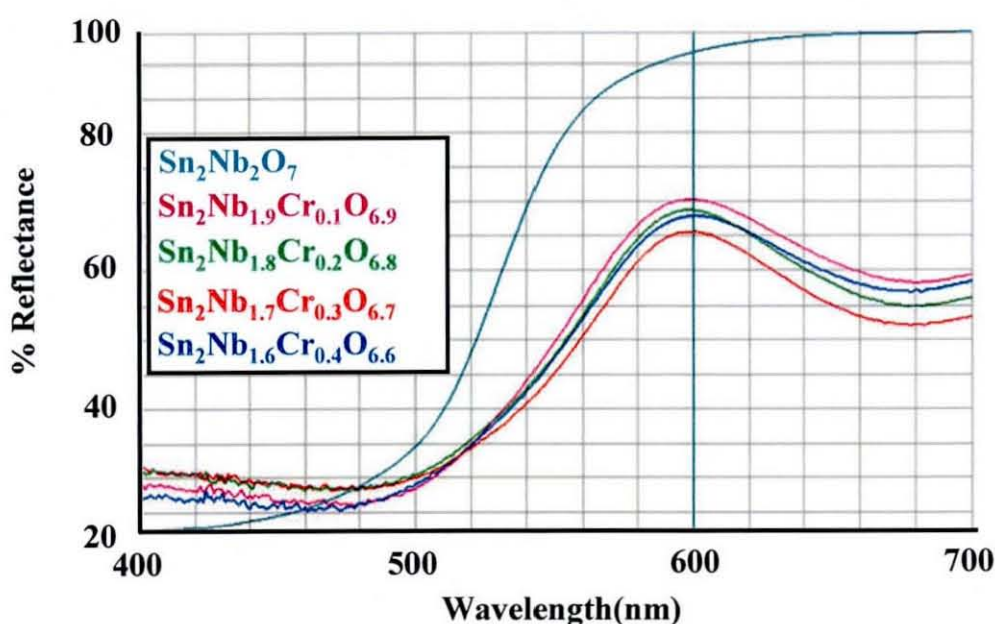


Fig 4.11: UV/Vis reflectance scans of $\text{Sn}_2\text{Nb}_{2-x}\text{Cr}_x\text{O}_{7-x}$ ($x = 0-0.4$).

The UV/VIS reflectance pattern for chromium dopant levels of 0-0.4 are shown in Fig 4.11. There is a significant difference between the un-doped sample ($\text{Sn}_2\text{Nb}_2\text{O}_7$) and the doped samples which can be seen in the data. The un-doped $\text{Sn}_2\text{Nb}_2\text{O}_7$ shows a classic absorption edge for a bright yellow compound which absorbs strongly at low wavelengths and reflects strongly at high wavelengths. The chromium doped samples absorb much more strongly in the yellow orange and red regions at wavelengths above 500 nm lowering the overall reflectance of the sample. The reflectance peak at 600 nm shows that the highest reflectance occurs in the yellow/orange regions of the visible spectrum. The general trend is that the reflectance at this point decreases with the addition of chromium (III).

When the chromium content of the sample reaches 0.5 the reflectance peak at 600 nm begins to decrease further and completely flattens in the 0.8 sample. There is also a shift of the absorption edge towards lower wavelengths into the green and blue regions of the spectrum. This is caused by the increasing Cr_2O_3 impurity detected by X-ray diffraction.

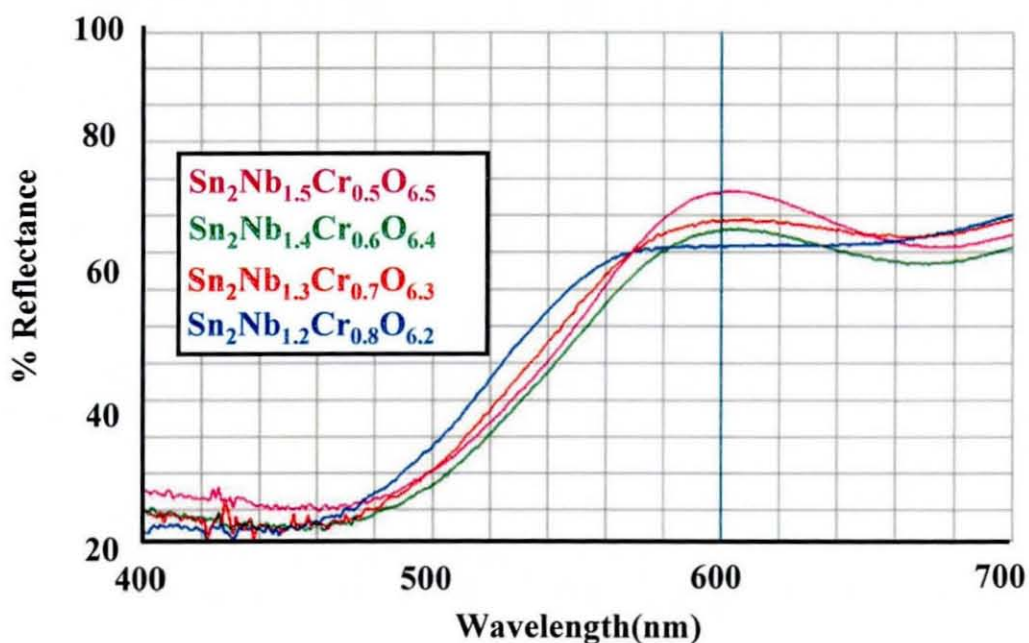


Figure 4.12: UV/VIS reflectance scans of $\text{Sn}_2\text{Nb}_{2-x}\text{Cr}_x\text{O}_{7-x}$ ($x = 0 - 0.4$)

Table 4.12: CIE Colour measurement results.

Composition	L*	a*	b*
$\text{Sn}_2\text{Nb}_2\text{O}_7$	91.28	13.74	54.76
$\text{Sn}_2\text{Nb}_{1.9}\text{Cr}_{0.1}\text{O}_{6.9}$	79.81	14.35	34.90
$\text{Sn}_2\text{Nb}_{1.8}\text{Cr}_{0.2}\text{O}_{6.8}$	78.97	13.58	30.65
$\text{Sn}_2\text{Nb}_{1.7}\text{Cr}_{0.3}\text{O}_{6.7}$	77.42	13.42	27.75
$\text{Sn}_2\text{Nb}_{1.6}\text{Cr}_{0.4}\text{O}_{6.6}$	78.66	14.15	34.08
$\text{Sn}_2\text{Nb}_{1.5}\text{Cr}_{0.5}\text{O}_{6.5}$	79.66	13.31	35.78
$\text{Sn}_2\text{Nb}_{1.4}\text{Cr}_{0.3}\text{O}_{6.4}$	77.76	12.05	36.89
$\text{Sn}_2\text{Nb}_{1.3}\text{Cr}_{0.2}\text{O}_{6.3}$	79.35	10.40	38.67
$\text{Sn}_2\text{Nb}_{1.2}\text{Cr}_{0.1}\text{O}_{6.2}$	79.49	6.00	37.53

Results from the UV/Vis reflectance data were analysed using a colour measurement program. The returned L^* , a^* and b^* values of each sample are shown in Table 4.12 and a graphical representation of the data is shown in Figure 4.13. There is a significant drop in the brightness of the sample (L^*) from the bright yellow un-doped sample ($\text{Sn}_2\text{Nb}_2\text{O}_7$) to the duller orange of the doped samples. After this initial decrease the L^* value remain relatively unchanged with extra chromium (III). The colour measurements show that the orange colouration of the doped samples is caused by a decrease in the b^* component of the colouration. The red/green a^* values remain unchanged suggesting that the sample colour is caused by a decrease in the ratio of yellow to red in the sample. This causes the red component of the colour to become the major factor and in turn darkens the orange colour of the sample. As the amount of chromium (III) reaches 0.5 and above the a^* value decreases rapidly towards the green. This agrees with the X-ray data and the UV/Vis data that show a major change in the composition and properties of the sample at this point caused by the presence of the Cr_2O_3 impurity.

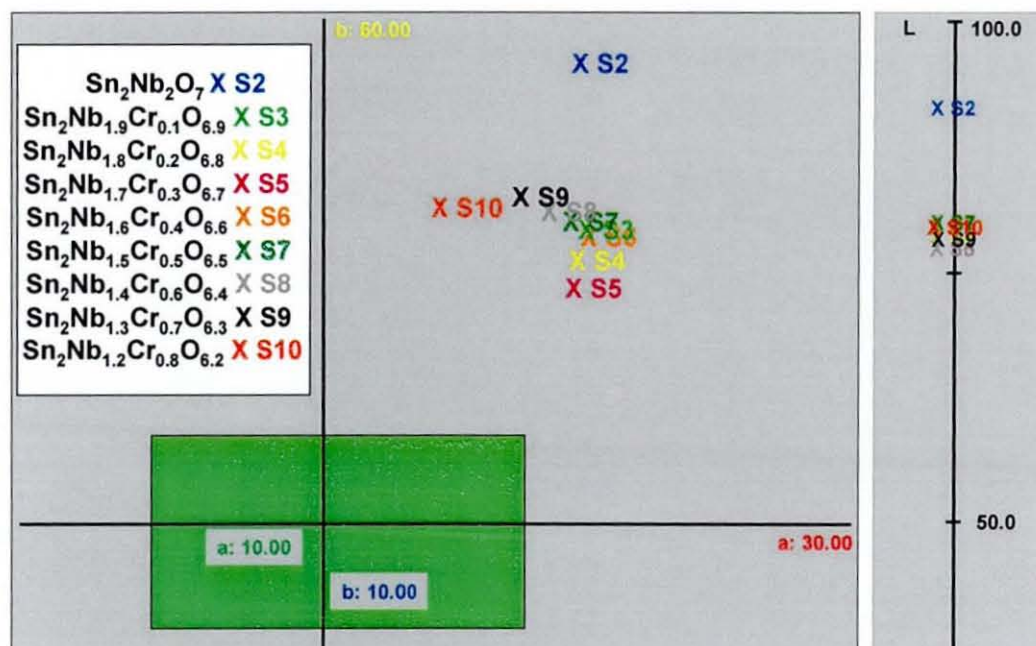


Figure 4.13: Visual representation of the colour measurement data. The x-axis is the a^* value positive is red negative is green and the y axis is the b^* value positive is yellow negative is blue. The right side shows the L^* value or the brightness of the sample.

4.10. Conclusions

The ability of the tin niobates to form oxysulfide pyrochlores is extremely rare and the formation of oxyselenide pyrochlores has not been reported previously. Although this kind of behaviour could be seen as unlikely, due to the size constraints of the anion sites, it is not unique. The other example of an oxysulfide pyrochlore is that of $\text{Cd}_2\text{Nb}_2\text{O}_6\text{S}$, which is discussed in the next chapter. This material can contain a whole sulfur anion in the formula unit, which implies that the 0.3 sulfides in tin niobates are also possible. The reason for the upper limit on the sulfide concentration could be due to the tin lone pair, the presence of which could inhibit the inclusion of too many larger anions.

The evidence for the formation of an oxysulfide pyrochlore, rather than the occurrence of another affect is reported in this chapter. The detection of new signals in the extended solid state NMR spectra is evidence of additional tin environments not detected in the pure oxide compounds. The anisotropy of both the original Sn^{2+} signal and the additional detected signal appear to be caused by the same distorted environment. The affects of the sulfide addition was also detected in the structural characterisation through neutron diffraction analysis.

The most important affect of the sulfide addition is the change in the colour of the tin niobium pyrochlore from yellow to dark red. This produces a series of stable orange/red pigments, which can be used as possible replacements to toxic heavy metal pigments such as cadmium sulfoselenides.

The doping of the niobium site with Cr^{3+} produces a series of orange polycrystalline powders. In this investigation the maximum dopant level before the Cr_2O_3 impurity appeared was 0.3, however this range could be extended with the use of a counter ion to reduce the non-stoichiometry. Although the addition of more Cr^{3+} may increase the colour properties, the method of colour production will still be based on *d-d* electronic transfer. This relatively weak transition may never match the intense red and orange of the oxychalcogenide phases.

4.11. References

- ¹ K. Fujiyoshi, H. Yokoyama, F. Ren, and S. Ishida, *J. Am. Ceram. Soc* **76** (1993) 981
- ² J. Pannetie, J. Lucas, *Mat. Res. Bull.* **5** 9 (1970) 797
- ³ D. Bernard, J. Pannetier, J. Y. Moisan, J. Lucas, *J. Solid State Chem.* **8** (1973) 31
- ⁴ R.S. Pavlov, V.B. Marzá J.B. Carda, *J. Mater. Chem.* **12** (2002) 2825
- ⁵ E. L- Navarrete, M. Ocana, *J. Eur. Ceram. Soc.*, **22** (2002) 353
- ⁶ R.S. Pavlov, V.B. Marzá, J.B. Carda, *J. Mater. Chem.*, **12** (2002) 2825
- ⁷ R.S. Pavlov, J.B. Carda, V.B. Marzá, J.M. Hohembergerger, *J. Am. Ceram. Soc.* **85** (2002) 1197
- ⁸ S. Sugano, Y. Tanabe and H. Kamimura, *Academic Press, New York*, (1970)
- ⁹ C. Cossement, J. Darville, J.-M. Gilles, J. B. Nagy, C. Fernandez, J.-P. Amoureux, *Magn. Reson. Chem.* **30** (1992) 263.
- ¹⁰ C. Mundus, G. Taillades, A. Pradel, and M. Ribes, *Solid State NMR* **7** (1996) 141.
- ¹¹ J. Miranday, G. Gauthier, R. DePape, C. R. *Acad. Sci., Ser. B* **273** (1971) 970.

Chapter 5
Synthesis and Characterisation of
Cadmium Niobate Pyrochlores

5.1 Introduction

The cadmium niobates are a group of divalent metal niobium oxides with the composition $\text{Cd}_2\text{Nb}_2\text{O}_6\text{X}$ ($\text{X} = \text{O}, \text{S}$)¹ that have been reported to crystallise with the cubic pyrochlore structure. These materials are particularly relevant to the work reported in this thesis on the tin niobate pyrochlores as they are the only other system known to form an oxysulfide pyrochlore. However, unlike the tin niobate materials there is no lone pair on the divalent cation and the phases formed are described as fully stoichiometric in their composition. The stoichiometry of the oxysulfide pyrochlore was determined as $\text{Cd}_2\text{Nb}_2\text{O}_6\text{S}$ showing that it is possible to insert much more sulfur in the pyrochlore structure than the 0.3 sulfur ions per unit cell described to the tin niobate oxysulfide phase. Although both the cadmium niobate oxide and oxysulfide phases have been studied previously, the authors concentrated on their electrical properties rather than their structural characterisation. Both the oxide and the oxysulfide show ferroelectric properties, which is unusual in pyrochlore type compounds as they are usually anti-ferroelectric. This kind of behaviour seems to be a peculiarity of the niobate pyrochlores generally as ferroelectric properties have also been seen in both the calcium and lead niobates.^{2, 3}

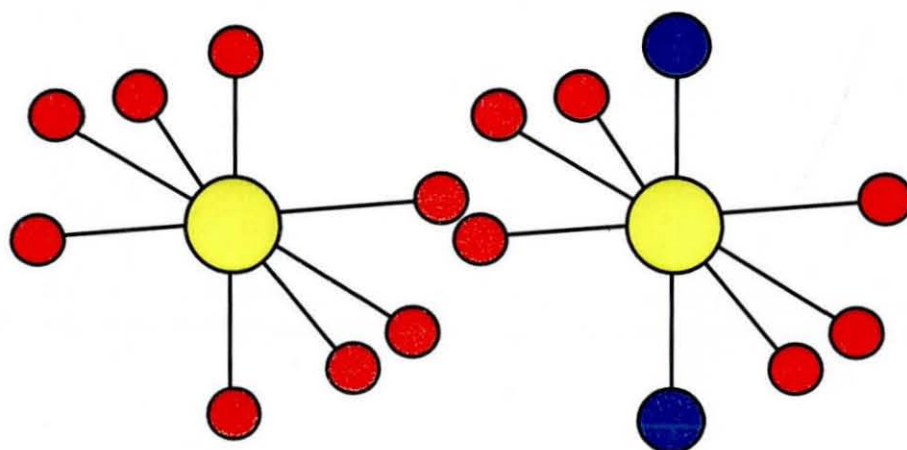


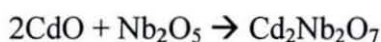
Figure 5.1: Cadmium geometry in the tin niobium oxide and oxysulfide phases.

Although both oxide and oxysulfide pyrochlore phases containing cadmium and niobium have been reported previously, very little data exists concerning the structure of these compounds. The known articles concerning the oxysulfide phases were published around the same time that the environmental issues

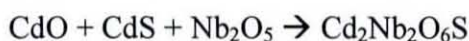
associated with cadmium compounds were first discovered. Unfortunately it appears that very little further research was carried out on these compounds, probably due to the deleterious effect of the new found toxicity of cadmium materials on their potential applications. Therefore there is no available literature to explain how the large sulfur anion was included in the structure or structural studies to compare with the structural data gleaned from the tin niobates oxysulfides phases. Despite the bright colouration of the simple cadmium sulfoselenides, these materials had no interest as potential pigments due to the lack of any notable colour properties of the pyrochlore oxysulfides. As the only other known sulfur containing pyrochlores however, they may result in a better understanding of the structural requirements in allowing the insertion of chalcogenides, and help in developing other such materials. This chapter studies the synthesis of cadmium niobium oxides and oxysulfides and their structural characterisation using X-ray and continuous wavelength neutron diffraction techniques. These results were compared with the tin niobium oxysulfides seen in the previous chapter to gain a better understanding of the stability of oxychalcogenide pyrochlores in general.

5.2 Experimental

The cadmium niobium oxide pyrochlore, general formula $\text{Cd}_2\text{Nb}_2\text{O}_7$, was formed by intimately grinding CdO and Nb_2O_5 in a 2:1 molar ratio. Samples were then fired in an alumina crucible at $500\text{ }^\circ\text{C}$ for 10 h to initiate the reaction. The product was then reground and heated at $1100\text{ }^\circ\text{C}$ for 24 h to complete the synthesis.



The oxysulfide sample was synthesised by mixing CdO , CdS and Nb_2O_5 in equal molar proportions. The mixture was sealed in an evacuated quartz tube to prevent the oxidation of cadmium sulfide and then heated to $1100\text{ }^\circ\text{C}$ at $3\text{ }^\circ\text{C min}^{-1}$. This temperature was maintained for 24 h.



5.3 X-ray Diffraction

Samples were initially studied using X-ray diffraction analysis on a Bruker D8 diffractometer in order to assess the phase purity and compare cell sizes. X-ray diffraction patterns collected for $\text{Cd}_2\text{Nb}_2\text{O}_7$ and $\text{Cd}_2\text{Nb}_2\text{O}_6\text{S}$, both showed primary phases which could be attributed to a cubic pyrochlore structure (space group $\text{Fd-}3\text{m}$). Phase analysis of the cadmium niobium oxide compound by X-ray diffraction shows that there is a significant amount of CdNb_2O_6 impurity as a secondary phase (Figure 5.2). The same CdNb_2O_6 impurity is also present in the cadmium niobium oxysulfides but to a much lesser extent than in the oxide. The fact that both phases have the same impurity suggested that there was a loss of cadmium oxide during the synthesis as this is the only cadmium reactant common to both materials.

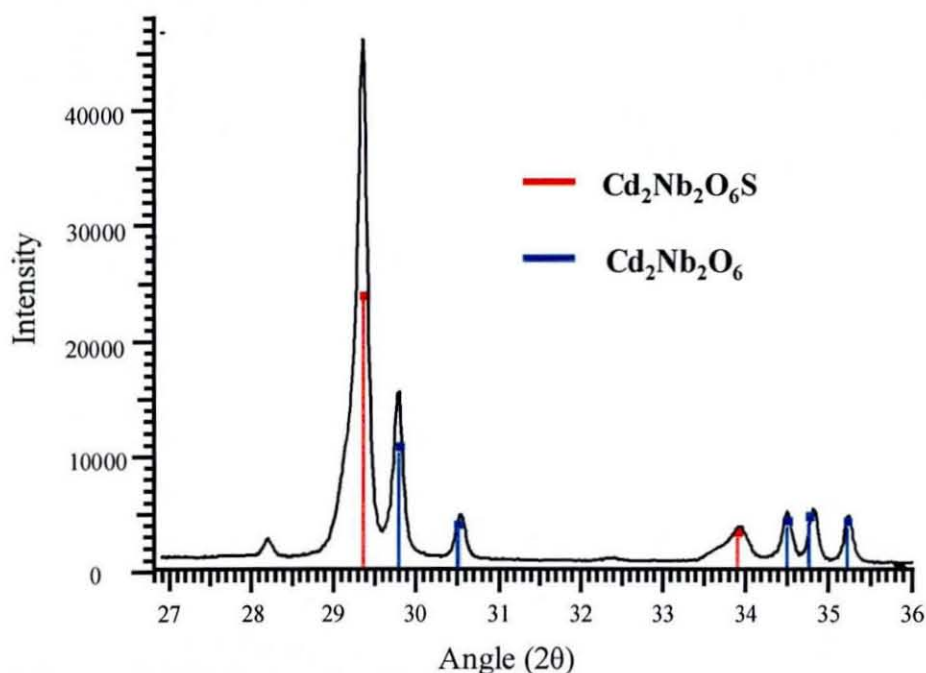


Figure 5.2: X-ray diffraction pattern of $\text{Cd}_2\text{Nb}_2\text{O}_7$ with CdNb_2O_6 impurity.

Previous authors⁴ working on cadmium containing sealed tube reactions have reported the formation of amorphous cadmium silicate during the process. Although crystalline cadmium silicate was not observed in the diffraction patterns of the cadmium niobate pyrochlores, amorphous material would not be immediately obvious with the possible exception of an increased background. However, it was apparent from the appearance of the sealed tubes that some reaction had occurred with the surface of the sample ampoule. In order to

minimise reaction of the cadmium oxide with the reaction vessel, the quartz tubes were coated with graphite by the pyrolysis of acetone using a oxy-methane torch prior to sample filling. Inspection of the fired tubes revealed that this reaction was still occurring and was a likely source for the loss of cadmium oxide. In a similar methodology used to the production of nitrides,⁵ the reactants were now sealed in inert tubes prior to insertion into the sample sealed tubes (Figure 5.3). Gold tubing was found to be suitably unreactive to the reaction constituents and was used for the reactions.

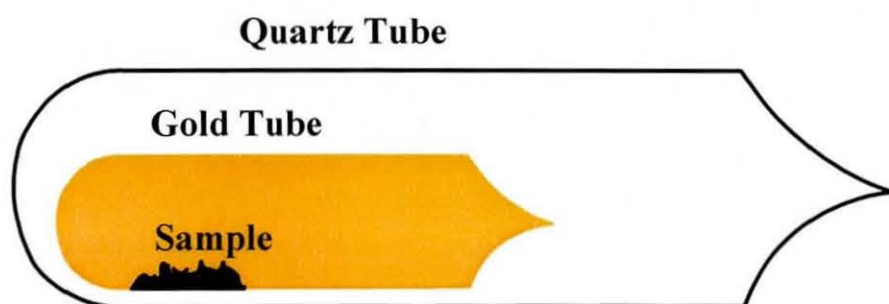


Figure 5.3: Schematic of the sealed sample tubes used in the synthesis of $\text{Cd}_2\text{Nb}_2\text{O}_7$ and $\text{Cd}_2\text{Nb}_2\text{O}_6\text{S}$

5.4 Neutron Diffraction

Previous experience in the structural characterisation of the tin niobate phases suggested that the positional determination of the anion sublattice would be impossible using powder X-ray diffraction alone. Unfortunately, naturally occurring cadmium contains $\sim 12\%$ ^{113}Cd , which has an extremely high absorption cross section (20600 barns), hence why cadmium is often used as a shield on vanadium cans. The use of normal cadmium reactants would therefore not allow data of suitable quality to be collected and necessitated the use of isotopically enriched reactants. The samples were therefore synthesised using pure 114-cadmium oxide in order to avoid the strongly absorbing cadmium isotope and collect good quality neutron diffraction data. This particular isotope was chosen due to the combination of its low absorption cross section and high scattering length. Unfortunately, due to the vast expense of the isotopically pure material, it was only possible to carry out the reaction for each sample once and

the samples produced were not as pure as materials produced from the naturally abundant material available in the laboratory.

Primary structural analysis of the oxide and oxysulfide pyrochlores was carried out using constant wavelength neutron diffraction data. Samples of $\text{Cd}_2\text{Nb}_2\text{O}_7$ and $\text{Cd}_2\text{Nb}_2\text{O}_6\text{S}$ were analysed on the D20 instrument at the ILL using a data range of $10\text{-}150^\circ$ over 10 h and a neutron wavelength of 1.3032 \AA . A sample with the general formula $\text{Cd}_2\text{Nb}_2\text{O}_{6.5}\text{S}_{0.5}$ was also synthesised in order to verify the existence of an intermediate composition that was closer to that of the tin niobate oxysulfides. The Rietveld refinement of the collected data was performed using the GSAS⁶ suite of programs using a combination of an ideal pyrochlore structure, and the distorted pyrochlore structure developed for other systems.

5.5 Results

5.5.1 X-ray Diffraction

Initial X-ray diffraction data of the cadmium niobium oxide ($\text{Cd}_2\text{Nb}_2\text{O}_7$) and oxysulfide ($\text{Cd}_2\text{Nb}_2\text{O}_6\text{S}$) showed that the use of gold tube as a reactant vessel greatly increase the purity of the final phase. Figure 5.4 shows the X-ray diffraction patterns of $\text{Cd}_2\text{Nb}_2\text{O}_6\text{S}$ synthesised via both the sealed quartz tube method and the gold tube method detailed above. A $\text{Cd}_2\text{Nb}_2\text{O}_7$ is also displayed here for comparison of cell size with the other phases. The diffraction patterns show that the SnNb_2O_6 impurity, detailed previously, is present in significantly high concentrations in the quartz tube samples. This is due to the loss of cadmium from the sample in the form of cadmium silicate as the starting materials react with the quartz. The gold tube sample, though not single phase, shows a significant reduction in this impurity allowing for an easier structural characterisation of this phase.

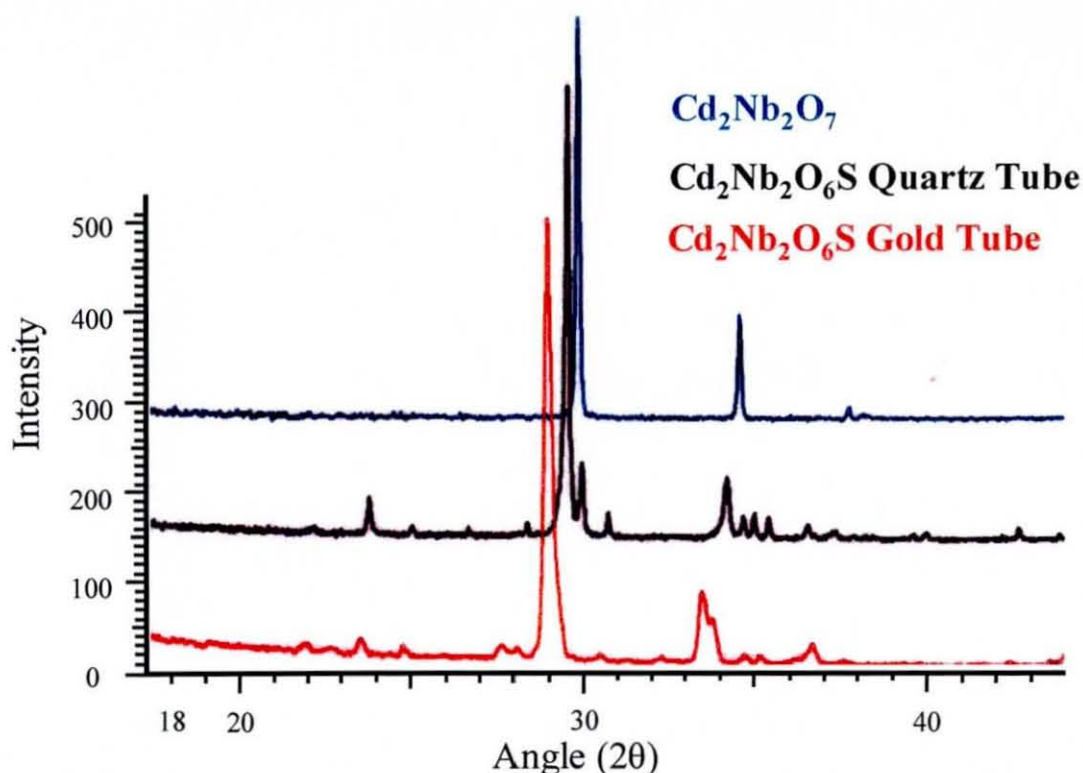


Figure 5.4: X-ray diffraction pattern of $\text{Cd}_2\text{Nb}_2\text{O}_7$, $\text{Cd}_2\text{Nb}_2\text{O}_6\text{S}$ synthesised in quartz tubes and $\text{Cd}_2\text{Nb}_2\text{O}_6\text{S}$ in gold tubes.

Closer analysis of the diffraction patterns in Figure 5.4 shows a change in cell dimensions across all three samples. The increase in cell size between the oxide and oxysulfide samples is expected due to the insertion of the larger sulfide anion into the structure. The increase in cell in this case, is much larger than in the tin niobium oxysulfides discussed in previous chapters. This is due to the greater amount of allowed sulfur included in the cadmium niobium pyrochlores and also related to the non-stoichiometric effects in the tin niobium compounds. Interestingly there appears to be a significant difference between the oxysulfides formed in the two different synthesis methods. This is evidence that these compounds also form pyrochlore phases with less than one sulfur atom per formula unit ($\text{Cd}_2\text{Nb}_2\text{O}_{7-x}\text{S}_x$; $x < 1$). It also shows that the reaction of CdS with the quartz tube appears to be greater than CdO creating a sulfur deficient phase as well as cadmium deficient.

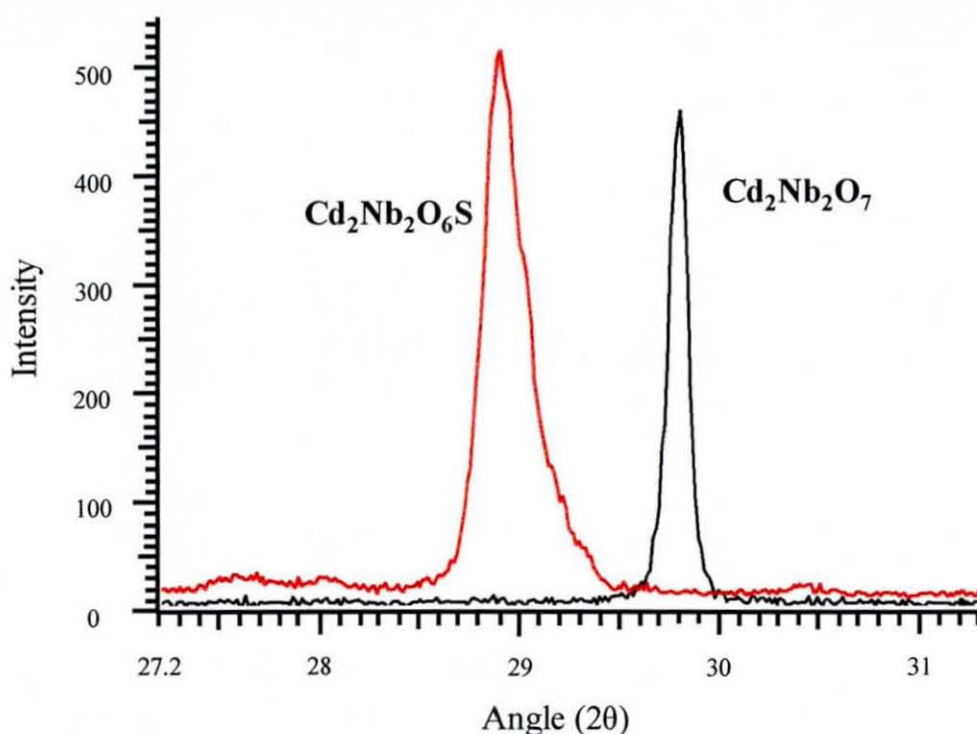


Figure 5.5: Comparison of $\text{Cd}_2\text{Nb}_2\text{O}_7$ and $\text{Cd}_2\text{Nb}_2\text{O}_6\text{S}$ reflection widths

Figure 5.5 shows a comparison between the 222 reflection of $\text{Cd}_2\text{Nb}_2\text{O}_7$ and $\text{Cd}_2\text{Nb}_2\text{O}_6\text{S}$ from the X-ray diffraction patterns of the two materials. The major differences between the two patterns are the change in diffraction angle and the increase in the overall peak width. Analysis of the reflection locations indicates that $\text{Cd}_2\text{Nb}_2\text{O}_7$ has a cell parameter of $\sim 10.3 \text{ \AA}$ and $\text{Cd}_2\text{Nb}_2\text{O}_6\text{S}$ has a parameter of $\sim 10.6 \text{ \AA}$. Comparing the oxysulfide X-ray pattern (Figure 5.4) to the oxide patterns shows that the sulfide sample has a much larger peak width than the sharp peaks of the oxide. The peak width can be influenced by a number of factors the major ones being crystallinity (cf. Debye-Scherrer equation) and structure. Generally sulfides give a wider peak shape than oxides because of a reduction in crystallinity due to their less ionic nature. In oxysulfide pyrochlores however the large peak width may indicate internal structural distortions such as large temperature factors or the static displacements seen previously in the tin niobates. In this case the peak shape of the oxysulfide compound is anisotropic when compared to the pure oxide reflections. This again indicates the existence of internal distortions within the structure which are seen in the oxysulfides and not in the oxide compounds.

5.5.2 Structural Characterisation

Even with the controlled synthesis conditions used in the formation of the ^{114}Cd enriched samples, the formed phases were still not pure pyrochlore materials. Analysis showed that there was a significant CdNb_2O_6 impurity in the oxide, and the oxysulfide phases, indicating a cadmium deficiency in the composition. It is likely that if the gold tubes were not completely sealed that some of the cadmium oxide would be able to sublime at high temperature. It would then pass out of the gold tube into the outer tube where it would be allowed to react with the silica in the quartz tubes once more. As several of the CdNb_2O_6 reflections were located at similar angles to those of the pyrochlore phase under study, the influence of the impurity could not be totally removed from the refinement and undoubtedly affected the quality of the results achieved.

Despite the impurities in the phase the refinement of the cadmium niobate phases was carried out on the neutron diffraction data. Final reliability factors for the refinement of the neutron diffraction data were calculated as $wR_p = 10.4\%$ and $R_p = 6.23\%$. Both of these results are very high for neutron diffraction data indicating a problem with the refinement. The calculated cell parameter for the oxide pyrochlore was found to be 9.985 \AA , which is much lower than both the values calculated from the X-ray diffraction and by previous authors.¹ Table 5.1 shows the refined atomic parameters for the neutron diffraction data.

Table 5.1: Refined atomic parameters from the neutron diffraction data of $\text{Cd}_2\text{Nb}_2\text{O}_7$; esd's are shown in parenthesis

Atom	Site	x	Y	Z	Occu	$U_{\text{iso}} \times 100$
Cd^{2+}	16c	0	0	0	1.000	0.446(64)
Nb^{5+}	16d	$\frac{1}{2}$	$\frac{1}{2}$	$\frac{1}{2}$	1.000	0.860(52)
O	48f	0.4312(2)	$\frac{1}{8}$	$\frac{1}{8}$	1.000	0.955(42)
O'	8a	$\frac{1}{8}$	$\frac{1}{8}$	$\frac{1}{8}$	1.000	0.807(99)

$$a = 9.9516(2) \text{ \AA}, wRp = 0.104 \text{ and } Rp = 0.062$$

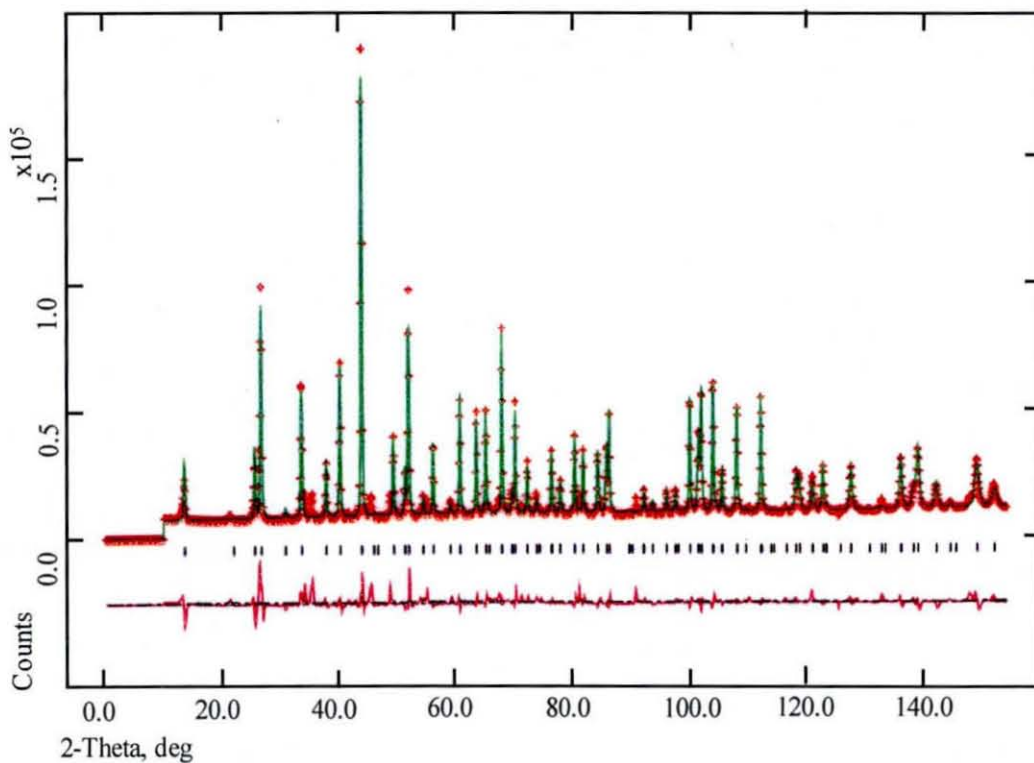


Figure 5.6: Refinement Neutron diffraction pattern for $\text{Cd}_2\text{Nb}_2\text{O}_7$; red crosses are the observed data, green line is the calculated profile and the purple line is the difference

The oxide phase was refined as a standard pyrochlore structure with all of the sites fully occupied. The diffraction pattern in Figure 5.6 shows the resulting neutron pattern from the above refinement. The fit to the data is good apart from a slight CdNb_2O_6 impurity that cannot be fitted. The cell size however is much too small for a stable pyrochlore, especially considering the ionic radii of Cd^{2+} (0.97 Å) compared with Sn^{2+} (0.69 Å). The tin niobates seen in previous chapters have a cell parameter ~ 10.5 Å, which is much larger than the calculated cell parameter from the refinement. Even with the stereoactive lone pair of the Sn^{2+} centre it would be expected that the cell parameter of the cadmium niobates would be much closer to this cell parameter.

The refinement of the oxysulfide phases had similar problems with much higher R -factors than the oxide pyrochlores. The refined cell parameters were again much smaller than expected at ~ 10.2 Å as opposed to those calculated from the X-ray diffraction data ~ 10.6 Å. Since both the oxide and the oxysulfide samples gave cell parameter 0.5 Å less than expected it was decided that there was a problem with both sets of diffraction data. The oxysulfide phases also suffered from a larger CdNb_2O_6 impurity than the oxide phase. This was probably due to the higher reactivity of CdS to the silicate tubes producing a cadmium deficiency in the resulting phase. Unfortunately due to expense of the isotopically enriched samples only very small sample size could be synthesised. The occurrence of even very small amounts of CdNb_2O_6 would result in a high phase concentration that obscured the pyrochlore reflections. Also due to the extremely small sample size no other analysis could be carried out without risking the loss of a significant proportion of the sample.

5.5.2.1 $\text{Cd}_2\text{Nb}_2\text{O}_7$

Due to the problems associated with the collected neutron diffraction data the refinement of the cadmium niobates was re-attempted with X-ray diffraction data. Unlike the tin niobates seen in previous chapters the cadmium cation does not possess a lone pair and is therefore not subject to the distortions seen for the tin niobate pyrochlores. This allows for the use of a standard pyrochlore structure as an initial refinement model. Also as cadmium does not undergo a

disproportionation reaction as seen in the tin compounds there was no indication that these phases were non-stoichiometric. These conclusions have been confirmed by the work of previous authors.⁷ Table 5.2 shows the refined atomic parameters from the X-ray diffraction refinement. Cd^{2+} has been placed on the 16c site (0,0,0), Nb is on the 16d site ($\frac{1}{2}, \frac{1}{2}, \frac{1}{2}$), and the two oxide sites are 48f ($x, \frac{1}{8}, \frac{1}{8}$) and 8a ($\frac{1}{8}, \frac{1}{8}, \frac{1}{8}$). The cell parameter has been calculated to be 10.4248(1) Å, which is much larger than the result from the neutron diffraction refinement and closer to previously reported cell lengths.

Table 5.2: Refined atomic parameters for $\text{Cd}_2\text{Nb}_2\text{O}_7$, esd's are shown in parentheses

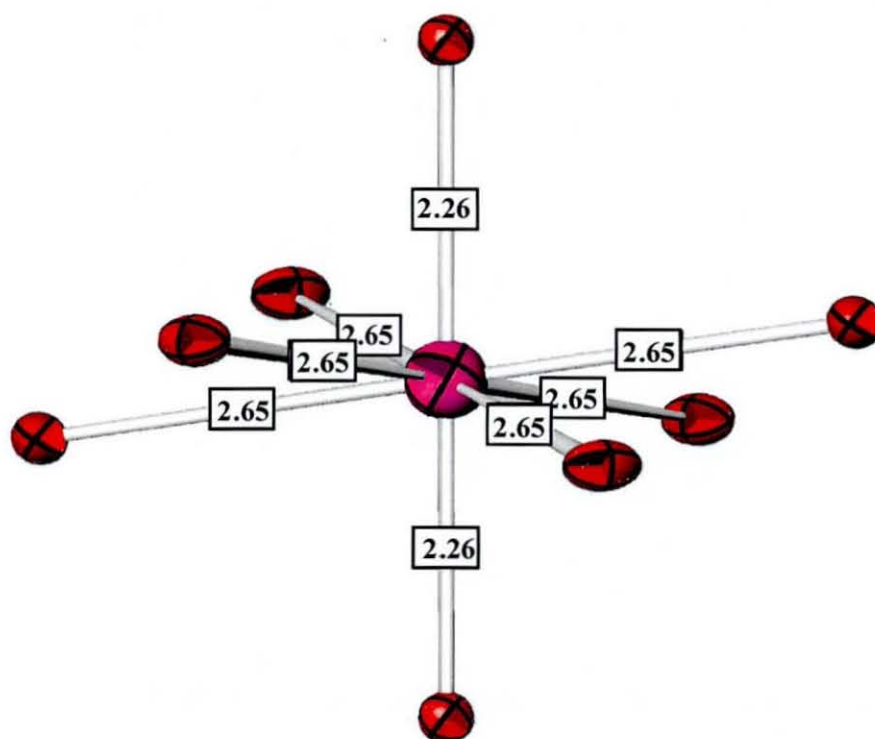
Atom	Site	x	Y	z	Occu	$U_{\text{iso}} \times 100$
Cd^{2+}	16c	0	0	0	1.000	2.96(14)
Nb^{5+}	16d	$\frac{1}{2}$	$\frac{1}{2}$	$\frac{1}{2}$	1.000	2.34(14)
O	48f	0.4312(2)	$\frac{1}{8}$	$\frac{1}{8}$	1.000	1.37(37)
O'	8a	$\frac{1}{8}$	$\frac{1}{8}$	$\frac{1}{8}$	1.000	1.25(59)

The calculated bond lengths and angles are shown in Table 5.3 along with the estimated standard deviations. The ideal pyrochlore model used here differs from the lone pair distorted models seen previously. The bond lengths for cadmium niobium oxide are comparable to the tin based pyrochlore bond lengths reported in Chapter 3. The main difference is in the bond angles of the divalent metal centre, which indicate a much more symmetrical structure (Figure 5.7). The $\text{O}'\text{-Cd-O}'$ bond angle is calculated as exactly 180° , which is indicative of the centro-symmetry of the A cation site. In the tin niobates this angle was distorted by the tin lone pair and approached 160° as the A cation was pushed of the centrosymmetric position by the pair electron density.

Table 5.3: Selected bond lengths for niobium and divalent cadmium centres.

Esd.'s are shown in parenthesis

Bond	Bond Length (Å)/Angle (°)
Nb ⁵⁺ -O	1.9735(20)
Sn ²⁺ -O	2.647(4)
Sn ²⁺ -O'	2.25705(1)
O-Nb-O	92.09(22)
O-Nb-O	87.91(22)
O-Cd-O	109.471(1)
O'-Cd-O'	180.000(0)

**Figure 5.7:** Cadmium environment in Cd₂Nb₂O₇. Purple sphere = Cd²⁺ centre, red sphere = O²⁻ anions

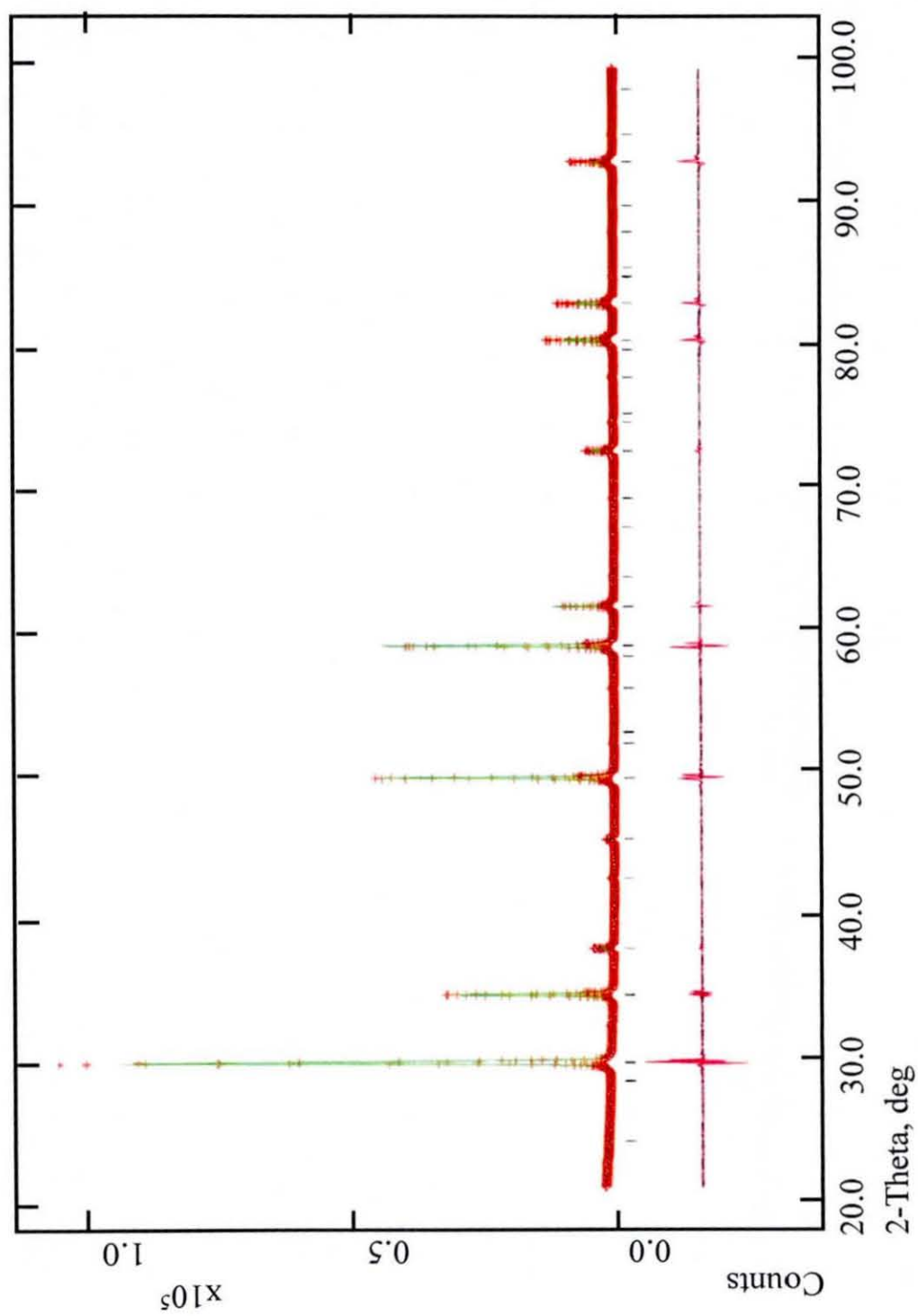


Figure 5.8: Refinement Neutron diffraction pattern for Cd₂Nb₂O₇; red crosses are the observed data, green line is the calculated profile and the purple line is the difference.

5.5.2.2 $Cd_2Nb_2O_6S$

The cadmium niobium oxide pyrochlore discussed previously has been shown to have a normal stoichiometric pyrochlore structure with none of the disorder seen in previous chapters. In the case of the oxysulfide pyrochlores, however, it is difficult to see how the sulfur anion can be inserted into a normal pyrochlore structure. It was felt that the creation of an oxysulfide phase would create internal distortions similar to those seen in lone pair pyrochlores. An indication of deviation from the ideal pyrochlore structure is the presence of the 442 reflection in the diffraction pattern. The 442 reflection only appears in pyrochlore structures that use non-standard low symmetry sites, and/or have large anisotropic thermal parameters.

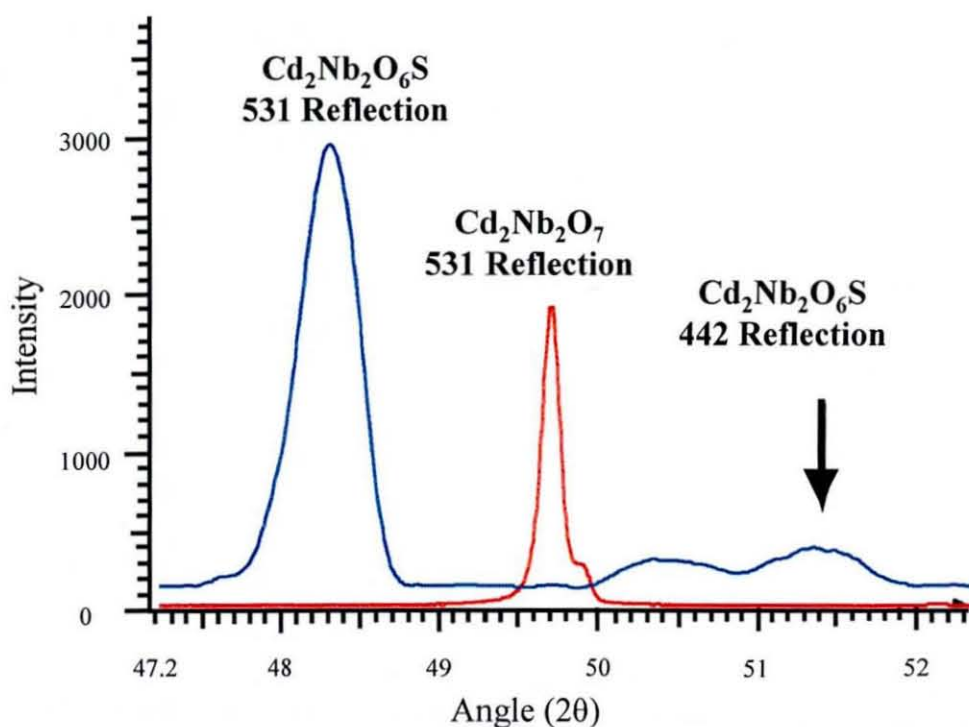


Figure 5.9: X-ray diffraction pattern showing 442 reflection of $Cd_2Nb_2O_6S$

Figure 5.9 shows a comparison of the diffraction patterns of the oxide and oxysulfide cadmium niobium pyrochlores. The 531 reflections of $Cd_2Nb_2O_6S$ and $Cd_2Nb_2O_7$ are displayed here and are present for all pyrochlore structures. For a unit cell of 10.67 Å as calculated from x-ray diffraction data, the diffraction angle of the 442 reflection can be calculated from:

$$\sin^2 \theta = \frac{\lambda^2}{4a^2} (h^2 + k^2 + l^2)$$

$$\sin^2 \theta = \frac{(1.5406)^2}{4(10.67)^2} (4^2 + 2^2 + 2^2) \quad [\text{Equation 5.1}]$$

$$2\theta = 51.0956$$

Figure 5.9 shows that there is a small peak in this region that is not present in the pure oxide phase. It is difficult to tell decisively whether this reflection is from the pyrochlore or a small impurity phase. The fact that a peak is present where predicted, coupled with the large peak width of the oxysulfide phase, are good indication that this phase has similar distortion to those found in the tin niobium oxysulfide. The lack of any 442 peak in the oxide pattern between 55 and 60° 2θ also confirms that the pure oxide compounds are based on the ideal pyrochlore structure and not a distorted model.

As for the cadmium niobium oxide phases the oxysulfide neutron data was too poor to allow a satisfactory refinement. Unfortunately unlike the oxide there were no high quality X-ray diffraction data collected to allow the structural refinement of this phase. Figure 5.10 shows an X-ray diffraction of the purest oxysulfide phase prepared by these methods. There is, however, still a small amount of impurity which can be seen in the uneven background and the shoulders on some of the main pyrochlore reflections.

Initial refinement results from the neutron diffraction data indicated that both the cadmium and sulfur anion displayed distortions on their sites. This may indicate that the cadmium niobium oxysulfides shows the same static displacements seen in the tin niobates and tin niobium oxysulfides. In the case of the tin niobates the Sn²⁺ site becomes statically displaced onto a 96*h* site, as the ideal 16*c* was not large enough for both the cation and the lone pair electrons. In the case of cadmium however, there are no lone pairs, indicating that the distortions originate from an alternative cause. In this case it could be hypothesised that, in the same way, the sulfide anion is too large for the ideal O' anion site. This would require that the sulfide is displaced onto another site to allow the

inclusion of the larger anion into the structure. This could cause the subsequent displacement of the cadmium cation in the reverse process of that seen in the tin niobates.

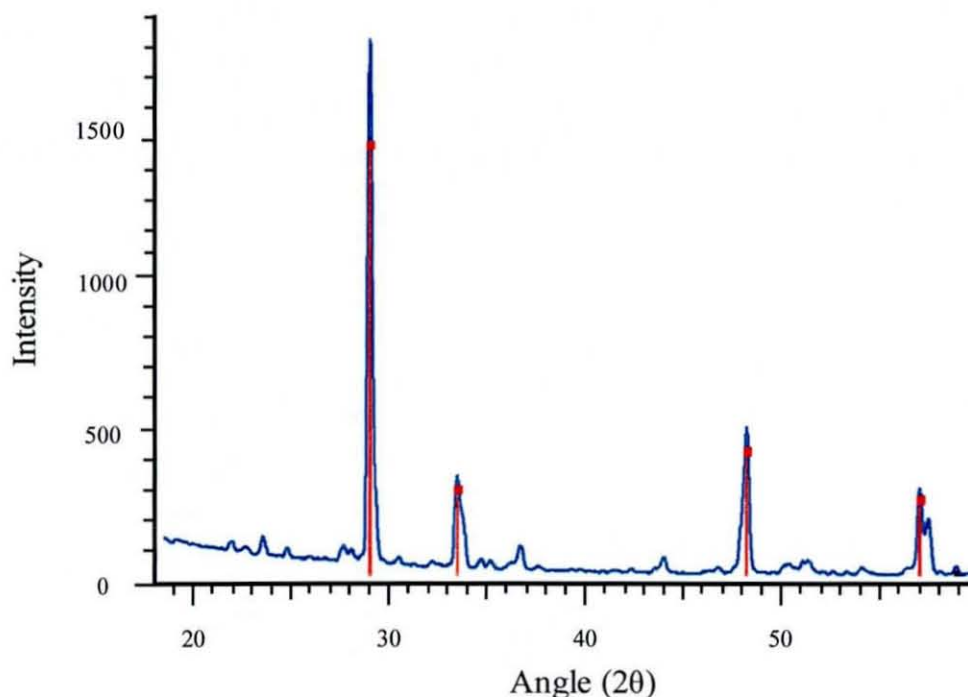


Figure 5.10: X-ray diffraction pattern of $\text{Cd}_2\text{Nb}_2\text{O}_6\text{S}$. The red lines indicate the main pyrochlore reflections

5.6 Conclusions

The formation of a cadmium niobium oxysulfide pyrochlore has been studied using X-ray diffraction techniques. The increase in cell size between the oxide and the oxysulfide phases is a result of the larger sulfide anion being included within the structure. The lack of any sulfur containing impurities in the final diffraction patterns is evidence of cadmium sulfide reacting to form the primary phase. As the only other known oxysulfide pyrochlore the confirmed formation of this compound is important in understanding the mechanism for sulfur inclusion in these materials. The fact that both of these pyrochlores are niobate based is unlikely to be coincidental, however the reason for this is not understood.

Unfortunately the formation of these compounds is complicated by the high reactivity and low sublimation temperature of the cadmium reactants. Isotopically enriched samples were used for neutron diffraction analysis, however, the difficult synthesis and the lack of available reactants made the formation of a pure phase very difficult. The formation of a pure oxysulfide phase was not completed, which made the refinement of the structure impossible. It was determined, using X-ray diffraction, that the cadmium niobium oxide compounds has an ideal pyrochlore structure. It was also determined that the oxysulfide phases had similar distortions to the lone pair pyrochlores reported previously. In other reported cases the pyrochlore distortions were caused by the activity of the *A* cation, either through a lone pair or atypical composition. $\text{Cd}_2\text{Nb}_2\text{O}_6\text{S}$ could be the first example of behavior of this type being induced by anion activity instead.

5.7 References

-
- ¹ D. Bernard, J. Pannetier, J. Y. Moisan, J. Lucas, *J. Solid State Chem.* **8** (1973) 31
 - ² L.P. Cruz, J. -M. Savariault, J. -C. Jumas, J. D. Pedrosa de Jesus, *J. Solid State Chem.* **159** (2001) 349
 - ³ L. P.Cruz, J. -M. Savariault, J. -C. Jumas, J. D. Pedrosa de Jesus, *J. Solid State Chem.* **177** (2004) 1549
 - ⁴ S. E. Dann and M. T. Weller, *Inorganic Chemistry*, **35** (1996) 555
 - ⁵ J. L. Hunting, M. M. Szymanski, P. E. Johnson, C. B. Kellar and F. J. DiSalvo, *J. Solid State Chem.* **180** (2007) 31
 - ⁶ A. C. Larson, R. von Dreele, GSAS 'Generalised Structure Analysis System'; 1986 MS805 LANSCE.
 - ⁷ K. Lukaszewicz, A. Pietraszko, Yu Stepen'-Damm, N. N. Kolpakova, *Mat. Res. Bul.* **29** (1994) 987

Chapter 6
Rare-Earth Bismuth Oxides
 $(\text{Bi}_{1-x}\text{Ln}_x)_2\text{O}_3$

6.1. Introduction

A large amount of research has been concentrated on the polymorphism of bismuth sesquioxide^{1,2,3,4,5,6} and the electrical properties that the various forms exhibit. Of particular interest is the cubic δ -phase, which has been found to exhibit a remarkably high oxide ion conductivity,^{7,8} resulting from the high number of anion vacancies in the defect fluorite type structure. The high oxide conductivity exhibited by this structure could make the bismuth oxide materials ideal candidates for devices such as oxygen pumps, oxygen gauges and as an electrolyte in solid oxide fuel cells.⁹ Unfortunately it has been found that the δ - Bi_2O_3 structure is metastable under ambient conditions and converts to the α - or β -form below 750°C ,^{3,7,10} effectively making it unsuitable for low temperature applications.¹¹

Numerous studies have been performed replacing the bismuth with a number of metal ions in order to maintain the defect fluorite type structure at room temperature. In particular this has been achieved by the partial substitution of the Bi^{3+} with Y^{3+} or trivalent lanthanides (Ln^{3+}).^{12,13,14,15,16,17} These phase-equilibrium studies have been carried out with the hope of reproducing this anion conductivity at low temperature. This has led to the discovery and formation of several stable phases depending on the amount and type of rare-earth substitution and the reaction conditions utilised. The face centred cubic structure of the δ - Bi_2O_3 type phase occurs for the Bi_2O_3 - Ln_2O_3 over a range of around 15-50 mole% Ln_2O_3 ($\text{Ln} = \text{Y}, \text{La-Er}$),⁹ and shows the same high anion conductance of the pure bismuth compound.¹² It seems however that the δ -phase cannot be stabilised at room temperature as these reported structures have also been found to be metastable at room temperatures.^{18,19,20,21} The fcc δ -phase slowly changes to a stable form below 750°C of which there are three reported structures known:

- Solid solutions of Bi_2O_3 - Ln_2O_3 with around 22.5 mol% Ln_2O_3 ($\text{Ln} = \text{Y}, \text{La-Er}$) form a hexagonal phase in the space group R-3m with $a \approx 4 \text{ \AA}$ and $c \approx 24 \text{ \AA}$. This phase shows a fair anion conductance, though not as high as the δ - Bi_2O_3 structure, again due to the presence of anionic vacancies within the cell.

- Rare-earth rich solid solutions with 48.5 mol% Ln_2O_3 ($\text{Ln} = \text{Dy-Er}$ and Y) and above form a stable structure with a tetragonal unit cell, space group $I4mmm$.
- Phases containing lanthanides to the right of the row (Sm , Eu , Gd , Tb and Dy) show a C-type rare-earth structure around 35 mol% Ln_2O_3 . The C-type structure has a $I2_13$ space group with $a \approx 11 \text{ \AA}$, and is closely related to the δ -phase as it has eight fluorite type sub-shells in a 2×2 arrangement.

The compositional ranges of these three structures are largely dependent on the type of rare-earth in the structure. Samples with compositions outside of these ideal ranges tend to be multiphase and contain mixtures of the above phases and/or Bi_2O_3 and Ln_2O_3 impurities.

Although the majority of articles regarding these compounds are based on their ion conduction properties, there have been groups studying the pigment properties of these phases. $(\text{Bi,R})_2\text{O}_3$ ($\text{R} = \text{Nd}$, Sm , Dy , Ce and Y) have been studied as environmentally friendly orange pigments for use in high temperature applications ($\text{Bi}_{1.2}\text{Sm}_{0.8}\text{O}_3$; $L^*a^*b^* = 71.21, 16.30, 43.98$).²² Although a range of rare-earth elements have been studied, no single article covers the whole range of rare-earth elements and dopant levels. This section reports a complete study of $(\text{Bi,R})_2\text{O}_3$ ($\text{R} = \text{Y}$, La , Nd , Pr , Sm , Gd , Dy , Er), for their pigment properties, and the structural characterisation of the δ -phase, with valence calculation, in order to further understand the metastability of this phase. Also reported here is a high temperature study of Bi_2O_3 using X-ray diffraction for a direct study of the metastable polymorphs.

6.2. Experimental

Samples of the composition $(\text{Bi}_{1-x}\text{R}_x)_2\text{O}_3$ ($\text{R} = \text{Y}$, La , Nd , Pr , Sm , Gd , Dy , Er $x = 0.1 - 0.9$) were synthesised via solid state synthesis. Bismuth (III) oxide stoichiometric amounts using an agate pestle and mortar, homogeneous mixing was achieved by wet grinding using acetone. Samples were dried and then

calcined in an alumina reaction boat in an electrical box furnace. Samples were initially heated to 700 °C for 2 h to initialise the reaction and then the temperature was raised to 1000 °C for 6 h to complete the calcination procedure.

6.3. X-ray Diffraction

Samples were analysed by powder X-ray diffraction on the Bruker 08 diffractometer to assess sample purity and characterisation of crystal structure. Single-phase compounds were characterised using the Rietveld refinement of X-ray diffraction patterns over a 10-100° 2 θ range with a step size of 0.0145° and a step time of 3 s. A sample of pure bismuth oxide was placed in the HTK1200 heating stage of the X-ray diffractometer and was heated in stages of 100 °C to 1100 °C and then slow cooled. Data were collected at 100 °C intervals on heating and 10 °C on cooling in order to investigate the appearance and disappearance of phases as a function of temperature.

6.4. UV/Visible Colour Measurements

The colour of all powdered samples was assessed on a Perkin Elmer Lambda 35 UV/VIS spectrometer fitted with a colour integration sphere. The resulting spectra were then processed using the Colour Methods for UV Winlab V3 software for the production of quantifiable colour measurement results.

6.5. Results – X-ray Diffraction

The solid state reactions resulted in a series of Ln₂O₃-Bi₂O₃ solid solutions, each of which gave a range of coloured polycrystalline powders. The nine solid solutions studied could be separated into two distinct groups, which had different resulting properties and structures. Each Ln metal in the group were related by their ionic radii, so Y, Er, Dy, Gd, Sm (0.881 - 0.964 Å) were in the first group and Nd, Pr, La (0.995 - 1.061 Å) were in the second. Lanthanides with ionic radii in the middle of this range, namely Sm and Nd, displayed properties relating to both of the groups. The first group (Ln = Y, Er, Dy, Gd, Sm) tended to form yellow to light orange powders depending on the relative proportions of Ln and Bi. These elements also formed the most stable δ -phase, as they temporarily maintained the defect fluorite structure at room temperature, probably due to the

size difference between the ionic radii (0.9 - 0.96 Å) of this lanthanide range and the ionic radii of Bi^{3+} (1.03 Å). The second group containing the larger lanthanide elements ($\text{Ln} = \text{La, Pr, Nd}$) tended to form polycrystalline powders with colours more closely related to the rare-earth element. In the case of these materials, the stability of the δ -phase at room temperature was greatly reduced due to similarity in size of the ionic radii (0.995-1.061 Å)

6.5.1. $\text{Ln}_2\text{O}_3\text{-Bi}_2\text{O}_3$ ($\text{Ln} = \text{Y, Er, Ho, Dy, Gd}$) Solid Solutions

The solid solutions containing rare-earths with ionic radii less than 0.95 Å all follow the same basic trend. Figures 6.1 and 6.2 show the recorded X-ray diffraction data for samples containing dysprosium as an example of the structural characteristics of this group of solid solutions. Figure 6.1 shows the X-ray diffraction patterns for samples of $(\text{Bi}_{1-x}\text{Dy}_x)\text{O}_3$ where $x = 0.1-0.4$ (mol% 10-40). Comparison with the JCPDS²³ database shows this to be the defect fluorite $\delta\text{-Bi}_2\text{O}_3$ structure, which is metastable at room temperature. The $x = 0.1$ sample shows a slight Bi_2O_3 impurity indicating that the δ -phase is only stable at compositions above $x = 0.1$.

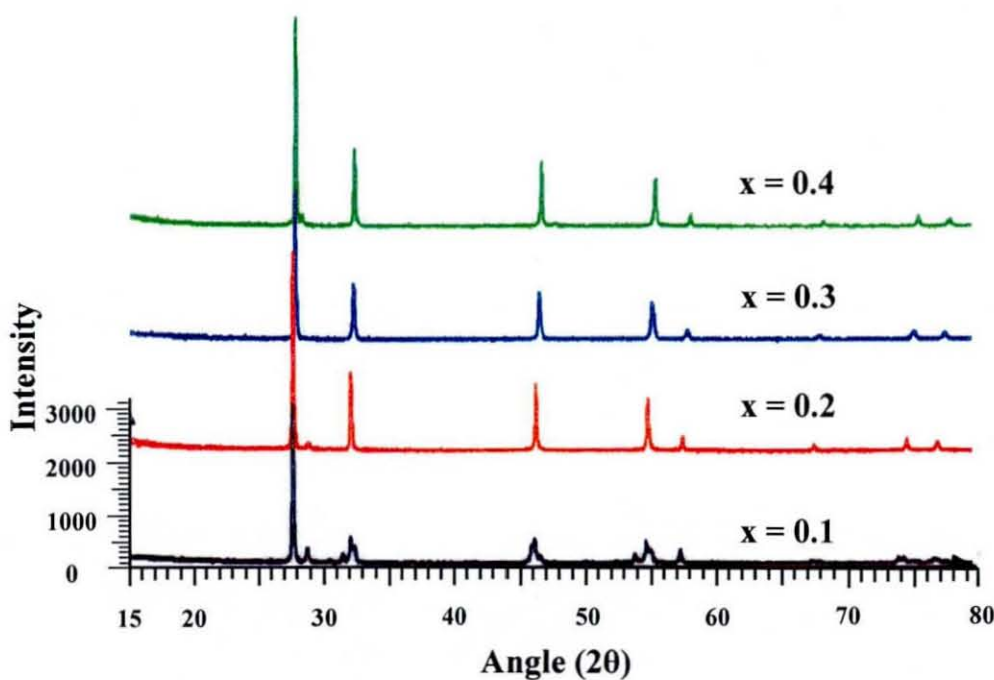


Figure 6.1: X-ray Diffraction Patterns of $\text{Dy}_2\text{O}_3\text{-Bi}_2\text{O}_3$ ($x = 0.1 - 0.4$)

The defect fluorite structure is the primary phase in the samples where $x = 0.2$, 0.3 and 0.4 (mol% = 20, 30 and 40). These samples appear single phase, indicating that the structure is stable over this range. Figure 6.2 shows the X-ray diffraction patterns of the remainder of the sample compositions from $x = 0.5$ to $x = 0.9$. The primary phase in the remainder of these samples is a tetragonal phase (space group $14mm$) and is stable up to $x = 0.9$, apart from where $x = 0.5$ which contains a mixture of the tetragonal structure and the defect fluorite.

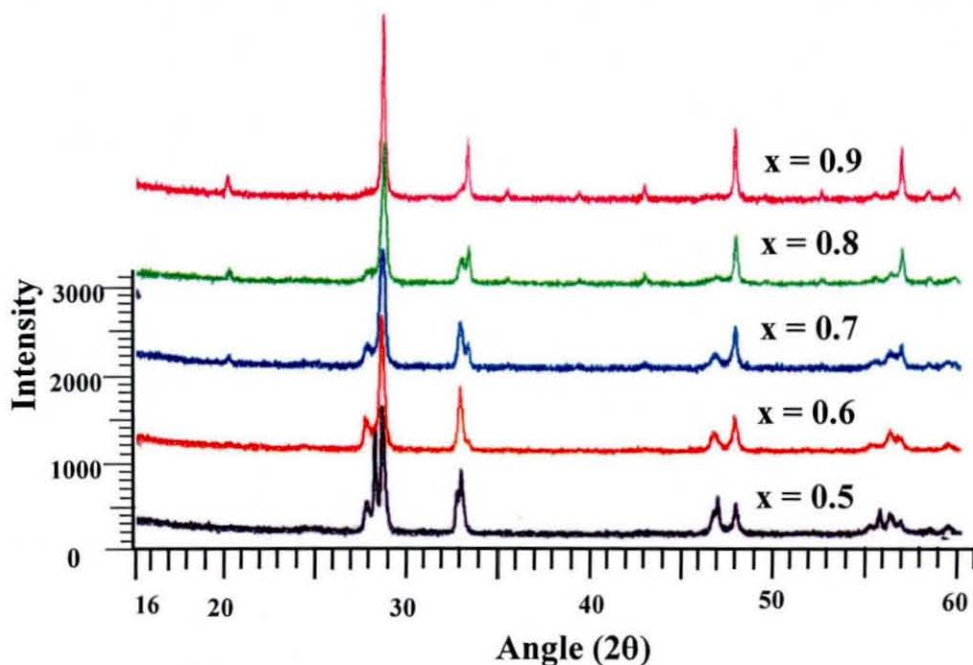


Figure 6.2: X-ray Diffraction Patterns of $(\text{Bi}_{1-x}\text{Dy}_x)_2\text{O}_3$ ($x = 0.5 - 0.9$)

6.5.2. Sm_2O_3 - Bi_2O_3 Solid Solution

The samarium solid solutions discussed here differ structurally from the previous samples shown in section 6.5.1. The defect fluorite structure that is a major phase with rare-earths with ionic radii less than 0.95 \AA is not seen as a pure phase in any of the samarium based material. Figure 6.3 shows the X-ray diffraction data collected for the samarium based samples with the composition $(\text{Bi}_{1-x}\text{Sm}_x)_2\text{O}_3$ where $x = 0.1 - 0.5$. The samarium samples do show signs of the formation of the δ -phase at low Sm concentrations ($x = 0.1$), which can be seen by the peak at 28° 2θ in this pattern. The defect fluorite, however, is mixed with the hexagonal R-3M structure, which is present in all the phases from $x = 0.1 - 0.5$. This hexagonal structure is single phase in both the $x = 0.2$ and $x = 0.3$ but mixes with the tetragonal structure (space group = $14mm$) above these concentrations.

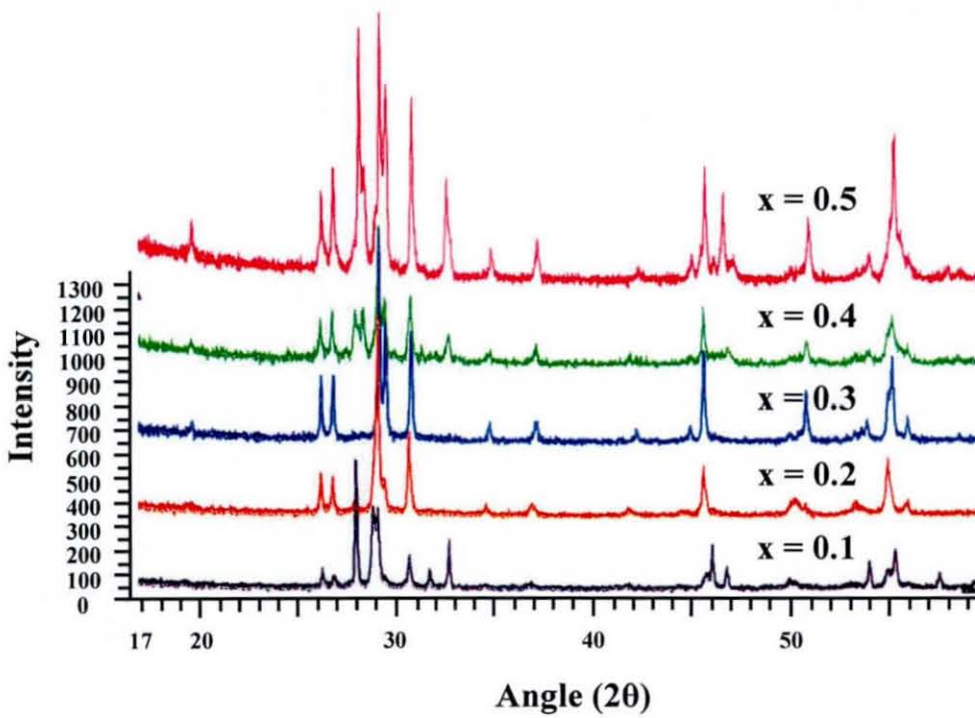


Figure 6.3: X-ray Diffraction Patterns of $(\text{Bi}_{1-x}\text{Sm}_x)_2\text{O}_3$ ($x = 0.6 - 0.9$)

Figure 6.4 shows the X-ray diffraction patterns of samples where $x = 0.5 - 0.9$. Sample $x = 0.6$ is a mixed phase sample of both hexagonal and tetragonal structures. Samples where $x = 0.7 - 0.9$ again shows a single phase tetragonal structure as seen for the high rare-earth concentrations in the dysprosium samples.

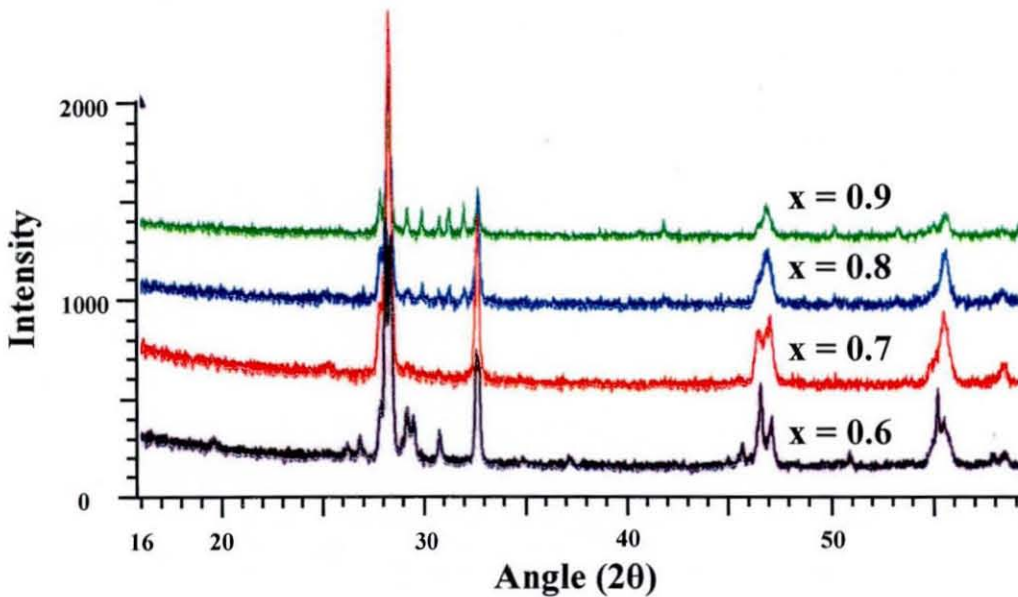


Figure 6.4: X-ray Diffraction Patterns of $(\text{Bi}_{1-x}\text{Sm}_x)_2\text{O}_3$ ($x = 0.6-0.9$)

As discussed previously samarium has an ionic radius in the middle of the range between Dy^{3+} and La^{3+} and therefore shares similar properties to lanthanides with larger and smaller ionic radii. This may indicate why the formation of a single phase was so difficult in the case of these materials. The high background signal seen in these samples shows them to be the least crystalline of the whole series which again may be caused by the ionic radii of the samarium. The lack of the defect fluorite structure in this solid solution indicates a lower stability caused by the similarity in size between Sm^{3+} and Bi^{3+} .

6.5.3. $\text{Ln}_2\text{O}_3\text{-Bi}_2\text{O}_3$ ($\text{Ln} = \text{Nd, Pr and La}$)

As for the rare-earth compounds with small ionic radii (<0.95), the rare-earth compounds with radii above 0.99 \AA also share similar structural properties. The X-ray diffraction patterns for samples $(\text{Bi}_{1-x}\text{Pr}_x)\text{O}_3$ where $x = 0.1$ to 0.5 are shown in Figure 6.5. There is no sign of the formation of the defect fluorite δ -phase at high bismuth concentrations as seen in the other samples. This is confirmation that the appearance of this metastable phase is related to the size of the rare-earth cation. Since the ionic radii of Nd^{3+} , Pr^{3+} , La^{3+} are close to that of Bi^{3+} the defect fluorite structure becomes destabilised at higher temperatures than rare-earths with smaller radii.

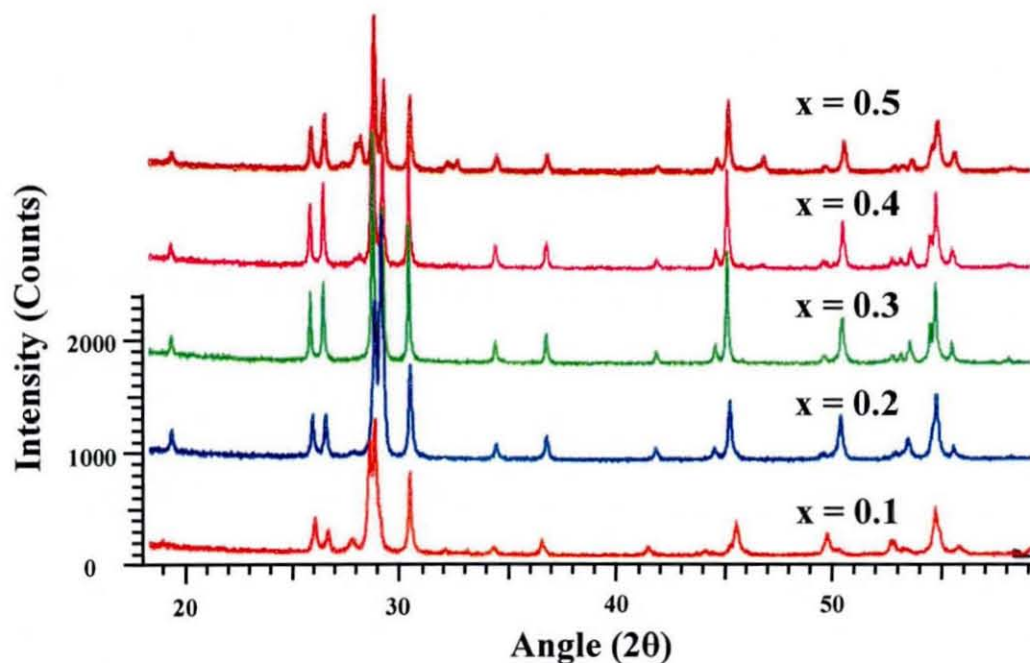


Figure 6.5: X-ray Diffraction Patterns of $(\text{Bi}_{1-x}\text{Pr}_x)_2\text{O}_3$ ($x = 0.1 - 0.5$)

The primary phase in the case of the Pr^{3+} samples seen above is the hexagonal -3M bases structure, Unlike the Sm^{3+} phases where this structure has been seen before this phase is the major phase in all five samples shown above with very little visible impurity. The increased size of the Pr^{3+} cation obviously increases the amount of rare-earth allowed in this particular structure. Figure 6.6 shows the remaining X-ray diffraction patterns for $x = 0.6 - 0.9$. As for the Sm^{3+} samples seen before the sample shown here are dual phase samples, between the hexagonal and tetragonal based structures, with the only pure tetragonal phase being the $x = 0.9$ composition. The tetragonal phase is less prominent in samples containing larger rare-earths and only appears at the very high concentrations of Pr^{3+} . In the Sm^{3+} samples, for example, the tetragonal structure is single phase in the $x = 0.7 - 0.9$ compositions.

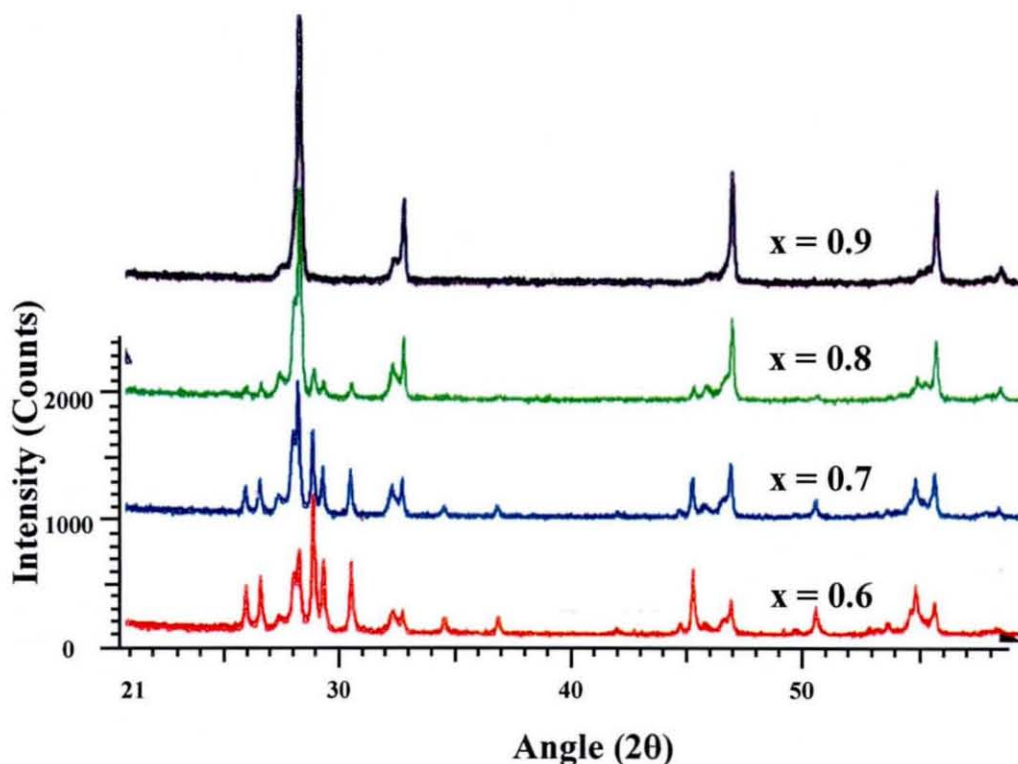


Figure 6.6: X-ray Diffraction Patterns of $(\text{Bi}_{1-x}\text{Pr}_x)_2\text{O}_3$ ($x = 0.6 - 0.9$)

6.6. Results – $L^*a^*b^*$ Colour Measurements

As for the structural analysis of these compounds, the colour measurement results can be grouped together into separate series with similar UV/VIS spectra and colour results. The smaller rare-earth compounds are now separated into two

groups, one containing Y, Dy, Gd and Sm and one containing Er, and Ho. Again La, Pr and Nd are also considered separately to the rest of the rare-earths due to their increased ionic radii.

6.6.1. $\text{Ln}_2\text{O}_3\text{-Bi}_2\text{O}_3$ Solid Solutions ($\text{Ln} = \text{Y, Dy, Gd, Sm}$)

The UV/Vis reflectance data for the above solid solutions are shown in Figure 6.7 - Figure 6.10. All of these samples show similar behaviour in their colour properties across each individual series. These data show that the samples can be separated into two sections, as the $\text{Ln} = 0.1$ and 0.2 samples (blue and red) give slightly different curves to the rest of the samples. The curve displayed by the first two samples is indicative of a light yellow sample, probably caused by the high concentration of yellow Bi_2O_3 in the samples. This is seen as a high reflectance across the spectrum apart from the very small wavelengths (<440 nm) where there is a reasonably sharp absorption edge. Generally the samples also become lighter from $\text{Ln} = 0.1$ to $\text{Ln} = 0.2$ as the overall reflectance increases but the shape of the absorption curve is very similar.

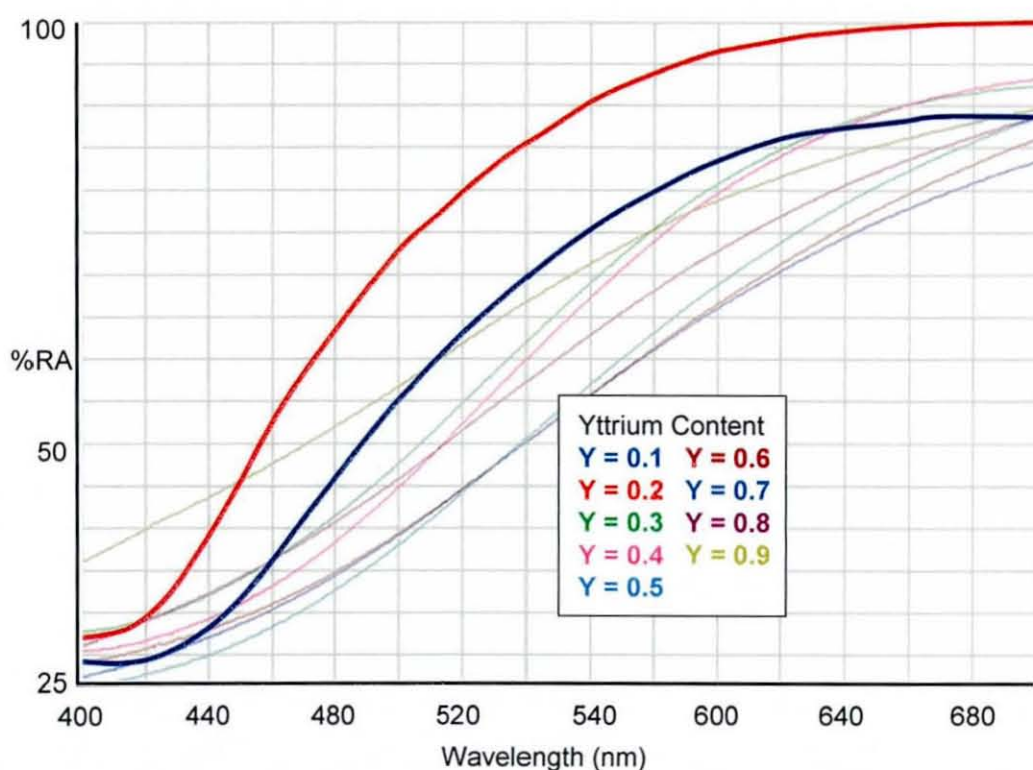


Figure 6.7: UV-Vis spectra of $(\text{Bi}_{1-x}\text{Y}_x)_2\text{O}_3$ ($x = 0.1 - 0.9$)

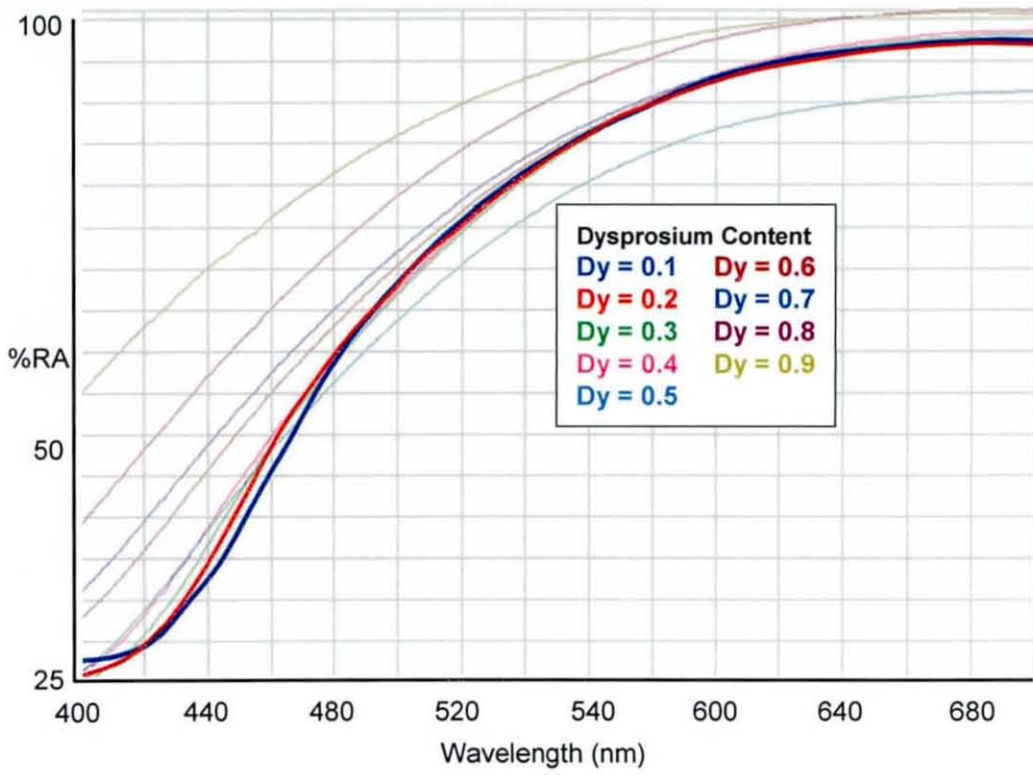


Figure 6.8: UV-Vis spectra of $(\text{Bi}_{1-x}\text{Dy}_x)_2\text{O}_3$ ($x = 0.1 - 0.9$)

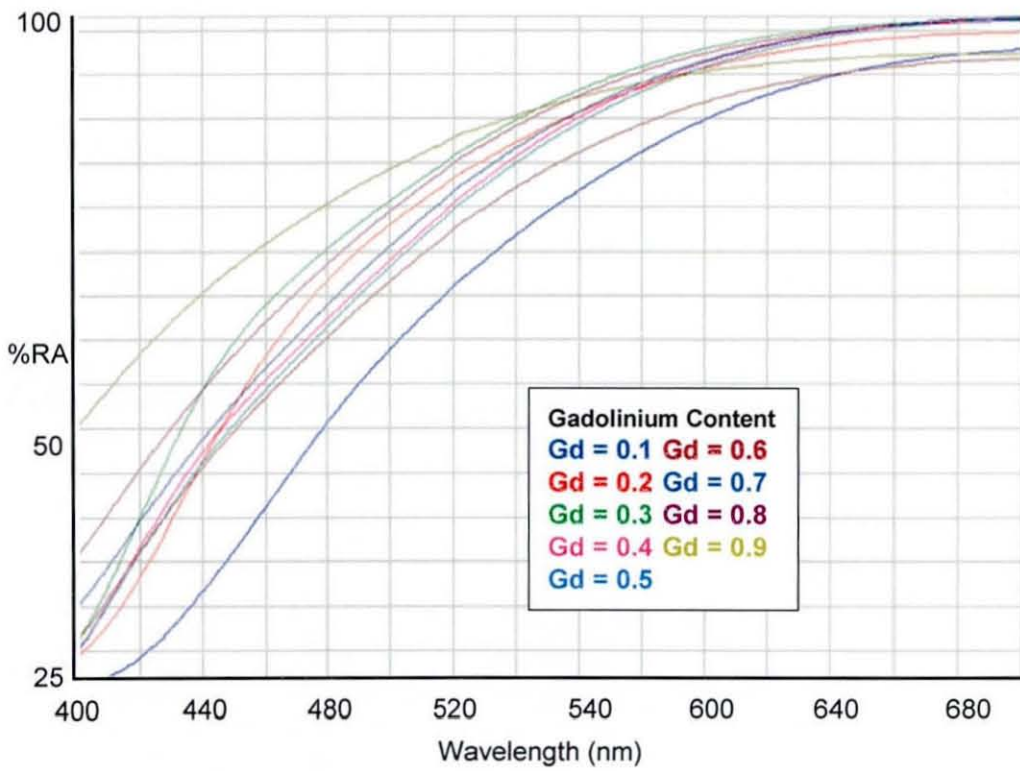


Figure 6.9: UV-Vis spectra of $(\text{Bi}_{1-x}\text{Gd}_x)_2\text{O}_3$ ($x = 0.1 - 0.9$)

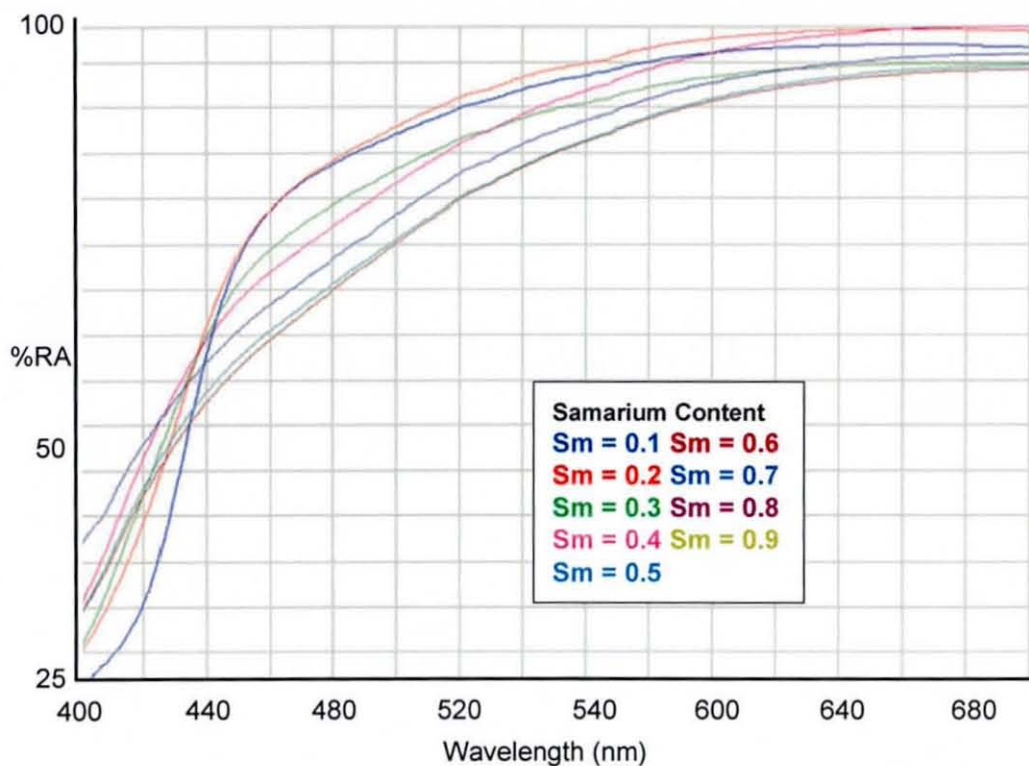


Figure 6.10: UV-Vis spectra of $(\text{Bi}_{1-x}\text{Sm}_x)_2\text{O}_3$ ($x = 0.1 - 0.9$)

The remaining samples create a second type of reflectance curve, which has a much lower overall reflectance and a much shallower absorption edge. Generally the samples increase in reflectance with increasing Ln content though there is a transition period between the lighter samples with Ln contents of 0.1 and 0.2 and the darker samples of the latter part of the series.

6.6.2. $\text{Ln}_2\text{O}_3\text{-Bi}_2\text{O}_3$ Solid Solutions (Ln = Ho, Er)

The holmium and erbium samples (Figure 6.10 – 6.12) distinguish themselves from the Y and Dy samples by the fact that they contain several $f-f$ transitions in the visible region of the spectrum. However the intensity of these transitions does not seem to be of high enough intensity to significantly affect the final colour. The erbium samples are more closely related to the Dy and Y samples as the first two have a significantly steeper absorption edge to the rest of the samples. In the case of the holmium samples, however the absorption edge does not appear to flatten out to the same degree as all the previous samples. The general trend in both the holmium samples and the erbium samples is that the materials tend to take on a higher reflectance as more rare-earth is added. In the erbium samples

however there appears to be an outlier. The 0.7 sample appears to have the lowest reflectance of all the samples while the 0.6 and 0.8 samples still obey the general trend seen previously.

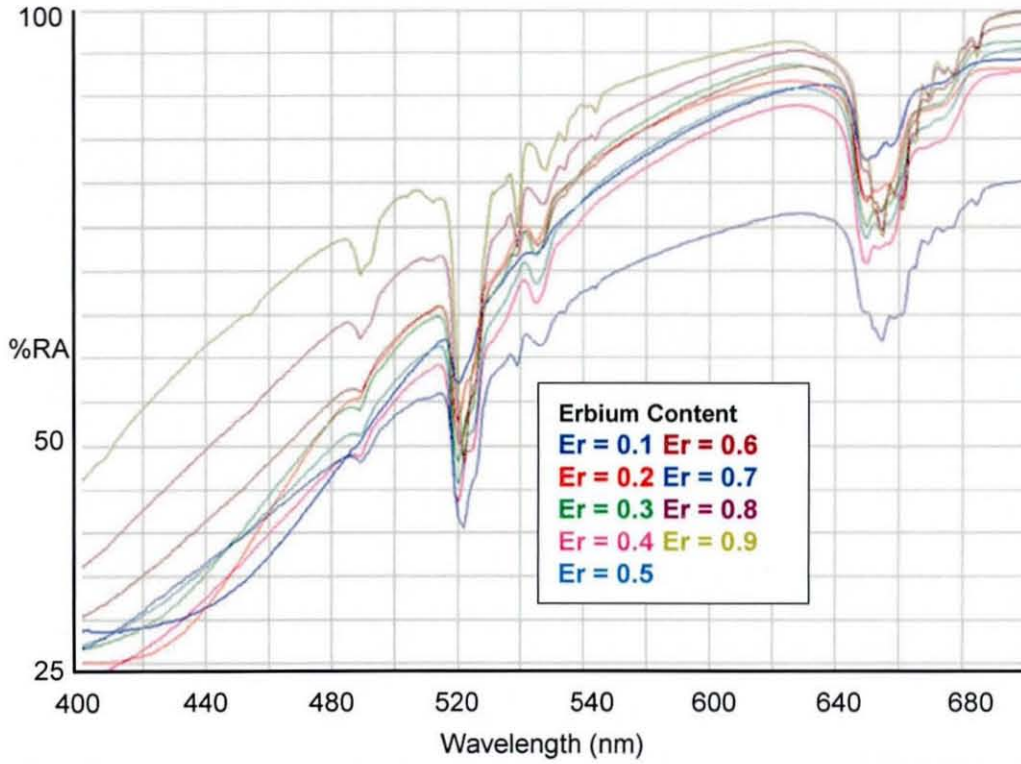


Figure 6.11: UV-Vis spectra of $(\text{Bi}_{1-x}\text{Er}_x)_2\text{O}_3$ ($x = 0.1 - 0.9$)

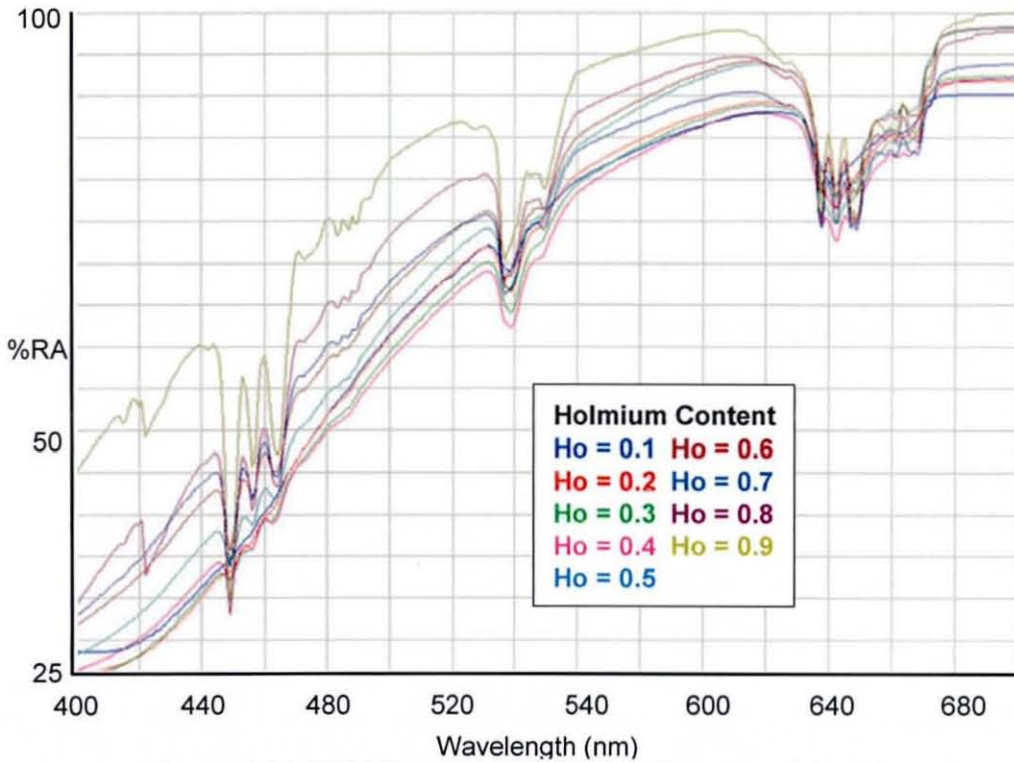


Figure 6.12: UV-Vis spectra of $(\text{Bi}_{1-x}\text{Er}_x)_2\text{O}_3$ ($x = 0.1 - 0.9$)

6.6.3. $\text{Ln}_2\text{O}_3\text{-Bi}_2\text{O}_3$ Solid Solutions ($\text{Ln} = \text{Pr, Nd, La}$)

The final solid solutions containing the larger rare-earth cations differ in their colour measurements as well as their structural behaviour. The colour of these compounds has a closer relationship to the native rare-earth colouration caused by the $f-f$ electronic transitions. The most notable difference is in the Pr^{3+} samples which give a light yellow type UV/Vis spectra for samples where $x = 0.1 - 0.3$ (Figure 6.13). The remaining compositions quickly decrease in reflectance giving dark brown to black samples. The Nd^{3+} samples (Figure 6.14) show very intense $f-f$ electron transitions creating green shade materials which increase in intensity as the concentration of Nd^{3+} is increased. Finally the UV/Vis spectra for the La^{3+} samples are shown in Figure 6.15 and indicate a bright yellow colouration. Unlike previous samples, however, these materials do not form orange coloured samples and increase in lightness across the series. As the colour of samples containing Pr^{3+} , Nd^{3+} and La^{3+} are not related to the other rare-earths, the further study of these materials were not necessary.

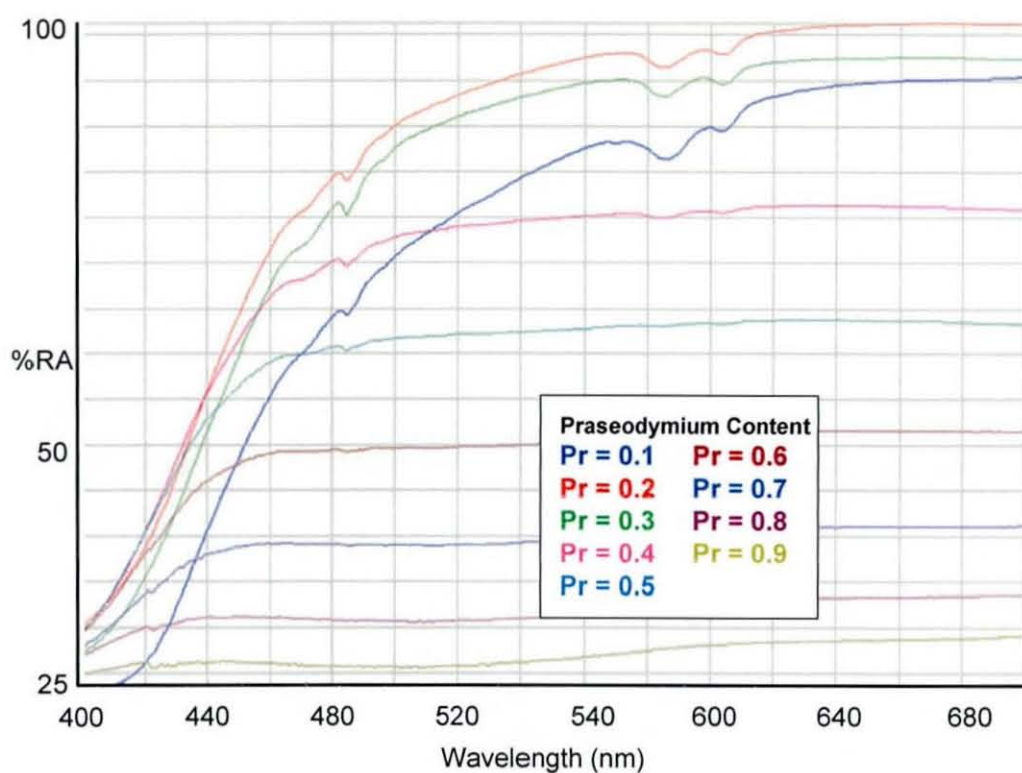


Figure 6.13: UV-Vis spectra of $(\text{Bi}_{1-x}\text{Pr}_x)_2\text{O}_3$ ($x = 0.1 - 0.9$)

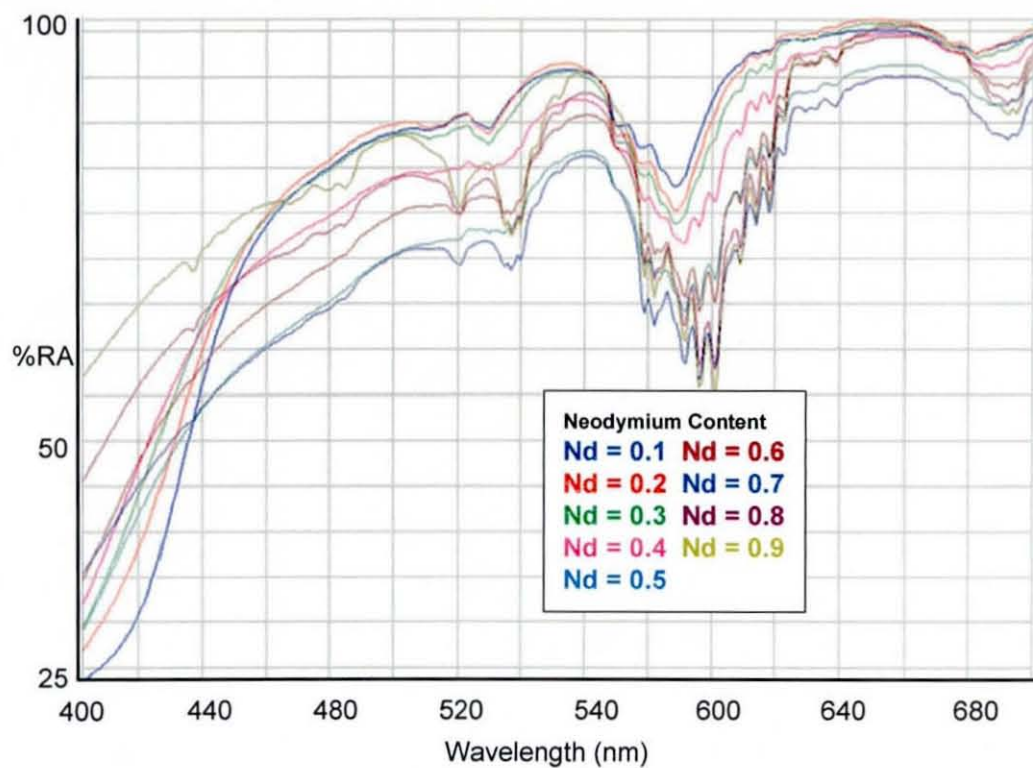


Figure 6.14: UV-Vis spectra of $(\text{Bi}_{1-x}\text{Nd}_x)_2\text{O}_3$ ($x = 0.1 - 0.9$)

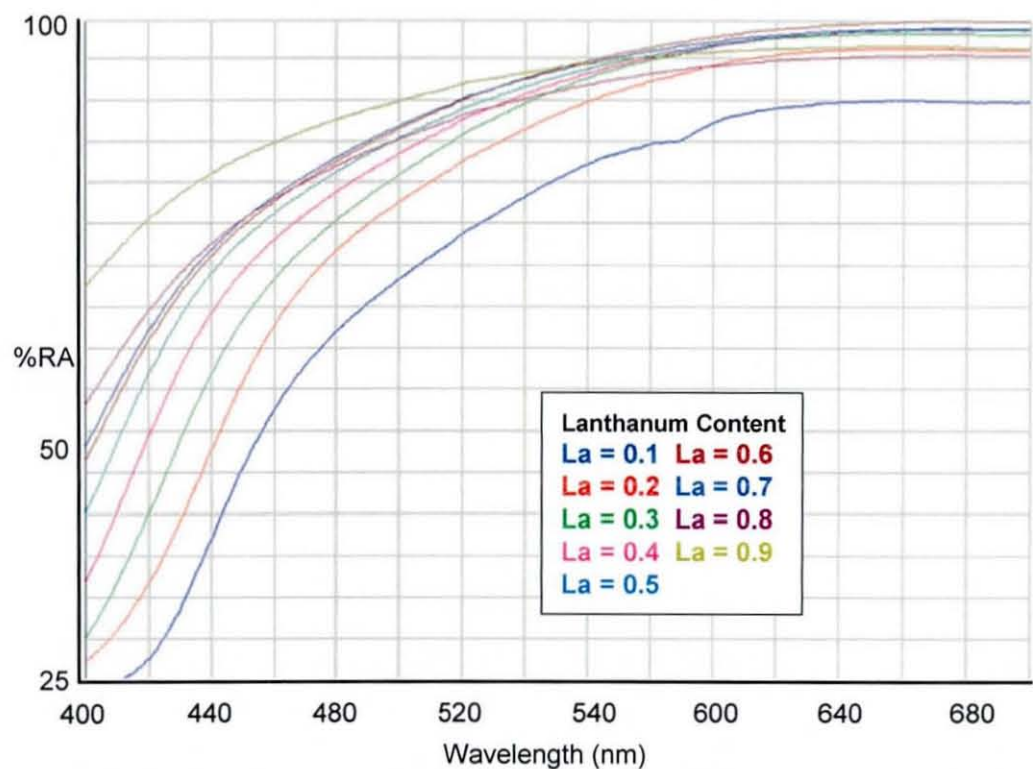


Figure 6.15: UV-Vis spectra of $(\text{Bi}_{1-x}\text{La}_x)_2\text{O}_3$ ($x = 0.1 - 0.9$)

6.7. Results – Structural Refinement

Colour analysis of the rare-earth bismuth oxides has shown that the materials containing those with smaller ionic radii give the most desirable colouration. The colouration of these compounds is mainly influenced by the defect fluorite structures seen at lower concentrations of rare-earth content. Samples lightened over time as the metastable defect fluorite converted to more stable structures. Although these phases are now known to be metastable, it was decided that the study of the defect fluorite structure would give insight into the lack of stability in the structure and colour of these phases.

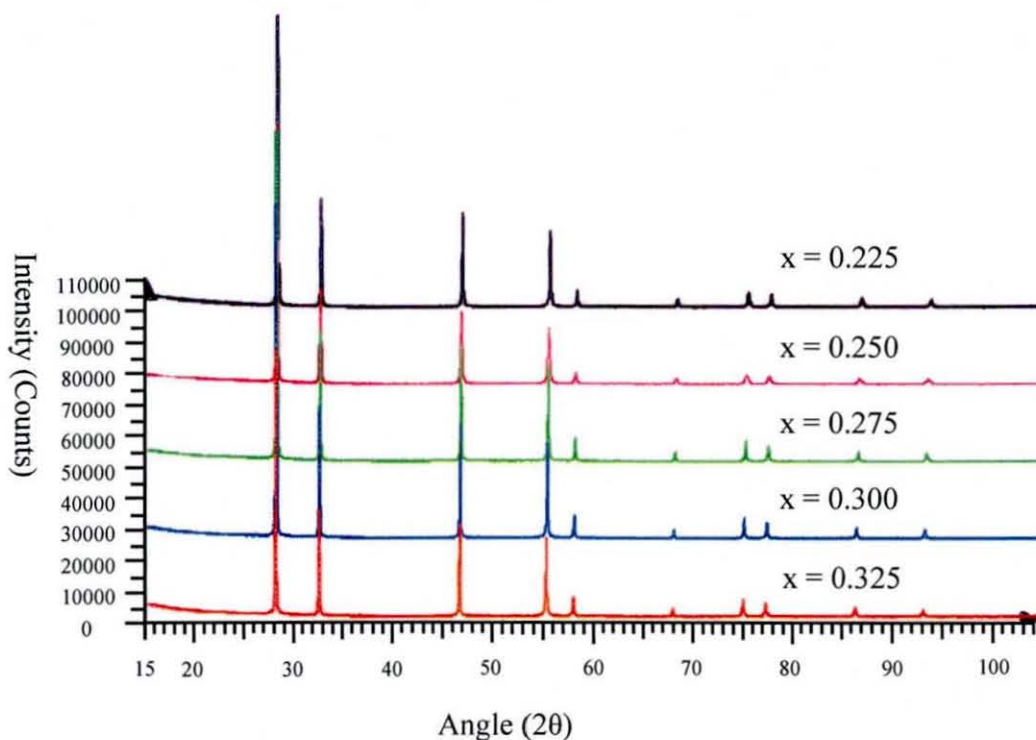


Figure 6.16: X-ray Diffraction of $(Dy_{1-x}Bi_x)O_3$ showing Fm3m cubic phases

Of the smaller rare-earths the dysprosium and erbium samples gave the best results though, because of the cost of erbium compounds, dysprosium was chosen for further study. X-ray diffraction results (section 6.5) showed that the defect fluorite structure was the major phase in samples with the composition $(Bi_{1-x}Dy_x)O_3$ where $x = 0.1-0.4$. Those samples where $x = 0.1$ and 0.4 had small secondary impurities showing that the defect fluorite appeared in between these

values. Compounds of the composition $(\text{Bi}_{1-x}\text{Dy}_x)\text{O}_3$ where $x = 0.225, 0.25, 0.275, 0.3$ and 0.325 were analysed by X-ray diffraction for structural refinement. Figure 6.16 shows the X-ray diffraction of the synthesised phases, which confirms the single phase purity of these samples.

6.7.1. Refinement of Dy Samples

Samples of the composition $(\text{Bi}_{1-x}\text{Dy}_x)_2\text{O}_3$ where $x = 0.5, 0.55, 0.6$ were selected for further analysis of the defect fluorite $\delta\text{-Bi}_2\text{O}_3$ structure detected in these samples. A full structural characterisation was carried out using Rietveld refinement techniques. Three possible structures have been reported for the $\delta\text{-Bi}_2\text{O}_3$ type phases and were outlined in Chapter 1. In order to find the best fit for the collected data, the phase was refined using all three structures as an initial model. The results of all three refinements are reported here.

The first model proposed was that of Sillen¹ where the oxygen vacancies of the defect fluorite are ordered in the **111** direction (Figure 6.17). This causes the symmetry of the face-centred fluorite to adopt a primitive $\text{Pn}3\text{m}$ space group. The trivalent Bi^{3+} and Dy^{3+} cations are placed on $0, \frac{1}{2}, \frac{1}{2}$ with occupancies corresponding to the composition, and the oxide anions are placed on $\frac{3}{4}, \frac{1}{4}, \frac{1}{4}$ (Table 6.1)

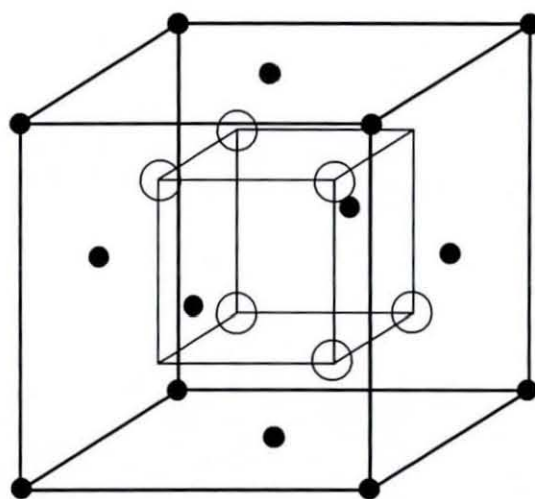


Figure 6.17: Primitive $\delta\text{-Bi}_2\text{O}_3$ model; black spheres = $\text{Bi}^{3+}/\text{Dy}^{3+}$
white spheres = O^{2-}

Table 6.1: Refinement Model for the Sillen primitive model

		$\text{Bi}_{1.55}\text{Dy}_{0.45}\text{O}_3$	$\text{Bi}_{1.55}\text{Dy}_{0.45}\text{O}_3$	$\text{Bi}_{1.55}\text{Dy}_{0.45}\text{O}_3$	$\text{Bi}_{1.55}\text{Dy}_{0.45}\text{O}_3$	$\text{Bi}_{1.55}\text{Dy}_{0.45}\text{O}_3$
Bi	Site	4a	4a	4a	4a	4a
	x, y, z	0, 1/2, 1/2	0, 1/2, 1/2	0, 1/2, 1/2	0, 1/2, 1/2	0, 1/2, 1/2
	Occu	0.775	0.750	0.725	0.700	0.675
Dy	Site	4a	4a	4a	4a	4a
	x, y, z	0, 1/2, 1/2	0, 1/2, 1/2	0, 1/2, 1/2	0, 1/2, 1/2	0, 1/2, 1/2
	Occu	0.225	0.250	0.275	0.300	0.325
O	Site	6b	6b	6b	6b	6b
	x, y, z	3/4, 1/4, 1/4	3/4, 1/4, 1/4	3/4, 1/4, 1/4	3/4, 1/4, 1/4	3/4, 1/4, 1/4
	Occu	1	1	1	1	1

Table 6.2: Refinement results for the Pn3m structural model.

Dy Content	0.225	0.25	0.275	0.3	0.325
Cell Parameter	5.50304(5)	5.49651(4)	5.49012(4)	5.48414(6)	5.47003(5)
Dy/Bi U_{iso}	0.0260(2)	0.0312(2)	0.0323(2)	0.0301(2)	0.0276(2)
O U_{iso}	0.0939(27)	0.106(3)	0.0898(23)	0.0831(19)	0.0771(26)
wRp	4.22%	4.18%	3.91%	3.10%	4.30%
Rp	3.18%	3.09%	2.86%	2.31%	3.11%
χ^2	3.723	4.195	4.068	2.502	4.909

The second proposed model is that of a defect fluorite structure proposed by Gattow and Schroder³ where the face centred Fm2m space group is retained but the three oxide anion are distributed over 75% of the available sites (Figure 6.18). This will be referred to as the "average" model as the oxide vacancies are distributed over all of the available sites randomly, which *averages* out to a 3/4 occupancy. The initial starting model is shown in Table 6.3 and the refinement results are shown in Table 6.4.

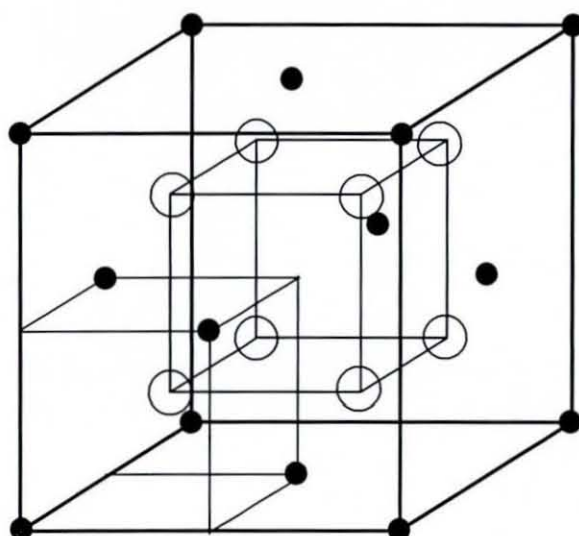


Figure 6.18: "Average" fluorite δ - Bi_2O_3 model; black spheres = $\text{Bi}^{3+}/\text{Dy}^{3+}$; white spheres = O^{2-}

Table 6.3: Refinement Model for the Gattow and Schroder "Average" model

	$\text{Bi}_{1.55}\text{Dy}_{0.45}\text{O}_3$	$\text{Bi}_{1.55}\text{Dy}_{0.45}\text{O}_3$	$\text{Bi}_{1.55}\text{Dy}_{0.45}\text{O}_3$	$\text{Bi}_{1.55}\text{Dy}_{0.45}\text{O}_3$	$\text{Bi}_{1.55}\text{Dy}_{0.45}\text{O}_3$
Bi	Site 4a	Site 4a	Site 4a	Site 4a	Site 4a
	x, y, z 0, 0, 0	x, y, z 0, 0, 0	x, y, z 0, 0, 0	x, y, z 0, 0, 0	x, y, z 0, 0, 0
	Occu 0.775	Occu 0.750	Occu 0.725	Occu 0.700	Occu 0.675
Dy	Site 4a	Site 4a	Site 4a	Site 4a	Site 4a
	x, y, z 0, 0, 0	x, y, z 0, 0, 0	x, y, z 0, 0, 0	x, y, z 0, 0, 0	x, y, z 0, 0, 0
	Occu 0.225	Occu 0.250	Occu 0.275	Occu 0.300	Occu 0.325
O	Site 6b	Site 6b	Site 6b	Site 6b	Site 6b
	x, y, z $\frac{1}{4}, \frac{1}{4}, \frac{1}{4}$	x, y, z $\frac{1}{4}, \frac{1}{4}, \frac{1}{4}$	x, y, z $\frac{1}{4}, \frac{1}{4}, \frac{1}{4}$	x, y, z $\frac{1}{4}, \frac{1}{4}, \frac{1}{4}$	x, y, z $\frac{1}{4}, \frac{1}{4}, \frac{1}{4}$
	Occu 1	Occu 1	Occu 1	Occu 1	Occu 1

Table 6.4: Refinement results for the "Average" model

Dy Content	0.225	0.25	0.275	0.3	0.325
Cell Parameter	5.50304(5)	5.49651(4)	5.49012(4)	5.48413(6)	5.47288(5)
Dy/Bi U_{iso}	0.0261(2)	0.0313(2)	0.0324(2)	0.0302(2)	0.0282(2)
O U_{iso}	0.0909(27)	0.102(3)	0.0840(23)	0.0799(19)	0.0714(22)
wRp	4.19%	4.15%	3.85%	3.04%	3.77%
Rp	3.16%	3.07%	2.82%	2.28%	2.64%
χ^2	3.671	4.139	3.946	2.402	3.705

The final model proposed by *Willis* is related to the "average" model as it still occupies a $Fm\bar{3}m$ space group, and the oxide vacancies are again distributed randomly throughout the structure (Figure 6.19). In this case however, the oxide anions are found on a lower symmetry $32e$ site rather than the ideal $8b$ site seen previously, hence it is referred to as the "distorted" model. This distortion would presumably perform a similar role as seen in the pyrochlore structures in previous chapters.

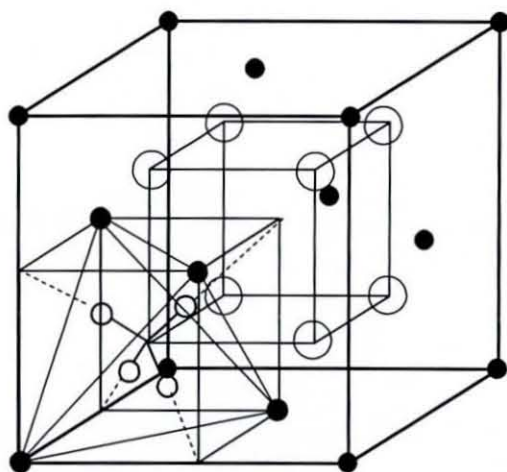


Figure 6.19: "Distorted" fluorite $\delta\text{-Bi}_2\text{O}_3$ model; black spheres = $\text{Bi}^{3+}/\text{Dy}^{3+}$; white spheres = O^{2-}

The oxide anions are distorted in four directions towards the vacant octahedral holes forming a tetrahedral arrangement of sites. This displacement causes the sites to take up a closer location to 3 of the 4 surrounding Bi cations producing a much shorter bond length. The initial structural model is shown in Table 6.5 and the results are in Table 6.6.

Table 6.5: Refinement Model for the Willis "Distorted" model

		$\text{Bi}_{1.55}\text{Dy}_{0.45}\text{O}_3$	$\text{Bi}_{1.55}\text{Dy}_{0.45}\text{O}_3$	$\text{Bi}_{1.55}\text{Dy}_{0.45}\text{O}_3$	$\text{Bi}_{1.55}\text{Dy}_{0.45}\text{O}_3$	$\text{Bi}_{1.55}\text{Dy}_{0.45}\text{O}_3$
Bi	Site	4a	4a	4a	4a	4a
	x, y, z	0, 0, 0	0, 0, 0	0, 0, 0	0, 0, 0	0, 0, 0
	Occu	0.775	0.750	0.725	0.700	0.675
Dy	Site	4a	4a	4a	4a	4a
	x, y, z	0, 0, 0	0, 0, 0	0, 0, 0	0, 0, 0	0, 0, 0
	Occu	0.225	0.250	0.275	0.300	0.325
O	Site	24e	24e	24e	24e	24e
	x, y, z	0.3, 0.3, 0.3	0.3, 0.3, 0.3	0.3, 0.3, 0.3	0.3, 0.3, 0.3	0.3, 0.3, 0.3
	Occu	1	1	1	1	1

Table 6.6: Refinement results for the "Distorted" model

Dy Content	0.225	0.25	0.275	0.3	0.325
Cell Parameter	5.50304(5)	5.49651(4)	5.49014(4)	5.48413(6)	5.47288(5)
Dy/Bi U_{iso}	0.0266(2)	0.0318(2)	0.0320(2)	0.0307(2)	0.0285(2)
O U_{iso}	0.008(4)	0.010(4)	0.003(4)	0.005(4)	0.002(22)
wRp	4.08%	4.09%	3.81%	2.99%	3.72%
Rp	3.05%	3.02%	2.81%	2.24%	2.60%
χ^2	3.482	4.019	3.867	2.331	3.591

All three of the models above give acceptable refinement results for the observed X-ray diffraction data highlighting the problems assigning the correct structure. In all three cases there is a small decrease in the size of the cell when increasing

amounts of dysprosium is substituted. The cell size of each composition is almost identical in each case showing that the change in space group has only a marginal change in the structure of the cell. The major difference in the three models is the treatment of the oxide anion and the affect this has on the refinement results. In the "average" and "primitive" models the oxide has higher than expected temperature factors, implying that there is a certain amount of distortion on this site. The "distorted" model however attempts to model this distortion with a displacement of the site which results in much lower thermal parameters. This increase in disorder is also coupled with an improvement in the refinement results (χ^2 , wRp and Rp), with the "disordered" giving the best results and the "primitive" model having the worst (Figure 6.19). These improved refinement results, however, are only slight and not enough to distinguish the most accurate model.

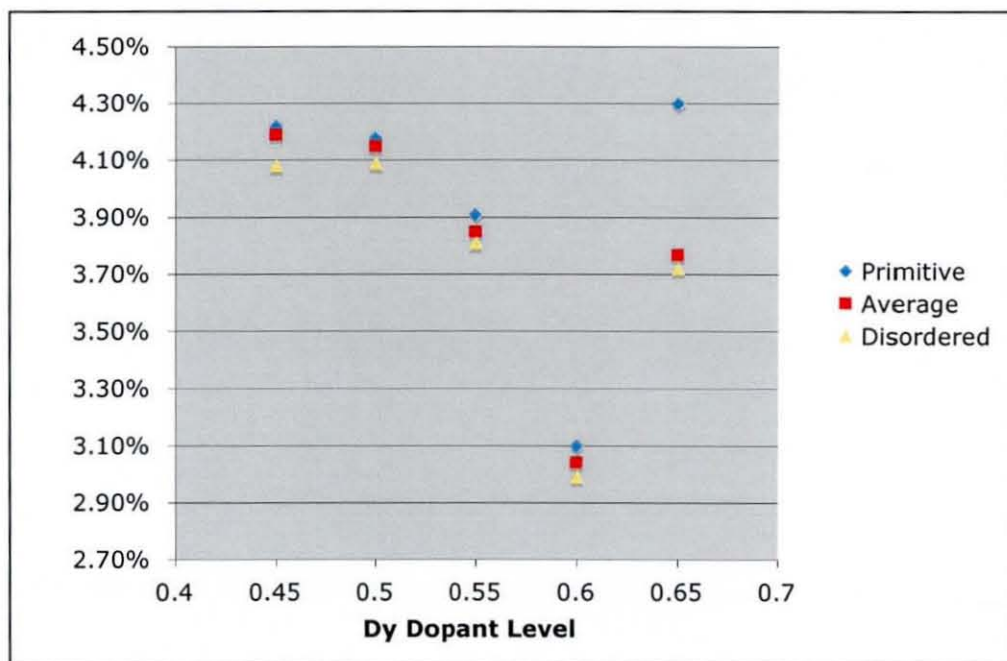


Figure 6.20: Change in refinement result wRp with amount of rare-earth cation

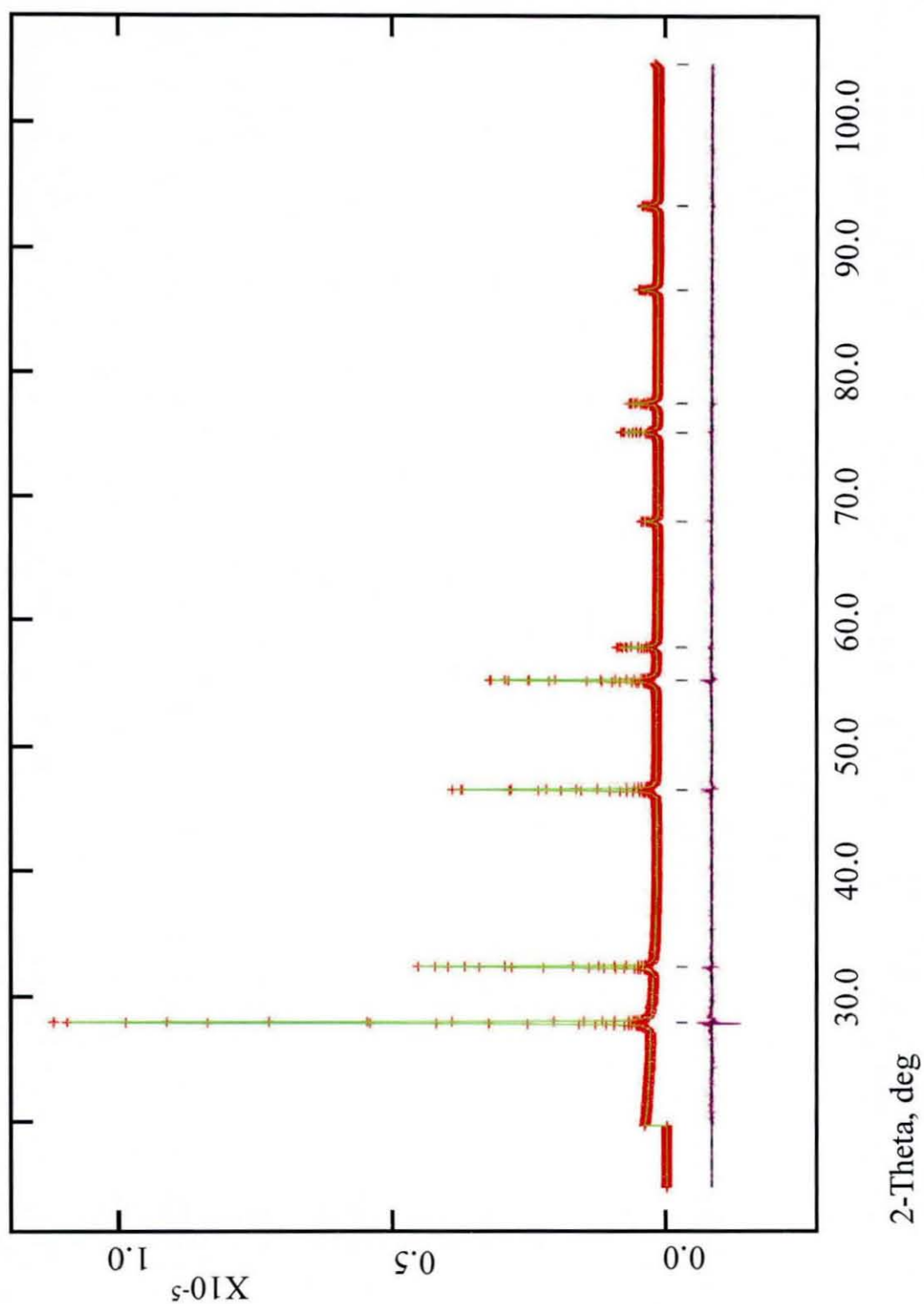


Figure 6.21: Refinement results from the structural characterisation of $(\text{Bi}_{0.7}\text{Dy}_{0.3})_2\text{O}_3$; red crosses are observed data, green line is calculated profile and purple line is the difference curve.

6.7.2. Valence Calculations

The difficulty in assigning the correct structure from the diffraction experiments alone stems from the quality of the data collected. As all three possible models have simple cubic unit cells with relatively high symmetry, it makes the differences between them difficult to spot using powder diffraction alone. This is coupled with the very small unit cell which causes only 11 independent reflections to appear in the operational range of the diffractometer. The lack of low angle reflections makes the detection of any small variations almost impossible to detect. It was decided to try and determine if there were any reasons why one particular model would be preferable to another from the stability of the cation and anion geometries. The best method in assessing the stability of an ions environment is to use valence calculations to look at the contribution of the varying bond lengths produced by all three models.

Table 6.7: $\text{Bi}^{3+}/\text{Dy}^{3+}$ bond length and bond valence results for "Primitive" and "Average" model

Dy Stoichiometry	Bond Length	Valence
0.45	2.38289(2)	0.458
0.5	2.38006(1)	0.462
0.55	2.37729(1)	0.465
0.6	2.37470(2)	0.468
0.65	2.36859(1)	0.476

Table 6.7 above shows the $\text{Bi}^{3+}/\text{Dy}^{3+}$ bond lengths and bond valence contributions of the "primitive" unit cell model, for each of the analysed compositions. Since there is a close relationship between the "primitive" and "average" structural models the bond lengths are the same in both cases. This is also true in the similarities between the Bi^{3+} and Dy^{3+} centres also, as the bond valences also are identical for both cations. The main difference between these two unit cells is that the ordered vacancies in the "primitive" model causes the $\text{Bi}^{3+}/\text{Dy}^{3+}$ centres to adopt a 6-fold geometry. In the "average" model, where the oxide vacancies are random, these cation centres are 6-fold on *average*. These

causes there to be a number of different geometries with 6-fold being the most probable configuration, but also allowing for a number of bonds both higher and lower. Generally however the probability of these alternative configurations becomes less likely the further they deviate from the ideal number of bonds making the overwhelming majority of sites 5, 6, or 7-fold.

Calculating the site valence in the case of the "primitive" model is relatively trivial and corresponds to the bond valence multiplied by the number of bonds (6). This gives a total valence between 2.78 and 2.86 depending on the composition, much too low for a stable Bi^{3+} site. The site valences in the "average" model are much harder to calculate as the relative proportion of 5, 6, and 7 coordinate sites in the structure are not known. However since the average geometry is 6-fold it is not unreasonable to assume that the proportion of 5 and 7-fold sites would be equal, thus any gain in site valence from the inclusion of a 7-fold site would be negated by a 5-fold site elsewhere in the structure. This would make the $\text{Bi}^{3+}/\text{Dy}^{3+}$ site valence similar to the "primitive" model already calculated as being too low for a stable site. It could be argued that there may be a local bonding arrangement in the case of the "average" model, which would allow for the inclusion of a higher proportion of 7-fold sites. The site valence for the O^{2-} sites in this structure however would not be affected by such a bonding arrangement and should be the same for both structures. The valence for this site was calculated as being between 1.832 and 1.904, both of which are still very low for a stable site.

Table 6.8 shows the bond lengths and valences for the final "distorted" model for each composition. In this case there is both a long and a short bond calculated in each compound with the corresponding valence calculation. This is due to the distortions that have been inserted for the O^{2-} site not present in the previous two models. Figure 6.22 shows a representation of the displaced site, which creates 4 identical sites of lower symmetry in the place of the original site. The sites form a tetrahedron of sites with the vertex's pointing towards the unoccupied octahedral holes located in the centre of the $\text{Bi}^{3+}/\text{Dy}^{3+}$ sites. This has the effect of forming 3 short and 1 long bond to each site, such as in the lone-pair pyrochlore

oxide sites seen in previous chapters, again only one of the four sites is occupied at any one time.

Table 6.8: $\text{Bi}^{3+}/\text{Dy}^{3+}$ Bond lengths and calculated bond valence for "Distorted" model

Dy Stoichiometry	Short Bonds		Long Bonds	
	Bond Length	Valence	Bond Length	Valence
0.225	2.2638(10)	0.632	2.899(8)	0.114
0.25	2.2636(13)	0.632	2.876(10)	0.121
0.275	2.2652(14)	0.630	2.842(10)	0.132
0.3	2.2643(14)	0.631	2.828(9)	0.138
0.325	2.26317(1)	0.633	2.79936(2)	0.149

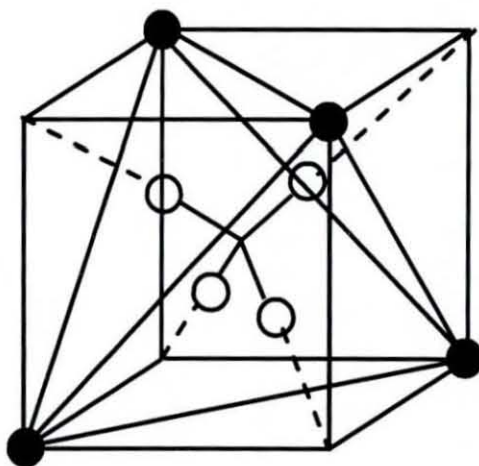


Figure 6.22: $\frac{1}{4}$ of distorted fluorite unit cell including oxide tetrahedron.

The valence calculations for the "distorted" model were calculated based on similar assumptions to the "average" model where the valence would average out to the same as a 6-fold site. Again the existence of other coordination's were not discounted, however the existence of higher geometries would be countered by a similar number of lower coordinations. As previously mentioned each oxide site will have 1 long and 3 short bonds to the surrounding $\text{Bi}^{3+}/\text{Dy}^{3+}$ sites. In six-fold coordination this equates to 1.5 bonds having a longer length and 4.5 having a

shorter length. Like the coordination this is an average value and equates to half of the sites having 4 short and 2 long bonds and half having 5 short and 1 long bonds. The site valence for the $\text{Bi}^{3+}/\text{Dy}^{3+}$ site valence varies between 3.015 and 3.072 depending on the compositions, similarly the calculated valence for the O^{2-} site varies between 2.01 and 2.05 (Table 6.9). In both these cases the valence falls within the expected values of 3.0 ± 0.1 for $\text{Bi}^{3+}/\text{Dy}^{3+}$ and 2.0 ± 0.1 for O^{2-} for every composition.

Table 6.9: Site valences for the "Distorted" refinement model

Dy stoichiometry	$\text{Bi}^{3+}/\text{Dy}^{3+}$ Valence	O^{2-} Valence
0.45	3.014	2.009
0.5	3.027	2.018
0.55	3.032	2.021
0.6	3.046	2.031
0.65	3.072	2.048

From the valence calculations it appears that the "distorted" structure is the only acceptable model from the view of cation and anion site stability. Both the "average" and "primitive" structures displayed a low site valence for the $\text{Bi}^{3+}/\text{Dy}^{3+}$ and O^{2-} ions. The distortions of the oxide anions in the "distorted" model appear to be required in order to form the 3 shorter bonds that are integral to raising the site valence to acceptable levels. Unlike the pyrochlore structures seen previously, where the anion displacements are caused by the associated cations, no relationship has been found between the Bi^{3+} lone pair and the anion distortions. It is likely that the metastable nature of this structure in these compounds is related to the displacements on the oxide site. Without a permanent stereochemical cause to the displacement, such as the lone-pairs or larger chalcogenide anions seen in the related pyrochlore structures, this arrangement may become too unstable to maintain at lower temperatures.

6.8. High Temperature Study of Bismuth Oxide

The high temperature cubic phase of $\delta\text{-Bi}_2\text{O}_3$ was studied using high temperature X-ray diffraction techniques in order to better understand the cause of the metastability at room temperature. As expected this phase was present at high temperatures and displayed a similar diffraction pattern to the rare-earth stabilised samples seen previously. Figure 6.23 shows an X-ray diffraction pattern displaying both the high temperature bismuth oxide phase (700 °C) and a dysprosium-doped sample with the composition $\text{Bi}_{1.4}\text{Dy}_{0.6}\text{O}_3$. Both samples show a high symmetry cubic phase with a relatively small unit cell size, evident from the low number of detected reflections and the lack of reflections at lower angles (less than 25°). The pure bismuth samples show additional reflections at low angles, which are most likely caused by the furnace apparatus used in the diffraction experiment. The high temperature phase also shows a slightly larger unit cell size that is due to the thermal expansion of the material at high temperature rather than any difference in the two phases.

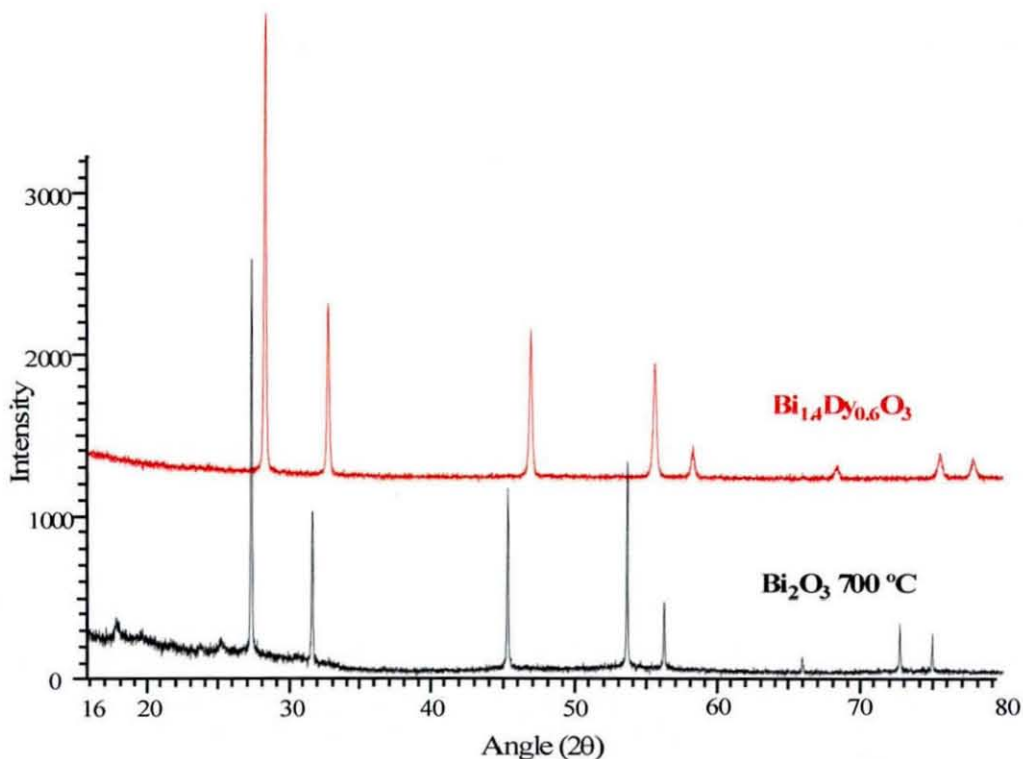


Figure 6.23: X-ray diffraction patterns of $\delta\text{-Bi}_2\text{O}_3$ at 700 °C (black) and $\text{Bi}_{1.4}\text{Dy}_{0.6}\text{O}_3$

Although there are slight differences between the two diffraction patterns above it is apparent that they are both from materials with very similar crystal structures. This is as expected since it has already been reported that bismuth and dysprosium both have very similar ionic radii, and these two phases would both share the defect fluorite type structure discussed previously. Regardless of the similarities between these two phases however, the bismuth phase is only stable at temperatures above 750 °C. The dysprosium sample however, though metastable at room temperature, is able to maintain the structure long enough to allow analysis in ambient conditions.

Figure 6.24 below displays two diffraction patterns of Bi_2O_3 at 650 °C and 660 °C for comparison. The diffraction data recorded at 660 °C displays the same oxide conducting defect fluorite structure as seen previously at higher temperatures. The 650 °C pattern however shows the result of the polymorphic transition of Bi_2O_3 from the δ -phase to the β -phase seen below. The almost complete transition from one polymorph to another occurs over a 10 °C step with only a small δ -phase impurity remaining in the 650 °C diffraction pattern. This is a surprisingly rapid transition, especially considering that the β -phase remains metastable down to room temperature.

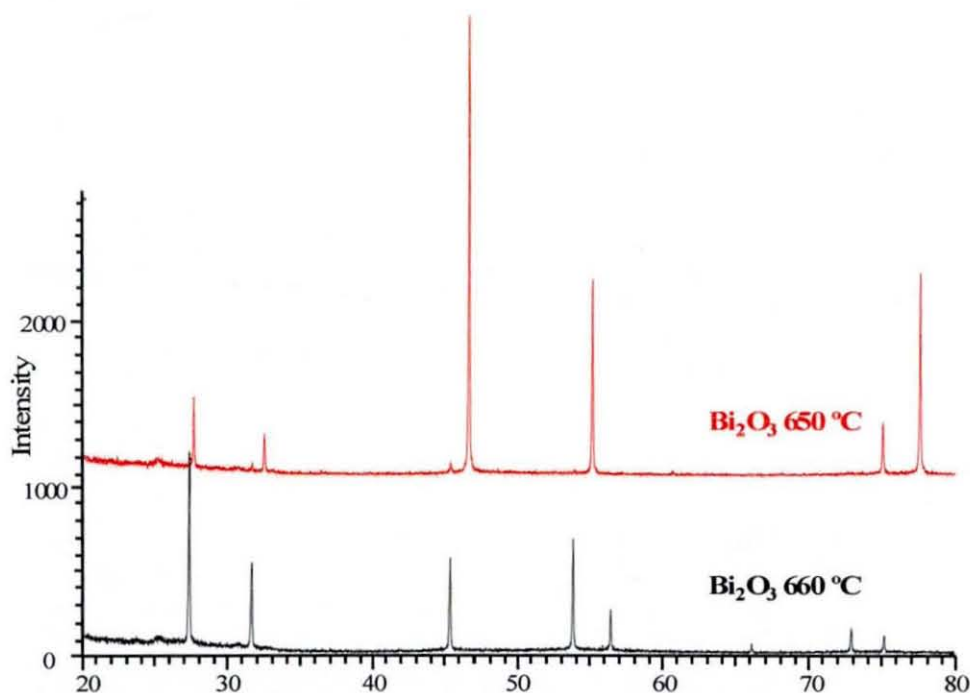


Figure 6.24: X-ray diffraction patterns of Bi_2O_3 at 650 °C and 660 °C

The β -phase has a tetragonal unit cell (space group P3d2) and is closely related to the primitive cubic phase put forward by Sillien as a possible structure for δ -Bi₂O₃. The tetragonal phase is essentially the same as the cubic phase described before with oxide anion vacancies in the 111 direction. Studying the transition between the cubic δ -phase and the tetragonal β -phase may give insight into the instability of the defect fluorite structure.

6.8.1. Refinement of δ -Bi₂O₃

The high temperature phase of δ -Bi₂O₃ was characterised using the Rietveld refinement method and X-ray diffraction data. The initial starting model used was the distorted defect fluorite structure (space group Fm3m) seen previously in the characterisation of the Bi₂O₃-Dy₂O₃ solid solutions. The X-ray diffraction data that were collected at 750, 700, 680, 670 and 660 °C were selected for analysis. The diffraction data were used in a structural refinement in order to study the change in the internal structure, from the high temperature down to the polymorphic transition, to β -Bi₂O₃ at 650 °C. Table 6.10 shows the atomic parameters, thermal parameters and cell parameters resulting from each refinement.

Table 6.10: Atomic parameters including isotropic thermal parameters and cell parameter a for each recorded temperature. Esd's are shown in parentheses

	750 °C	700 °C	680 °C	670 °C	660 °C
^a Bi ³⁺					
B _{iso} (Å ²)	3.8255	2.0181	1.8255	1.9250	1.7228
Esd	0.0647	0.1050	0.1192	0.1153	0.1169
^b O ²⁻					
X	0.288(9)	0.3043(25)	0.3090(22)	0.3278(36)	0.3228(29)
B _{iso}	3.1101	3.6312	5.5767	0.4587	3.0580
Esd	1.9613	1.1804	1.0691	1.4110	1.1425
Parameter a (Å)	5.6528(3)	5.6442(5)	5.6424(5)	5.6412(6)	5.6400(6)

^a Bi³⁺ is located on the 4a at coordinates (0,0,0)

^b O²⁻ is located on the 8c at coordinates (x,x,x)

The chart shown in figure 6.25 above shows the refined cell parameter a for $\delta\text{-Bi}_2\text{O}_3$ at each recorded temperature. As expected there is a gradual decrease in cell parameter a as the temperature is lowered due to the thermal expansion of the unit cell. The change in unit cell size however, appears to be less as the temperature reaches the transition point at 650 °C. This means that the greatest change in the refined cell parameters (0.0104 Å) occurs between 750 and 700 °C, this is four times the change between 700 and 660 °C (0.0024 Å). It was therefore hypothesised that the transition between $\delta\text{-}$ and $\beta\text{-Bi}_2\text{O}_3$ is driven by the reduction in cell size as the material is cooled. The small change in cell parameter below 700 °C could indicate the minimum stable cell size being reached and maintained in a metastable state. One effect the decrease in cell size would have is a shortening of the bond lengths within the structure. Bond valence calculations may indicate the source of the instability and a possible method of stabilisation.

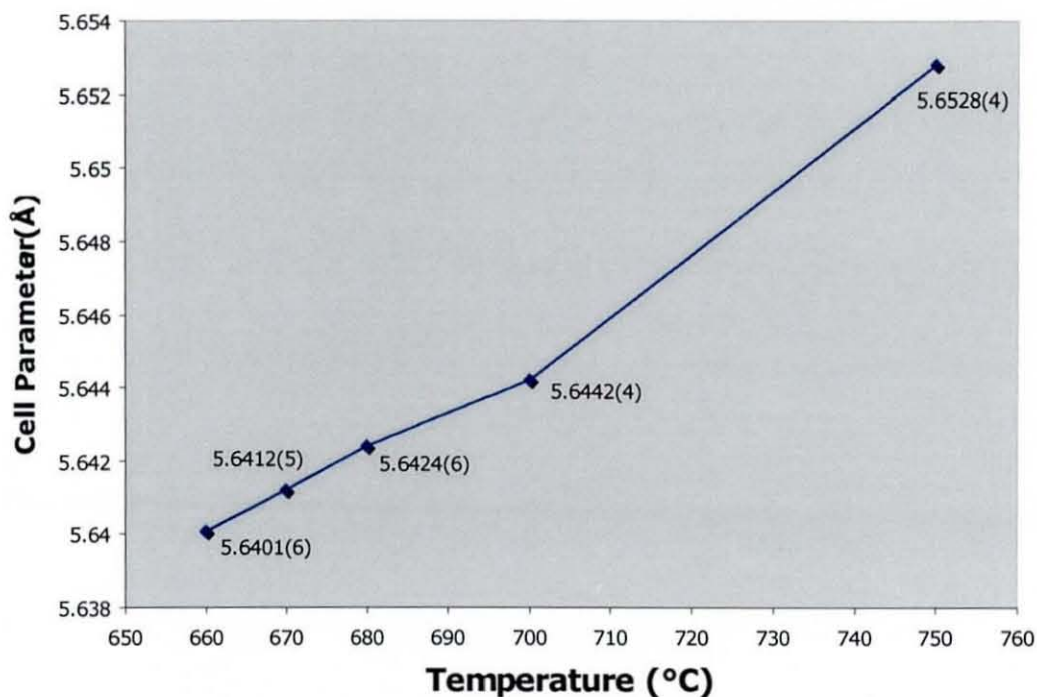


Figure 6.25: Refined cell parameters of $\delta\text{-Bi}_2\text{O}_3$ versus temperature.

Table 6.11: Bi-O bond lengths, associated bond valence and final Bi site valence at each refined temperature. Bond length esd's are shown in parentheses.

Temperature	Short Bonds		Long Bonds		Bi ³⁺ site valence
	Bond Length	Valence	Bond Length	Valence	
750 °C	2.350(16)	0.501	2.82(9)	0.141	2.877
700 °C	2.3216(30)	0.541	2.975(25)	0.092	3.001
680 °C	2.3157(22)	0.549	3.020(21)	0.082	3.026
670 °C	2.3036(8)	0.567	3.203(9)	0.05	3.064
660 °C	2.3049(13)	0.566	3.153(28)	0.057	3.071

The Bi-O bond lengths and their associated bond valences displayed in Table 6.11, are separated into a short and a long bond length as seen for the Bi₂O₃-Dy₂O₃ solid solutions previously. These two different lengths are caused by the distortions on the oxide site, which are related to the pyrochlore distortions described in Chapters 3 and 4. The resulting Bi³⁺ site valence has been calculated in the same manner as for the Bi₂O₃-Dy₂O₃ solid solutions and is described in detail here. The calculations show that the decrease in cell size due to the decreasing thermal influence causes the valence of the Bi³⁺ site to increase. The reduction in cell volume results in the space available for the Bi³⁺ cation and its lone pair to grow smaller. This also increases the disorder of the of the O²⁻ site as it is repelled away from the Bi cation, this is seen in an increase in the x coordinate as the oxygen moves further away from the undistorted location (1/4, 1/4, 1/4).

6.9. Conclusions

Samples have been prepared with the composition (Bi_{1-x}Ln_x)₂O₃ where Ln = Y, Er, Ho, Dy, Gd, Sm, Pr, Nd, La and have been analysed for use as inorganic pigments. Colour measurements have shown that the orange colouration of these compounds only occurs in rare-earths where the ionic radii are > 0.96. In compounds containing the larger rare-earths (*i.e.* Nd, Pr, La) the colour tended to

be dominated by the $f-f$ electronic transitions. For the smaller rare-earths orange coloured material were only present for the lower %mol concentrations of Ln, as the colour tended to lighten above a threshold concentration, which was dependent on the rare-earth in question.

X-ray diffraction techniques have shown that the best colouration is seen in compounds with the δ -Bi₂O₃ defect fluorite type structure. Unfortunately this phase is metastable at room temperature and changes over time to a more stable structure, which tends to reduce the colour properties.

Structural characterisation of the (Bi_{1-x}Dy_x)₂O₃ ($x = 0.225, 0.250, 0.275, 0.300$ and 0.325) phases has been used to select the correct structural model for the δ -Bi₂O₃ phase. Refinement results and bond valence calculations have shown that these compounds adopt a defect fluorite structure (Fm3m) with 14 of the anion sites vacant. The anion sites are also distorted off of their ideal location onto a site of lower symmetry. This is likely to be related to the Bi³⁺ lone pair, which repels the oxides away from the central site and towards the vacant octahedral holes where there is less electron density.

The high temperature X-ray diffraction study of B₂O₃ has allowed the observation of the loss of the δ -phase directly. The metastability of this defect fluorite phase seems to be linked to the reducing cell size as the material cools from high temperature. Once the cell size drops below 5.6400 Å there is not enough space within the fluorite cell to allow both the bismuth and its lone pair causing a transition to a more stable phase.

6.10. References

- ¹ L.G. Sillén, *Ark. Kemi. Mineral. Geog.* **12 A** (1937) 1
- ² W.C. Schume and E. S. Rittner, *J. Amer. Chem. Soc.* **65** (1948) 1055
- ³ G. Gattow and H. Schröder, *Z. anorg. allg. Chem.* **318** (1962) 176
- ⁴ G. Gattow and D Schütze, *Z. anorg. allg. Chem.* **328** (1964) 44
- ⁵ E.M. Levin and R.S Roth, *J. Res. Nat. Bur. Stand.* **68 A** (1964) 189
- ⁶ H. Harwig, *Z. anorg. allg. Chem.* **444** (1978) 151
- ⁷ T. Takahashi, H. Iwahara and Y. Nagai, *J. Appl. Electrochem.* **2** (1972) 97
- ⁸ H. Harwig, and A.G. Gerards, *J. Solid State Chem.* **26(3)** (1978) 265
- ⁹ M.J. Verkerk and A.J. Burggraaf, *Solid State Ionics* **3/4** (1981) 463
- ¹⁰ H.A. Harwig and A.G. Gerards, *Thermochim. Acta*, **28** (1979) 121
- ¹¹ W. Changzhen, X. Xiuguang and L. Baozhen, *Solid State Ionics*, **13** (1984) 135
- ¹² T. Takahashi, T. Esaka, and T. Arao, *J. Appl. Electrochem.* **5** (1975) 187
- ¹³ H. Iwahara, T. Esaka, T. Sato, and T. Takahashi, *J. Solid State Chem.* **39** (1981) 173
- ¹⁴ A. Watanabe and T. Kikuchi, *Solid State Ionics* **21** (1986) 287
- ¹⁵ P. Conflant, C. Follet-Houttemane, and M. Drache, *J. Mater. Chem.* **1** (1991) 649
- ¹⁶ A. Watanabe, M. Drache, J.P. Wignacourt, P. Conflant and J.C. Boivin, *Solid State Ionics*, **67** (1993) 25
- ¹⁷ A. Watanabe, *Solid State Ionics* **34** (1989) 35
- ¹⁸ M. Drache, P. Conflant, S. Obbade, and J. P. Wignacourt, *J. Solid State Chem.* **129** (1997) 98
- ¹⁹ A. Watanabe, *Solid State Ionics* **40/41** (1990) 889.
- ²⁰ A. Watanabe, *Solid State Ionics* **79** (1995) 84
- ²¹ A. Watanabe, *J. Solid State Chem.* **120** (1995) 32
- ²² B. Gonzalvoa, J. Romeroa, F. Fernández, M.J. Torralvoa, *J. Alloys Compounds*, **323** (2001) 372
- ²³ Joint Committee of Powder Diffraction Standards, 2002

Chapter 7
Structure and Properties of the
Egyptian Blue Series
(Ba,Ca,Sr)CuSi₄O₁₀

7.1. Introduction

The mineral cuprorivaite, which is better known as Egyptian Blue, is a naturally occurring material that is chemically known as calcium copper silicate ($\text{CaCuSi}_4\text{O}_{10}$). Egyptian blue been used as a pigment for thousands of years and was first used by the Egyptians in the third millennium BC,¹ and is widely considered as the first synthetic pigment. It was utilised in a variety of applications and was used to as to colour stone, wood, plaster, papyrus and canvas. The cuprorivaite mineral is closely related to both wesselsite ($\text{SrCuSi}_4\text{O}_{10}$) and effenbergerite ($\text{BaCuSi}_4\text{O}_{10}$), which form a group of naturally occurring silicate sheet minerals.^{2,3} Like cuprorivaite (Egyptian Blue), effenbergerite (Hans Blue) has also been used as a blue pigment since ancient times, and historic samples of both these materials have been investigated by a number of authors using both spectroscopy and X-ray diffraction.^{4,5,6}

The original composition of cuprorivaite was determined by Fouque⁷ by the chemical analysis of single crystals of the material. Later, powder diffraction data were reported by Jope and Huse⁸ for several powdered natural samples, although no intensity data were reported. More recently, these minerals have been synthesised and characterised by both X-ray and neutron diffraction,^{9,10} and their colour properties have been investigated.¹¹ Early studies by Pabst⁹ gave poorly defined parameters for the silicate layers of cuprorivaite due to the complexity of the structure and the quantity of light atoms.

Powder neutron diffraction data were used to successfully refine the structures and accurately determine the light atom positions using Rietveld methods by Hughes *et al.*,¹⁰ for $\text{MCuSi}_4\text{O}_{10}$ where M is a single alkali-earth cation. The layered copper silicates, $[\text{MCuSi}_4\text{O}_{10}]$ where M = Ca, Sr or Ba, are isostructural and crystallize in the tetragonal space group P4/ncc, $Z = 4$. The cell parameters increase anisotropically with the changing alkali-earth metal cation, where a decreases much less rapidly than c . The calcium analogue has cell parameters of $a=7.30 \text{ \AA}$, $c=15.10 \text{ \AA}$, while for strontium: $a = 7.37 \text{ \AA}$, $c = 15.59 \text{ \AA}$ and for barium: $a = 7.44 \text{ \AA}$, $c = 16.14 \text{ \AA}$. The structure is composed of rings of four SiO_4 tetrahedra, $[\text{Si}_4\text{O}_{10}]_4$, which are linked together by square-planar coordinated

copper. Each SiO_4 tetrahedron is connected to two neighbouring tetrahedra in the same ring and a third from a different ring. The rings are connected together by square-planar coordinated copper to form double copper silicate layers which are joined by alkali-earth cations in a distorted cubic geometry. The incorporation of different alkali-earth metal cations is possible due to the flexibility of the layered structure (Figure 7.1). One phenomenon that has been observed in the natural materials is that bright natural light can cause dulling of the colour of these materials.¹² The chemical cause of this darkening has not been identified. This work investigates the structural and colour properties of $(\text{M}_{1-x}\text{M}_x)\text{CuSi}_4\text{O}_{10}$ materials containing solid solutions of the alkali-earth cations, in order to obtain a greater understanding of the colour mechanism and the structural stability of these materials. The effect of strong light sources on the samples was also examined to generate a hypothesis to explain the colour loss in bright light.

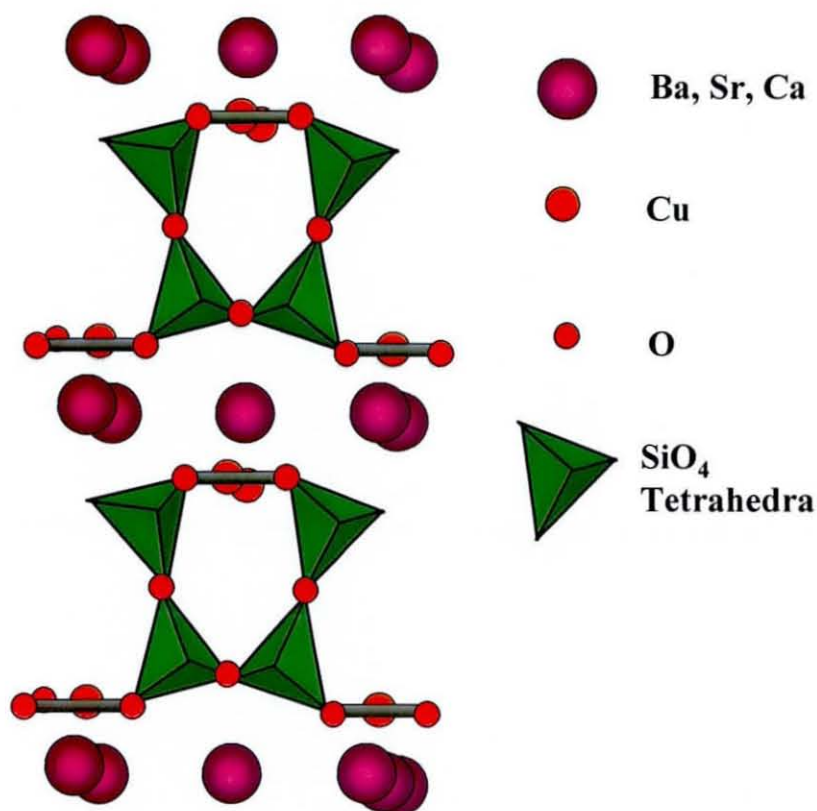


Figure 7.1: Layered structure of $\text{BaCuSi}_4\text{O}_{10}$ showing silica ring network connected by square-planar coordinated copper, interspersed by barium cations

7.2. Experimental

$(M_{1-x}M'_x)CuSi_4O_{10}$ where M and M' are Ca, Sr or Ba were synthesised using conventional solid state reactions. SiO_2 , $CaCO_3$, $SrCO_3$, $BaCO_3$ and CuO were ground in a pestle and mortar, in the correct stoichiometric proportions to form a homogeneous mixture. The mixture was placed in alumina boats and fired at $1000\text{ }^\circ\text{C}$ for 16 h. After cooling the products were reground and re-fired at $1000\text{ }^\circ\text{C}$ for another 16 h.



The products were washed initially by stirring in concentrated HCl to remove any unreacted starting materials before washing with distilled water and then air dried.

7.3. X-ray Diffraction Analysis

Preliminary powder X-ray diffraction data were collected on a Phillips X'pert diffractometer operating with copper radiation using a scintillation counter. High quality powder X-ray diffraction data were collected in the 2θ range $10\text{-}100^\circ$ with a step size of 0.015° over a period of 13 h, for analysis using the Rietveld method. Rietveld refinements were performed on the data using the GSAS¹³ suite of programs.

7.4. UV/VIS Colour Measurements

Diffuse reflectance UV/Vis were collected on undiluted ground powdered samples over a range $300\text{-}1000\text{ nm}$ using a Perkin Elmer Lambda 35 Spectrophotometer operating with WINLAB 4.2 software and colour parameters were determined using Colour Methods V3.0 software. The data were corrected using the Kubelka Munk function in order to obtain absorption maxima, and normalised to the highest intensity.

7.5. Results

Initial X-ray diffraction results showed that the formation of a $M_{1-x}M'_x\text{CuSi}_4\text{O}_{10}$ solid solution occurred across the whole series of x for a mixture of both calcium and strontium or strontium and barium cations. In both these cases a single phase was formed containing a mixture of the two alkali-earth cations. It was, however, not possible to produce a solid solution consisting of a mixture of calcium and barium cations. In the latter case, a dual phase system of $\text{CaCu}_4\text{O}_{10}$ and $\text{BaCu}_4\text{O}_{10}$ resulted with relative proportions dependent on the ratio of the alkali-earth cations in the original reaction mixture.

7.5.1. X-ray Diffraction

The starting model used for the structural refinement of the X-ray diffraction data, for both the calcium-strontium solid solution and the strontium-barium solid solution, was taken from the work of Pabst.⁹ The structure consists of one site for the alkali-earth metal, one site for the copper centre and a single site for the four silicon cations. There are two oxide anion sites incorporated within the structure, which have very distinct structural environments. The first site (O1) corresponds to the oxide anions of the copper square planar unit, which separate the alkali-earth cations from the silicate layers. The second site (O2) corresponds to the oxide anions within the Si_4O_{10} silicate rings, which are linked together by the copper centres.

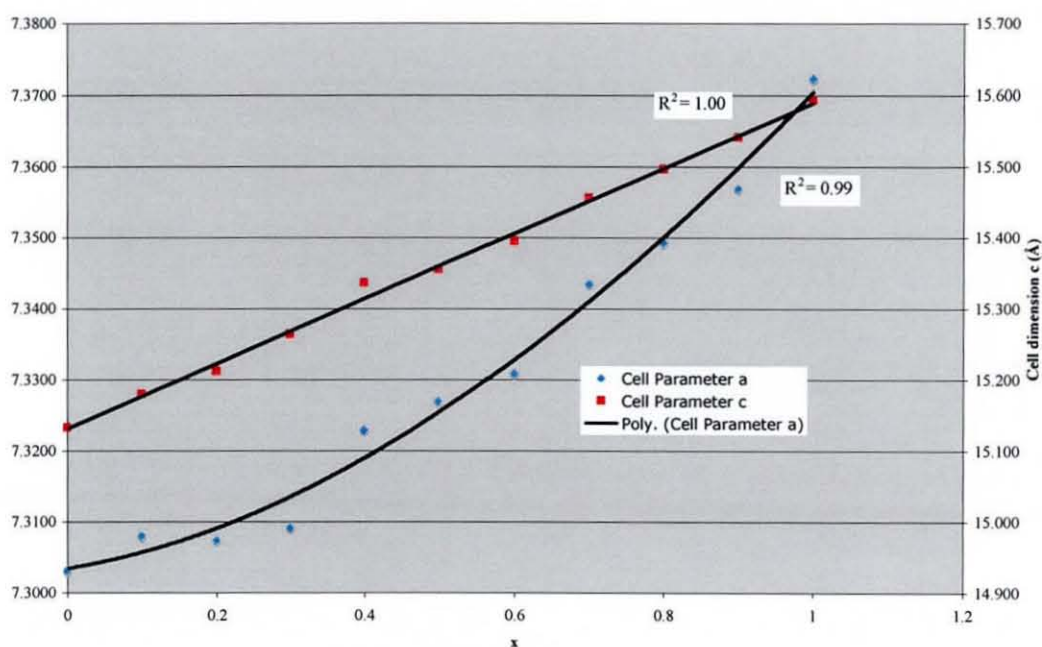
The relative ratios of the alkali-earth metals were assumed to be approximately the same as the ratio of BaCO_3 and SrCO_3 used in the reaction. No other impurity was detected that would indicate that all of the reactant was not present in the final solid solution, and these ratios were later confirmed by elemental analysis.

7.5.1.1. Calcium-Strontium Solid Solution $\text{Ca}_{1-x}\text{Sr}_x\text{CuSi}_4\text{O}_{10}$

Table 7.1 shows the refined cell parameters of the solid solution series along with the wRp and the χ^2 value. R factors were refined below 5% and the χ^2 values are below 10% showing good agreement with the observed data.

Table 7.1: Refinement results and refined cell parameters for $\text{Ca}_{1-x}\text{Sr}_x\text{Cu}_4\text{O}_{10}$

x	Rwp	χ^2	$a(\text{\AA})$	$c(\text{\AA})$
0	0.039	4.28	7.3032(6)	15.133(1)
0.1	0.0533	7.81	7.308(1)	15.180(3)
0.2	0.0448	4.29	7.3074(8)	15.212(2)
0.3	0.0365	3.65	7.3092(7)	15.264(1)
0.4	0.0483	6.81	7.323(2)	15.337(3)
0.5	0.0365	3.77	7.3270(7)	15.355(1)
0.6	0.0389	4.3	7.3309(9)	15.395(2)
0.7	0.0388	4.56	7.3435(8)	15.456(2)
0.8	0.0342	3.53	7.3493(6)	15.496(1)
0.9	0.0336	3.39	7.3569(4)	15.541(1)
1	0.0448	6.03	7.3723(5)	15.593(1)

**Figure 7.2:** Anisotropic change in lattice parameters a and c of $\text{Ca}_{1-x}\text{Sr}_x\text{CuSi}_4\text{O}_{10}$ with x .

As expected the refined cell parameters increase significantly with the replacement of calcium with the larger strontium cation. There is, however, a noticeable difference in the amount of size change that occurs for parameter a

(0.07 Å) compared to parameter b (0.46 Å). It also appears, looking at Figure 7.2, that the a parameter increases as a function of power while the cell dimension c increases linearly. The increase in cell size with amount of strontium in the solid solution is shown in Figure 7.2 and the increase in volume with respect to x is shown in Figure 7.3.

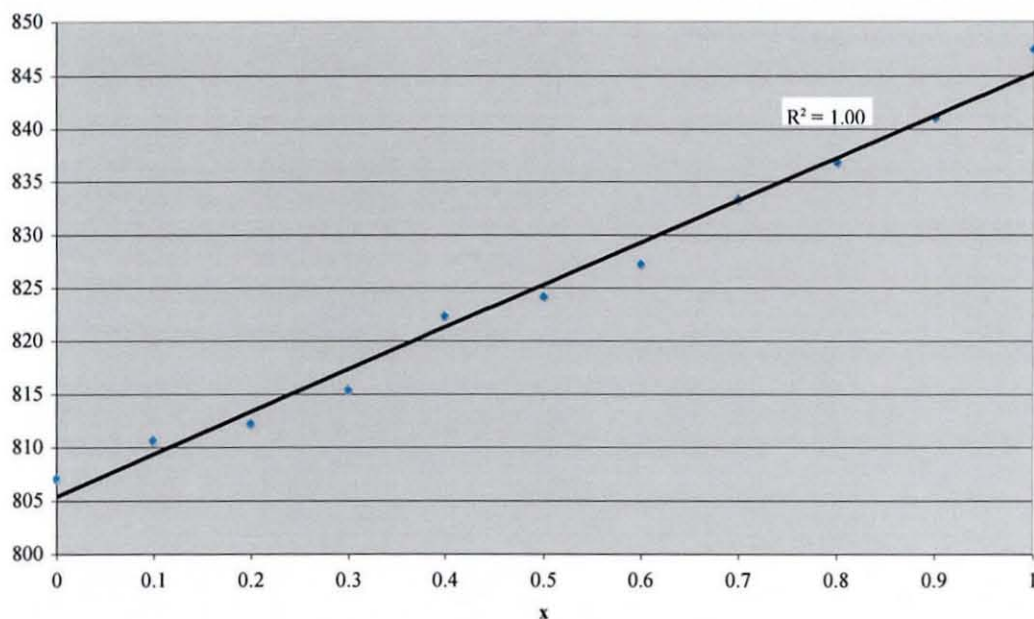
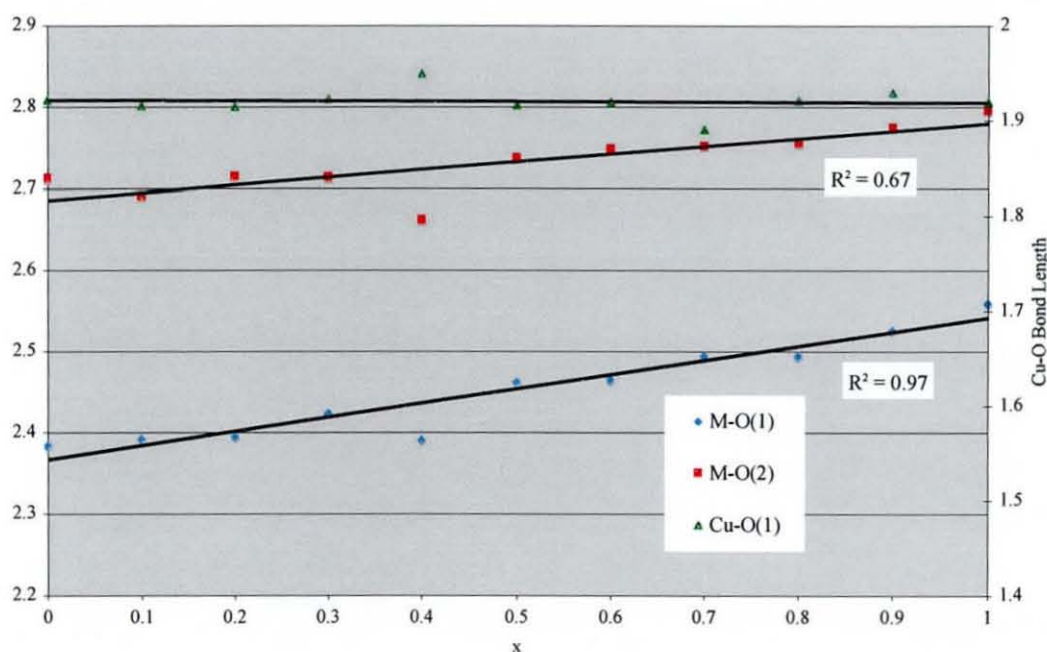


Figure 7.3: Isotropic change in cell volume of $\text{Ca}_{1-x}\text{Sr}_x\text{CuSi}_4\text{O}_{10}$ with x .

It is clear, from the calculated bond lengths (Table 7.2), that the Cu-O bond lengths remain constant at approximately 1.9 Å, despite the increasing strontium levels. This shows that replacing calcium with strontium has little effect on the bond distances within the $[\text{Si}_4\text{O}_{10}]_4$ ring, where the copper square-plane links four of these units together. Since the Si-O bond lengths also remain constant at 1.6 Å, it is apparent that the double layers are also relatively unaffected by the changing alkali-earth metal cation.

Table 7.2 Metal-oxide bond lengths in $\text{Sr}_{1-x}\text{Ba}_x\text{Cu}_4\text{O}_{10}$

x	M-O1(Å)	M-O2(Å)	Cu-O(Å)
0	2.385(3)	2.713(3)	1.922(3)
0.1	2.393(5)	2.692(5)	1.916(5)
0.2	2.396(4)	2.715(4)	1.915(4)
0.3	2.425(4)	2.714(3)	1.923(3)
0.4	2.392(7)	2.663(6)	1.950(6)
0.5	2.463(4)	2.738(3)	1.917(3)
0.6	2.466(4)	2.749(3)	1.920(4)
0.7	2.495(4)	2.752(3)	1.891(4)
0.8	2.495(3)	2.756(3)	1.921(3)
0.9	2.527(3)	2.775(2)	1.930(3)
1	2.560(4)	2.795(3)	1.920(3)

**Figure 7.4:** Change in derived metal-oxygen bond lengths in $\text{Ca}_{1-x}\text{Sr}_x\text{CuSi}_4\text{O}_{10}$ with x

In contrast to the Cu-O bonds, the two bond lengths around the eight-fold alkali-earth metal cation clearly lengthen as the larger strontium cation replaces the smaller calcium cation. This lengthening occurs in an anisotropic manner, where the bonding interaction to the oxygen involved in the copper-oxygen square-plane lengthens more rapidly than the alkali-metal-O bonding interaction to the

oxygen within the Si-O ring. In effect, the overall structure of the copper-silicate layers remains unchanged by the addition of the strontium cation. It is the distance between these layers that undergoes the most significant alteration as it widens to incorporate the larger cation.

7.5.2. Strontium-Barium Series

Table 7.3 shows the refined cell parameters for the strontium barium solid solutions as well as the weighted R factor and the χ^2 for the refinement. The refinement results were within acceptable limits with R_{wp} less than 5% and χ^2 less than 10% for the whole series.

Table 7.3: Refinement results and refined cell parameters for $\text{Ca}_{1-x}\text{Sr}_x\text{Cu}_4\text{O}_{10}$

x	R_{wp}	χ^2	$a(\text{\AA})$	$c(\text{\AA})$
0	0.0448	6.03	7.3723(5)	15.593(1)
0.1	0.0526	7.21	7.3695(6)	15.640(1)
0.2	0.0453	4.88	7.3816(7)	15.713(1)
0.3	0.0556	6.76	7.384(1)	15.775(2)
0.4	0.0487	3.5	7.3932(9)	15.842(2)
0.5	0.0584	5.97	7.3925(7)	15.886(2)
0.6	0.0413	2.75	7.4011(5)	15.942(1)
0.7	0.0413	2.75	7.4116(6)	16.005(1)
0.8	0.0394	2.39	7.4187(4)	16.044(1)
0.9	0.0579	4.62	7.4287(5)	16.087(1)
1	0.0546	4.18	7.4378(3)	16.124(6)

The situation in the strontium-barium solid solution mirrors that of calcium-strontium series seen earlier. The cell parameters, a and c , increase anisotropically as the level of barium in the solid solution increases across the series. The difference in the increase in parameter a (0.07 Å) and c (0.531 Å) is still very apparent. The change in the size of parameter c is slightly larger in the strontium-barium series than in the calcium-strontium series seen previously. This is due to the difference in size between the radii of the two alkali-earth

metals, which is much larger between in strontium and barium than between strontium and calcium.

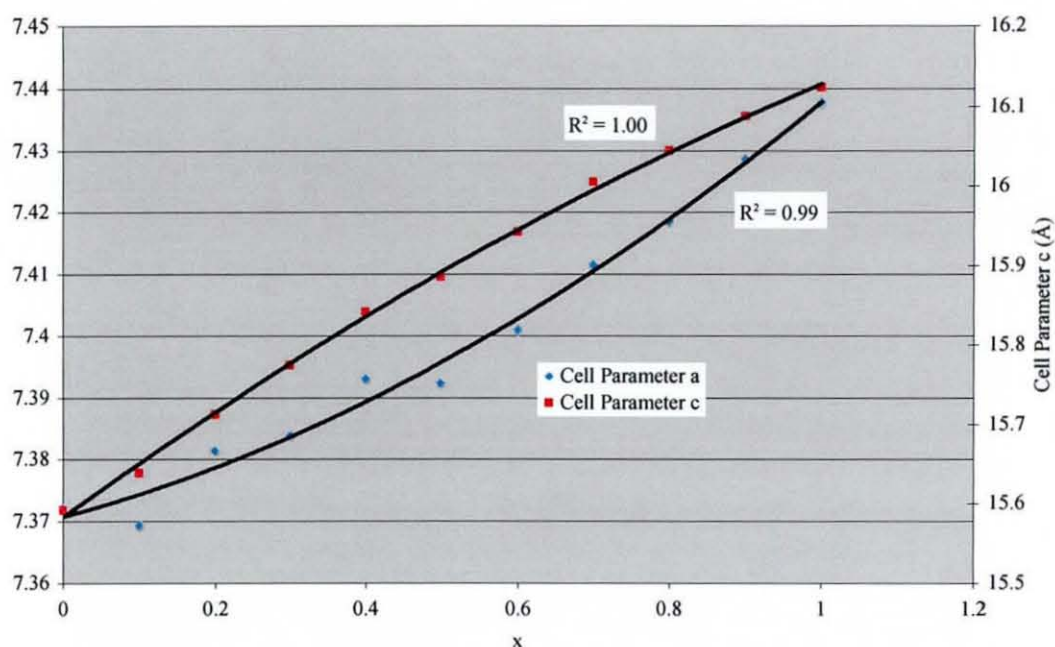


Figure 7.5: Change in lattice parameters a and c of $\text{Sr}_{1-x}\text{Ba}_x\text{CuSi}_4\text{O}_{10}$ with x .

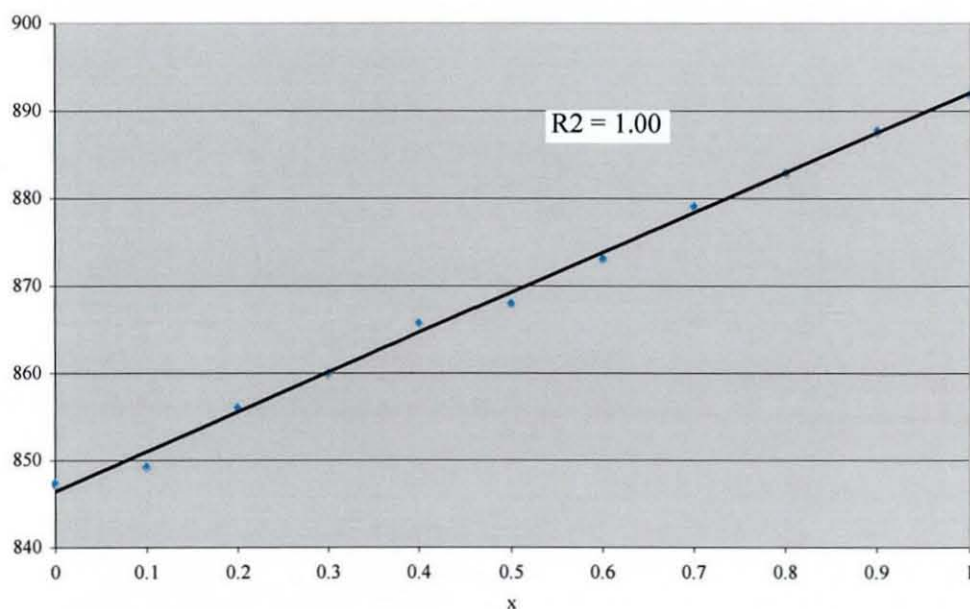


Figure 7.6: Isotropic change in cell volume of $\text{Sr}_{1-x}\text{Ba}_x\text{CuSi}_4\text{O}_{10}$ with x .

The calculated metal-oxide bond lengths are shown in Table 7.4 below. As for the calcium-strontium series the Cu-O(1) bond length remains virtually constant across the whole range. This is also true of the alkali-earth oxide bonds lengths

where a much larger change in the M-O1 bond length is observed compared with the M-O2 bond length (Figure 7.8). Similarly, the geometry of the species within the silicate double layer remains relatively unchanged, while the distance between the layers increases to accommodate the larger alkali-earth metal cation.

Table 7.4: Metal-oxide bond lengths in $\text{Sr}_{1-x}\text{Ba}_x\text{Cu}_4\text{O}_{10}$

x	M-O1 (Å)	M-O2 (Å)	Cu-O (Å)
0	2.560(4)	2.795(3)	1.920(3)
0.1	2.564(5)	2.804(4)	1.906(5)
0.2	2.604(5)	2.835(4)	1.923(4)
0.3	2.627(7)	2.867(5)	1.907(5)
0.4	2.652(7)	2.867(5)	1.912(5)
0.5	2.679(7)	2.888(5)	1.921(5)
0.6	2.687(5)	2.894(4)	1.919(4)
0.7	2.714(6)	2.897(4)	1.930(5)
0.8	2.738(4)	2.906(3)	1.915(3)
0.9	2.762(7)	2.895(4)	1.936(5)
1	2.795(5)	2.929(4)	1.920(4)

Although both strontium-barium and calcium-strontium give a solid solution across the full series of x , no sign of a solid solution was ever observed between calcium and barium for any value of x . The likely cause of this must be due to the difference in size of the cations. Since these cations are acting as a spacer between the layers and no major structural change occurs within the silicate layers, it can be hypothesised that the large size mismatch between calcium and barium could cause an instability in the structure causing phase separation, where the difference between the Ca-O and Ba-O bond lengths is substantial (0.4 Å). This large difference in bond lengths would cause the interlayer distance required to stabilize the calcium cation would be too small to allow the inclusion of the larger barium. Conversely the distance that would allow the inclusion the barium cation is too large to stabilize the calcium cation.

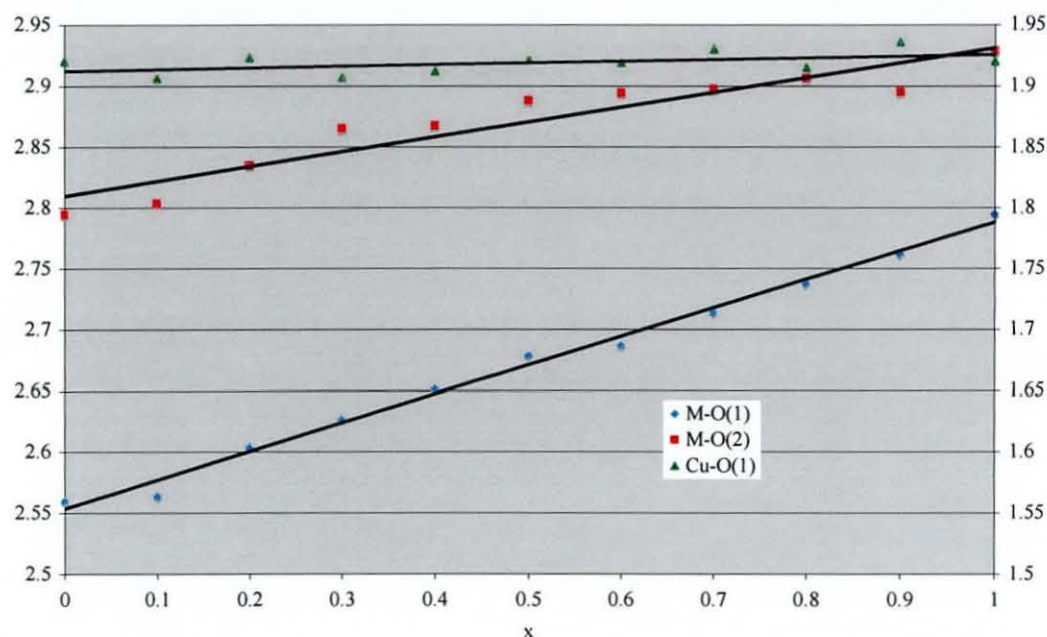


Figure 7.8: Change in derived metal-oxygen bond lengths in $\text{Sr}_{1-x}\text{Ba}_x\text{CuSi}_4\text{O}_{10}$ with x

7.5.3. UV-Vis

A typical UV-Vis electronic spectrum for the Ca/Sr series for the $\text{Ca}_{0.5}\text{Sr}_{0.5}\text{CuSi}_4\text{O}_{10}$ sample is shown in Figure 7.6 and is similar to those obtained previously^{10,14,15}.

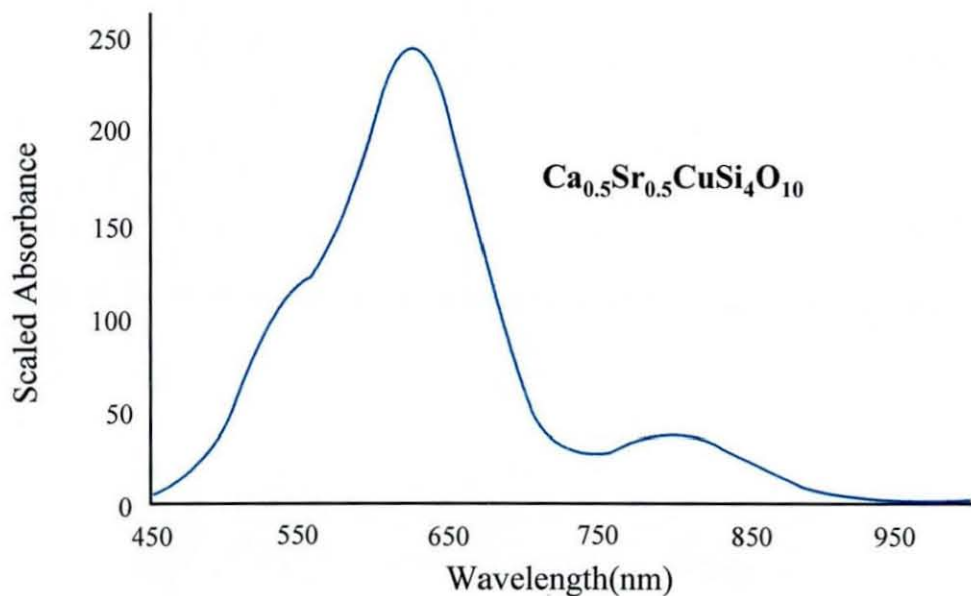


Figure 7.9: Kubelka-Munk corrected UV-Vis spectrum of the $\text{Ca}_{0.5}\text{Sr}_{0.5}\text{CuSi}_4\text{O}_{10}$

The three broad transitions observed in the visible region originate from $d-d$ transitions which are weakly allowed, despite approximate D_{4h} symmetry at the copper centre, due to vibronic coupling. The three transitions occur in near identical wavelengths in the series at 800 nm (${}^2B_{1g} \rightarrow {}^2B_{2g}$), 630 nm (${}^2B_{1g} \rightarrow {}^2E_g$) and 540 nm (${}^2B_{1g} \rightarrow {}^2A_{1g}$).

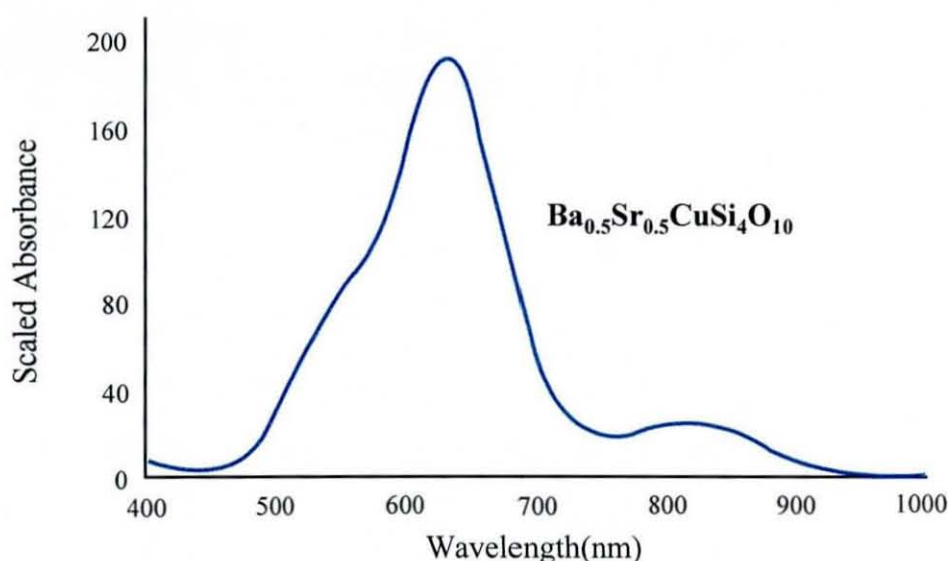


Figure 7.10: Kubelka-Munk corrected UV-VIS spectrum of the $\text{Ca}_{0.5}\text{Sr}_{0.5}\text{CuSi}_4\text{O}_{10}$

Table 7.5: Absorption maxima for the Ca-Sr and Sr-Ba phases

x	$\text{Ca}_{1-x}\text{Sr}_x\text{CuSi}_4\text{O}_{10}$		$\text{Sr}_{1-x}\text{Ba}_x\text{CuSi}_4\text{O}_{10}$	
	Absorption Maxima (nm)		Absorption Maxima (nm)	
0	626	794	623	801
0.1	627	794	626	803
0.2	630	799	626	805
0.3	629	798	628	811
0.4	629	797	628	811
0.5	628	803	631	817
0.6	626	801	630	817
0.7	627	799	630	817
0.8	626	801	629	821
0.9	626	799	628	818
1	624	799	627	820

A typical UV/vis reflectance spectrum for the barium-strontium series for the $\text{Sr}_{0.5}\text{Ba}_{0.5}\text{CuSi}_4\text{O}_{10}$ sample is shown in Figure 7.10. The first maximum is shifted to a lower wavelength in comparison to the calcium-strontium series (Figure

7.9). The three transitions occur in near identical wavelengths throughout the series at 820 nm ($2B_{1g} \rightarrow 2B_{2g}$), 630 nm ($2B_{1g} \rightarrow 2E_g$) and 540 nm ($2B_{1g} \rightarrow 2A_{1g}$). There is possibly a small shift to lower wavelength for the ($2B_{1g} \rightarrow 2B_{2g}$) transition, although due to the width and overlap of the bands, it is impossible to ascertain how accurately these bands can be deconvoluted.

Colour parameters for these systems are summarised in Table 7.6 and indicate no obvious trend in the colour parameters although a visible lightening of the colour of the sample is apparent with the naked eye. Attempts were also made to record the Raman data using the 633 nm laser line but only poor quality data could be collected. Examination of the samples after treatment with the laser showed that the samples were dotted with grey spots. The reason for this colour loss is discussed in further detail later.

Table 7.6: $L^*a^*b^*$ colour measurement results for the $Ca_{1-x}Sr_xCuSi_4O_{10}$ solid solution

Composition	L^*	a^*	b^*
$CaCuSi_4O_{10}$	86.54	-4.62	-17.40
$Ca_{0.8}Sr_{0.2}CuSi_4O_{10}$	81.68	-4.10	-18.49
$Ca_{0.6}Sr_{0.4}CuSi_4O_{10}$	84.44	-4.46	-19.24
$Ca_{0.4}Sr_{0.6}CuSi_4O_{10}$	83.19	-4.59	-19.49
$Ca_{0.2}Sr_{0.8}CuSi_4O_{10}$	85.94	-4.90	-18.65
$SrCuSi_4O_{10}$	82.79	-6.50	-23.52

Unlike the data for the calcium-strontium series, the colour parameters of the strontium-barium series (Table 7.7) clearly show a correlation between the colour parameters and the cations within the unit cell. As the barium content increases there is an increase in the overall absorption of the sample and a decrease in the L^* value. There is also a decrease in both the a^* colour coordinate, as it moves away from the red towards the blue, and the b^* coordinate as it moves through yellow towards the green. The samples visibly lighten in colour as the barium content increases

Table 7.7: L*a*b* colour measurement results for the
 $\text{Sr}_{1-x}\text{Ba}_x\text{CuSi}_4\text{O}_{10}$ solid solution

Composition	L*	a*	b*
$\text{SrCuSi}_4\text{O}_{10}$	82.79	-6.50	-23.52
$\text{Sr}_{0.8}\text{Ba}_{0.2}\text{CuSi}_4\text{O}_{10}$	81.8	-7.02	-24.55
$\text{Sr}_{0.6}\text{Ba}_{0.4}\text{CuSi}_4\text{O}_{10}$	78.57	-7.11	-28.59
$\text{Sr}_{0.4}\text{Ba}_{0.6}\text{CuSi}_4\text{O}_{10}$	77.31	-7.53	-28.19
$\text{Sr}_{0.2}\text{Ba}_{0.8}\text{CuSi}_4\text{O}_{10}$	75.07	-7.53	-29.76
$\text{Ba}_{0.2}\text{CuSi}_4\text{O}_{10}$	76.23	-7.98	-29.91

Samples left in bright sunlight for long periods (*ca.* 12 weeks) showed a notable darkening with time. in comparison to those kept in a brown glass jar. Powder X-ray diffraction analysis of the light aged samples showed a small amount of copper oxide in the X-ray pattern after light exposure. Tenorite (CuO) has also been detected in powdered samples of natural Egyptian Blue and was assumed to have been generated by aerial oxidation. However, since Egyptian Blue contains copper in the divalent state, it is more likely that the compound is showing light instability rather than air instability as confirmed by the colour loss caused by irradiation of the samples with high intensity laser light during the attempted Raman experiment. Degradation by bright light may therefore be the cause of the darkening observed in the historic samples.¹²

7.6. Conclusions

Analysis of the layered copper silicate solid solutions of $\text{Ca}_{1-x}\text{Sr}_x\text{CuSi}_4\text{O}_{10}$ and $\text{Sr}_{1-x}\text{Ba}_x\text{CuSi}_4\text{O}_{10}$ have shown them to be isostructural over the whole range from $x = 0 - 1$. The structure consists of alternating silicate layers and alkali-earth metals with copper square planer groups separating them. The composition of the alkali-earth metal within the copper silicate layers plays little part in the structure of the layers themselves. The main change is in the alkali-earth bond lengths, which increase or decrease depending on the size and proportions of the cations between the layers. The main restriction on the composition of the alkali-earth layer is that the no compositions exist between Ca^{2+} and Ba^{2+} due to the size difference between them. In this case no interlayer distance can be found which

stabilizes both cations simultaneously. Colour measurements showed that there was no significant difference in the colour properties of each compound, though a visible lightening of the compounds could be observed. The degradation of samples during a Raman experiment showed evidence that these phases are light sensitive explaining the loss of colour in historical samples.

7.7. References

-
- ¹ H. Jaksch, W. Seipel, K.L. Weiner, A. Elgoresy, *Naturwissen* **70** (1983) 525
- ² G. Giester, B. Rieck, *Miner. Mag.* **58** (1994) 663
- ³ G. Giester, B. Rieck, *Miner. Mag.* **60** (1996) 795
- ⁴ P. Mirti, A. Appolonia, A. Casoli, R.P. Ferrari, E. Laurenti, A.A. Canesi *Spectrochim. Acta A*, **51** (1995) 437
- ⁵ M.C. Edreira, M.J. Feliu, C. Fernandex-Lorenzo, J. Martin, *Helv. Chim. Acta*, **86** (2003) 29
- ⁶ S. Bouherour, H. Berke, H.G. Wiedemann, *Chimia*, **55** (2001) 942
- ⁷ F. Fouque, *Bull. Soc. Fr. Miner.* **12** (1889) 36
- ⁸ E.M. Jope, G. Huse. *Nature*, **146** (1946) 26
- ⁹ A. Pabst, *Acta Crystallogr.* **12** (1959) 733
- ¹⁰ E. M. Hughes, M.J. Pack, S.E. Dann, M.T. Weller. *An Quim*, **93** (1997) 233
- ¹¹ I.L. Botto, E.J. Baran, G. Minelli. *An. Assoc. Quim. Argent.* **75** (1987) 429
- ¹² Daniels V. Natural History Museum, Personal Communication.
- ¹³ R.C. Larson and R. von Dreele *GSAS 'Generalised structure analysis system'*; 1986, MS805 LANSCE.
- ¹⁴ M.G. Clark, R.G. Burns, *J. Chem. Soc. A*, (1967) 1034
- ¹⁵ M.G. Clark, R.G. Burns, *Inorg. Chem.* **5** (1966) 1268

Chapter 8
Summary and Further Work

8. Summary and Further Work

A large proportion of the work reported in this thesis has concentrated on the structure and properties of pyrochlore compounds. Particular reference has been given to the tin niobate pyrochlores mainly because of their potential application as inorganic pigments. The combination of the high chemical and thermal stability of this particular structure, the intense yellow colouration that arises and the easy synthetic route, makes them an ideal material for high temperature pigments. The complex structure of these materials is both problematic towards understanding and characterising these compounds, but also essential to the final pigment properties.

Tin niobium oxide was perhaps the first pyrochlore structure reported with stereoactive lone pairs on the *A* cation site. Although there are now other examples, which have been discussed in previous chapters, none of these examples are as profoundly affected by the presence of a lone pair as the tin niobates. The active lone pair on the Sn^{2+} cation is instrumental to the formation of the pyrochlore structure, much more so than in other examples. The Sn^{2+} cation on its own would normally be too small to form a cubic pyrochlore compound with Nb^{5+} . It is for this reason that the cadmium niobate pyrochlores have a smaller cell parameter than the tin niobates (10.4 Å vs. 10.6 Å) even though the Cd^{2+} cation is much smaller than Sn^{2+} (0.9 Å vs. 0.7 Å). Even though the Sn^{2+} cation would normally be considered too small for this pyrochlore structure, the Sn^{2+} and the lone pair cannot fit on the *A* cation site. This causes the Sn^{2+} cations to distort off of their ideal site to create the space required.

As well as the *A* cation site the lone pair also extends its influence to the *O'* anion site also. The Sn^{2+} lone pair may effectively increase the size of the cation; however these electrons are not involved in the bonding arrangement of the metal centre. This means that on a normal *O'* *8a* site the bond length to Sn^{2+} is much longer than is normally observed. This problem is fixed by the static displacement of the anion site towards the tin anion shortening the bonds and stabilising the metal centre. The anion distortion causes other problems, as in order to maintain the stability of the structure some of the *A* cation site must now be vacant to avoid the use of sites surrounded by the longer bonds created.

This sequence of requirements leads to the non-stoichiometric distorted pyrochlore seen in this thesis.

It has been said previously that not only is the lone pair the driving force behind the structural anomalies of the tin niobate pyrochlore, it is also essential to the final pigment properties. As discussed in Chapter 3 there seems to be a high degree of mixing between of the niobium *d*-orbitals and the vacant tin *p*-orbitals. This gives a convenient charge-transfer pathway between the Sn^{2+} lone pair and the vacant Nb^{5+} . This kind of mechanism is the most obvious cause of the tin niobates intense colouration, especially since neither Sn^{2+} nor Nb^{5+} has any available *d* or *f* electrons. The utilisation of this charge transfer pathway could be the route to future inorganic pigments. By choosing elements with the same electronic configuration it may be possible to recreate this transition in related compounds. A good example of this is the replacement of Nb^{5+} with cations of the same electronic configuration such as Mo^{6+} . Tin niobates which have been doped with small amounts of Mo^{6+} , become dark brown/black in colouration, even with concentrations as low as 1 mg per 100 g. Although the pigment properties of these compounds are not ideal the principle of recreating the charge transfer pathway is still demonstrated.

Although the pigment properties of the tin niobium oxides are impressive both from the point of view of the stability and for their vibrant yellow colour, their properties can be enhanced further by the addition of a chalcogenide anion. The formation of an oxysulfide or oxyselenide causes a change in colour from yellow to orange to red depending the amount of oxychalcogenide added. The formation of oxychalcogenide pyrochlores is very rare and only one other example is known. The successful formation of cadmium niobium oxysulfide ($\text{Cd}_2\text{Nb}_2\text{O}_6\text{S}$) is proof that these materials can exist. Since one whole sulfur unit is present in the cadmium niobium pyrochlores the maximum dopant level of 0.3 from the tin niobium compounds should also be possible. The reason for the inability of the tin niobates to accept more sulfur is probably linked to the lone pair, which will take up extra room in the unit cell leaving less space for the large sulfide anions.

It seems that the best way of increasing the pigment properties of the oxysulfides would be to increase the amount of sulfide in the system. Unfortunately the lone pair, which seems to inhibit the amount of sulfide in the cell is also thought to be the cause of the intense colour. It may be possible to replace some of the Sn^{2+} centres with another metal, which may allow the addition of extra sulfide anions. The perfect metal centre for this purpose would be Cd^{2+} since this forms oxysulfide pyrochlores as well. The use of cadmium however would no longer be environmentally friendly. It may be possible however to use a similar sized ion such as Ca^{2+} instead.

The fact that the only two pyrochlore oxysulfides are both niobates seems more than coincidental. The reason why sulfide can be used in these compounds and in no other pyrochlore is not understood. Further research is needed to understand the mechanism which makes niobate oxysulfides stable, and to therefore design new sulfur containing pyrochlores. Other niobate pyrochlores need to be tested to see whether this is a common occurrence or just a peculiarity of these two phases.

Aside from the work on the pyrochlore phases, two other groups of compounds were studied for use as inorganic pigments. The first group were the rare-earth bismuth oxides have been studied for use as light orange pigments. Previous work on these compounds concentrated on the oxide conduction properties of the $\delta\text{-Bi}_2\text{O}_3$ defect fluorite phase. Compounds of the composition $(\text{Bi}_{1-x}\text{Ln}_x)_2\text{O}_3$ where $\text{Ln} = \text{Y}, \text{Er}, \text{Ho}, \text{Dy}, \text{Gd}, \text{Sm}, \text{Nd}, \text{Pr}, \text{La}$, and $x = 0 - 1$ were synthesised and studied both by X-ray diffraction and colour measurement. X-ray diffraction was used to show that the Ln concentration where certain structures were stable was dependent on the ionic radii of the lanthanide in question. For example a hexagonal phase appeared at low Ln concentrations, but the larger the lanthanide the more could be inserted into the structure. The opposite was true of the tetragonal structure which appeared at high Ln concentrations.

X-ray diffraction of dysprosium samples showed that the defect fluorite structure can only be stabilised at room temperature with lanthanides of smaller ionic radii. The lanthanide used must have a significantly different ionic radii to

Bi^{3+} in order to stabilise the structure. Comparison of the dysprosium samples with high temperature diffraction data of the $\delta\text{-Bi}_2\text{O}_3$ phase showed that once the cell drops below a threshold size the structure becomes unstable. As the temperature of the Bi_2O_3 phase was reduced the cell size dropped and eventually the structure became unstable. By substituting in smaller Ln cations for the Bi^{3+} the threshold cell size where the structure became unstable was reduced. This allowed the temporary stabilisation of these phases at low temperature for a short time.

The final group of phases reported were the alkali-earth copper silicates, which form a layered structure alternating between alkali-earth sheets and copper silicate layers. Samples of the composition $\text{M}_{1-x}\text{M}^*_x\text{CuSi}_4\text{O}_{10}$ where M and $\text{M}^* = \text{Ca}, \text{Ba}$ and Sr were synthesised and analysed using X-ray diffraction techniques and colour measurement. X-ray diffraction showed that phases containing Ca and Sr could be formed and similarly phase with Sr and Ba could also be made. No material could be synthesised using both Ca and Sr however due to the large size difference between the ions. Colour measurements showed that there was very little difference between the synthesised compounds even though a visible lightening of the samples could be seen.

